Explorations in de Sitter Space and Amorphous Black Hole Bound States in String Theory

Explorations in de Sitter Space and Amorphous Black Hole Bound States in String Theory

A dissertation presented

by

Tarek Anous

to

The Department of Physics

in partial fulfillment of the requirements

for the degree of

Doctor of Philosophy

in the subject of

Physics

Harvard University

Cambridge, Massachusetts

May 2013

Thesis advisor

Frederik Denef

Author

Tarek Anous

Explorations in de Sitter Space and Amorphous Black Hole Bound States in String Theory

Abstract

This dissertation is split into two distinct halves. The first covers various calculations done in order gain insights on holography in de Sitter space. The dispersion relation of linear perturbations of empty de Sitter space are numerically computed as a function of the location of a hypersurface on which conformal Dirichlet boundary conditions are imposed. When the hypersurface is near the south pole, the dispersion relation is linear, whereas for a hypersurface near the cosmological horizon, it satisfies that of the incompressible Navier-Stokes equation. This result is shown to hold for non-linear perturbations. We also compute the thermodynamic stability of rotating black holes in dS_4 as a function of their mass and angular momentum. We focus particularly on the rotating Nariai geometry, which is a near horizon limit of the rotating black hole as the outer and cosmological horizons tend towards each other. We study massless scalar fields in these backgrounds and obtain their quasinormal mode spectrum explicitly. We uncover an interesting structure in their two-point functions, namely that they resemble thermal Green's functions of a two-dimensional conformal field theory. The second half of this dissertation deals with the study of multicentered black holes in string theory and their finite temperature extensions. We show that there exist finite temperature single-centered solutions in $\mathcal{N} = 2$ supergravity

in asymptotically flat space that admit bound states with BPS probe particles. We compute the existence regions of these bound states as well as their dependence on temperature. We embed these solutions in Fayet-Illiopoulos gauged supergravity and show that bound states persist in asymptotically AdS_4 spacetimes. We make attempts to understand these disordered bound states as amorphous/glassy phases of the dual conformal field theory.

Contents

Citations to Previously Published Work

Chapters 2 and 3 appear, almost in their entirety in the following two papers:

> "Incompressible Fluids of the de Sitter Horizon and Beyond", D. Anninos, T. Anous, I. Bredberg, and G.S. Ng **JHEP 1205 (2012) 107**, `arXiv:1110.3792`;
>
> "A de Sitter Hoedown", D. Anninos, and T. Anous, **JHEP 1008 (2010) 131**, `arXiv:1002.1717`.

Much of chapters 5 and 6 appear in:

> "Supergoop Dynamics", D. Anninos, T. Anous, F. Denef, G. Konstantinidis, and E. Shaghoulian **JHEP 1303 (2013) 081**, `arXiv:1205.1060`;
>
> "Hot Halos and Galactic Glasses (Carbonado)", D. Anninos, T. Anous, J. Barandes, F. Denef, and B. Gaasbeek **JHEP 1201 (2012) 003**, `arXiv:1108.5821`.

Finally, chapter 7 appears almost entirely in

> "AdS Hot Halos", D. Anninos, T. Anous, F. Denef, L. Peeters *To Appear*

Electronic preprints (shown in `typewriter font`) are available on the Internet at the following URL:

> `http://arXiv.org`

Acknowledgments

Part of what makes an epic so exciting are the myriad challenges beset upon the protagonist and the manner in which he learns to overcome them, invariably through the help and support of many benefactors, mentors, friends, abettors and guardians. I would first like to single out two such friends: Dionysios Anninos and Frederik Denef. Dionysios is the Tiresias of this story and has seen in me from our first encounter what I fail to see in myself even to this day. I have learned much from our discussions, which have been invaluable in shaping me as a physicist and as a person. No less can be said about Frederik whose brilliant insights have been a beacon for me over the past five years. He is the Hermes of this tale, the cunning benefactor of mortals, the bringer of good luck. Both have taught me the treasured value of persistence and the humbling lesson of relentless questioning in research. I will forever be in their debt.

There would certainly be no adventure without the brothers and sisters that share them with you. Sharif Anous, thanks for putting up with me. Your optimism is inspiring, don't ever pay heed to anyone who doubts you. Omar El Zayat, thanks for taking up the arms, I was merely following in your footsteps. Mohamed El Zayat, bez. Karim Goessinger, thanks for the vagabonding, our travels are just beginning. Ali Kassem, Osman El Sharnoubi, and Ahmed Omar—Horreya. Hussein Omar, beach–joust, beer–oust. The biker gang: Carlos Aguilar, Geoff Fudenberg, Nour Kteily, and Nick Stone, those were some crazy nights. The biker girls: Amanda White-Lief, Satori Bailey, Mars Sarango, and Annie Smith..... Miracle? Sharon Knight, you are the kindest person I know, and I won't forget it. Chris Trowbridge, why don't we start a band where you play all the instruments? Jonah Waissman, why dance when we can samba? Mikhail Kats, we'll always have Yenching. Also, thank you Ski Lodge

for taking me and Carlos as your denizens.

To the ballasts, the companions in battle who endured the trip: Murad Alim, Curtis Asplund, Petar Bakalov, M'boyo Esole, Sam Espahbodi, George Coss, Bram Gaasbeek, Greg Kestin, Winny O'kelly de Galway, Ashwin Rastogi, Doug Rubin, Edgar Shaghoulian, Nick Vanmeter, Bert Van-Pol, and Bert Vercnocke. Calypso is as bewitching as she is treacherous, as sardonic as she is naive. Where did all those years go?

Most importantly is family, Telemachus and Penelope, the compass that sets the course. Nihal Amin, much of my success is due to your hard work, thank you for the unending support and care that kept me afloat all these years. Maher Anous, thank you for planting the early seeds of my interest in science and working your bones dry to ensure I could get the best possible education. Nino, thanks for your warmth, and for making me laugh late into the night. Mans, thank you for joining the family, you're a brave man for staying. Candi, thank you for your infinite kindness.

I would finally like to thank the members of my committee: Frederik Denef, Andrew Strominger, and Subir Sachdev for their helpful comments and discussions as well as for their time spent reading through this dissertation and attending my defense.

To those unsung heroes who have gone unmentioned, you are not forgotten! Thank you all for the meals shared, the late night discussions, the book suggestions, the dance parties, the adventures and the misadventures.

Dedicated to the past: my father Maher and mother Nihal,
present: my brother Sharif,
and future: my sisters Alexia and Abigail.

Chapter 1

Act I: De Sitter Space

The future of our universe is bleak. Its energy density is dominated by a positive cosmological constant [1, 2] that pushes spacetime points apart. As a result, only a finite region of spacetime, known as the causal or static patch, can communicate with a single observer. Everything outside of this region, beyond the cosmological horizon, accelerates too quickly for signals to ever reach our intrepid experimenter. What is the nature of the cosmological horizon? At first glance it appears very similar to the horizon of a black hole in the sense that they both act like one-way membranes for light signals. Upon further inspection one sees that the semiclassical (or slightly quantum) behavior of these horizons is very similar as well, in the sense that they both have an associated entropy and temperature [3]. Is it then the case that cosmological horizons and black hole horizons are one and the same objects? If we manage to understand the quantum mechanical features of black holes, can we then say that we understand the quantum mechanical features of de Sitter space and its horizon?

The answer is no. While it is true that the low energy behavior of these two

horizons exhibit universal properties that match nicely (as we demonstrate further in chapter 2), the questions we are concerned with involve high energies. Furthermore, even before we confront the quantum behavior of these different spacetimes, we are struck with the fact that, while the black hole horizon is a unique null surface defining the causal structure of the spacetime, the de Sitter horizon depends on the observer's specific timelike worldline. Furthermore, the de Sitter observer will never be able to approach her horizon or probe it! This difference, although mild seeming, is an added confusion in an already mired field of theoretical physics. The fact that horizons have an entropy is but one of many puzzles that have confused theoretical physicists for the past 40 years. If we accept there is an entropy, then we must ask what it counts, and why it is so large. For black holes we have the intuitive picture that the entropy must be counting inequivalent ways of constructing the black hole, hidden behind the horizon. The de Sitter entropy moves with the observer, and therefore the interpretation of the counting is much more mysterious.

For black hole horizons, some insights into the nature of the horizon entropy have come from string theory. For some classes of supersymmetric black holes in asymptotically flat space, the microstate counting can be done exactly [4, 5, 6] revealing exact agreement with Hawking's calculation. The new ingredients that were required to account for the enormous increase in entropy of the black holes were given by D-branes, extended objects that can wrap internal cycles of a microscopic compact space. The complexity of these wrapped configurations—the multiple ways in which these branes can wrap these cycles—was just the ingredient needed to ensure the agreement in counting.

Before continuing we would like to mention a caveat. Successfully counting the microstates of black holes suggests we have a microscopic theory that captures the degrees of freedom of the black hole when gravity is strongly coupled. However, D-branes in string theory are well defined solitonic objects when gravity is *weakly* coupled. So how can we trust the counting? As it turns out, we can because the number of wrapped D-brane configurations is an index protected by supersymmetry. That is, the counting does not change as we crank up the coupling strength of gravity. It was only later understood that there was another effect at play, in terms of a much more powerful strong/weak duality known as the AdS/CFT correspondence [17] which posits that strongly coupled gravity in asymptotically Anti de Sitter spacetimes, maximally symmetric solutions to Einstein gravity with a negative cosmological constant, are holographically dual to weakly interacting conformal gauge theories living at the (conformal) boundary of these spacetimes at spatial infinity. Indeed since the near horizon regions of the supersymmetric black holes studied in [4, 5, 6] all have AdS factors, the microstate counting is simply an application of the Cardy formula [7, 8] from the point of view of the dual conformal field theory.

We do not have a similar picture for de Sitter space and its horizon. There are no weakly gravitating states that we know of that, as we crank up the strength of gravity, backreact into the cosmological constant and give rise to horizons that surround every distinct observer. Viewed in this light, the black hole horizon and the cosmological horizon are two disparate objects whose quantum gravity interpretations will generically be quite different.

Motivated by these differences, quantum gravity in the context of de Sitter space

has been the subject of much speculation and research [9, 10, 11, 12, 13, 14, 15, 16, 18, 19, 20] (for a thorough review, see also [28]). The goal of this research has namely been to understand holography in the context of de Sitter space and moreover shed light on the nature of the de Sitter entropy, albeit such attempts have so far been unsatisfactory. One particularly successful avenue towards tackling this problem [14, 15, 16, 21, 22, 23, 24] has been the suggestion that quantum gravity in de Sitter space is also holographically dual to a CFT, although unlike in AdS holography, the CFT is Euclidean and lives on the *future* boundary at $\mathcal{I}^+$ (see figure 2.1). A naive use of the Cardy formula for a certain small class of de Sitter backgrounds where the asymptotic symmetry group can be identified with a Virasoro algebra (such as dS_3 or the Nariai geometry in dS_4) seems to give the correct counting. However a detailed understanding of these dual CFT states, the analogs of the wrapped D-branes, and what they imply on the gravity side is still lacking.

In search of more motivation to think about this problem, may we add that not only is our universe tending towards a de Sitter phase in the future, but it also exited a phase well approximated by de Sitter space, known as inflation, in the past. Thus if we are to gain any grasp on the evolution of the universe, we are twice confronted with the need to understand quantum gravity in de Sitter space.

The successes of AdS/CFT can act as a guiding principle for how to make sense of holography in dS. However, while de Sitter space and Anti-de Sitter space are related by analytic continuation, their holographic duals are, at least naively, not. Thus we gain little insight from analytically continuing results from AdS/CFT for

use in the de Sitter context[1]. One point of view is that, unlike AdS/CFT, de Sitter holography should only be capable of describing a single static patch [11, 13, 26, 27, 29, 30, 31, 32, 33, 34, 35, 36]. It is not at all clear how the physics of the static patch observer is captured by the theory at $\mathcal{I}^+$, whose observables are given by correlators between causally disconnected points. The static patch observer can at most observe a tiny region of $\mathcal{I}^+$ where her worldline intersects the future boundary. The geometry outside her future horizon thus seems akin to a gauge choice since it will never affect the physics she observes [35].

In the following chapters, we will try to address some of the issues raised above. The focus will be exploratory given the conceptual nature of the challenges at hand. In chapter 2 we attempt to address the issue of relating the data of the observer's worldline with the data on $\mathcal{I}^+$. This is done by allowing the experimenter to perturb the spacetime around her while imposing (conformal) Dirichlet boundary conditions on the timelike hypersurface of the lab wall. We look at the spectrum of linear and non-linear perturbations of the background spacetime with these boundary conditions and study how the spectrum changes continuously as we move the lab wall closer to the de Sitter horizon (and beyond). What we uncover might suggest a novel interpretation of holography in dS. To be specific, in AdS/CFT we identify the boundary at spatial infinity with the UV of the CFT; in dS, the data at $\mathcal{I}^+$ is seen to be equivalent to the worldline of the observer deep in the bulk of the static patch. Furthermore, if we study the near horizon dynamics of the de Sitter horizon, a surface that is *not* deep within the static patch, we find that it is mathematically equivalent, upon analytic

[1]For an example where analytic continuation of AdS results can prove quite useful for de Sitter space see [25].

continuation, to the near horizon dynamics of a hyperbolic black hole deep within the bulk of AdS, usually identified with the IR description of the CFT. These mappings suggest a role reversal of IR and UV physics in dS when comparing with the standard AdS/CFT dictionary.

In chapter 3 we look at the spectrum of rotating black holes in dS_4 and study them in depth. The classical evolution of these backgrounds tends toward empty de Sitter space, the most entropic configuration, via a superradiant instability. Even so, empty de Sitter space is unstable to the nucleation of large black holes, mediated by a Euclidean instanton [37] and hence the Nariai (largest possible) [38] black hole is of particular interest. We also study free scalar fields in rotating Nariai, whose wave equation can be solved explicitly in terms of hypergeometric functions. With these solutions, we compute the quasinormal mode spectrum and find that they correspond precisely to the poles of the boundary-to-boundary correlation functions at future infinity. Furthermore, these correlation functions are exactly of the form of retarded thermal Green's functions of a two-dimensional CFT, giving credence to the duality proposed in [74].

It is our hope that the observations made in chapters 2 and 3 will be understood from the point of view of a full quantum gravity theory, but until then we can only wish that they can give some insights into how to frame ones' thoughts when trying to understand holography in de Sitter.

Chapter 2

Incompressible Fluids of the de Sitter Horizon and Beyond

2.1 $\mathcal{I}^+$/Static Patch Schizophrenia

There have been several attempts to relate general relativity to fluid mechanics dating back to the 1970s with the black hole membrane paradigm [39, 40, 41] (see [42] for an application to de Sitter space). The membrane paradigm focuses on the observation that the equations governing the dynamics of horizon surfaces in general relativity can be written in a form analogous to that of the Navier-Stokes equation of fluid mechanics. However, whilst finding a striking analogy, the central equation of the membrane paradigm is often referred to as the Damour-Navier-Stokes equation, highlighting the fact that it differs from the Navier-Stokes equation in key ways. Building on this, recent papers [43, 44, 45] constructed a setup where near horizon dynamics in gravity precisely relates the Einstein equation to the incompressible Navier-Stokes

equation. These studies were also inspired by analyses of connections between gravity and fluid mechanics in the context of the AdS/CFT correspondence [46, 47, 48] and the low energy limit of the dual field theory. Given the striking similarities between the thermodynamics of a black hole horizon and a cosmological horizon, it is natural to extend such a fluid/gravity correspondence to include spacetimes with a cosmological horizon.

After reviewing the classical geometry of de Sitter space, the first part of this chapter will explore some of the classical features of the cosmological horizon as viewed by an observer in a purely de Sitter universe – the static patch observer. We examine the Einstein equation both linearly and non-linearly and uncover that the solutions are characterized by solutions to the incompressible Navier-Stokes equation on a two-sphere.[1] This same equation recently appeared in the context of the Schwarzschild black hole [45] and requires the velocity field $v_i(\tau, \Omega^j)$ where $\Omega^i = \{\theta, \phi\}$ and the pressure $P(\tau, \Omega^j)$ to satisfy

$$\partial_\tau v^i + \nabla^i_{S^2} P + v_j \nabla^j_{S^2} v^i - \nu \left(\nabla^2_{S^2} v^i + R^i_j v^j \right) = 0 \ , \quad \nabla^i_{S^2} v_i = 0 \tag{2.1.1}$$

where ν is the viscosity. Indices are raised and lowered with respect to the round metric g_{ij} on the S^2 of radius r_S for which $R_{ij} (= g_{ij}/r_S^2)$ is the Ricci tensor. At the linearized level, this is done by imposing Dirichlet boundary conditions on a timelike surface arbitrarily close to the cosmological horizon and the absence of incoming flux from the past horizon of the static patch. These boundary conditions resemble the solipsistic boundary conditions of [36], which allow for an examination of the isolated

[1] As in [45], we analyze the metric through the first three orders in a near-horizon expansion. A generalization of the all-orders proof of [49] might be possible in our case, but we will not attempt to do so herein.

static patch dynamics, unperturbed by external sources from the past horizon. We find that the linearized solutions must obey the dispersion relation of the incompressible, linearized (pressureless) Navier-Stokes equation (2.3.19). At the non-linear level, again in a near cosmological horizon expansion, we impose (conformal) Dirichlet boundary conditions on a timelike slice and regularity of the solutions as they approach the future horizon. By (conformal) Dirichlet boundary conditions, we mean analysing perturbations which leave the induced geometry on a fixed timelike hypersurface of constant extrinsic curvature unchanged up to a conformal factor.[2] Then, we comment briefly on the possibilities of deforming this non-linear fluid by placing a small black hole at the origin of the static patch. In an attempt to connect our fluid dynamical modes to the analogous excitations of the worldline, which are the quasinormal modes, we return to the linearized analysis to study how the linearized dispersion relation varies as we push the surface from the cosmological horizon to the worldline.

In the second part of this chapter we make some mathematical observations about spacelike slices foliating the region outside the future horizon of the static patch. We examine the behavior of linearized solutions to the Einstein equation near, but outside, the future cosmological horizon. Our solutions are subjected to Dirichlet boundary conditions on a fixed spacelike surface and to contain incoming flux solely from a single static patch observer. We find a discrete set of modes obeying the dispersion relation of the linearized Navier-Stokes equation, where the time coordinate has become the non-compact spacelike coordinate moving us along the spacelike slice. The non-linear

[2]Henceforth, in the non-linear analysis, we will refer to these boundary conditions as Dirichlet boundary conditions.

solutions to the Einstein equation which satisfy Dirichlet boundary conditions on the spacelike slice and which are regular at the horizon from which flux is coming, are indeed characterized by solutions to the incompressible Navier-Stokes equation. The Navier-Stokes equation uncovered here on the spacelike slice is equivalent to that discussed in the context of the timelike surface, except that the sign of the viscosity is flipped. We end by noting that the setup of the problem in this future diamond of de Sitter space, and in particular the pole structure at $\mathcal{I}^+$, is connected by an analytic continuation to analogous problems in Lorentzian AdS_4 with hyperbolic slicing.

2.2 Geometry and Framework

In what follows we will study the geometries of several patches of de Sitter space pertinent to our analysis. Instead of the global patch of de Sitter space containing the past and future infinities, denoted by $\mathcal{I}^-$ and $\mathcal{I}^+$, we will focus on patches that are more suited to the description of local observers.

2.2.1 The Static Patch

The four-dimensional static patch metric solves the Einstein equation in the presence of a cosmological constant $\Lambda > 0$,

$$\mathcal{G}_{\mu\nu} \equiv G_{\mu\nu} + \Lambda g_{\mu\nu} = 0 \tag{2.2.2}$$

and is given by:

$$ds^2 = -\left(1 - (r/\ell)^2\right) dt^2 + \left(1 - (r/\ell)^2\right)^{-1} dr^2 + r^2 d\Omega_2^2 \,, \tag{2.2.3}$$

where $r \in [0, \ell]$, $t \in \mathbb{R}$ and $d\Omega_2^2$ is the round metric on S^2. The quantity ℓ is the de Sitter length and is related to the cosmological constant as $\Lambda = +3/\ell^2$. The above metric covers a quarter of the global de Sitter geometry, it describes the intersection of the future and past causal diamonds of a constant r worldline beginning at $\mathcal{I}^-$ and ending at $\mathcal{I}^+$. We call this the Southern patch of de Sitter space.

One notices that $r = \ell$ corresponds to a cosmological event horizon, beyond which events are forever out of causal contact from the Southern observer. The Killing vector ∂_t becomes null at $r = \ell$ and the above coordinate system breaks down.

The Southern patch can be smoothly connected to another region covering an additional quarter of de Sitter space, by continuing the above metric to $r \in [\ell, \infty]$. For $r > \ell$, t becomes a spacelike coordinate and r becomes timelike. We can consider gluing two such regions, one behind the past cosmological horizon, known as the past diamond containing $\mathcal{I}^-$, and the other beyond the future cosmological horizon, known as the future diamond containing $\mathcal{I}^+$.

The remaining quarter of the global de Sitter space is given by an additional static patch system known as the Northern patch. The Southern and Northern patches each intersects $\mathcal{I}^\pm$ at a single point. In figure 2.1 we demonstrate the several patches discussed above in a Penrose diagram.

2.2.2 Null Foliations

It will be convenient to introduce an additional coordinate system which smoothly covers both the Southern patch and the future diamond. This is achieved by the

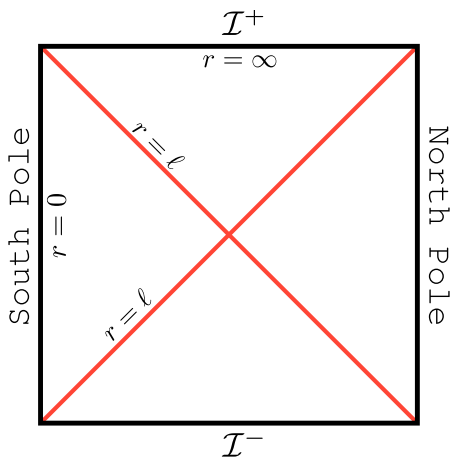

Fig. 2.1: Penrose diagram of de Sitter space indicating the various static patches and future/past diamonds.

following coordinate transformation:

$$\ell du = dt - \frac{dr}{(1-(r/\ell)^2)} \ , \qquad v = \frac{r}{\ell} \ , \tag{2.2.4}$$

leading to the metric

$$\frac{ds^2}{\ell^2} = -(1-v^2)du^2 - 2dudv + v^2 d\Omega_2^2 \ . \tag{2.2.5}$$

Up to a constant time shift we find $u\ell = t - \ell \tanh^{-1} r/\ell$. Constant u surfaces are null lines emanating from the origin at $v = 0$ and ending at $\mathcal{I}^+$ where $v = \infty$. The norm of the Killing vector ∂_u changes sign at $v = 1$.

2.2.3 Approaching the Horizon

Finally, we would like to introduce a dimensionless parameter $\alpha > 0$ allowing us to approach the cosmological horizon. In order to achieve this, we rescale time to $u = \tau/2\alpha$ and define $\rho = (1-v)/2\alpha$. As we take the limit $\alpha \to 0$, we redshift time

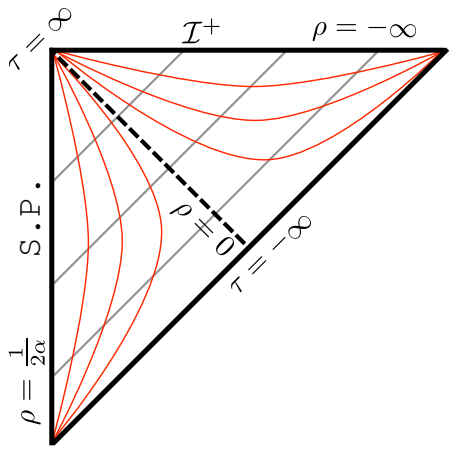

Fig. 2.2: Penrose diagram of de Sitter space indicating constant ρ (red) and τ (gray diagonal) slices.

and for any finite ρ, v will be forced to lie near the cosmological horizon. The metric is given by:

$$\frac{ds^2}{\ell^2} = \left(-\frac{\rho}{\alpha} + \rho^2\right) d\tau^2 + 2d\tau d\rho + (1 - 2\alpha\rho)^2 \, d\Omega_2^2 \, . \tag{2.2.6}$$

The coordinate range of ρ covering the Southern patch is given by $\rho \in [0, 1/2\alpha]$ and the norm of ∂_u vanishes at $\rho = 0$. The constant ρ and τ surfaces are shown in figure 2.2.

As opposed to the Schwarzschild case, where a similar expansion would continue for indefinite powers of α, the above expansion terminates at order $\mathcal{O}(\alpha^3)$. This is due to the absence of a term $\sim 2M/r$ in the $g_{\tau\tau}$ component. We could of course add such a term, which would correspond to introducing a small mass or black hole centered at the origin of the static patch.

2.3 Incompressible Fluids

Having specified the geometry relevant to our problem, we proceed to discuss the nature of perturbations solving the Einstein equation with positive Λ near the cosmological horizon. We begin with a linearized analysis.

2.3.1 Linearized Analysis

Linearized gravity about spherically symmetric spaces with non-zero cosmological constant was examined in [50, 51]. The two gravitational degrees of freedom transform as a (divergenceless) vector and a scalar under the $SO(3)$ symmetry of the S^2. There is no transverse-traceless tensorial spherical harmonic for a two-sphere. Let us work in a gauge where $\delta g_{ij} = 0$ for $x^i \in \{\Omega\}$. The metric vector perturbations can be expressed as:

$$\delta g_{it} = \mathcal{V}_i \times \left(1 - (r/\ell)^2\right)(1 + r\partial_r)\,\Phi_v \ , \tag{2.3.7}$$

$$\delta g_{ir} = \mathcal{V}_i \times \frac{r}{(1 - (r/\ell)^2)}\partial_t \Phi_v \ . \tag{2.3.8}$$

The vector spherical harmonic $\mathcal{V}_i$ satisfies the following relations on the unit two-sphere:

$$\left(\nabla^2_{S^2} + k_V^2\right)\mathcal{V}_i = 0 \ , \quad \nabla^i_{S^2}\mathcal{V}_i = 0 \ , \tag{2.3.9}$$

with eigenvalues are $k_V^2 = l(l+1) - 1$ and $l = 1, 2, \ldots$ The master field Φ_v obeys the master equation:

$$\left(\nabla^2_{g^{(2)}} - \frac{l(l+1)}{r^2}\right)\Phi_v = 0 \ , \tag{2.3.10}$$

where $g^{(2)}$ corresponds to the two-dimensional de Sitter static patch. A similar result holds for the scalar perturbations, which we discuss in appendix A.1.

The solutions to the above equation were analyzed in [35] and are found to be hypergeometric functions. For our purposes we would like to obtain the linearized solutions in the null coordinate system (2.2.5). Assuming a Fourier decomposition in time, $\Phi_v = e^{-2i\alpha\omega t(\tau,\rho)/\ell}\varphi_v(\rho)$, the equation of motion becomes:

$$\Big(4\rho^2\left(1-\alpha\rho\right)^2\partial_\rho^2 + 4\rho\left(1-\alpha\rho\right)\left(1-2\alpha\rho\right)\partial_\rho + \frac{4\alpha^2(1-2\alpha\rho)^2\omega^2 - 4\alpha\rho\left(1-\alpha\rho\right)\left(k_V^2+1\right)}{(1-2\alpha\rho)^2}\Big)\varphi_v = 0\ . \quad (2.3.11)$$

The two linearly independent solutions for $l > 1$ are given by:

$$\varphi_v^{out} = \rho^{-i\alpha\omega}\ {}_2F_1\left[a_1, b_1; c_1; \frac{\alpha\rho}{-1+2\alpha\rho}\right]\ \frac{(1-2\alpha\rho)^{2i\alpha\omega}}{(1-\alpha\rho)^{i\alpha\omega}}\ , \quad (2.3.12)$$

$$\varphi_v^{in} = \rho^{+i\alpha\omega}\ {}_2F_1\left[a_2, b_2; c_2; \frac{\alpha\rho}{-1+2\alpha\rho}\right]\ (1-\alpha\rho)^{-i\alpha\omega}\ , \quad (2.3.13)$$

with:

$$a_1 = -l-2i\alpha\omega\ , \quad b_1 = 1+l-2i\alpha\omega\ , \quad c_1 = 1-2i\alpha\omega\ ; \quad (2.3.14)$$

$$a_2 = -l\ , \quad b_2 = 1+l\ , \quad c_2 = 1+2i\alpha\omega\ . \quad (2.3.15)$$

The superscripts 'out' and 'in' indicate that the mode is purely outgoing at the future horizon or purely incoming from the past horizon. The above expressions are linearly independent solutions for $(c_i - a_i - b_i) = 2i\alpha\omega \notin \mathbb{Z}$ (see [52]). In the case where $(c_i - a_i - b_i) = 2i\alpha\omega$ is an integer, logarithmic solutions will appear. Given that a_2 and b_2 are integers φ_v^{in} is in fact a finite polynomial for $2i\alpha\omega \notin \mathbb{Z}$, as it can be shown that the hypergeometric series terminates. For $l = 1$, the linearized perturbations become time independent and are like the introduction of a small amount of angular momentum (we discuss this case in appendix A.2).

The linearized purely outgoing metric components (2.3.7) in the (τ, ρ)-coordinate system become:

$$\delta g^{out}_{i\tau} = 2\mathcal{V}_i \times e^{-i\omega\tau}\, \rho^{i\alpha\omega+1}(1-\alpha\rho)^{-i\alpha\omega+1}\left(1 - \frac{(1-2\alpha\rho)}{2\alpha}\partial_\rho\right)\varphi^{out}_v \ , \tag{2.3.16}$$

$$\delta g^{out}_{i\rho} = -2\alpha\mathcal{V}_i \times e^{-i\omega\tau}\, \left(\frac{1-\alpha\rho}{\rho}\right)^{-i\alpha\omega}\left[\left(1 - \frac{i\omega(1-2\alpha\rho)}{2\rho(1-\alpha\rho)}\right) - \frac{(1-2\alpha\rho)}{2\alpha}\partial_\rho\right]\varphi^{out}_v \ . \tag{2.3.17}$$

Both $\delta g^{out}_{i\tau}$ and $\delta g^{out}_{i\rho}$ are regular at the future horizon $\rho = 0$.

2.3.2 Linearized Fluid Modes

Having written down the linearized solutions, we now discuss the choice of boundary conditions. We impose Dirichlet boundary conditions on a given timelike hypersurface at some fixed ρ, and without loss of generality, we choose the location of this timelike hypersurface to be at $\rho = 1$. Taking $\alpha \to 0$ pushes this hypersurface arbitrarily near the cosmological horizon and thus allows us to probe the near horizon dynamics.

Our particular Dirichlet boundary condition, shown in figure 2.3, is that the linearized perturbations are purely outgoing and leave the intrinsic geometry of the $\rho = 1$ hypersurface unchanged.[3] Imposing $\delta g^{out}_{i\tau}(\rho = 1) = 0$ enforces a discrete dispersion relation, which to leading order in α is given by:

$$\omega_f = -i\left(l(l+1) - 2\right) \ , \quad l = 1, 2, \ldots \tag{2.3.18}$$

We interpret these linearized modes as fluid modes of the velocity field v^i of the

[3]This is the simplest choice of Dirichlet boundary conditions and thus allows for a clear analysis. In general, we can choose more involved Dirichlet boundary conditions on the $\rho = 1$ hypersurface.

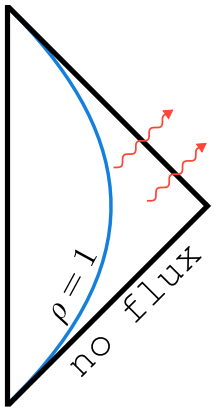

Fig. 2.3: Our boundary conditions for the linearized modes are such that the induced metric on the $\rho = 1$ slice is unchanged and there is no incoming flux from the past horizon.

incompressible, linearized (pressureless) Navier-Stokes equation on a sphere:

$$\partial_\tau v_i = \nu \left(\nabla^2_{S^2} v_i + R_{ij} v^j \right) \ , \quad \nabla^i_{S^2} v_i = 0 \ , \tag{2.3.19}$$

where the viscosity $\nu = 1$. The incompressibility of the fluid is equivalent to the vanishing divergence of $\mathcal{V}_i$, which can be seen by identifying $v_i \sim e^{-i\omega\tau}\mathcal{V}_i$. We further note that the explicit modes (2.3.16) with $\omega = \omega_f$ decay in time and are regular at the future horizon $\rho = 0$.[4]

By arguments similar to those in [43], one expects that the result $\nu = 1$ corresponds to a ratio of shear viscosity to entropy density which is $1/4\pi$. This suggests that the incompressible fluid we have found near the de Sitter horizon shares this feature with the fluids found near the Schwarzschild, Rindler and planar AdS black hole horizons [43, 44, 45, 53] (see also [42]).

[4]If these modes are taken back in time to $t \to -\infty$ they diverge and the perturbative solution is no longer reliable. As usual we only consider wavepackets of the linearized solutions which are finite for all asymptotia.

There is also a decoupled set of scalar excitations which transform as scalars under the $SO(3)$ of the S^2. However, the incompressibility condition implies that we could only consider the spherically symmetric scalar mode, which reduces the fluid vector field to a trivial one(see appendix A.1). We will not consider such modes in what follows and simply set them to zero in the linearized analysis.

2.3.3 Non-linear Analysis

Having analyzed the linearized case, we now turn to the question of non-linear deformations. The analysis follows directly the Schwarzschild case analyzed in [45].[5] In particular, in this non-linear analysis, we impose the (conformal) Dirichlet boundary conditions on the hypersurface as in [45].

To be precise, we will consider the following finite deformation of the static patch geometry as an expansion in α:[6]

$$\begin{aligned}\frac{ds^2}{\ell^2} &= -\frac{\rho}{\alpha}d\tau^2 \\ &+ \rho^2 d\tau^2 + 2d\tau d\rho + d\Omega_2^2 + (1-\rho)\left[v^2 d\tau^2 - 2v_i d\tau dx^i\right] - 2\rho P d\tau^2 \\ &+ \alpha\Big[(-4\rho+2P)\,d\Omega_2^2 + (1-\rho)v_i v_j dx^i dx^j \\ &- \left(\rho^2-1\right)\left(\nabla^2 v_i + R_{ji}v^j\right)d\tau dx^i - 2v_i d\rho dx^i + \left(v^2+2P\right)d\tau d\rho + 2\left(1-\rho\right)\phi_i^{(\alpha)} d\tau dx^i\Big] \\ &+ \alpha^2\left(4\rho^2 d\Omega_2^2 + 2g_{\rho i}^{(\alpha^2)}dx^i d\rho + g_{ij}^{(\alpha^2)}dx^i dx^j\right) + \dots .\end{aligned} \tag{2.3.20}$$

The v^i, P and $\phi_i^{(\alpha)}$ are functions of (τ, Ω^i) only while the $g_{i\rho}^{(\alpha^2)}$ and $g_{ij}^{(\alpha^2)}$ are functions

[5] It should be noted that we have presented a more complete linearized analysis than would be possible for the Schwarzschild case, given the existence of exact linearized solutions in dS_4.

[6] When writing out the metric (2.3.20) we have omitted the metric components $g_{\tau\tau}^{(\alpha)}, g_{\tau\tau}^{(\alpha^2)}, g_{\rho\tau}^{(\alpha^2)}, g_{i\tau}^{(\alpha^2)}$ and higher order contributions since these do not affect the Einstein equation to the order that we consider.

of (τ, ρ, Ω^i). We have chosen a gauge where $g_{\rho\rho} = 0$. As boundary conditions we require the perturbations to preserve the induced metric on the hypersurface $\rho = 1$

$$ds^2_{3d} = \left(-\frac{1}{\alpha} + 1\right) d\tau^2 + (1 - 2\alpha)^2 \, d\Omega_2^2 \ , \tag{2.3.21}$$

up to a conformal factor

$$1 + 2\alpha P + \mathcal{O}(\alpha^2) \ . \tag{2.3.22}$$

We also study perturbations such that this hypersurface has constant mean extrinsic curvature and that the solution is regular at the future horizon $\rho = 0$. These boundary conditions are the natural extension of the boundary conditions imposed on the linearized fluid modes of the last section.

We now examine the conditions on the deformation parameters imposed by the Einstein equation with a positive cosmological constant $\mathcal{G}_{\mu\nu} = 0$ up to and including $\mathcal{O}(\alpha^0)$. We further assume that the only excited field is the metric. The first non-trivial condition appears at $\mathcal{O}(\alpha^{-1})$. Here, for $\mathcal{G}_{\tau\tau} = 0$ to be satisfied, the velocity field v^i is required to be incompressible. At the next order $\mathcal{O}(\alpha^0)$, the non-trivial equations are $\mathcal{G}_{\tau\tau} = \mathcal{G}_{\tau i} = 0$. From the $\mathcal{G}_{\tau i} = 0$, it follows that the (v^i, P) need to satisfy the non-linear incompressible Navier-Stokes equation (2.1.1) on a unit S^2. Our result is in complete accordance with the linearized analysis.[7]

From the $\mathcal{G}_{\tau\tau} = 0$ Einstein equation at $\mathcal{O}(\alpha^0)$ we find the requirement

$$\nabla^i_{S^2} \phi_i^{(\alpha)} = 2\partial_\tau P + \partial_\tau(v^2) + \textbf{total derivatives on the 2-sphere}. \tag{2.3.23}$$

[7]We would not expect to see the pressure in the linearized analysis since at the linear level vector and scalar representations of $SO(3)$ decouple. This is no longer the case at second order in perturbation theory where we expect the equation for the vector representation to be affected by scalars as in the non-linear case. As in the linearized analysis, we have not considered sound modes, which would contribute to the divergence of v^i.

The above relation implies:

$$\partial_\tau \left(\int v^2 d\Omega_2 \right) = -2\partial_\tau \left(\int P d\Omega_2 \right) \ . \tag{2.3.24}$$

There is a similar condition between the velocity and pressure fields in the Schwarzschild case [45]. Such an integral relation can be compared to changes in the horizon area. This component of the Einstein equation also determines a scalar function involving $g_{\rho i}^{(\alpha^2)}, g_{ij}^{(\alpha^2)}$.

2.3.4 Deformations of the Fluid

A natural question to ask about the fluid is whether one can deform it. In this section, we discuss two simple examples of possible deformations of the fluid.

The first is given by adding a small non-rotating black hole of mass M at the origin of the static patch. This changes the $-g_{tt} = g^{rr}$ components of the metric (2.2.3) to $V(r) = 1 - (r/\ell)^2 - 2M/r$. For positive values of M, adding the black hole has the effect of pulling in the cosmological horizon and thus decreasing its size. For small $\varepsilon \equiv M/\ell$, the new position of the cosmological horizon is given by $r_{cos} = \ell(1-\varepsilon)$ to leading order. In the analogous case of the Schwarzschild black hole, placing a mass at the center of the static patch corresponds to extracting some mass from the black hole, thus shrinking its horizon. The mass deformation we have described preserves the spherical symmetry of the background and thus the near horizon dynamics are expected to be governed by the Navier-Stokes equation on a sphere.

A slightly more involved deformation corresponds to placing a small rotating mass at the origin of the static patch. This will cause the cosmological horizon itself to

rotate. The function determining the positions of the horizons is now given by:

$$V(r) = (1 + (a/r)^2)\left(1 - (r/\ell)^2\right) - 2M/r \ . \tag{2.3.25}$$

As with the mass term, adding angular momentum shrinks the cosmological horizon. To lowest order in small ε and small $\upsilon \equiv (a/\ell)^2$ we find that:

$$r_{cos} = \ell\left(1 - \varepsilon(1-\upsilon) - \frac{3}{2}\varepsilon^2 + \mathcal{O}(\varepsilon^3, \varepsilon^2\upsilon, \varepsilon\upsilon^2, \upsilon^3)\right) \ . \tag{2.3.26}$$

The angular momentum of the space-time becomes $\mathcal{Q}_{\partial_\phi} = -aM/\left(1 + (a/\ell)^2\right)$. It should be noted that a finite deformation with angular momentum will also deform the sphere into a spheroidal surface. Thus we lose spherical symmetry and it might be possible that the near horizon dynamics is no longer governed by the Navier-Stokes equation on the round metric of S^2.

2.4 Pushing the Timelike Surface

So far we have analyzed the behavior near the cosmological horizon. Another timelike surface of interest in the static patch is given by the observer's worldline at $r = 0$.[8] Returning to the analysis of linearized gravity, if we impose Dirichlet boundary conditions leaving the worldline unperturbed for purely outgoing modes, we obtain another set of discrete modes known as quasinormal modes (see for example [54]). In the original static patch coordinates (2.2.3) these are given (for the vector

[8]Due to its resemblance with the boundary of AdS in the presence of an eternal black hole, recent work has emphasized the potential importance of the worldline as a candidate for the ultraviolet (holographic) description of the static patch [33, 36]. Although such a holographic duality is far from clear, one expects that the infrared behavior must give rise to the Navier-Stokes equation described in the former section.

modes) by:

$$\omega_n \ell = -i\,(n + l + 1) \ , \quad n = 0, 1, 2, \ldots \tag{2.4.27}$$

Due to the fact that $l \geq 1$, a gapless mode is absent in the above spectrum of quasinormal modes. This is in contrast to the fluid modes (2.3.18) which have $\omega_f = 0$ at $l = 1$. The gapless mode is absent due to the fact that the $\omega = 0$, $l = 1$ perturbation diverges on the worldline, as shown in appendix A.2. It reappears in the spectrum as soon as we 'puff up' the thickness of the worldline.

2.4.1 'Flowing' the Dispersion Relations

Our aim is to study the behavior of perturbative data on constant r surfaces as we push them from the horizon toward the worldline. There is a clear distinction between the lowest $n = 0$ quasinormal modes (2.4.27) and the fluid modes (2.3.18). Given a constant r slice at some position $r = r_c$ we impose Dirichlet boundary conditions leaving the induced metric on the $r = r_c$ unchanged. This constant r surface is directly analogous to the timelike hypersurface at $\rho = 1$ considered above. Furthermore, we require that the modes are purely outgoing. As before, these two conditions will only be satisfied for a discrete set of modes, but the dispersion relation will now depend on the dimensionless parameter $x = r_c/\ell$. For the surface near the horizon we have $x \to 1$ and as we approach the worldline we have $x \to 0$. For general x, the problem cannot be approached analytically and we must resort to numerics.

The dispersion relation corresponds to the pole structure of the Green's function of the vector modes on the particular cutoff surface. Thus, naturally, a flow of the dispersion relation corresponds to a flow of the Green's function itself. For an in-

compressible fluid on an S^2 described by (2.1.1) we can readily obtain the tree level retarded Green's function of v^i (see for example [56]).

To perform the analysis, it is in fact more convenient to use the (τ, ρ)-coordinate system introduced in (2.2.6). To study different timelike hypersurfaces we fix $\rho = 1$ and tune α from the horizon at 0 to the worldline at 1/2. We must then study for what values of (complex) ω the purely outgoing solutions $\delta g^{out}_{i\tau}$ in (2.3.16) vanish at the $\rho = 1$ hypersurface. It is relatively straight forward to compute the corrections to the dispersion relation perturbatively in α. For instance, to linear order in α we find:[9]

$$\nu = 1 + \frac{\alpha}{2}\left(5 + 3k_V^2\right) \ . \tag{2.4.28}$$

Expression (2.4.28) is only reliable for $l^2 \lesssim 2/3\alpha$.

2.4.2 Numerical Results

Since we impose Dirichlet boundary conditions at $\rho = 1$, α parametrizes the location of our cutoff surface r_c with respect to the cosmological horizon. The relation is given by

$$\alpha = \frac{\ell - r_c}{2\ell} = \frac{1 - x}{2} \ . \tag{2.4.29}$$

As we move r_c away from the cosmological horizon, we expect to deviate from our quadratic dispersion relation (2.3.18). Generically when searching for zeros of $\delta g^{out}_{i\tau}(\rho = 1)$ in (2.3.16) for arbitrary but fixed r_c and l, one runs the risk of finding any one of a tower of such zeros (see (2.4.27) for example).

[9] It is amusing to note that such a correction could be obtained by adding a suitable forcing term to our incompressible Navier-Stokes equation [56].

In order to make our analysis clear, we perform a search for the lowest lying zeros at a given r_c and l and do not present the rest of the tower. In the plots in figures 2.4 and 2.5 we have not searched for the $l = 1$ mode as this is where $\omega = 0$ and therefore our solutions φ_v^{out} and φ_v^{in} degenerate. We cover this case in appendix A.2. In what follows we will only examine the case of pure (negative) imaginary ω given that both the quasinormal modes (2.4.27) and the fluid modes (2.3.18) obey this property. It would be interesting to extend the analysis to general ω in the lower complex plane.

We now describe how the spectrum behaves as we approach $r_c = \ell$. As a reference, we also present the results for r_c close to the pole $r_c = 0$ in figure 2.4 where the linear dispersion relation is apparent. As r_c is increased, we start to observe a deviation from the linear behavior and the poles start to cluster into staircase-like behavior. For r_c close to the horizon, starting from the plot at the top left corner of figure 2.5, we note that there are (at least) three distinct sets of modes separated by large gaps. The $l = 2$ mode lies on the fluid dispersion relation line (meaning that it satisfies the

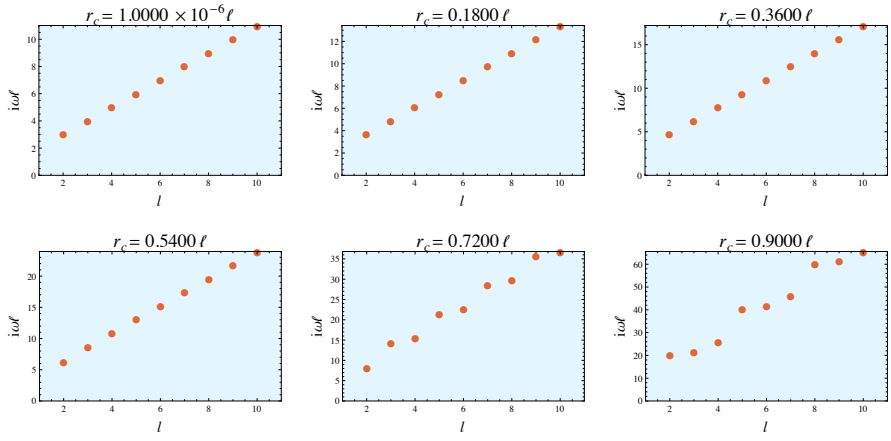

Fig. 2.4: Flow of frequency spectrum $i\omega\ell$ vs l as we move away from $r_c \approx 0$ toward the cosmological horizon.

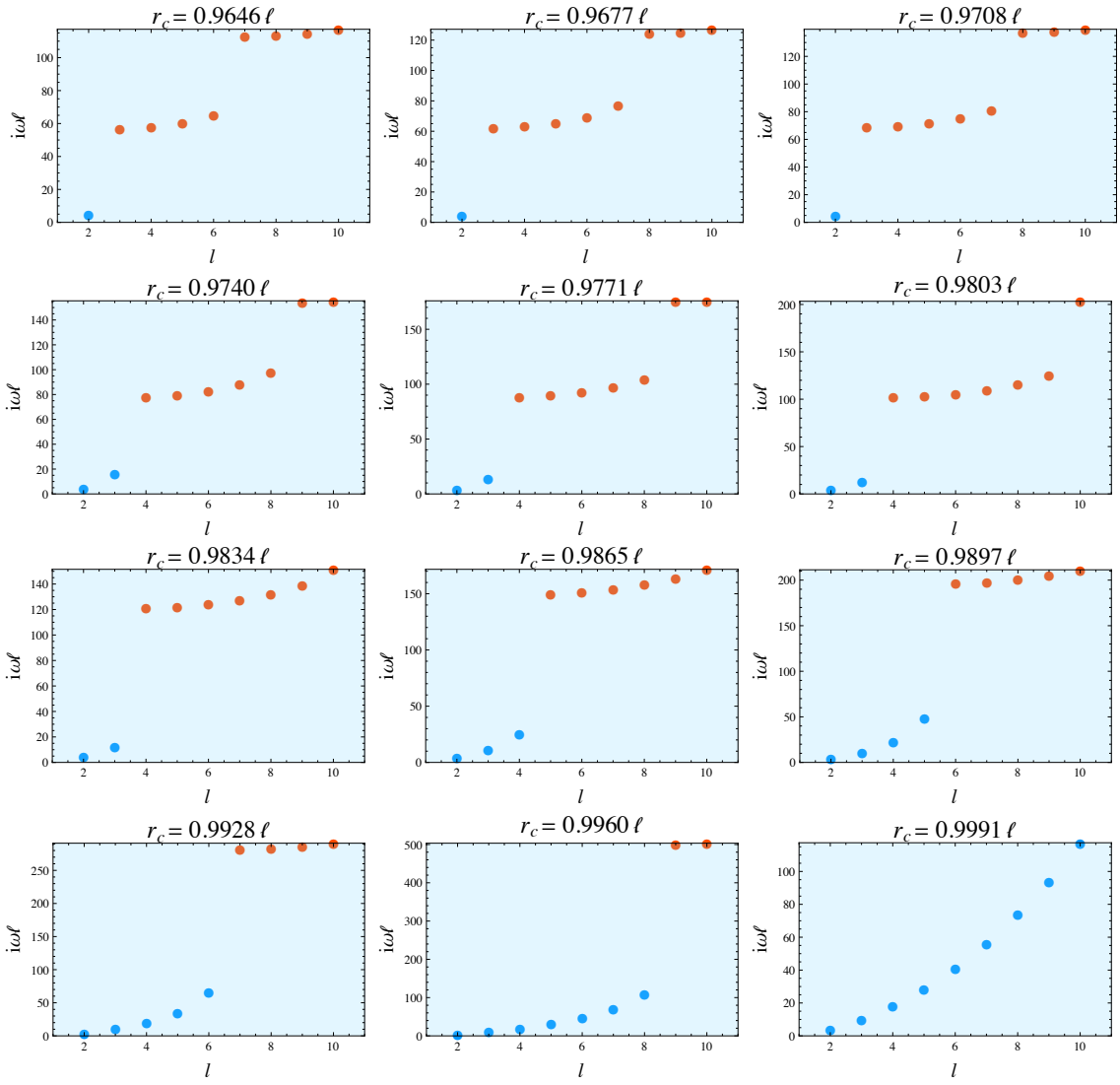

Fig. 2.5: Flow of frequency spectrum $i\omega\ell$ vs l as we approach $r_c = \ell$. Points obeying the fluid dispersion relation are represented in blue.

dispersion relation given by (2.3.18) with quartic corrections as in (2.4.28)), whereas the rest do not. As we move r_c closer to the horizon, we see that the non-fluid modes get pushed higher and in the fourth plot, the $l = 3$ mode is plucked down to the fluid line. This happens once again for the $l = 4$ mode near $r_c = 0.9865\ell$ whereas

the non-fluid modes keep getting pulled higher. The reason for these jumps is that the lowest lying zeroes of $\delta g^{out}_{i\tau}$ are modified discontinuously as a function of r_c as is visually depicted in figure A.1 of appendix A.3. Finally, we find that arbitrarily close to the horizon the dispersion relation lies entirely on the fluid dispersion relation (2.3.18) computed analytically.

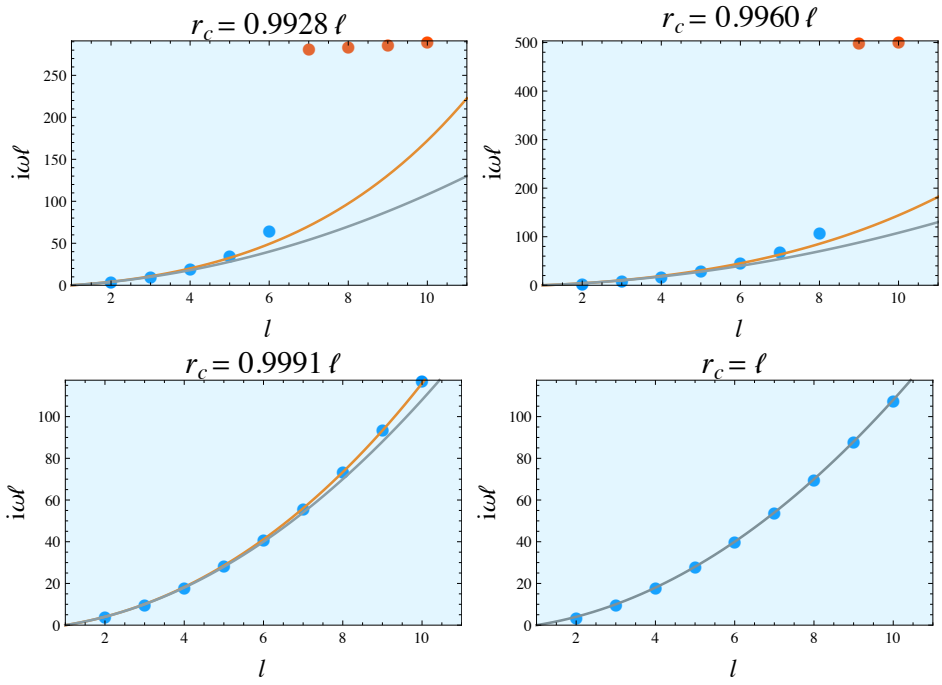

Fig. 2.6: Flow of fluid mode frequencies with fit lines. The gray line is given by $i\omega\ell = (l(l+1)-2)$ while the orange line is given by $i\omega\ell = \nu(\alpha)\,(l(l+1)-2)$ with $\nu(\alpha)$ given by (2.4.28). Note that the orange line fits the data better away from $r_c = \ell$ and the gray and orange lines coincide at the horizon, as expected.

As a check of our analysis in the previous section, in figure 2.6 we show that the correction at $\mathcal{O}(\alpha)$ of the fluid viscosity gives the correct behavior for the fluid mode frequencies for small but nonzero α. Notice that the orange line in figure 2.6 fits the

data better than the gray line for r_c parametrically displaced from the cosmological horizon. The orange line is precisely the dispersion relation corrected to $\mathcal{O}(\alpha)$ in our analysis of linear perturbations of the background metric of the static patch. The gray line does not include $\mathcal{O}(\alpha)$ corrections.

It is interesting to note that all observed spectra of $i\omega\ell$ are monotonically increasing functions of l. This is a feature that we may expect by continuity away from the modes analytically computed at $r_c = \ell$, but holds as we push r_c a finite amount from the surface, even when jumps occur.

2.5 Incompressible Fluids on Spacelike Slices?

So far we have discussed several aspects of the static patch, which is the region accessible to a single observer. We would now like to briefly discuss some aspects of the future diamond. After all, future infinity is clearly a viable candidate location for the non-perturbative definition of an asymptotically de Sitter universe. Ordinarily, we would not associate the dual theory on $\mathcal{I}^+$ with the static patch observer. On the other hand, if we impose boundary conditions where there is no incoming flux from the Northern diamond, such that all data reaching $\mathcal{I}^+$ is coming from a single static patch one might conceive of such a relation.[10] In this section we will make some simple mathematical observations about the behavior of metric deformations on a spacelike slice just outside the cosmological horizon.

[10]Such 'holographic projections' of the static patch observer were also considered in the rotating Nariai geometry [57, 74, 59]. In that case a near cosmological horizon limit allowed for an isolated space-time whose (spacelike) boundary is of the same type as the spacelike slice we are discussing here.

2.5.1 Linearized Analysis

Our aim is to solve the linearized equations in the future diamond, imposing Dirichlet boundary conditions on a constant r surface arbitrarily close to the cosmological horizon. In order to choose an appropriate near horizon coordinate system we begin with the future diamond, described by (2.2.3) with $r \in [\ell, \infty]$. As before, we introduce the following coordinate transformation:

$$\frac{t}{\ell} = \frac{1}{2\alpha}\tilde{\tau} - \frac{1}{2}\log\left(-\tilde{\rho}\,(1-\alpha\tilde{\rho})^{-1}\right) \ , \quad r = \ell(1-2\alpha\tilde{\rho}) \ . \tag{2.5.30}$$

In what follows we will drop the tildes. The metric becomes:

$$\frac{ds^2}{\ell^2} = \left(-\frac{\rho}{\alpha} + \rho^2\right) d\tau^2 + 2d\tau d\rho + (1-2\rho\alpha)^2\, d\Omega_2^2 \ . \tag{2.5.31}$$

Taking $\alpha \to 0$ with $\alpha > 0$, constant ρ slices for $\rho < 0$ now correspond to spacelike slices just above the cosmological horizon. This slice receives data from the future horizons of *both* the Southern and Northern patches. If we are to isolate one of the observers, say the Southern observer, we must impose that the incoming flux from the Northern static patch vanishes, as shown in figure 2.7.

The vector mode with vanishing flux from the Northern patch is generated by a master field $\Phi_v^S = e^{-2i\alpha\omega t(\tau,\rho)/\ell}\varphi_v^S$, with:

$$\varphi_v^S = (-\rho)^{-i\alpha\omega}{}_2F_1\left[a_1, b_1; c_1; \alpha\rho(-1+2\alpha\rho)^{-1}\right]\ (1-\alpha\rho)^{-i\alpha\omega}(1-2\alpha\rho)^{2i\alpha\omega} \ , \tag{2.5.32}$$

where

$$a_1 = -l - 2i\alpha\omega \ , \quad b_1 = 1 + l - 2i\alpha\omega \ , \quad c_1 = 1 - 2i\alpha\omega \ . \tag{2.5.33}$$

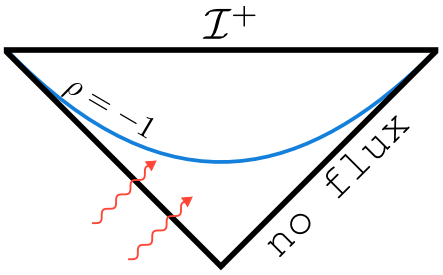

Fig. 2.7: Our boundary conditions for the linearized modes are such that the induced metric on the $\rho = -1$ slice is unchanged and there is no incoming flux from the Northern static patch.

The linearized metric deformation is given by:

$$\delta g^S_{i\tau} = 2\mathcal{V}_i \times e^{-i\omega\tau}(-\rho)^{i\alpha\omega+1}(1-\alpha\rho)^{-i\alpha\omega+1}\left(1-\frac{(1-2\alpha\rho)}{2\alpha}\partial_\rho\right)\varphi^S_v \ , \tag{2.5.34}$$

$$\delta g^S_{i\rho} = -2\alpha\mathcal{V}_i \times e^{-i\omega\tau}\left(\frac{1-\alpha\rho}{-\rho}\right)^{-i\alpha\omega}\left[\left(1-\frac{i\omega(1-2\alpha\rho)}{2\rho(1-\alpha\rho)}\right)-\frac{(1-2\alpha\rho)}{2\alpha}\partial_\rho\right]\varphi^S_v \ . \tag{2.5.35}$$

Demanding that the above vector modes vanish at the spacelike $\rho = -1$ hypersurface in the limit where $\alpha \to 0$ gives the discrete relation:

$$\omega_{sf} = +i\left(l(l+1)-2\right) \ , \quad l = 1, 2, \ldots \tag{2.5.36}$$

This is precisely the same dispersion relation that was found earlier in (2.3.18) for the Lorentzian hypersurface but with $\nu_{sf} = -1$.[11] To linear order in α we find:

$$\nu_{sf} = -1 + \frac{\alpha}{2}\left(5 + 3k_V^2\right) \ . \tag{2.5.37}$$

[11]We note that a time-reversal $\tau \to -\tau$ transformation leads to $v^i \to -v^i$ and thus introduces a sign change to the viscosity term ν_{sf} in the non-linear Navier-Stokes equation (2.1.1). Thus, one can interpret a negative viscosity fluid as a time-reversed version of a positive viscosity fluid. We thank R. Loganayagam for pointing this out to us.

It is not hard to show perturbatively in α that $\nu_{sf}(\alpha) = -\nu(-\alpha)$. Upon evaluating the linearized metric modes on the 'spacelike fluid' frequencies (2.5.36) we find that the vector modes are regular as we approach the $\rho \to 0$ horizon.

2.5.2 Non-linear Analysis

We would now like to perform a non-linear analysis of the metric deformations in an α expansion, again in the context of the spacelike slices. The cutoff surface will now be at $\rho = -1$. Non-linear deformations analogous to those presented for timelike slicings are:

$$\begin{aligned}
\frac{ds^2}{\ell^2} &= -\frac{\rho}{\alpha}d\tau^2 \\
&+ \rho^2 d\tau^2 + 2d\tau d\rho + d\Omega_2^2 + (1+\rho)\left[v^2 d\tau^2 - 2v_i d\tau dx^i\right] + 2\rho P d\tau^2 \\
&- \alpha\Big[(4\rho + 2P)\, d\Omega_2^2 - (1+\rho)v_i v_j dx^i dx^j \\
&+ \left(\rho^2 - 1\right)\left(\nabla^2 v_i + R_{ji}v^j\right) d\tau dx^i + 2v_i d\rho dx^i - \left(v^2 + 2P\right) d\tau d\rho + 2\,(1+\rho)\,\phi_i^{(\alpha)} d\tau dx^i\Big] \\
&+ \alpha^2\left(4\rho^2 d\Omega_2^2 + 2g_{\rho i}^{(\alpha^2)} dx^i d\rho + g_{ij}^{(\alpha^2)} dx^i dx^j\right) + \ldots .
\end{aligned} \tag{2.5.38}$$

On the spacelike slice at $\rho = -1$, the internal geometry is conformally equal to

$$ds_{3d}^2 = \left(\frac{1}{\alpha} + 1\right) d\tau^2 + (1+2\alpha)^2\, d\Omega_2^2 \ , \tag{2.5.39}$$

with a conformal factor

$$1 - 2\alpha P + \mathcal{O}(\alpha^2) \ . \tag{2.5.40}$$

Similarly to the timelike case, for this metric to solve the Einstein equation through $\mathcal{O}(\alpha^0)$, (v_i, P) are required to solve the incompressible Navier-Stokes equation:

$$\partial_\tau v^i + v_j \nabla_{S^2}^j v^i + \nabla_{S^2}^i P - \nu_{sf}\left(\nabla_{S^2}^2 v^i + R_j^i v^j\right) = 0 \tag{2.5.41}$$

with

$$\nu_{sf} = -1 \ . \tag{2.5.42}$$

Note again that the viscosity ν_{sf} has changed sign from the fluid on the timelike slices. By integrating the $\mathcal{G}_{\tau\tau} = 0$ condition at $\mathcal{O}(\alpha^0)$ over the sphere, we again find the constraint that

$$\partial_\tau \left(\int v^2 d\Omega_2 \right) = -2\partial_\tau \left(\int P d\Omega_2 \right) \ . \tag{2.5.43}$$

Hence the structure of the Einstein equation with positive cosmological constant on the timelike slice near the cosmological horizon with the specified boundary conditions is closely mimicked in this spacelike context.

2.5.3 Pushing the Spacelike Slice to $\mathcal{I}^+$

We now wish to push the spacelike slice all the way to $\mathcal{I}^+$ and study the constraints on ω. We impose fast-falling Dirichlet boundary conditions at $\mathcal{I}^+$ and no incoming flux from the Northern patch.

Reverting to static patch (r,t)-coordinates, the solutions $\Phi_v(r,t) = e^{-i\omega t}\varphi_v(r)$ analogous to (2.3.12) and (2.3.13) near $\mathcal{I}^+$ were computed in [35] and are given by:

$$\varphi_v^- = \left(\frac{r^2}{\ell^2} - 1 \right)^{-i\omega\ell/2} \left(\frac{r}{\ell} \right)^{i\omega} {}_2F_1 \left(a_1; b_1; c_1; \frac{\ell^2}{r^2} \right) \ , \tag{2.5.44}$$

$$\varphi_v^+ = \left(\frac{r^2}{\ell^2} - 1 \right)^{-i\omega\ell/2} \left(\frac{r}{\ell} \right)^{-1+i\omega\ell} {}_2F_1 \left(a_2; b_2; c_2; \frac{\ell^2}{r^2} \right) \ , \tag{2.5.45}$$

with

$$a_1 = \frac{1}{2}(1 + l - i\omega\ell) \ , \quad b_1 = \frac{1}{2}(-l - i\omega\ell) \ , \quad c_1 = \frac{1}{2} \ ; \tag{2.5.46}$$

$$a_2 = \frac{1}{2}(1 - l - i\omega\ell) \ , \quad b_2 = \frac{1}{2}(2 + l - i\omega\ell) \ , \quad c_2 = \frac{3}{2} \ . \tag{2.5.47}$$

As we approach $\mathcal{I}^+$ in the limit $r \to \infty$ we find $\varphi_v^- \sim 1$ and $\varphi_v^+ \sim \ell/r$. Note that $(c_2 - a_2 - b_2) = i\omega\ell$. In order to eliminate deformations of the conformal metric at $\mathcal{I}^+$ we switch off the slow falling mode φ_v^-.

Our task is to eliminate the incoming Northern flux upon turning on φ_v^+. It is not hard to see that this will require $(c_2 - a_2 - b_2) = i\omega\ell$ to be an integer. We must further ensure that metric fluctuations are analytic for $i\omega\ell \in \mathbb{Z}^+$. To achieve this, we must eliminate the logarithmic term in the hypergeometric identity (A.4.10). This implies that either

$$a_2 = -n_1 \quad \text{or} \quad \mathrm{b}_2 = -\mathrm{n}_2 \ , \quad \mathrm{n_i} = 0, 1, 2, \ldots \tag{2.5.48}$$

It turns out that of the two possibilities, only the second one is sufficient to eliminate the Northern incoming flux. In the first case, we have to impose a further inequality $n_1 \geq l$, whose origin is explained in appendix A.4. Hence, defining $n_1 \equiv l + \tilde{n}_1,\ \tilde{n}_1 = 0, 1, 2, \ldots$ and imposing no further condition on the integer n_2, we obtain the following conditions:

$$\omega_n^{\mathcal{I}^+}\ell = -i(2\tilde{n}_1 + 1 + l) \ , \quad \tilde{n}_1 = 0, 1, 2, \ldots \tag{2.5.49}$$

$$\omega_n^{\mathcal{I}^+}\ell = -i(2n_2 + 2 + l) \ , \quad n_2 = 0, 1, 2, \ldots \tag{2.5.50}$$

which combines into one single tower of modes

$$\omega_n^{\mathcal{I}^+}\ell = -i(n + l + 1) \ , \quad n = 0, 1, 2, \ldots \tag{2.5.51}$$

Curiously, and perhaps interestingly, this is exactly the same set of modes as the quasinormal mode spectrum (2.4.27) in the Southern patch.

2.5.4 Topological Black Holes in AdS_4

In fact, the above calculation is mathematically equivalent to the computation of quasinormal modes for the massless topological black hole in AdS_4 [60, 61, 62] (see also [63]) upon continuing $k_V^2 \to -k_V^2$. This is due to the fact that the metric of the massless topological AdS_4:

$$ds^2 = -\left(-1+\left(\frac{\tilde{r}}{\ell_{AdS}}\right)^2\right)d\tilde{t}^2 + \left(-1+\left(\frac{\tilde{r}}{\ell_{AdS}}\right)^2\right)^{-1} d\tilde{r}^2 + \tilde{r}^2 d\mathcal{H}_2^2 \tag{2.5.52}$$

is related to the static patch metric by an analytic continuation. The two-dimensional space: $d\mathcal{H}_2^2 = (d\xi^2 + \sinh^2\xi d\tilde{\phi}^2)$ is the standard metric on the hyperbolic two-manifold. The analytic continuation from the static patch metric (2.2.3) to the above metric is given by:

$$\ell \to i\ell_{AdS}\ , \quad t \to i\tilde{t}\ , \quad r \to i\tilde{r}\ , \quad \theta \to i\xi\ , \quad \phi \to \tilde{\phi}\ . \tag{2.5.53}$$

An observer in the massless topological AdS_4 geometry observes a Hawking temperature given by $T = 1/2\pi\ell_{AdS}$. If one considers compact quotient of $\mathcal{H}_2$, there is a finite entropy proportional to $(\ell_{AdS}/\ell_P)^2$ associated with the horizon at $\tilde{r} = \ell_{AdS}$. We also expect such mathematical similarities to hold between the boundary correlators near the boundary of topological AdS_4 black holes and those near $\mathcal{I}^+$ (using the boundary conditions discussed above). It is also interesting to note that at the non-linear level one can add negative energy to (2.5.52) and create spherically symmetric asymptotically AdS_4 topological black holes. This occurs up to a critical negative mass, for which one finds a solution interpolating between AdS_4 near the boundary and $AdS_2 \times \mathcal{H}^2$ [60]. Similarly, adding sufficient mass to the static patch leads to the Nariai solution which interpolates between dS_4 near $\mathcal{I}^+$ and $dS_2 \times S^2$. We hope to

further uncover this map in future work, as it may provide insight into the nature of the static patch observer.

Chapter 3

A de Sitter Hoedown

3.1 Rotating Black Holes

We continue our explorative work by switching focus and examining the thermodynamics of black holes in dS. In particular we will study the properties of general Kerr-de Sitter black holes [67, 68]. We treat the black hole and cosmological horizons as thermal entities in their own right and obtain the regions of phase space where they have positive and negative specific heats. Generally, the black hole horizons are out of thermal equilibrium with the cosmological horizon. However, there are three limits where one can define a Euclidean instanton associated to the Lorentzian spacetime [57]. Firstly, the black hole may be extremal, in which case the Euclidean time coordinate need not be periodically identified. Secondly, there is the lukewarm solution which is defined by the black hole and cosmological horizons sharing the same temperature. Finally, there is the rotating Nariai geometry where the black hole and cosmological horizons approach each other.

Of the three limits, it is only in the rotating Nariai geometry that the angular velocities of the black hole and cosmological horizons tend to coincide. Thus, even though the lukewarm configuration may be in thermal equilibrium, it is out of rotational equilibrium and will generally exchange particles carrying angular momentum, a process enhanced by superradiance at the quantum level [69]. We will find that this effect is absent in the rotating Nariai limit. Upon perturbations of this spacetime, however, thermodynamic evolution of the system leads it to the most entropic configuration - pure de Sitter space. Thus, the equilibrium of the rotating Nariai geometry is found to be unstable. Even so, this geometry is interesting in its own right given that it is mediated from a Euclidean instanton and can thus serve as a natural starting point in the thermal evolution.

In the second part of the chapter we focus on the rotating Nariai geometry and in particular we consider massless scalar waves about this geometry. We find explicit solutions to the wave equation, which are given explicitly by hypergeometric functions. Equipped with these solutions we proceed to compute the quasi-normal modes of the rotating Nariai geometry by imposing that the waves are purely ingoing at the black hole horizon and purely outgoing at the cosmological horizon (see for example [70]). These quasinormal modes encode the dissipative information of the spacetime upon scalar perturbations. We find two quantization conditions, one related to the frequency and the other to the axial angular momentum of the modes.

Finally, we discuss our results in light of the proposal that the rotating Nariai geometry is holographically dual to a two-dimensional Euclidean CFT [74]. The evidence for the proposal rests in the study of the asymptotic symmetry group [75] of

the rotating Nariai geometry, which is given by a single copy of the Virasoro algebra with a positive central charge. It is found that there is a striking agreement between the various quantities computed for the bulk scalars and those expected from the CFT, upon a suitable identification of the scalar field parameters. In particular, the thermal boundary-to-boundary correlators of the scalar field at $\mathcal{I}^+$ take the form of a two-point function at finite temperature in a two-dimensional CFT. In fact, they imply the presence of both left and right-moving sectors. The right-moving temperature is precisely the Hawking temperature of the cosmological horizon in the dS_2 part of the geometry and the left moving temperature is related to the periodicity of the axial coordinate of the black hole. To have complete consistency, we have to also posit the existence of an additional $U(1)$ symmetry whose zero-mode coincides with the zero-mode of the left moving Virasoro.

Some of our discussion bears resemblance to the analogous discussion for the Kerr/CFT correspondence [76]. On the other hand, we have found clear distinctions between the two. For instance, one can define various vacua for the scalar field in the rotating Nariai geometry. Moreover, one observes cosmological particle production at $\mathcal{I}^+$ as opposed to Schwinger pair-production at the timelike boundary of NHEK geometry. This is reminiscent of the striking difference between scalar fields in de Sitter space, which contain a complex valued parameter worth of vacua, and scalars in anti-de Sitter space which exhibit no such family. Thus, although classically the NHEK and rotating Nariai geometries are related by an analytic continuation in the coordinates, they are significantly different at the quantum level.

3.2 Geometry and Conserved Charges

Our story begins with the four-dimensional Einstein-Hilbert action endowed with a positive cosmological constant

$$I_g = \frac{1}{16\pi G}\int_{\mathcal{M}} d^4x\sqrt{-g}\,(R-2\Lambda)\,, \quad \Lambda \equiv +\frac{3}{\ell^2}, \tag{3.2.1}$$

where we set $G=1$ in what follows. The metric of the rotating black hole in de Sitter space is a two-parameter solution given by

$$ds^2 = -\frac{\Delta_r}{\rho^2}\left(dt - \frac{a}{\Xi}\sin^2\theta d\phi\right)^2 + \frac{\rho^2}{\Delta_r}dr^2 + \frac{\rho^2}{\Delta_\theta}d\theta^2 + \frac{\Delta_\theta}{\rho^2}\sin^2\theta\left(adt - \frac{r^2+a^2}{\Xi}d\phi\right)^2 \tag{3.2.2}$$

where we have defined the following objects:

$$\Delta_r = (r^2+a^2)\left(1-\frac{r^2}{\ell^2}\right) - 2Mr, \quad \Xi = 1+\frac{a^2}{\ell^2}, \tag{3.2.3}$$

$$\Delta_\theta = 1+\frac{a^2}{\ell^2}\cos^2\theta, \quad \rho^2 = r^2+a^2\cos^2\theta. \tag{3.2.4}$$

The parameters a and M will be related to the angular momentum and mass of the black hole solution. We will be mostly concerned in the parameter space allowing Δ_r to contain four (possible repeated) real roots.[1] We generally write Δ_r as

$$\Delta_r = -\frac{1}{\ell^2}(r-r_c)(r-r_+)(r-r_-)(r+r_n), \quad r_n > r_c \geq r_+ \geq r_- > 0 \tag{3.2.5}$$

with the following conditions obeyed:

$$(r_c+r_+)(r_c+r_-)(r_++r_-) = 2M\ell^2, \quad \prod_i r_i = a^2\ell^2 = -\ell^2\sum_{i\leq j} r_i r_j, \quad r_n = \sum_{i\neq n} r_i. \tag{3.2.6}$$

[1] Solutions with two positive real and two complex roots also exist, however such configurations require imaginary a and $M<0$.

We have denoted the locations of the cosmological, outer, inner and negative horizons as r_c, r_+, r_- and r_n respectively. Note that the negative root $-r_n$ may be physical in the case of rotating black holes given that the singularity is a ring singularity that observers can go through. Furthermore, note that 3.2.6 implies $M > 0$. The de Sitter length is denoted by ℓ.

Conserved Charges and the First Law

The conserved charges of the full spacetime have been computed in [77, 78] based on the classic construction by Brown and York [79], and are given by

$$\mathcal{Q}_{\partial_t} = -\frac{M}{\Xi^2}, \quad \mathcal{Q}_{\partial_\phi} = -\frac{aM}{\Xi^2}. \tag{3.2.7}$$

It may seem surprising to find a negative energy however this follows quite naturally from a thermodynamic argument. As we shall see, the most entropic configuration is given by pure de Sitter space which in four-dimensions has vanishing energy. Thus, it is natural that low entropy fluctuations such as the black holes carry less energy than de Sitter space itself.

On the other hand our interest will lie in the thermodynamic properties of the black hole horizon which can be treated as a thermodynamic entity in itself. The energy and angular momentum of the black hole horizon can be defined to be

$$E \equiv -\mathcal{Q}_{\partial_t} = \frac{M}{\Xi^2}, \quad J \equiv -\mathcal{Q}_{\partial_\phi} = \frac{aM}{\Xi^2}. \tag{3.2.8}$$

The reason we choose these definitions is that they reduce to the Minkowksi values in the limit $\ell \to \infty$. Additionally, as we shall soon see, they are the ones that give

the correct first law of thermodynamics.[2]

The entropies of the cosmological horizon S_c and black hole S_{BH} are given by

$$S_c = \frac{\pi(r_c^2 + a^2)}{\Xi}, \quad S_{BH} = \frac{\pi(r_+^2 + a^2)}{\Xi}. \tag{3.2.9}$$

In the presence of rotation the first law of thermodynamics becomes

$$dE = T_H dS + \tilde{\Omega}_H dJ, \tag{3.2.10}$$

where $\tilde{\Omega}_H$ and T_H are the angular velocity of the black hole horizon with respect to a non-rotating boundary and Hawking temperature of the black hole. Explicitly, they are given by

$$T_H = \frac{|\Delta_r'(r_+)|}{4\pi(r_+^2 + a^2)} = \frac{\ell^2 r_+^2 - 3r_+^4 - a^2 r_+^2 - a^2\ell^2}{4\pi\ell^2 r_+(r_+^2 + a^2)} \tag{3.2.11}$$

$$\tilde{\Omega}_H \equiv \Omega_H - \Omega_\infty = \frac{a\Xi}{r_+^2 + a^2} - \frac{a}{\ell^2}. \tag{3.2.12}$$

Note that the angular velocity as $r \to \infty$ is defined as

$$\Omega_\infty \equiv -\lim_{r\to\infty}\left(\frac{g_{t\phi}}{g_{\phi\phi}}\right) = \frac{a}{\ell^2}. \tag{3.2.13}$$

Finally, the temperature and angular momentum of the cosmological horizon, T_c and $\tilde{\Omega}_c$, are given by 3.2.11 and 3.2.12 with r_+ replaced by r_c.

The Various Limits of Parameter Space

There are various regions of interest in the parameter space of the rotating de Sitter black hole. We list them below:

[2]It is an interesting point that the definitions of energy and angular momentum for the black hole are precisely minus those for the full cosmological horizon. It is tempting to view the black hole as inducing an equal and negative energy and angular momentum at the horizon, as an electric charge inside a conducting sphere would [12].

- The *Extremal Limit* corresponds to $r_+ \to r_-$ such that the black hole becomes extremal and its temperature vanishes.
- The *Lukewarm Limit* corresponds to the black hole and cosmological horizons having the same temperature without necessarily coinciding.
- The *Rotating Nariai Limit* corresponds to $r_+ \to r_c$ such that the black hole and and cosmological horizons coincide.

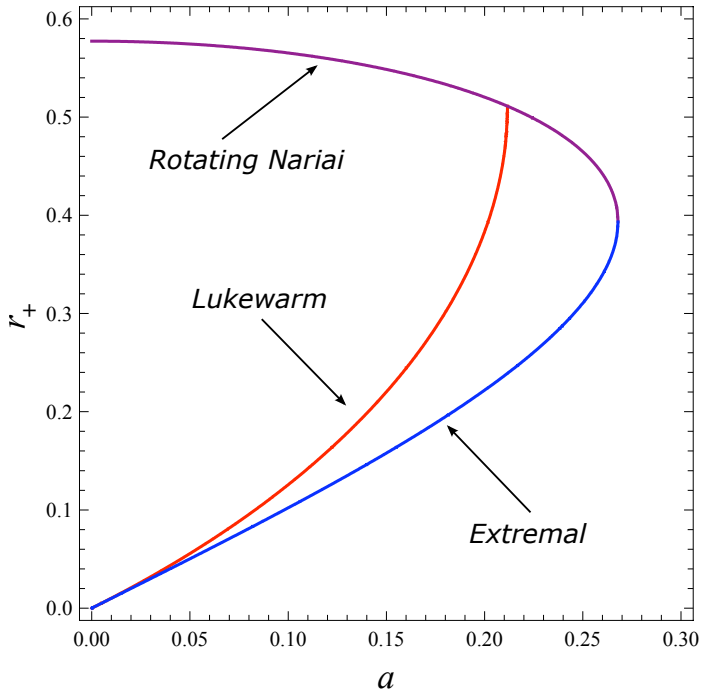

Fig. 3.1: The physically allowed configurations for Kerr-de Sitter space. We are using units where $\ell = 1$.

It is important to note that in all these limits, one can take a sensible analytic continuation to the Euclidean instanton [57]. This is in sharp contrast to the generic de Sitter black hole which is out of thermal equilibrium with the cosmological horizon.

Particularly, the rotating Nariai instanton is argued to mediate the nucleation of rotating black holes in direct analogy to the original case of the non-rotating Nariai instanton as studied by Ginsparg and Perry [37] (see also [80]).

The lukewarm solution also plays a potentially interesting role as the unique rotating black hole which is in a stable thermal equilibrium with the cosmological horizon at non-zero temperatures. One can obtain an explicit condition for when the black holes are lukewarm, namely

$$M_{lw} = a\left(1 + \frac{a^2}{\ell^2}\right). \tag{3.2.14}$$

Having said this, it should also be noted that to attain a system which is in complete thermal equilibrium all thermodynamic chemical potentials must be equal. The angular velocity of the cosmological and black hole horizons for the lukewarm configurations are not equivalent unless we are also at the rotating Nariai limit so in general there will be exchange of particles carrying angular momentum.

Geometry of the Rotating Nariai Limit

As mentioned above, the rotating Nariai geometry possesses the interesting feature of being in thermal equilibrium with respect to both its temperature and its angular velocity. Here we present the near horizon limit leading to the rotating Nariai geometry.

We will take the Nariai limit $r_+ \to r_c$ and the near horizon limit simultaneously. This is the Nariai analog of the near-NHEK limit of extremal black holes considered in [81, 82]. We define the non-extremality parameter

$$\lambda = \frac{r_c - r_+}{\epsilon r_c}. \tag{3.2.15}$$

where ϵ is a small parameter which we will take to zero. In order to go to the near horizon limit, we must go to a non-rotating frame with respect to the cosmological horizon and rescale the coordinates as follows:

$$\hat{t} = b\epsilon t \ , \quad x = \frac{r - r_+}{\epsilon r_c} \ , \quad \hat{\phi} = \phi - \Omega_H t, \tag{3.2.16}$$

where

$$\Omega_H \equiv \frac{\Xi a}{r_+^2 + a^2}, \quad b \equiv \frac{r_c(r_c - r_-)(3r_c + r_-)}{\ell^2(a^2 + r_c^2)}. \tag{3.2.17}$$

Taking $\epsilon \to 0$ with λ, t, r, ϕ held fixed, we find the rotating Nariai metric [57]

$$ds^2 = \Gamma(\theta)\left(-x(\lambda - x)d\hat{t}^2 + \frac{dx^2}{x(\lambda - x)} + \alpha(\theta)d\theta^2\right) + \gamma(\theta)(d\hat{\phi} + kxd\hat{t})^2, \tag{3.2.18}$$

with $\hat{\phi} \sim \hat{\phi} + 2\pi$, $x \in (0, \lambda)$, and

$$\Gamma(\theta) = \frac{\rho_c^2 r_c}{b(a^2 + r_c^2)}, \quad \alpha(\theta) = \frac{b(a^2 + r_c^2)}{r_c \Delta_\theta}, \quad \gamma(\theta) = \frac{\Delta_\theta (r_c^2 + a^2)\sin^2\theta}{\rho_c^2 \Xi^2}, \tag{3.2.19}$$

$$k = \frac{2ar_c^2\Xi}{b(a^2 + r_c^2)^2}, \quad \rho_c^2 = r_c^2 + a^2\cos^2\theta.$$

At fixed polar angle, one can recognize the above geometry as an S^1 fibration over two-dimensional de Sitter space [83]. The black hole horizon is located at $x = 0$ and the cosmological horizon is located at $x = \lambda$ and they have the same Hawking temperature

$$T_{RN} = \lambda/4\pi. \tag{3.2.20}$$

Furthermore, both horizons have vanishing angular velocity in the limit $\lambda \to 0$.

Global Coordinates

It will be useful to write down the rotating Nariai geometry in global coordinates. This amounts to writing the dS_2 piece in its global form

$$ds^2 = \Gamma(\theta)\left(-d\tau^2 + \cosh^2\tau d\psi^2 + \alpha(\theta)d\theta^2\right) + \gamma(\theta)\left(d\phi - k\sinh\tau d\psi\right)^2 \tag{3.2.21}$$

where $\tau \in (-\infty, \infty)$ and $\psi \sim \psi + 2\pi$ in order to have a single cover of the global dS_2. Constant time slices in this spacetime have an $S^1 \times S^2$ topology.

3.3 Thermal Phase Structure

In this section we wish to explore the thermodynamic stability and thermal evolution of the Kerr-de Sitter spacetimes. We begin by discussing stability of the black holes as it arises in the canonical and grand canonical ensembles. We conclude with an evaluation of the thermal evolution based on the total entropy of our system, which we take to be the sum of the cosmological and black hole horizon entropies. Explicit expressions for the objects we compute are presented in appendix B.1.

Thermal Stability

In addition to the first law of thermodynamics, one can study the thermal stability of our system. The measure of thermal stability depends on the ensemble we choose.

Canonical Ensemble

The *canonical ensemble* is defined at a fixed temperature and angular momentum for the black hole. The relevant thermodynamic potential is given by the Helmoltz free energy

$$\mathcal{F} = E - T_H S_{BH} \tag{3.3.22}$$

and we must examine the specific heat capacity at fixed angular momentum,

$$C_J = \left(\frac{\partial E}{\partial T_H}\right)_J = T_H \frac{\partial S_{BH}}{\partial T_H}. \tag{3.3.23}$$

From the above expression, one notes that both the extremal and rotating Nariai solutions have vanishing specific heat.

In Fig. 2 (a) we exhibit the allowed rotating black hole configurations in the (r_+, a)-plane. The black hole horizons with positive specific heat inhabit the region below the dotted line. Notice that for a given angular momentum, there is a phase transition from positive to negative specific heat as one increases r_+. This was first observed in [67] and corresponds to the point where the temperature of the black hole reaches a maximum with respect to r_+. The physically allowed parameter space is bounded by the rotating Nariai solutions, and the extremal black hole solutions. The point where the two curves meet is the ultracold point.

We note that most but not all lukewarm configurations have positive specific heat. Extremal and rotating Nariai configurations have vanishing specific heat. Finally, regions where the cosmological horizon has greater (smaller) temperature than the black hole horizon is given by the region above (below) the lukewarm curve.

Grand Canonical Ensemble

The *grand canonical ensemble* is defined at a fixed temperature and angular velocity. In this case, the relevant thermodynamic potential is given by the Gibbs free energy,

$$\mathcal{G} = E - T_H S_{BH} - \tilde{\Omega}_H J \tag{3.3.24}$$

which is a function of the intrinsic parameters T_H and $\tilde{\Omega}_H$. The stability in the grand canonical ensemble is given by analyzing the full Hessian

$$H_{ij} = \left(\frac{\partial^2 S_{BH}}{\partial X_i \partial X_j} \right), \quad X_i = E, J. \tag{3.3.25}$$

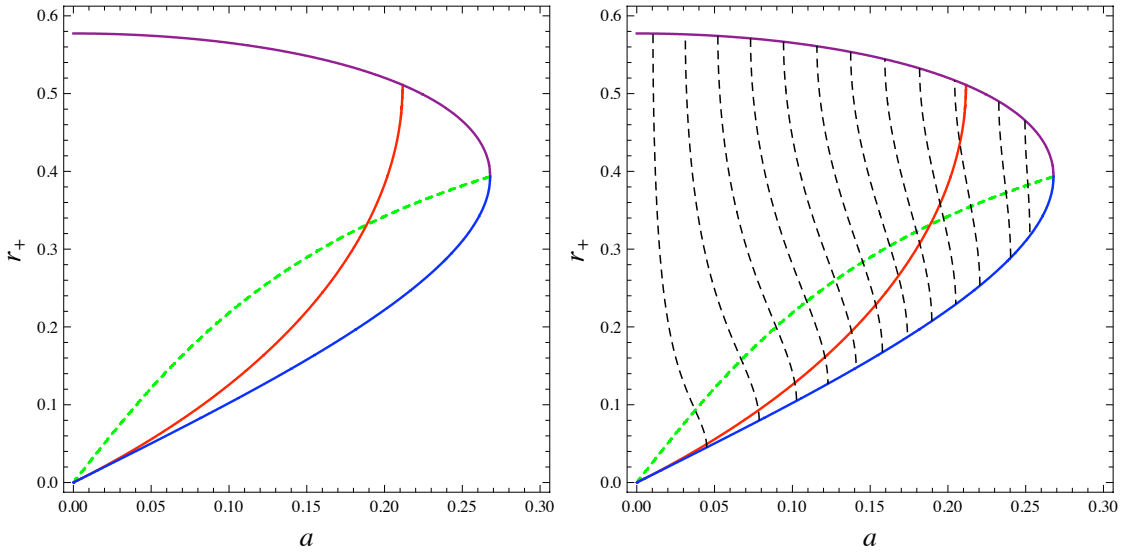

Fig. 3.2: **Left**: Phase space of allowed solutions in the (r_+, a)-plane. Above the green (dotted) line, the black hole horizon has negative specific heat. The red (solid) line indicates the lukewarm configurations. **Right**: Constant J curves in the (r_+, a)-plane. We are plotting in units where $\ell = 1$.

A system that is thermally stable will have a total entropy function lying at a maximum, as a function of the extensive parameters. This gives rise to the conditions

$$\frac{\partial^2 S_{BH}}{\partial E^2} < 0, \quad \frac{\partial^2 S_{BH}}{\partial J^2} < 0, \quad \frac{\partial^2 S_{BH}}{\partial J^2}\frac{\partial^2 S_{BH}}{\partial E^2} - \left(\frac{\partial^2 S_{BH}}{\partial J \partial E}\right)^2 > 0. \tag{3.3.26}$$

The first condition is equivalent to the specific heat at fixed angular momentum being positive, the second condition is the analogous statement for fixed energy fluctuations and the third is the requirement that the Hessian have positive determinant. In Fig. 3 (a) we demonstrate the regions of positive and negative $\partial S_{BH}^2/\partial J^2$. It is further found that the Hessian, given explicitly in B.1.3 is negative definite for all configuration space, indicating that all black holes are thermally unstable once we allow angular momentum to be exchanged.

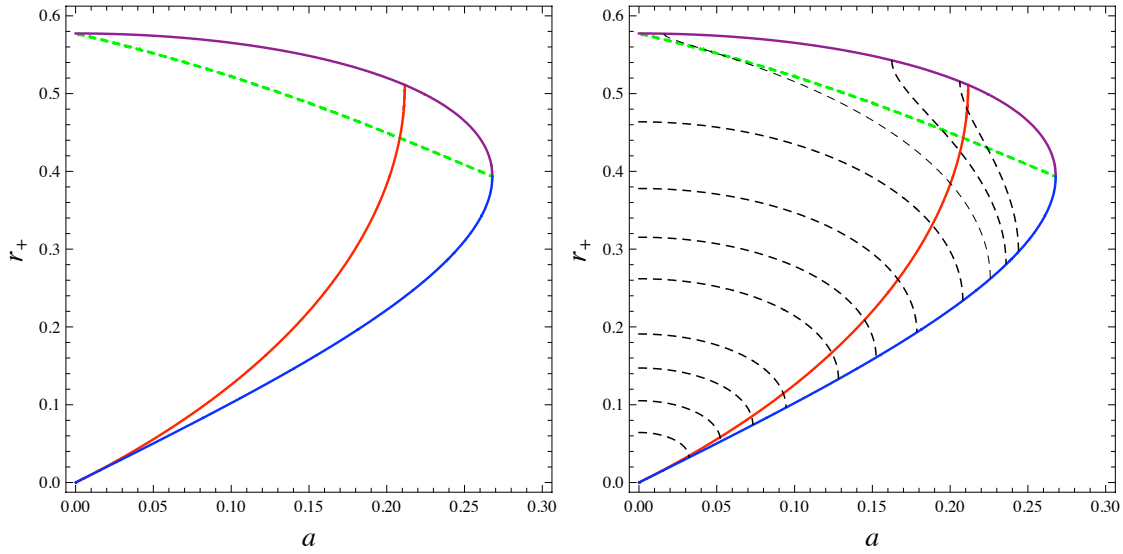

Fig. 3.3: **Left**: Regions of negative $\partial S_{BH}^2/\partial J^2$ below the green (dotted) curve. **Right**: Constant E curves in the (r_+, a)-plane. We are plotting in units where $\ell = 1$.

Thermal Evolution

We would like to address the issue of the thermal evolution of the black holes immersed within the cosmological horizon. First note that the cosmological horizon has lower temperature than the black hole horizon when we are in the region above the lukewarm line in Fig. 1. Secondly, the cosmological horizon has an angular velocity that is less or equal to that of the black hole horizon, where equality only holds in the rotating Nariai limit. Thus, most configurations are out of thermal equilibrium and will thermally evolve.

The total entropy of our system is taken to be the sum of the black hole and cosmological entropies,

$$S_{tot} \equiv S_{BH} + S_c = \frac{\pi(r_+^2 + a^2)}{\Xi} + \frac{\pi(r_c^2 + a^2)}{\Xi}. \tag{3.3.27}$$

Furthermore, the total energy and angular momentum of our spacetime is zero, as it

was noticed earlier that the conserved charges of the cosmological horizon are equal and opposite to those of the black hole.

Our system will evolve thermodynamically in the direction that maximizes total entropy for fixed total energy and angular momentum. In Fig. 4 we demonstrate constant S_{tot} contours throughout the configuration space. The system evolves to the pure de Sitter configuration which indeed is the most entropic configuration. Particularly, upon nucleation of the rotating Nariai black hole the two horizons will exchange angular momentum and energy until the black hole spins down and fully evaporates.

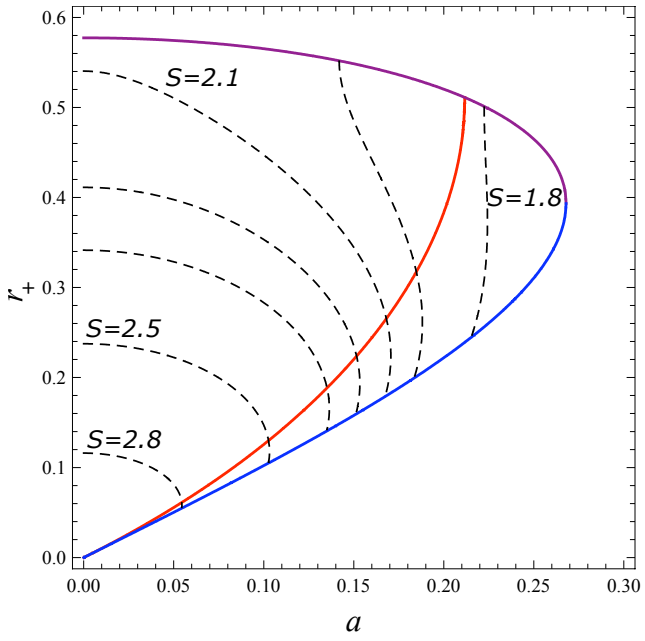

Fig. 3.4: Contour plot of constant total entropy curves. The direction of increasing entropy is toward the origin of the configuration space, i.e. pure de Sitter space. We plot in units where $\ell = 1$.

In order to determine the direction in which the thermal evolution proceeds

throughout our configuration space, we would require knowledge of the emission rates of angular momentum and energy from one horizon to the other (e.g. [69, 84]). In appendix B.2 we present the qualitative possibilities that may appear as we vary the relative rate of emission of energy and angular momentum.

3.4 Scalar Waves

At this point we will turn to the issue of the wave equation for scalar fields [85] in the Kerr-de Sitter geometry. We will not be able to obtain explicit solutions in general, the only exception being when we take the rotating Nariai limit. Indeed, the rotating Nariai instanton mediates the semi-classical production of the rotating Nariai geometry [57] and it is thus a natural configuration to study as the starting point in the thermal evolution of Kerr-de Sitter space. Furthermore, the asymptotic symmetry group of this geometry was recently studied and found to consist of a centrally extended copy of the Virasoro algebra [74] suggesting that there may be a holographic interpretation of the spacetime in terms of a two-dimensional conformal field theory.

Scalar Wave Equation

A simple way to examine the superradiant properties of a rotating black hole are by analyzing a scalar field in the black hole background. The equation of motion for a massless scalar is given by

$$\nabla^2\Phi(r,t,\Omega) = 0. \tag{3.4.28}$$

One can impose an ansatz for which the variables separate and obtain an angular and radial equation. If we choose $\Phi(r,t,\Omega) = R(r)Y_{lm}(\theta)e^{-i\omega t+im\phi}$, with $m \in \mathbb{Z}$, we find two decoupled equations for the angular and radial parts.

The angular equation is given by the spheroidal harmonic equation

$$\left(\frac{1}{\sin\theta}\frac{d}{d\theta}\Delta_\theta \sin\theta\frac{d}{d\theta} - \frac{\left(m\Xi - a\omega\sin^2\theta\right)^2}{\Delta_\theta\sin^2\theta} + j_{lm}\right)Y_{lm}(\theta) = 0. \tag{3.4.29}$$

It is not hard to prove that the separation constants j_{lm} are discrete for a given ω, however their values are only known numerically. Our normalization for the Y_{lm} is given in appendix B.4. The radial equation is given by

$$\left(\frac{d}{dr}\Delta_r\frac{d}{dr} + \frac{1}{\Delta_r}\left(a\Xi m - \omega(a^2+r^2)\right)^2 - j_{lm}\right)R(r) = 0. \tag{3.4.30}$$

The above equations are generally not analytically solvable. They are, however, regions where an approximate analytic grasp is possible. For instance, when the black hole is near-extremal, i.e. $r_+ \to r_-$, we can solve the wave-equation in the near horizon region. More precisely, if we define the parameter

$$x = \frac{r - r_+}{r_+} \tag{3.4.31}$$

and a unitless Hawking temperature $\tau_H \propto (r_+ - r_-)$ then one can match the $x \gg \tau_H$ and $x \ll 1$ solutions in the region $\tau_H \ll x \ll 1$ and compute the reflection coefficient. This situation has been discussed for the near-extremal Kerr black hole [81], and we will not pursue it here.

Rotating Nariai Limit

We will instead focus on the rotating Nariai limit. In this limit, the black hole and cosmological horizons coincide and we must take a near horizon limit to reveal the

underlying geometry where observers reside. The small parameters relevant to this limit are the near extremality parameter λ and the near horizon variable x defined by

$$x = \frac{(r - r_+)}{\epsilon r_c}, \quad \lambda = \frac{(r_c - r_+)}{\epsilon r_c}. \tag{3.4.32}$$

In the limit $\epsilon \to 0$ with λ fixed, we find that our radial equation tends to

$$\left(x(x-\lambda)\frac{d^2}{dx^2} + (2x-\lambda)\frac{d}{dx} + \frac{(\tilde{\omega} + mkx)^2}{x(x-\lambda)} + \tilde{j}_{lm} \right) R(x) = 0, \tag{3.4.33}$$

where we have defined

$$k \equiv \frac{a r_c \Xi}{(r_c^2 + a^2)} \frac{2\ell^2}{(3r_c + r_-)(r_c - r_-)}, \quad \tilde{j}_{lm} \equiv \frac{j_{lm}\ell^2}{(3r_c + r_-)(r_c - r_-)}. \tag{3.4.34}$$

We note that in order to obtain the above equation, we have to restrict ourselves to frequencies satisfying the 'near superradiant bound'

$$\omega = m\Omega_H + \epsilon\tilde{\omega}\frac{r_c(r_c - r_-)(3r_c + r_-)}{\ell^2(a^2 + r_c^2)}, \quad \Omega_H \equiv \frac{a\Xi}{r_+^2 + a^2} \tag{3.4.35}$$

and the sign of $\tilde{\omega}$ determines if we are above or below the bound $\omega = m\Omega_H$. In this limit the black hole horizon resides at $x = 0$ and the cosmological horizon resides at $x = \lambda$.

It is interesting to note that $R(x)$ obeys the equation of motion for the radial part of a charged massive scalar field in two-dimensional de Sitter space (with de Sitter radius ℓ_2), in the presence of an **E**-field [86]. Explicitly, the **E**-field and mass m_2^2 are related to the four-dimensional quantities by:

$$q\mathbf{E} = mk, \quad m_2^2\ell_2^2 = \tilde{j}_{lm}. \tag{3.4.36}$$

Furthermore, we identify the radial equation as the equation satisfied by the radial part of a massive scalar field in the rotating Nariai geometry 3.2.18. The frequency $\tilde{\omega}$

becomes the frequency of the modes in the $\hat{t}$-coordinate, thus giving a time dependence of the form $e^{-i\tilde{\omega}\hat{t}}$.

The solution to this equation is given by a linear combination of hypergeometric functions. An explicit solution in the region $0 < x < \lambda$ is given by

$$R(x) = (\lambda - x)^{-in_R} \left[c_1 \times x^{i\tilde{\omega}/\lambda} \, R_1(x) + c_2 \times x^{-i\tilde{\omega}/\lambda} \, R_2(x) \right] \tag{3.4.37}$$

where

$$R_1(x) = {}_2F_1 \left(h_- - imk, h_+ - imk, 1 + 2i\tilde{\omega}/\lambda, x/\lambda \right), \tag{3.4.38}$$

$$R_2(x) = {}_2F_1 \left(h_- - i(n_R + \tilde{\omega}/\lambda), h_+ - i(n_R + \tilde{\omega}/\lambda), 1 - 2i\tilde{\omega}/\lambda, x/\lambda \right) \tag{3.4.39}$$

We have defined the following convenient quantities

$$h_\pm \equiv \frac{1}{2} \pm i\frac{\mu}{2}, \quad \mu = \sqrt{4\tilde{j}_{lm} + 4m^2k^2 - 1}, \tag{3.4.40}$$

$$n_R \equiv mk + \tilde{\omega}/\lambda, \tag{3.4.41}$$

and we assume for later convenience that $i\mu = h_+ - h_-$ (when real) is non-integral. The expressions $h_\pm$ are complex for large angular momentum along the two-sphere. This property will be related to the oscillatory behavior of modes at $\mathcal{I}^\pm$. Also, it is worth noting that $h_\pm$ have an implicit dependence on $\tilde{\omega}$ through the $\tilde{j}_{lm}$.

We now proceed to explore the above solution in the various interesting regions of the geometry: the horizons and the boundary of the rotating Nariai geometry.

Behavior Near the Cosmological Horizon

Demanding that our wavepackets have ingoing group velocity at the black hole horizon leads us to impose $c_1 = 0$. Having done so, we can expand our solution

near the cosmological horizon[3] and find a linear combination of ingoing and outgoing waves[4]

$$R(x) = \left[A_{out}(\lambda - x)^{-in_R} + A_{in}(\lambda - x)^{in_R}\right] \tag{3.4.42}$$

where the ingoing and outgoing coefficients are given by

$$A_{out} = \frac{\Gamma[1 - 2i\tilde{\omega}/\lambda]\Gamma[2in_R]\lambda^{-i\tilde{\omega}/\lambda}}{\Gamma[h_+ + imk]\Gamma[h_- + imk]}, \tag{3.4.43}$$

$$A_{in} = \frac{\Gamma[1 - 2i\tilde{\omega}/\lambda]\Gamma[-2in_R]\lambda^{-i(2n_R+\tilde{\omega}/\lambda)}}{\Gamma[h_+ - i(n_R + \tilde{\omega}/\lambda)]\Gamma[h_- - i(n_R + \tilde{\omega}/\lambda)]}. \tag{3.4.44}$$

It is important to note that in the above, we are implicitly considering the case where $\mathrm{Re}\, n_R > 0$. In the case where $\mathrm{Re}\, n_R < 0$, one must switch the labels A_{in} and A_{out}.

Behavior at Late/Early Times

We now want to consider the behavior of scalar waves in the rotating Nariai geometry as they approach the asymptotic past or future, i.e. $\lambda < x < \infty$. In order to do so we introduce the following two linearly independent solutions to 3.4.33:

$$R_-(x) = x^{-h_- + in_R}(x - \lambda)^{-in_R}\, {}_2F_1\left(h_- - i(n_R + \tilde{\omega}/\lambda), h_- - imk, 2h_-, \lambda/x\right) \tag{3.4.45}$$

$$R_+(x) = x^{-h_+ + in_R}(x - \lambda)^{-in_R}\, {}_2F_1\left(h_+ - imk, h_+ - i(n_R + \tilde{\omega}/\lambda), 2h_+, \lambda/x\right) \tag{3.4.46}$$

Note that in the large x limit, the above solutions behave as:

$$R_\pm(x) \sim x^{-h_\pm}. \tag{3.4.47}$$

[3] In what follows we perform each expansion using hypergeometric function identities found in Abramowitz & Stegun [87].

[4] The subscripts *out*, *in* refer to the direction in which positive energy flux is traveling, i.e. the *out* modes have positive flux escaping the cosmological horizon. These need not coincide with the direction of the group velocity. We define flux in 3.6.68.

Given that x becomes timelike in the region $x > \lambda$, $R_+(x)$ corresponds to positive frequency modes and $R_-(x)$ corresponds to negative frequency modes for real μ at $\mathcal{I}^+$, where increasing x corresponds to the direction of increasing time. Note that $\hat{t}$ is now a spacelike variable whose range is $[-\infty, \infty]$ in the region $x > \lambda$. Forward spatial motion in this patch is defined along the direction of decreasing $\hat{t}$.

As in the previous subsection, we can expand both R_- and R_+ near $x = \lambda$ using hypergeometric function identities. We find

$$R_-(x) = x^{-h_- + in_R} \left(B^-_{out} (x-\lambda)^{-in_R} + B^-_{in} (x-\lambda)^{in_R} x^{-2in_R} \right), \tag{3.4.48}$$

where the coefficients are found to be

$$B^-_{out} = \frac{\Gamma[2h_-]\Gamma[2in_R]}{\Gamma[h_- + imk]\Gamma[h_- + i(n_R + \tilde{\omega}/\lambda)]}, \tag{3.4.49}$$

$$B^-_{in} = \frac{\Gamma[2h_-]\Gamma[-2in_R]}{\Gamma[h_- - imk]\Gamma[h_- - i(n_R + \tilde{\omega}/\lambda)]}. \tag{3.4.50}$$

Similarly, the R_+ modes near $x = \lambda$ are given by

$$R_+(x) = x^{-h_+ + in_R} \left(B^+_{out} (x-\lambda)^{-in_R} + B^+_{in} (x-\lambda)^{in_R} x^{-2in_R} \right), \tag{3.4.51}$$

where the coefficients are found to be

$$B^+_{out} = \frac{\Gamma[2h_+]\Gamma[2in_R]}{\Gamma[h_+ + imk]\Gamma[h_+ + i(n_R + \tilde{\omega}/\lambda)]}, \tag{3.4.52}$$

$$B^+_{in} = \frac{\Gamma[2h_+]\Gamma[-2in_R]}{\Gamma[h_+ - imk]\Gamma[h_+ - i(n_R + \tilde{\omega}/\lambda)]}. \tag{3.4.53}$$

Matching the Flux

At this point, we would like to match the outgoing flux across the future cosmological horizon. We begin by defining the general solution for $x > \lambda$:

$$R_{tot}(x) = \alpha R_-(x) + \beta R_+(x). \tag{3.4.54}$$

Matching the outgoing flux across the future cosmological horizon $x = \lambda$, amounts to matching the *out* coefficient in 3.4.42 with the *out* coefficients in 3.4.54. More precisely, we would like to solve the following set of equations

$$\alpha B^{-}_{out} + \beta B^{+}_{out} = A_{out}, \tag{3.4.55}$$

$$\alpha B^{-}_{in} + \beta B^{+}_{in} = 0 \tag{3.4.56}$$

where 3.4.56 implies no localization of flux on the future cosmological horizon. Explicit expressions for α and β are provided in appendix B.3. For future reference, however, we would like to note the ratio of these coefficients:

$$\frac{\alpha}{\beta} = \lambda^{-i\mu} \frac{\Gamma[i\mu]\Gamma[h_- - imk]\Gamma[h_- - i(n_R + \tilde{\omega}/\lambda)]}{\Gamma[-i\mu]\Gamma[h_+ - imk]\Gamma[h_+ - i(n_R + \tilde{\omega}/\lambda)]}. \tag{3.4.57}$$

3.5 Dissipation and Correlation

Given the explicit form of the solution, it is natural to study two objects. The first is related to the dissipative properties of the thermal background, which are encoded in the quasinormal modes. The second object we will study is the thermal boundary-to-boundary correlator at $\mathcal{I}^{\pm}$. The motivation for studying such correlators stems from the possibility that there exists a holographic theory living at the $\mathcal{I}^{\pm}$ boundary [74].

Quasinormal Modes of Rotating Nariai

As was noted, having found the solution in the rotating Nariai geometry we can obtain the quasinormal modes due to scalar fluctuations. These are obtained imposing that the scalar wave has purely ingoing flux at the black hole horizon and

purely outgoing flux at the cosmological horizon. As we mentioned, they encode the dissipative behavior of the thermal background under scalar perturbations.

For $\mathrm{Re}\, n_R > 0$ and $\mathrm{Re}\, \tilde{\omega} > 0$, this amounts to restricting the values of the angular momentum to the following discrete set

$$\tilde{\omega} = -i\lambda(n + h_\pm)/2 - \lambda m k/2, \quad n = 0, 1, 2, 3, \ldots \tag{3.5.58}$$

$$= -2\pi i T_{RN}\,(n + h_\pm) - \lambda m k/2, \quad n = 0, 1, 2, 3, \ldots \tag{3.5.59}$$

since they would lead to a vanishing A_{in} coefficient in 3.4.42. The imaginary part of the quasinormal modes is clearly related to the temperature of the horizons 3.2.20.

For $\mathrm{Re}\, n_R < 0$ and $\mathrm{Re}\, \tilde{\omega} > 0$, we find that the quasinormal modes become

$$|m|k = -i\,(n + h_\pm)\,, \quad n = 0, 1, 2, 3, \ldots \tag{3.5.60}$$

It is important to note that the set of modes 3.5.60 imposes a condition on the frequencies $\tilde{\omega}$ through the implicit dependence of $h_\pm$ on $\tilde{\omega}$. When $m = 0$, the quasinormal modes 3.5.58 reduce to those of the non-rotating Nariai geometry [88].

Two-Point Functions: Thermal Background

According the the notion that there is a holographic dual living at $\mathcal{I}^+$ [74], it is natural to obtain the retarded thermal boundary-to-boundary correlators [89, 90] at $\mathcal{I}^+$ of the near horizon region 3.2.18.

By imposing the boundary condition that our excitations are purely incoming at the horizon we fix the behavior of the scalar field at $\mathcal{I}^+$. The thermal boundary-to-boundary two-point function is defined by taking variational derivatives of the action

with respect to the boundary value Φ_0 of the scalar field

$$G_R^{th}(q,q') \equiv \frac{\delta}{\delta\Phi_0(q)}\frac{\delta I_{matter}}{\delta\Phi_0(q')}, \quad q,q' \in \{\tilde{\omega}, m, l\}. \tag{3.5.61}$$

and the matter action for the scalar field is given by the expression[5]

$$I_{matter} = \frac{1}{2}\int_{\mathcal{M}} d^4x\sqrt{-g}\partial_\mu\Phi\partial^\mu\Phi. \tag{3.5.62}$$

As we observed earlier, the late time behavior of the scalar field (in momentum space) about the thermal background is given by

$$\Phi \sim \alpha x^{-h_+} + \beta x^{-h_-}. \tag{3.5.63}$$

Modes with either of the falloffs $h_\pm$ are normalizable with respect to the Klein-Gordon inner product given by,

$$(\Phi_1, \Phi_2) = -i\int_\Sigma d^3x\sqrt{h}n^\mu\left(\Phi_1\overleftrightarrow{\partial_\mu}\Phi_2^*\right) \tag{3.5.64}$$

where Σ is a constant time slice with unit normal vector n^μ and h_{ij} is the induced metric on Σ. Thus, we have the freedom to choose whether we are 'sourcing' an operator with conformal weight h_+ or h_-, i.e. whether we take variational derivatives of the action with respect to β or α as the boundary value. The two different choices lead to the following two Green's functions

$$G_R^{th} \sim \frac{\alpha}{\beta} \quad \text{or} \quad \mathrm{G}_\mathrm{R}^{\mathrm{th}} \sim \frac{\beta}{\alpha} \tag{3.5.65}$$

for a conformal weight h_+ or h_- respectively. The ratio α/β was given in 3.4.57.

[5]Further details of the derivation are given in appendix B.4.

3.6 Superradiance/Cosmological Particle Production

Rotating black holes are known to superradiate. Classically, this means that an incoming wave toward the black hole horizon will be reflected back from the gravitational potential with a reflection coefficient larger than unity. Quantum mechanically it gives rise to spontaneous emission of radiation from the black hole horizon carrying angular momentum.

We can get a basic idea of the process by considering the heat transfer $T_H dS$ of a black hole upon the scattering of a quantum with energy ω and angular momentum $m > 0$. The first law of thermodynamics tells us that

$$T_H \delta S_{BH} \approx \delta E_{BH} \left(1 - \frac{m}{\omega}\Omega_H\right) \tag{3.6.66}$$

giving us a simple condition $\omega < m\Omega_H$ for the extraction of energy from the black hole.

It has been further noted [69, 91] that the presence of a cosmological horizon introduces another condition for superradiance. Namely, given the conserved charges of the cosmological horizon 3.2.7, one obtains a first law for the cosmological horizon. The crucial difference with the black hole horizon is that there is a relative sign between the charges which leads to the following condition for the onset of superradiance

$$T_c \delta S_c \approx \delta E_c \left(-1 + \frac{m}{\omega}\Omega_c\right) \tag{3.6.67}$$

which leads to the relation $\omega > m\Omega_c$. Clearly, this condition is only relevant when the incoming wave is sent from a region near the cosmological horizon.

Superadiance in the Rotating Nariai Limit

We can effectively analyze superradiance in the rotating Nariai limit using our analysis of the scalar wave. We choose boundary conditions such that we have an incoming wave originating near the cosmological horizon which is purely ingoing at the black hole horizon. The flux is given by

$$f = \frac{1}{2i}\left[x(\lambda - x)R^* \frac{d}{dx}R - x(\lambda - x)R\frac{d}{dx}R^*\right]. \tag{3.6.68}$$

The absorption cross-section of the black hole is given by the ratio of the absorbed flux at the black hole horizon to incoming flux from the cosmological horizon and is found to be

$$\sigma_{abs} = \frac{f_{abs}}{f_{in}} = \frac{2\sinh(2\pi\tilde{\omega}/\lambda)\sinh(2\pi n_R)}{\cosh(2\pi(n_R + \tilde{\omega}/\lambda)) + \cosh(\pi\mu)}. \tag{3.6.69}$$

Thus, when $-mk\lambda < \tilde{\omega} < 0$ the absorption cross-section becomes negative and our system exhibits superradiance. This agrees with our original definition of $\tilde{\omega}$, since it is precisely the deviation away from the superradiant bound. Thus, we can recover the condition on the original frequency ω:

$$m\Omega_c < \omega < m\Omega_H. \tag{3.6.70}$$

Notice that as $\lambda \to 0$, with $\tilde{\omega}$ and m fixed, the absorption cross-section tends to unity, implying that all incoming radiation is absorbed by the black hole horizon and thus superradiance is absent.

Particle production in the Rotating Nariai Limit

Given that we are in a cosmological spacetime, we must also investigate the production of particles at late times starting from a given initial vacuum state [71, 72].

The appropriate metric to address this question is the global metric given by

$$ds^2 = \Gamma(\theta)\left(-d\tau^2 + \cosh^2\tau d\psi^2 + \alpha(\theta)d\theta^2\right) + \gamma(\theta)\left(d\phi - k\sinh\tau d\psi\right)^2, \qquad (3.6.71)$$

where $\tau \in [-\infty, \infty]$ and $\psi \sim \psi + 2\pi$. Notice that this metric contains no horizons, and no single observer can fully access it.

Choosing an ansatz of the form $\Phi(\tau, \psi, \Omega) = T(\tau)Y_{lm}(\theta)e^{i(q\psi+m\phi)}$ with m and q being integers, we find that $T(\tau)$ obeys

$$\left(\frac{d^2}{d\tau^2} + \tanh\tau\frac{d}{d\tau} + \mathrm{sech}^2\tau\left(q + mk\sinh\tau\right)^2 + \tilde{j}_{lm}\right)T(\tau) = 0. \qquad (3.6.72)$$

If we perform the coordinate transformations $t = \sinh\tau$ and subsequently $z = t - i$, the solution is found to be

$$T(z) = (z+2i)^{(-i\tilde{n}+2q)/2}\left(c_1 \times z^{i\tilde{n}/2}\, T_1(z) + c_2 \times z^{-i\tilde{n}/2}\, T_2(z)\right) \qquad (3.6.73)$$

where the expressions for $T_1(z)$ and $T_2(z)$ are:

$$T_1(z) = {}_2F_1\left(h_- + q, h_+ + q, 1 + i\tilde{n}, iz/2\right), \qquad (3.6.74)$$

$$T_2(z) = {}_2F_1\left(h_- - imk, h_+ - imk, 1 - i\tilde{n}, iz/2\right) \qquad (3.6.75)$$

and we have defined $\tilde{n} \equiv mk - iq$.

We can obtain the form of the solution for early times, $t \to -\infty$, by using hypergeometric identities. We choose c_1 and c_2 such that

$$T_{in}(t) = \frac{(-t)^{-h_-}}{\sqrt{\mu}}, \qquad (3.6.76)$$

where we have normalized with respect to the Klein-Gordon inner product 3.5.64. Notice that when h_- becomes complex and thus acquires a negative imaginary part,

and we obtain an incoming particle state with positive frequency at $\mathcal{I}^-$. Thus we can expand the in-modes as a sum of creation an annihilation operators of the $|\text{in}\rangle$ vacuum:

$$\Phi_{in}(t,\psi,\Omega) = \sum_{n\in\{m,l,q\}} \left(\Phi_{in}^{(n)}(t,\psi,\Omega)a_{in,n} + \Phi_{in}^{(n)*}(t,\psi,\Omega)a_{in,n}^\dagger\right) \tag{3.6.77}$$

with

$$\Phi_{in}^{(n)}(t,\psi,\Omega) = T_{in}(t)Y_{lm}(\theta)e^{i(m\phi+q\psi)}. \tag{3.6.78}$$

normalized by the Klein-Gordon inner product 3.5.64. The creation and annihilation operators obey the usual commutation relations with the following normalization

$$[a_{in,n}, a_{in,m}^\dagger] = \delta_{nm}, \quad [a_{in,n}, a_{in,m}] = 0, \quad [a_{in,n}^\dagger, a_{in,m}^\dagger] = 0. \tag{3.6.79}$$

Furthermore, the $a_{in,n}$ operators annihilate the $|\text{in}\rangle$ vacuum, i.e. $a_{in,n}|\text{in}\rangle = 0$.

The choice of c_1 and c_2 giving rise to the purely incoming particle state at past infinity 3.6.76 gives rise to the following behavior at future infinity $\mathcal{I}^+$

$$\lim_{t\to+\infty} T_{in}(t) = b_+\left(\frac{t^{-h_+}}{\sqrt{\mu}}\right) + b_-\left(\frac{t^{-h_-}}{\sqrt{\mu}}\right). \tag{3.6.80}$$

Thus, if we define $|\text{out}\rangle$ as the vacuum state with no outgoing particles on future infinity, which is annihilated by modes of the form

$$T_{out}(t) = \frac{t^{-h_+}}{\sqrt{\mu}} \tag{3.6.81}$$

we find the following Bogoliubov transformation

$$a_{out,n} = b_+ a_{in,n} + b_-^* a_{in,n}^\dagger. \tag{3.6.82}$$

Thus, cosmological particle production due to the fact that b_- is non-vanishing. In other words,

$$|\text{in}\rangle \neq |\text{out}\rangle. \tag{3.6.83}$$

The expectation value of the number of out-particles produced in the $|\text{in}\rangle$ vacuum is given by

$$\langle \text{in}|\text{a}^{\dagger}_{\text{out,n}}\text{a}_{\text{out,n}}|\text{in}\rangle = |b_-|^2 \tag{3.6.84}$$

$$= \cosh^2(\pi m k)\,\text{csch}^2\left(\frac{\pi\mu}{2}\right) \tag{3.6.85}$$

and one can check explicitly that the relation

$$|b_+|^2 - |b_-|^2 = 1 \tag{3.6.86}$$

is satisfied.[6] As a consistency check, one may observe that for $m \to 0$, the result tends to that of cosmological particle production in dS_2.

Since the form of the wave equation is qualitatively similar for the rotating Nariai geometry in any number of dimensions, we don't expect this result to be sensitive to the dimensionality of our spacetime. This is in contrast to the regular de Sitter geometry which only exhibits particle production in *even* dimensions [92].

Euclidean Modes - A Proposal

We would like to explore one last vacuum in the global coordinates which we will call the Euclidean vacuum. In regular de Sitter space, it is well known that there exists a family of de Sitter invariant vacua known as the α-vacua, which are parameterized by the complex parameter α [71, 72, 73]. The α-vacuum modes are given by a Bogoliubov transformation of the in-modes. The corresponding Green's function in the α-vacuum has a singularity both along null separations as well as

[6] We work in the Riemann sheet with $-\pi \leq \text{Arg}z < \pi$ such that $e^{-i\pi} = -1$.

separations on antipodal points of the sphere, which are separated by a horizon for any given observer.

There is a particular value of α for which the modes become analytic in the lower hemisphere of the Euclidean de Sitter geometry, which is of course S^{d+1}, and the vacuum defined becomes the CPT invariant Euclidean vacuum $|E\rangle$. This is the unique α-vacuum that reduces to the Minkowski vacuum at short distances. The boundary-to-boundary two-point function in the Euclidean vacuum behaves as that of a d-dimensional Euclidean conformal field theory at zero temperature [15].

In a similar fashion, we would like to define the positive frequency Euclidean modes Φ_n^E in the global rotating Nariai geometry as those which are analytic in the lower hemisphere of the S^2 arising from the Euclideanization of the dS_2 part of the geometry. A motivation for this definition is the physical relation between the rotating Nariai geometry and dS_2 in the presence of an **E**-field, as was previously noted. Furthermore, they reduce to the Euclidean modes (without the $Y_{lm}(\theta)$) for a massive scalar in dS_2 in the limit $m \to 0$.

Let us analytically continue τ to $i\vartheta$ such that our z-variable in 3.6.73 becomes

$$z \to z_E = i(\sin\vartheta - 1). \tag{3.6.87}$$

The upper and lower hemispheres of the S^2 are parameterized by $\vartheta \in [0, \pi/2]$ and $\vartheta \in [-\pi/2, 0)$ respectively. The argument of the solution in global coordinates then becomes $iz/2 \to (-\sin\vartheta + 1)/2$ which in turn becomes unity at the pole of the lower hemisphere. Thus, we order for 3.6.73 to be analytic in the lower hemisphere, we

have to take a linear combination given by

$$c_1 = -2^{-i\tilde{n}}\, e^{-\pi\tilde{n}/2} \times \frac{\Gamma[h_+ + imk]\Gamma[h_- + imk]\Gamma[1 - i\tilde{n}]}{\Gamma[h_+ - q]\Gamma[h_- - q]\Gamma[1 + i\tilde{n}]}\, c_2. \tag{3.6.88}$$

Thus, we can obtain the Wightman function in the Euclidean vacuum as usual

$$G_W^{Euc}(x, x') = \langle E|\Phi^E(x)\Phi^E(x')|E\rangle = \sum_{n\in\{l,m,q\}} \Phi_n^E(x)\Phi_n^{E*}(x'). \tag{3.6.89}$$

We hope to study the Euclidean modes and more generally the possibility of α-vacua in the rotating Nariai geometry in a future work.

3.7 The rotating Nariai/CFT Correspondence

Having discussed various properties of the Kerr-de Sitter geometry and in particular the rotating Nariai limit, we would like to make contact with the proposal that quantum gravity in a rotating Nariai background is holographically dual to a two-dimensional Euclidean conformal field theory living at $\mathcal{I}^+$.

Asymptotic Symmetries

In [74] it was shown that upon defining suitable boundary conditions, the asymptotic symmetry group of the extremal rotating Nariai geometry was given by a single centrally extended Virasoro algebra

$$[L_m, L_n] = (m-n)L_{m+n} + m(m^2-1)\frac{c_L}{12}\delta_{m,-n} \tag{3.7.90}$$

with positive central charge given by,

$$c_L = \frac{12r_c^2\sqrt{(1 - 3r_c^2/\ell^2)(1 + r_c^2/\ell^2)}}{-1 + 6r_c^2/\ell^2 + 3r_c^4/\ell^4}, \tag{3.7.91}$$

and the L_n are the generators of the algebra. Assuming unitarity and modular invariance, the Cardy formula was then used to compute the cosmological entropy of the extremal Nariai geometry

$$S_c = \frac{\pi^2}{3} T_L c_L, \quad T_L = \frac{1}{2\pi k} \tag{3.7.92}$$

where the reciprocal of the left-moving temperature was precisely the chemical potential conjugate to the angular momentum,

$$dS_c = \frac{1}{T_L} d\mathcal{Q}_{\partial_\phi}. \tag{3.7.93}$$

Finite Temperature Two-point Function

One of the most generic features of a two-dimensional conformal field theory is given by the structure of its two-point functions at finite temperature. More precisely, the thermal two-point function in Euclidean momentum-space is given by [93]

$$G_E(\omega_L, \omega_R) \sim T_L^{2h_L-2} T_R^{2h_R-2} \Gamma\left[h_L + \frac{\omega_L}{2\pi T_L}\right] \Gamma\left[h_L - \frac{\omega_L}{2\pi T_L}\right] \times \\ \Gamma\left[h_R + \frac{\omega_R - i q_R \Omega_R}{2\pi T_R}\right] \Gamma\left[h_R - \frac{\omega_R - i q_R \Omega_R}{2\pi T_R}\right] \tag{3.7.94}$$

where for a spin-zero field $h_L = h_R$ and the Euclidean Matsubara frequencies $\omega_{L/R}$ are related to the Lorentzian frequencies $\tilde{\omega}_{L/R}$ by an analytic continuation. The Lorentzian Green's function G_R is given by,

$$G_R(i\tilde{\omega}_L, i\tilde{\omega}_R) = G_E(\omega_L, \omega_R). \tag{3.7.95}$$

We have also included a chemical potential Ω_R and charge q_R for the right movers for reasons that will soon be clear.

The poles of the Lorentzian retarded correlator lying in the lower half-plane characterize the decay of perturbations in the CFT and are given by the following discrete set of Lorentzian frequencies[7]

$$\tilde{\omega}_L = -2\pi i T_L(n + h_L), \quad n = 0, 1, 2, 3, \ldots \tag{3.7.96}$$

$$\tilde{\omega}_R = -2\pi i T_R(n + h_R) + q_R \Omega_R, \quad n = 0, 1, 2, 3, \ldots \tag{3.7.97}$$

The above pole structure can be compared to the poles of the thermal boundary-to-boundary correlator 3.5.65 computed earlier. We immediately observe that they have an identical structure provided that we make the following identifications[8]

$$T_L = \frac{1}{2\pi k}, \quad T_R = \frac{\lambda}{4\pi}, \quad \tilde{\omega}_L = m, \quad \tilde{\omega}_R = \tilde{\omega}, \tag{3.7.98}$$

$$h_L = h_R = h_\pm, \quad q_R = -m, \quad \Omega_R = \frac{k\lambda}{2}. \tag{3.7.99}$$

One can recognize T_L as the left-moving temperature used in 3.7.92. The right moving temperature T_R is precisely the cosmological temperature observed by observers in the rotating Nariai geometry with non-zero λ, equation 3.2.20. The left and right moving frequencies are given by the $\partial_{\hat{t}}$ and ∂_ϕ eigenvalues of the scalar modes, and the right moving $U(1)$ charge is also given by the ∂_ϕ eigenvalue. Thus, if we are to identify the right moving frequency in the CFT with the $\partial_{\hat{t}}$ eigenvalue we must also posit the existence of a $U(1)$ current algebra whose zero mode coincides with the zero mode of the right moving Virasoro algebra. This is a similar situation to that encountered in the Kerr/CFT correspondence [81, 94].

[7] The relation $\Gamma[z]\Gamma[1-z] = \pi \csc(\pi z)$ is helpful to verify the pole structure.

[8] Interestingly, the quasinormal modes of the rotating Nariai spacetime obtained in 3.5.58 and 3.5.60 also have the same structure.

3.8 Summary and Outlook

We have explored various aspects of rotating black holes in de Sitter space. Starting with the thermal phase structure, we have discussed a one-parameter family of black hole configurations which has both cosmological and black hole horizons with equal temperature and angular velocity - the rotating Nariai configurations. Geometrically, these solutions are the near horizon region between the black hole and cosmological horizons in the limit where the two coincide. They are given by an S^2 fibration over dS_2. It is found that they are in an unstable thermodynamic equilibrium, in that small thermal fluctuations result in the system thermally evolving to the most entropic configuration - pure de Sitter space.

Nevertheless, the rotating Nariai geometries serve as a natural starting point for thermal evolution as they can be created from a Euclidean instanton out of nothing [57, 80]. Furthermore, they are an interesting type of extremal geometry with a rich asymptotic symmetry group consisting of (at least) one copy of the Virasoro algebra, indicating a possible holographic interpretation [74]. Thus, we ventured into the study of scalar perturbations about this geometry.

We uncovered the explicit quasinormal mode structure of this spacetime, as well as the absorption cross-section of the black hole horizon due to an incoming wave originating near the cosmological horizon. Generally, there is a regime in the frequencies of the incoming waves where the absorption cross-section is negative, indicating superradiant scattering. However, in the strict limit where the black hole and cosmological horizons coincide we have found that the absorption cross-section tends to unity and thus superradiance is no longer present. Quantum mechanically, this may

imply that spontaneous emission is suppressed in this limit.

Furthermore, we have explored the cosmological properties of the rotating Nariai geometry. We have found evidence for at least three vacua. The $|\text{in}\rangle$ and $|\text{out}\rangle$ vacuum states are those with no incoming particles from $\mathcal{I}^-$ and no outgoing particles at $\mathcal{I}^+$ respectively. Starting at $\mathcal{I}^-$ with the $|\text{in}\rangle$ vacuum, we observed the cosmological production of particles at $\mathcal{I}^+$ and explicitly computed the expectation value of the number of particles produced. We have also proposed that the Euclidean vacuum is simply given by those modes which are analytic in the lower hemisphere of the Euclidean dS_2, i.e. S^2, part of the geometry. It would be very interesting to put the proposed Euclidean vacuum on a firm footing by carefully examining its analytic structure. Furthermore, it would be extremely interesting to examine the possibility of a complex parameter worth of vacua analogous to the α-vacua of de Sitter space [71, 92] in the rotating Nariai geometry.

Finally, we have computed the boundary-to-boundary correlation functions in the static patch coordinates of the rotating Nariai geometry. The poles of these correlators precisely match the poles of the correlators of a two-dimensional conformal field theory, provided we make a suitable identification of the quantum numbers of the scalar field with those of the operator dual to the scalar in the CFT. This resonates well with the aforementioned proposal that these geometries have a holographic dual given by a two-dimensional conformal field theory. Natural objects to study along this direction would be three-point functions and boundary-to-boundary correlators of vector fields and fermions. The study of fermions in this background might also be motivated by recent results uncovering a Fermi surface in the $AdS_2 \times S^2$ near horizon

region of an extremal charge black hole in AdS_4 [95, 96]. A possible de Sitter analogue might be a Fermi surface in the $dS_2 \times S^2$ near horizon region of the non-rotating Nariai geometry and rotational generalizations thereof.

Chapter 4

Act II: String Glasses and Multicentered Black Holes

We now pass from de Sitter space to what seems to be the completely unrelated world of multicentered black hole bound states and their potentially glassy nature. There is reason to believe, however, that the departure is not so extreme. To show this, we will take a brief detour.

4.1 The case for glasses

We encounter *most* of the phases of water early on in life: liquid water, solid ice, vapor gas. We emphasize the word most because water also has a glass phase [97] (or two) known as (low/high density) amorphous ice which arises when it is cooled extremely quickly. The difference between amorphous and conventional ice is that ice is a hexagonal crystal whereas amorphous ice, microscopically, looks disordered.

If we compare two snapshots of microscopic arrangements of water in its liquid and glass phase, it would be difficult or near impossible to tell which is which without any information about the time scales involved in the motion of these molecules. This is true of any substance that has a glass transition.

It is difficult to swallow the idea that this is an actual phase transition without any discontinuous phenomena or changes in behavior. It could very well be that glasses are simply slow moving liquids, with the slow speed dictated by the low temperature. This is not the case. Experimental evidence for the liquid-glass phase transition is obtained by observing the dramatic growth of viscosity of the supercooled liquid, at which point it falls out of equilibrium. We gather this because all macroscopic observables measured in the lab continue to evolve, and their time evolution depends on the cooling rate, allowing us to tell, in principle, when the glass fell out of equilibrium. The glass is now stuck, and the time it takes for the glass to relax into its equilibrium state starts to diverge; all this despite any changes in the microscopic structure [98].

Glasses are thus out of equilibrium, disordered systems, with time dependent phenomena, whose relaxation time scales diverge. All the interesting physical behavior comes from the fast process by which the glass is cooled, trapping it in one of a plethora of local metastable states that are 'far' from the ground state equilibrium configuration. One would thus conclude that gaining any theoretical control over this glassy transition is a daunting task, given the lack of symmetries or organizing structures that we are accustomed to in physics. This intuition is correct.

Despite the seemingly impossible and ambitious task of understanding the nature of glasses and the glass transition, progress has been made. This is especially true in

the theory of *spin glasses*. These are systems that can be formed by sprinkling magnetic impurities in a metal such as copper at random points. They can be modeled by discrete spins on a lattice, like the Ising model, where the couplings J_{ij} between lattice sites i and j are random and disordered, sampled from a probability distribution $P(J_{ij})$. Spin glasses are theoretical models with quenched disorder, that is, where the disorder is manifest in the Hamiltonian of the system (in the couplings J_{ij}) and time independent on experimental time scales. This is in contrast with the window-type "structural" glasses, where the disorder is spontaneously generated in the solution space. It may be possible to use the important advances in the understanding of spin and structural glasses towards the study of string theory and the disordered states that arise there. We hold this opinion.

4.2 Glasses and de Sitter space

Disorder is a crucial feature of glassy systems and is responsible for much of the characteristic features of glasses. One effect of disorder in a glass, is that state space breaks up into different ergodic components—small valleys in the free energy landscape that obey the ergodic theorem, despite ergodicity being broken over the whole state space. Within each ergodic component, cluster decomposition (the factorization of correlation functions at large distances) holds, although it fails for correlation functions taken with respect to the Gibbs measure.

Let us be explicit. In the study of spin glasses, the failure of the ergodic theorem and cluster decomposition is characterized by the state space splitting up into different "pure states" [100]. Each pure state is an ergodically connected component

of configuration space—ensembles of states that are 'close enough' to each other in configuration space such that any configuration can reach another via thermal fluctuations at low temperatures. For a spin glass below a critical temperature, the Gibbs measure breaks into a sum over these pure states, each obeying cluster decomposition within them. Although not a spin glass, a simple example where this occurs is the Ising model with spins at lattice site i denoted by s_i. At high temperatures, cluster decomposition holds and implies $\langle s_i\, s_j\rangle = 0 = \langle s_i\rangle\langle s_j\rangle$ as $|i-j| \to \infty$, where expectation values are taken with respect to the Gibbs measure. At low temperatures, the Ising model has a phase transition and $\langle s_i\, s_j\rangle = m^2 \neq \langle s_i\rangle\langle s_j\rangle = 0\cdot 0$. If we break up the Gibbs measure into pure states, however,

$$p_G = \tfrac{1}{2}p_+ + \tfrac{1}{2}p_- \ , \tag{4.2.1}$$

where we have defined $p_\pm = \lim_{h\to 0^\pm} \frac{1}{Z} e^{-\beta(H+h\sum_i s_i)}$, then correlation functions taken with respect to the pure state probability measures $p_\pm$ do obey cluster decomposition: $\langle s_i\, s_j\rangle_\pm = m^2 = \langle s_i\rangle_\pm\langle s_j\rangle_\pm$. In a generic glassy system, the splitting into different, multiple pure states will not be as straightforward as in the Ising example, but it is certainly a generic feature.

In [99], it was observed that scalar field correlation functions in a de Sitter background also fail to obey cluster decomposition. Specifically, they noticed that the state space of a quantum field in de Sitter space continuously breaks apart as different parts of the wavefunction fall out of causal contact across super-horizon scales. Correlation functions within the regions that do remain in causal contact with each other obey cluster decomposition, whereas correlation functions across super-horizon scales do not. Is it the case that field configurations within a single cosmological

horizon act like the ergodic components of a spin glass? If this is true, we certainly need more evidence.

As shown in [99, 101], a light quantum field in de Sitter space exhibits another feature reminscent of glassiness: ultrametricity. Ultrametricity, is a qualifier for a metric space where distances between a triplet of points (x, y, z) obey a stronger condition than the triangle inequality, specifically $d(x, y) \leq \max\{d(x, z), d(z, y)\}$. In an ultrametric space, any three points form an isosceles triangle with one short side. Moreover, ultrametricity is manifest for systems where points can be placed as leaves on a a hierarchical tree, such as the evolutionary tree to give but one example. The distance between any two leaves is equal to how far up the tree one must go to find a common parent node. For a spin glass, the points in the ultrametric space are precisely the pure states mentioned above. This was crucially the organizing principle that led to the solution of the Sherrington Kirkpatrick model [102] and is a characteristic feature of a whole slew of other spin glass models. In the context of de Sitter we have a very similar story where ultrametricity manifests itself in a suitably defined distance between late time field configurations of a light scalar.

This is striking. Mean field configurations of glasses and of quantum fields in de Sitter space break up into ergodic components, and the distances between these mean field configurations lie in an ultrametric space. There is, however, a key difference between spin glasses and de Sitter space in *how* this splitting up into ergodic components occurs. The picture we are painting is that a quantum field in de Sitter space breaks up into different ergodic components because the inflating universe on which it lives acts like a branched diffusion process, at each step taking parts of the quantum

field out of causal contact with one another and thus forcing these individual pieces to freeze and classicalize. This is very much in contrast with spin glasses, where the breaking up into pure states occurs for purely static configurations. Namely the branching process does not happen in time, but with the lowering of temperature. If the analogy is to hold, then time evolution for a scalar in a fixed de Sitter background is related to the lowering of temperature in a glass.

This analogy is curious and by no means fully explored, but we will shift our focus away from de Sitter space for the remainder of the dissertation. Instead we will look for systems in string theory that appear to have explicit glassy characteristics, namely disorder and complexity.

4.3 Complexity in string theory

What exactly do we mean by complexity? For the purpose of illustration let us discuss the specific Sherrington-Kirkpatrick Hamiltonian, given by $H = \sum_{i,j} J_{ij} s_i s_j$ where J_{ij} are random couplings between *all* spins on the lattice, sampled from a random probability distribution. Because the couplings are random, and all spins feel each other, a generic configuration will thus have frustrated bonds and will exhibit, at low enough temperatures, very slow relaxation, getting stuck in a local minimum of the rugged free energy landscape of H. Finding the true ground state is an NP-hard problem, giving a precise meaning to what we take to be the complexity of the glass. And this complexity in turn is another way of saying that the free energy landscape of H is rugged and therefore breaks up into superselection sectors at low temperatures.

String theory, in fact, presents us with similarly, if not more, complex microscopic

systems. These appear when studying the microstates that give rise to the entropy of black holes, as alluded to in chapter 1. Consider for instance (as reviewed in detail in [100]), a "3-charge" D4-brane wrapped on a smooth four-cycle Σ inside a six-torus $T^6 = (T^2)_1 \times (T^2)_2 \times (T^2)_3$, and bound to n pointlike D0-branes. Denote the number of intersection points of Σ with the sub-tori $(T^2)_A$ by P^A, $A = 1, 2, 3$ — these are the D4-charges of the system. Then Σ has $\sim \mathcal{P}^3 \equiv 6\, P^1 P^2 P^3$ worldvolume deformation and flux degrees of freedom.

In the Cardy regime, when $n \gg \mathcal{P}^3$, the pointlike D0-brane degrees of freedom dominate the degeneracy of supersymmetric ground states, and a simple computation shows that the number of these states agrees exactly with the exponential of the Bekenstein-Hawking entropy of the D4-D0 black hole. However, away from the Cardy regime, i.e. when $\mathcal{P}^3 \gtrsim n$, the order $\mathcal{P}^3$ D4-degrees of freedom, coming from worldvolume and flux deformations of Σ, become entropically dominant and the microstate counting problem becomes far more difficult. Each choice of worldvolume fluxes induces a different, highly complex potential on the moduli space of deformations of Σ, and the ground states of the system correspond to the minima of this vast D-brane landscape. On the other hand, on the black hole side, an exponentially large number of molecule-like, multicentered stationary black hole bound state configurations appears [104], all with the same total charge, and they entropically dominate the single centered black hole [105]. In chapter 6, we study the temperature dependence of these multi-black hole bound states and argue in a probe analysis that black hole bound states persist at least metastably for nonextremal black holes, up to a critical temperature where the single-centered D4-D0 black hole regains dominance (see also

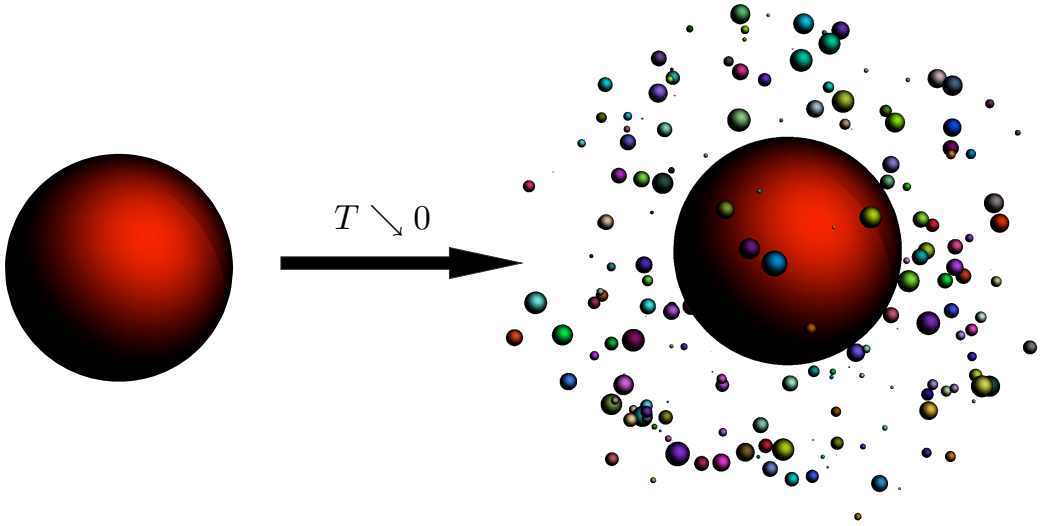

Fig. 4.1: The transition from a hot state single centered black hole to a multi-probe bound state configurations consisting of many probe halos orbiting the giant "galactic" black hole. This arises as the black hole is cooled and freezes into a multicentered state that lowers its free energy.

[107] for a closely related analysis). This is akin to a glass melting as it is heated up. In chapter 7 we extend the argument to multicentered black holes in AdS, and give a holographic interpretation of the glassiness of the system.

This transition between a single black hole and a zoo of metastable multi-black hole configurations is reminiscent of a structural glass transition and the rugged free energy landscape picture associated to the glass phase. Pictorially, once in a particular multicentered configuration, it may take exponentially long for the system to find its most entropic equilibrium configuration, as it evolves via exponentially suppressed thermal and quantum tunneling. The slow relaxation is exacerbated, far from equi-

librium, by local relaxation processes that push the system in the direction of other highly stable quasi-equilibrium states rather than towards the true maximal entropy equilibrium configuration.

This picture is compelling, and is the focus of the remainder of this dissertation. However, before delving into a discussion on whether a glass transition actually occurs for large and static multicentered black molecules, in chapter 5 we take a step back and try to understand the dynamics of these multicentered systems in a limit known as *supergoop*. We do this to get a handle on how these system behave dynamically, whether their motion is classically integrable, and if they exhibit chaos. We then return to the static problem in chapters 6 and 7 where we attempt to characterize the glassiness of the transition from single black hole to multicentered black hole bound states.

Chapter 5

Supergoop Dynamics

5.1 Introduction

5.1.1 Supergoop

When sufficiently far separated and moving slowly close to a ground state configuration, the black hole constituents of a black molecule can be thought of as point-like particles, moving in an approximately flat background, interacting with each other through specific static and velocity dependent interactions. These effective inter-particle interactions are highly constrained by the fact that these BPS systems preserve four supercharges: A nonrenormalization theorem [103] implies that once a metric has been fixed on the configuration space, the static and first order velocity dependent interactions are of a fixed form. For the flat metric:

$$H = \sum_{p=1}^{N} \frac{1}{2m_p} \left[(\mathbf{p}_p - \mathbf{A}_p)^2 + \left(\sum_{q=1}^{N} \frac{\kappa_{pq}}{|\mathbf{x}_p - \mathbf{x}_q|} + \theta_p \right)^2 \right] + \text{fermions}\,, \tag{5.1.1}$$

where $\mathbf{A}_p$ is the vector potential produced at $\mathbf{x}_p$ by a collection of Dirac monopoles of charge κ_{pq} at positions $\mathbf{x}_q$. The coefficients $\kappa_{pq} = -\kappa_{qp}$ equal the electric-magnetic symplectic products between the charges of the centers p and q. The parameters θ_p and masses m_p are fixed by the BPS central charge of each center. If the configuration space metric is not flat, the m_p may depend on $\mathbf{x}_p$.

As a result of this nonrenormalization theorem, exactly the same supersymmetric Lagrangians also appear in very different physical contexts where four supercharges are preserved and the low energy degrees of freedom can be identified with spatial positions. One example is a mixture of well-separated elementary particles obtained by wrapping D-branes around various internal cycles of a Calabi-Yau manifold, interacting with each other through gravitational, vector and scalar interactions. Clearly this can be viewed as an extreme limit of the multi-black hole systems considered above, where the dyonic black holes have been replaced by dyonic particles. Another example are monopoles and dyons in $\mathcal{N} = 2$ Yang-Mills theories [108].

A more remote example [103] is a collection of space-localized wrapped D-branes at weak string coupling in the *substringy* distance regime. Their low energy degrees of freedom are given by a (0+1)-dimensional supersymmetric quiver quantum mechanics, with a position 3-vector and a $U(1)$ gauge symmetry for each singly wrapped brane (identified with the nodes of the quiver) and the lightest brane-brane stretched open string modes represented as bifundamental oscillator degrees of freedom (identified with the arrows of the quiver). When the branes are all well separated, i.e. when the quiver theory is on the Coulomb branch, the open string modes become very massive and can be integrated out. Again, the resulting effective theory for the position

degrees of freedom must necessarily be of the form (5.1.1) fixed by supersymmetry. The coefficients κ_{pq} are now identified with the net number of arrows between two nodes.

Thus this type of supersymmetric multi-particle mechanics appears in many contexts, in widely different regimes. Much effort has been put into understanding and counting the supersymmetric ground states of such systems, in part because of their key role in physics derivations of BPS wall-crossing formulae [103, 105, 109, 110, 111]. However, little has been said about excitations or dynamics for these systems. There are a few exceptions: [112] studied the classical and quantum dynamics of the two-particle system and found it was integrable, and in [106] the persistence of the black hole molecular configurations at finite temperature was studied. However, no studies of multi-particle dynamics or statistical mechanics have been done so far. In this paper we wish to take steps in these directions.

Besides the motivation for understanding D-brane and black hole statistical mechanics and their potentially interesting interpretation as holographic glasses, such studies would also be of intrinsic interest, as these systems are rather unusual in several aspects. Due to the special form of the potential (5.1.1), an N-particle bound state will have a $2(N-1)$-dimensional moduli space of zero energy ground state configurations folded in a very complicated way into the $3(N-1)$-dimensional full configuration space (factoring out the center of mass). Naively one might therefore think that even at very low temperatures, the system would behave like a liquid, exploring large parts of the configuration space by flowing along the continuous valley of minimal energy configurations. As a simple example consider the case $N = 2$.

The particle distance is fixed and the moduli space is a sphere. One might think a probability density initially localized near a point on that sphere would quickly diffuse out over it. However, due to the effective electron-monopole Lorentz interaction between the particles, this is not quite right, as diffusion is obstructed by magnetic trapping. Another way of understanding this is conservation of angular momentum: Monopole-electron pairs carry intrinsic spin directed along their connecting axis, of magnitude equal to half their symplectic product. Hence they behave like gyroscopes. They resist changing direction; kicks will just cause them to wobble.

Thus it is natural to hypothesize that these supersymmetric multi-particle systems behave partly like a liquid and partly like a solid at very low temperatures — like goop. We will therefore refer to this peculiar state of matter as *supergoop*.

5.1.2 Dynamics

Many times we study Hamiltonian systems that are classically integrable. For this to be the case one requires the existence of at least N conserved charges (with all mutual Poisson brackets vanishing) for a system with a $2N$-dimensional phase space. Examples include single one-dimensional particles with an arbitrary potential, since the energy is conserved, and two body problems with a central force. Phase space trajectories of a classically integrable system will map N-dimensional tori. Generally, however, our system will not be classically integrable and we must confront a chaotic system. The simplest example of a chaotic system is the double pendulum which has a four-dimensional phase space with a single conserved quantity: the energy. One then studies the phase space trajectories of the double pendulum as a function of increasing

energy. For sufficiently low energies the trajectories are constrained to live on a two-dimensional torus displaying quasi-integrable behavior. As the energy is increased this torus is deformed and eventually breaks apart into smaller tori. This process is seen to continue until there is no visible structure in the phase diagram, i.e. the system tends toward ergodicity. What is perhaps most remarkable about the transition to chaos is that it occurs in a gradual fashion in which smaller and smaller islands of regular behavior are spawned before the system loses all manifest structure. A crucial question, especially for a system with many degrees of freedom, is quantifying when all ordered behavior disappears and how it depends on the parameters of the system (see for example [113, 114]).

It is our aim to begin a systematic study of the dynamical aspects of the underlying brane system on the Coulomb branch. In this paper we mainly address the case of a three particle configuration. This is already a difficult non-integrable three-body problem. To render the problem tractable, we study first the classical ground states and subsequently the motion of a probe particle in a fixed background consisting of a two-centered bound state. Remarkably, we discover that the motion of the probe is classically integrable! This is due to the presence of an additional hidden conserved quantity and is somewhat reminiscent of the integrability of a Newtonian probe particle interacting gravitationally with a background of two fixed masses, as discovered by Euler and Jacobi. We then study the transition to chaos for a system of two probes in the presence of a heavy fixed particle, with the motion restricted to live on a line. This setup is directly analogous to the double pendulum, allowing us to exploit many of the tools developed for the study of the double pendulum. As for the

double pendulum, by studying Poincaré sections we observe the formation of islands in phase space and the eventual transition to global chaos with no apparent structure in phase space. Finally, we begin to address the far more intricate dynamics of a system with a large number of centers. We provide a brief exposition of the behavior of a probe particle inside a molecule with a given number of fixed centers. We observe highly complex trajectories that become trapped for long times in the sense that they do not explore the entire molecule.

We would like to add that, after this work was submitted for publication, we became aware of [115, 116, 117, 118], which elegantly prove the classical integrability that we discuss in Section 5.5.

5.2 General Framework

Consider a system of branes wrapped on the cycles of a six-dimensional compact space, such that they are pointlike in the non-compact $(3 + 1)$-dimensions. The interactions between them are governed by strings whose ends reside on the branes themselves. The low energy physics is governed by an $\mathcal{N} = 4$ supersymmetric quiver quantum mechanics [119]. The nodes of the quivers have gauge groups associated to them and the low energy string degrees of freedom are chiral multiplets transforming in the bifundamental between two given nodes. The position degrees of freedom $\mathbf{x}_p$ of the branes are scalars in the vector multiplets of the gauge groups. It was shown in [103] that if we study the Coulomb branch of the branes, i.e. integrate out the massive chiral multiplets, a non-trivial potential is generated which governs the dynamics of the $\mathbf{x}_p$. The system of branes allows for a large family of bound states with fixed

equilibrium distances as classical ground states. If the branes move too close the stretched strings become light and even tachyonic and the system enters the Higgs phase.[1] On the other hand, if there is a sufficiently large number n_B of branes placed at a single point, such that the product of the string coupling g_s and n_B becomes large, the system is best described by closed string exchange and hence supergravity. In what follows we will consider the theory of supersymmetric multiparticle mechanics describing the Coulomb branch of the brane system. This has the advantage of being a simple setup which is interesting in and of its own right while reproducing many of the features of the multicentered configurations that exist in supergravity.

5.2.1 Supersymmetric multiparticles

The theory we consider is the multiparticle supersymmetric mechanics, which we refer to as *supergoop*, studied for example in [103, 104, 112, 120, 121, 122, 123, 124, 125, 126, 127, 128, 129]. We simply state the Lagrangian of the system, referring to [103] for details.

The supergoop Lagrangian is given by:

$$L = \sum_p \frac{m_p}{2}\left(\dot{\mathbf{x}}_p^2 + D_p^2 + 2i\bar{\lambda}_p\dot{\lambda}_p\right) + \sum_p \left(-U_p D_p + \mathbf{A}_p\cdot\dot{\mathbf{x}}_p\right) + \sum_{p,q}\left(C_{pq}\bar{\lambda}_p\lambda_q + \mathbf{C}_{pq}\cdot\bar{\lambda}_p\boldsymbol{\sigma}\lambda_q\right) , \tag{5.2.2}$$

where λ_p is the fermionic superpartner to $\mathbf{x}_p$. The D_p fields are auxiliary non-dynamical scalars. We have defined the functions:

$$U_p = \sum_q \frac{\kappa_{pq}}{2r_{pq}} + \theta_p \ , \quad \mathbf{A}_p = -\frac{1}{2}\sum_q \kappa_{pq}\left[\mathbf{A}^d(\mathbf{r}_{pq}) + \mathbf{A}^d(\mathbf{r}_{qp})\right] \ , \tag{5.2.3}$$

[1] In fact, the weak string coupling limit $g_s \to 0$ always pushes the system to the Higgs phase.

where:

$$\mathbf{A}^d(\mathbf{x}) = \frac{-y}{2r(z \pm r)}\hat{x} + \frac{x}{2r(z \pm r)}\hat{y} \tag{5.2.4}$$

is the vector potential of a single magnetic monopole of unit charge at the origin and $\mathbf{r}_{pq} \equiv \mathbf{x}_p - \mathbf{x}_q$. For the Lagrangian to be supersymmetric we further require $\kappa_{pq} = -\kappa_{qp}$. In the quiver quantum mechanics context, the κ_{pq} are the number of bifundamentals connecting two nodes. The supercharges are given by:

$$Q_\alpha = -\sum_p i\,\boldsymbol{\sigma}_\alpha^\gamma \lambda_\gamma^p \cdot (\mathbf{p}_p - \mathbf{A}_p) + \lambda_\alpha^p U_p\ , \quad \bar{Q}^\beta = \sum_q i\,\boldsymbol{\sigma}_\gamma^\beta \bar{\lambda}_q^\gamma \cdot (\mathbf{p}_q - \mathbf{A}_q) - \bar{\lambda}_q^\beta U_q\ . \tag{5.2.5}$$

The Weyl spinors obey $(\lambda_\alpha)^* \equiv \bar{\lambda}^\alpha$ and the $\boldsymbol{\sigma}_\alpha^\beta$ are the usual Pauli matrices. The Hamiltonian of our system is defined as:

$$H = \sum_p \mathbf{p}_p \cdot \dot{\mathbf{x}}_p - L\ , \quad \mathbf{p}_p \equiv m_p \dot{\mathbf{x}}_p + \mathbf{A}_p\ . \tag{5.2.6}$$

Upon integrating out the the D-terms we find:

$$H = \frac{1}{2m_p}\sum_p \left[(\mathbf{p}_p - \mathbf{A}_p)^2 + U_p^2\right] + \sum_{p<q} \frac{\kappa_{pq}}{2r_{pq}^3}\mathbf{r}_{pq} \cdot \bar{\lambda}_{pq}\boldsymbol{\sigma}\lambda_{pq}\ , \tag{5.2.7}$$

where $\lambda_{pq} \equiv \lambda_p - \lambda_q$. Notice that the particle interactions include velocity dependent forces. Furthermore, the system has three-body interactions due to the appearance of U_p^2 in H.

As usual our Hamiltonian H is related to the supercharges as $\{Q_\alpha, \bar{Q}^\beta\}_{D.B.} = -2i\delta_\alpha^\beta H$. However this is most easily checked in the quantum mechanics context where $\mathbf{p}_p \to -i\nabla_p$ and we replace the above Dirac bracket relation with the anticommutation relation:

$$\{Q_\alpha, \bar{Q}^\beta\} = 2\delta_\alpha^\beta H\ , \tag{5.2.8}$$

where $\{\lambda_\alpha^p, \bar{\lambda}_q^\beta\} = m_p^{-1}\delta_q^p\delta_\beta^\alpha$.

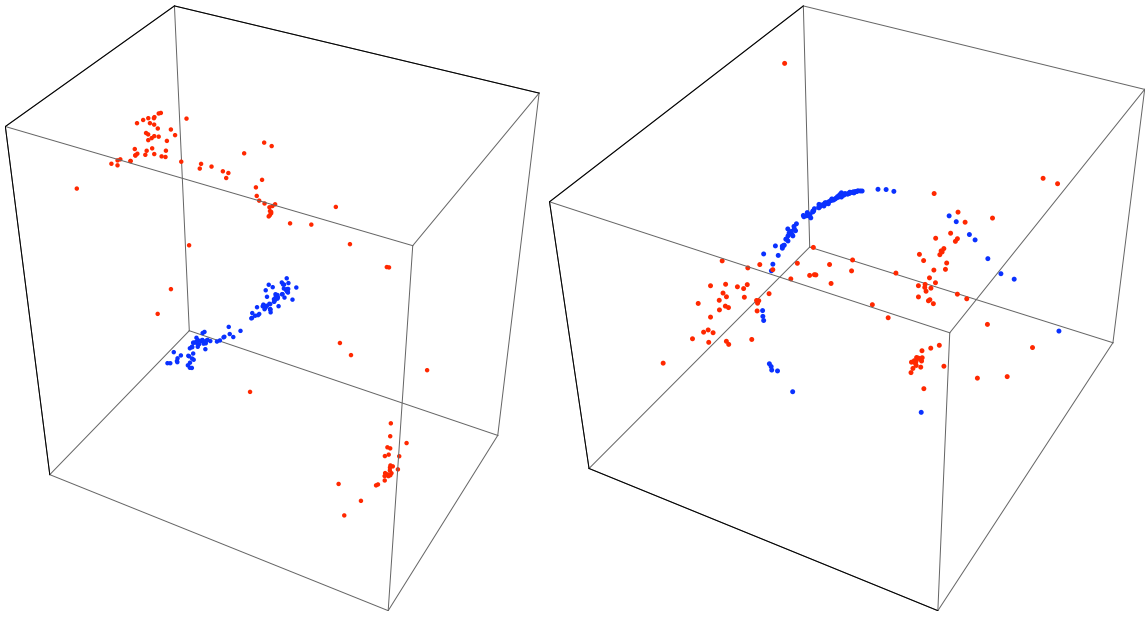

Fig. 5.1: Examples of ground states for 100 electric $\Gamma_e = (0, 1)$ plus 100 magnetic $\Gamma_m = (1, 0)$ particles.

5.2.2 Classical features and multicentered black holes

To study the classical properties of this theory, we can turn the fermionic fields off and only consider the bosonic part of (5.2.2). Static BPS configurations occur when $U_p = 0$ for all p, i.e. when:

$$\sum_q \frac{\kappa_{pq}}{2r_{pq}} = -\theta_p \ , \quad \forall \ p \ . \tag{5.2.9}$$

Taking the sum over p of (5.2.9) we find that the θ_p's must satisfy: $\sum_p \theta_p = 0$. The solutions to equation (5.2.9) are bound states of particles, see for example figure 5.1. Given that a system of N particles has $3N$-degrees of freedom which are constrained only by $(N-1)$ equations, the bound states have a $(2N+1)$-dimensional classical moduli space $\mathcal{M}$. This moduli space cannot be accessed dynamically at low temper-

atures however, due to the velocity dependent forces which constrain the particles to oscillate about a fixed location if given a small kick (just like an electron in the presence of a magnetic field). As the energy is increased, the rigid structure of the bound state is deteriorated and eventually lost completely. In the following sections we study the dynamical features of this system, with a particular focus on the three-particle system.

Equation (5.2.9) is a familiar expression in supergravity. It recreates the integrability condition of [104] for multi-centered black hole bound states in four-dimensional $\mathcal{N} = 2$ supergravity:

$$\sum_{q}^{N} \frac{\langle \Gamma_p, \Gamma_q \rangle}{|\mathbf{x}_p - \mathbf{x}_q|} = 2\mathrm{Im}\left[\mathrm{e}^{-\mathrm{i}\alpha}\mathrm{Z}_\mathrm{p}\right]_{\mathrm{r}=\infty} \ . \tag{5.2.10}$$

The above expression involves electric-magnetic charge vectors $\Gamma = \left(P^I, Q_I\right)$ with a duality invariant symplectic product given by:

$$\langle \Gamma, \tilde{\Gamma} \rangle = P^I \tilde{Q}_I - Q_I \tilde{P}^I \ . \tag{5.2.11}$$

Expression (5.2.10) also involves a function called the central charge $Z_p(z)$ which depends on the vector multiplet scalars z^a of the supergravity theory, as well as the charge vector Γ_p. At spatial infinity we can write $Z_p|_{r=\infty} = m_p e^{i\alpha_p}$ where m_p is the ADM mass of a BPS particle of charge Γ_p. If we denote $Z = \sum_p Z_p$ then the parameter α in (5.2.10) is given by $\alpha = \arg\left(\mathrm{Z}|_{\mathrm{r}=\infty}\right)$. Thus we may rewrite (5.2.10) as

$$\sum_{q}^{N} \frac{\langle \Gamma_p, \Gamma_q \rangle}{2r_{pq}} = m_p \sin\left(\alpha_p - \alpha\right) \ . \tag{5.2.12}$$

The supersymmetric multi-particle mechanics in (5.2.2) may be considered as a toy model for the dynamics of the multi-centered black hole bound states if we make the

identifications

$$\kappa_{pq} = \langle \Gamma_p, \Gamma_q \rangle \quad \text{and} \quad \theta_{\rm p} = -{\rm m}_{\rm p} \sin\left(\alpha_{\rm p} - \alpha\right) \ . \tag{5.2.13}$$

5.2.3 Three particles

Much of the discussion that follows will concern the three particle system, which already exhibits rich dynamic and non-dynamic features. Here we describe some of the characteristic features of its zero energy configurations.

Classically, the (supersymmetric) ground states are found by setting $U_1 = U_2 = U_3 = 0$. Explicitly:

$$\frac{\kappa_{12}}{2r_{12}} - \frac{\kappa_{31}}{2r_{31}} = -\theta_1 \ , \quad -\frac{\kappa_{12}}{2r_{12}} + \frac{\kappa_{23}}{2r_{23}} = -\theta_2 \ , \quad -\frac{\kappa_{31}}{2r_{31}} + \frac{\kappa_{23}}{2r_{23}} = \theta_3 \ , \tag{5.2.14}$$

with $\theta_3 = -(\theta_1 + \theta_2)$. Notice that the third equation follows from the other two. We also require that the three relative distances r_{12}, r_{23} and r_{13} satisfy the triangle inequality. The three particles have nine position degrees of freedom and the above equations only constrain two of them. Factoring out the center of mass leaves us with $(9 - 2 - 3) = 4$ unconstrained degrees of freedom. Hence, even when three-particle bound states form, there is an infinite classical moduli space of connected (and possibly also disconnected) ground states. In the case of a two-particle bound state the classical moduli space is simply a two-sphere of fixed radius $\kappa_{12}/2\theta_1$.

If we have κ_{31}, κ_{12} and κ_{23} positive we find there exist *scaling solutions* given by $r_{ij} \to \lambda\kappa_{ij}$ with $\lambda \to 0$ with the κ's obeying the triangle inequality [105]. Thus, in this regime the particles can come arbitrarily close to each other with no cost in energy.[2]

[2]When thinking about scaling solutions in the gravitational context from the point of view of a far away observer, the scaling solutions are continuously connected to a single center and will

Away from the scaling regime the solution to (5.2.14) corresponds to a bound state for which the particles may oscillate about a fixed equilibrium radius upon small perturbations.

As an example, when $\theta_3 = -3$, $\theta_2 = -2$, $\theta_1 = 5$, $\kappa_{12} = -1$, $\kappa_{13} = -1$ and $\kappa_{23} = 1$, with the three particles living on a line and particle 3 between particles 2 and 1, we find the solution:

$$r_{12} = \tfrac{1}{20}\left(7+\sqrt{19}\right) \approx 0.57, \quad r_{13} = \tfrac{1}{30}\left(8-\sqrt{19}\right) \approx 0.12\ , \quad r_{23} = \tfrac{1}{12}\left(1+\sqrt{19}\right) \approx 0.45\ . \tag{5.2.15}$$

Note that the triangle inequality is saturated since we have considered a collinear example. We should note, however, that there are clear instances where no solutions exist, such as when $(\kappa_{13}, \kappa_{23}, \theta_3) > (0, 0, 0)$, for example.

5.2.4 Regime of validity

Since we are free to choose the set of α_p, (5.2.13) does not really constrain the values of the θ_p in any way. There is, however, a restriction stemming from the requirement of the validity of the Coulomb branch description assuming our system comes out of integrating strings [103, 130]. The distances between particles must be smaller than the string scale, but larger than the ten dimensional Planck scale. For larger distances, the suitable description is given by the exchange of light closed strings (in which case supergravity is the reliable description). Furthermore, the velocities should be small compared to the speed of light to avoid higher derivative

look like a single centered black hole or particle. On the other hand, nearby observers will observe that the proper distance between the particles never shrinks to zero due to the formation of infinite throats (at least at zero temperature).

corrections to the non-relativistic Lagrangian (5.2.2).

Consider first two particles with masses m_1 and m_2 and call the string length l_s. The restriction is found to be [103]: $\kappa_{12} \ll l_s\theta_1$ and $\mu \gg l_s^2\theta_1^3/\kappa_{12}^2$, where $\mu \equiv m_1m_2/(m_1+m_2)$ is the reduced mass of two particles. Indeed, if $\kappa_{12} \gg l_s\theta_1$ the distance between the two particles in a bound state will be much larger than l_s and the appropriate description becomes that of supergravity. When $\mu \ll l_s^2\theta_1^3/\kappa_{12}^2$, the open strings between the branes become light and the appropriate description becomes that of the Higgs branch and eventually the fused D-brane system itself. For the multiparticle system, the Coulomb branch description is reliable so long as the inter-particle distances are sufficiently large that the massive strings can be reliably integrated out, i.e. $r_{ij} \gg l_s\sqrt{|\theta_i/m_i - \theta_j/m_j|}$ and sufficiently small that we remain in the substringy regime, i.e. $r_{ij} \ll l_s$.

5.3 Classical Phase Space

Having discussed the general framework of the system under study, we now discuss some of its dynamical features, beginning with the classical phase space. Recall that the Hamiltonian of our system is given by:

$$H = \frac{1}{2m_p}\sum_p \left[(\mathbf{p}_p - \mathbf{A}_p)^2 + U_p^2\right] \tag{5.3.16}$$

The Hamilton equations of motion are given by:

$$\nabla_{\mathbf{x}_p} H = -\dot{\mathbf{p}}_p \ , \quad \nabla_{\mathbf{p}_p} H = \dot{\mathbf{x}}_p \ . \tag{5.3.17}$$

For N-particles we have a $3 \times 2N = 6N$ dimensional phase space. As manifest conserved quantities we have the energy, the center of mass momentum, and the

center of mass angular momentum.

5.3.1 Two particles are integrable

We review the classical properties of the two particle problem in appendix C.1. Recall that a classically integrable system with a $2N$-dimensional phase space has at least N conserved quantities with mutually vanishing Poisson brackets. Phase space trajectories for integrable systems reside on N-dimensional tori. In the case of two-particles we have a 12-dimensional phase space. There are six manifest conserved quantities given by the net momentum and angular momentum. As shown by D'Hoker and Vinet [122, 123], the presence of a conserved Runge-Lenz vector (C.1.2) leads to an enhanced $SO(3,1)$ symmetry. The angular momentum and Runge-Lenz vector are three-vectors, the Hamiltonian is a scalar and there exist two relations amongst the seven quantities, hence there is a total of $(3+3+2) = 8$ conserved quantities. Factoring out the center of mass yields a (maximally) *super-integrable* system.[3] The super-integrability implies its equations can be separated in more than one coordinate system and one can solve for the quantum mechanical spectrum algebraically, as done in [112]. Further, it implies that trajectories in coordinate space follow paths which are closed in the case of bound orbits.

5.3.2 Three particles are chaotic

In the case of three-particles we have an 18-dimensional phase space and there is no longer a sufficient number of conserved quantities to render the system integrable.

[3] A super-integrable system [131] is a system with a $2N$-dimensional phase space which has *more* than N conserved quantities. A maximally super-integrable system has $2N-1$ conserved quantities.

Thus, such systems will exhibit chaotic behavior.

We may use several numerical tools to analyze the chaotic nature of such a system. For instance, we can study the Lyapunov exponent λ parameterizing the divergence of phase space trajectories with nearby initial conditions. Given two trajectories in phase space with initial separation δz_0, the Lyapunov exponent is defined by the limit:

$$\lambda = \lim_{t\to\infty} \lim_{\delta z_0 \to 0} \frac{1}{t} \log \frac{\delta z(t)}{\delta z_0} \ . \tag{5.3.18}$$

We can also study Poincaré sections in phase space. These are found by recording the location of a trajectory in a particular subspace of phase space each time it crosses some fiducial point (such as crossing the origin with positive velocity). These are particularly useful for lower dimensional systems such as the double pendulum, where they clearly depict the breakdown of the integrable motion on a two-torus as the energy is increased (see chapter 11 of [113] for a discussion). We will discuss and examine the Poincaré sections of a collinear three particle system in section 5.6.

Six of the phase space dimensions can be eliminated from net momentum conservation and factoring out the center of mass. We can also kill another four due to net angular momentum and energy conservation. The remaining 8-dimensions in phase space (as far as we know) are unconstrained by symmetries. Needless to say, systems with more than three particles will also display chaotic properties. A simpler setup, which we refer to as the Euler-Jacobi setup, is that of a probe particle moving in the background of two fixed centers.

5.4 Euler-Jacobi Ground States

The simplest question we can ask about our system is what the (supersymmetric) ground states are, both classically and quantum mechanically. Classically there may be continuous moduli spaces of zero energy configurations. Quantum mechanically, given that the probe is a particle in the presence of a background magnetic field, we expect the continuous classical moduli space to give rise to a degenerate set of quantum ground states due to Landau degeneracies.

5.4.1 Euler-Jacobi three body problem

We will consider a probe particle of mass m_3 in the background of two fixed centers unless otherwise specified. The background particles have masses m_1 and m_2 both very large compared to m_3, charge vectors Γ_1 and Γ_2 with symplectic product $\kappa_{12} > 0$ and Fayet-Iliopoulos constant $\theta_1 = -\theta_2 < 0$. They sit along the z-axis at $z = \pm\kappa_{12}/4\theta_1 \equiv \pm a$. By choosing m_1 and m_2 much larger than m_3, the backreaction of the probe on the fixed centers is suppressed by $\mathcal{O}(m_3/m_1, m_3/m_2)$. The probe also has charge vector γ_3 and Fayet-Iliopoulos constant θ_3.

We may also consider the possibility of forming supersymmetric bound states between the probe and the fixed centers. In such a case, a non-zero θ_3 requires us to modify the background condition $\theta_1 = -\theta_2$, since now the θ's must add to zero. We thus demand $|\theta_3| \ll |\theta_1|, |\theta_2|$ such that the correction to the positions of the original fixed centers is of order $\mathcal{O}(\theta_3/\theta_1, \theta_3/\theta_2)$. The intersection products of the probe with the centers are given by κ_{31} and κ_{32}. To avoid any large backreaction from the probe due to the κ interactions we further require that κ_{31}/r_{31} and κ_{32}/r_{32}

are small compared to $\kappa_{12}/r_{12} \sim \theta_2$.

The Hamiltonian governing the dynamics of the probe is given by:

$$H_{probe} = \frac{1}{2m_3}\left(\mathbf{p}_3 - \mathbf{A}_3\right)^2 + \frac{1}{2m_3}\left(\theta_3 + \frac{\kappa_{31}}{2r_{31}} + \frac{\kappa_{32}}{2r_{32}}\right)^2 \ . \tag{5.4.19}$$

Notice that the two scaling transformations:

$$(\mathbf{p}_3(t), \mathbf{x}_3(t)\ ;\ \kappa_{ij}, \theta_3, m_3, r_{12}, t) \to (\sigma\ \mathbf{p}_3(t), \lambda\ \sigma^{-1}\ \mathbf{x}_3(t)\ ;\ \lambda\ \kappa_{ij}, \sigma\ \theta_3, \sigma^2\ m_3, \lambda\ \sigma^{-1}\ r_{12}, \lambda\ t)\ , \tag{5.4.20}$$

generate a family of solutions parameterized by λ and σ. Given a solution to the equation of motion for some $\mathcal{O}(1)$ parameters, we can exploit the scaling symmetries to map the solution to a rescaled one in the regime of validity for the Coulomb branch description as discussed in section 5.2.4. In particular, we require $\lambda \gg \sqrt{\sigma}$ and $\lambda \ll \sigma$ which can be achieved for large σ. Notice that in this regime the velocity (which scales as σ^{-1}) becomes parametrically small.

5.4.2 Classical Ground States

As noted in (5.2.9), the space of classical ground states $\mathcal{M}$ is given by setting $U_p = 0$. Satisfying this condition gives rise to time independent classical bound states. In the probe limit, where the two background centers are fixed, this amounts to solving the algebraic equation:

$$\frac{1}{2}\frac{\kappa_{31}}{\sqrt{\rho^2 + (z-a)^2}} + \frac{1}{2}\frac{\kappa_{32}}{\sqrt{\rho^2 + (z+a)^2}} = -\theta_3\ , \tag{5.4.21}$$

where $\rho^2 = x^2 + y^2$ and $\phi = \tan^{-1}(y/x)$. One can easily prove that the effective magnetic field $\mathbf{B} = \boldsymbol{\nabla}_3 \times \mathbf{A}_3$ is always perpendicular to the tangent of $\mathcal{M}$. This

remains true for the moduli space of a probe in a background of more than two centers as well.

Consider first the case $\theta_3 = 0$. We find:

$$\rho^2 = \frac{(a-z)^2\kappa_{32}^2 - (a+z)^2\kappa_{31}^2}{(\kappa_{31}^2 - \kappa_{32}^2)} \ . \tag{5.4.22}$$

For $\rho(z)$ above to have solutions we choose $\kappa_{31} > 0 > \kappa_{32}$ and furthermore $|\kappa_{31}| > |\kappa_{32}|$, we find a continuum of solutions between $z = [z_-, z_+]$ where:

$$z_\pm = \pm a \frac{|\kappa_{32}| \mp |\kappa_{31}|}{|\kappa_{31}| \pm |\kappa_{32}|} \ . \tag{5.4.23}$$

Note that $z_- < -a < z_+ < a$ and thus the $\theta_3 = 0$ surfaces enclose the fixed charge at $z = -a$ in this case. Similarly, for $|\kappa_{31}| < |\kappa_{32}|$ the probe encloses only the center at $z = a$. For $\kappa_{31} = -\kappa_{32}$ and θ_3, the classical moduli space $\mathcal{M}$ becomes the $z = 0$ plane.

For $\theta_3 \neq 0$ finding $\rho(z)$ amounts to solving a quartic equation. In order to do so, it is convenient to go to prolate spheroidal coordinates:

$$\rho = a\sqrt{(\xi^2 - 1)(1 - \eta^2)} \ , \quad z = a\xi\eta \ , \quad \phi = \phi \ , \tag{5.4.24}$$

such that:

$$2a\theta_3(\eta^2 - \xi^2) = (\kappa_{31} + \kappa_{32})\xi + (\kappa_{31} - \kappa_{32})\eta \ . \tag{5.4.25}$$

In the above we have implicitly used that $\eta \in [-1, 1]$ and $\xi \in [1, \infty]$. We can easily find a solution for $\eta = \eta(\xi)$:

$$\eta(\xi) = \frac{1}{4}\left(\delta_1 - \delta_2 \pm \sqrt{(\delta_1 - \delta_2)^2 + 8(\delta_1 + \delta_2)\xi + 16\xi^2}\right) \ , \tag{5.4.26}$$

where $\delta_1 \equiv \kappa_{31}/(a\theta_3)$ and $\delta_2 \equiv \kappa_{32}/(a\theta_3)$. In figure 5.2 we show the different qualitative types of $\mathcal{M}$ as a function of δ_1 and δ_2. The qualitative features of each region

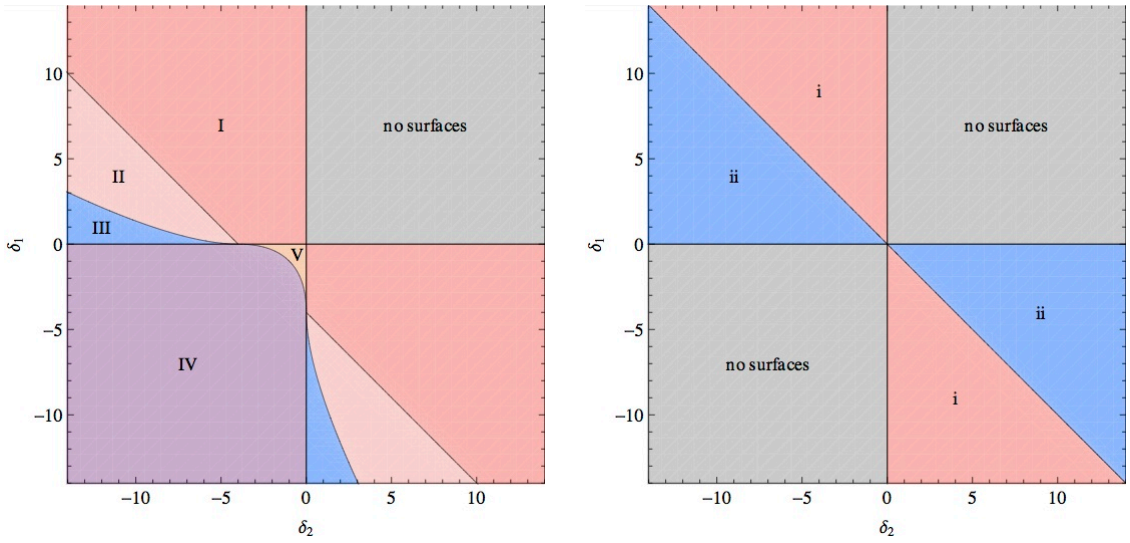

Fig. 5.2: Left: Classical moduli space $\mathcal{M}$ in the $\delta_1 - \delta_2$ plane for $\theta_3 \neq 0$. The nature of $\mathcal{M}$ for the different regions is shown in figure 5.3. Right: Classical moduli space for $\mathcal{M}$ with $\theta_3 = 0$. In regions i and ii the centers at $z = a$ and $z = -a$ are enclosed respectively.

are shown in figure 5.3. Notice that upon defining the prolate coordinates (5.4.24) we have scaled out the distance $r_{12} = a$ between the fixed centers. To obtain physical distances we simply multiply by $r_{12} = a$.

5.4.3 Quantum Ground States

From the classical point of view, our particle is nothing more than a charged particle in the presence of magnetic fields constrained to live on a surface. Thus, given a time independent supersymmetric bound state configuration we can compute the lowest Landau degeneracies d_L by computing the degeneracy of states with vanishing energy for the constrained particle. Such a setup has been addressed for non-uniform

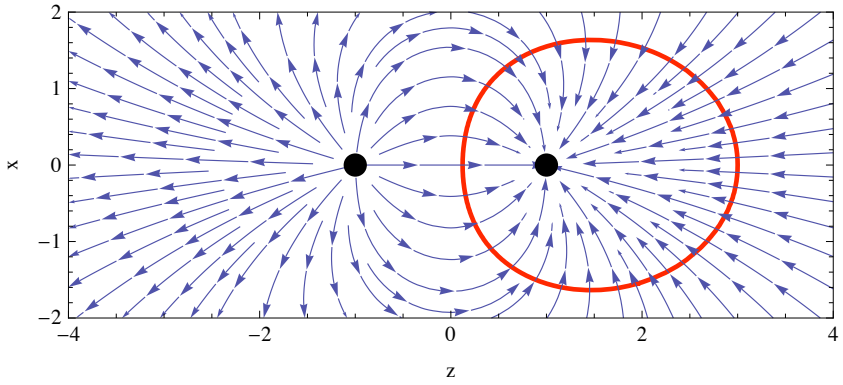

(a) Region I

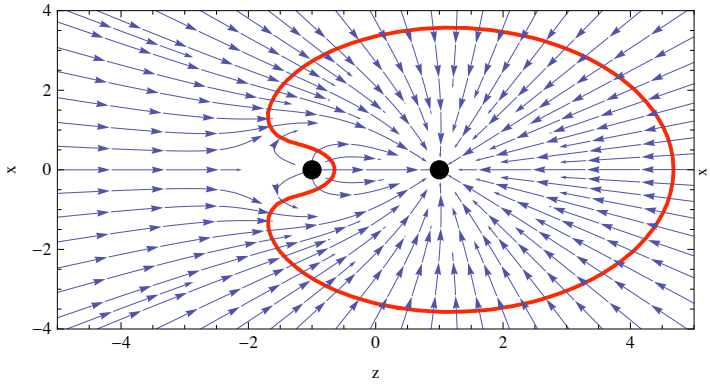

(b) Region II

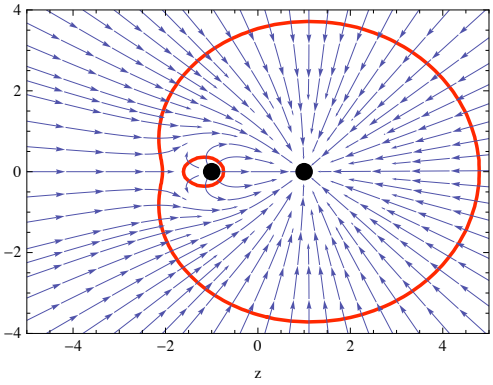

(c) Region III

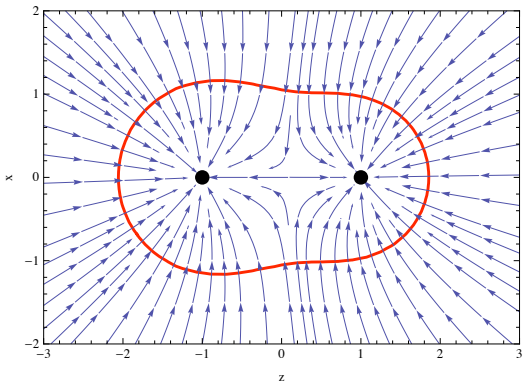

(d) Region IV

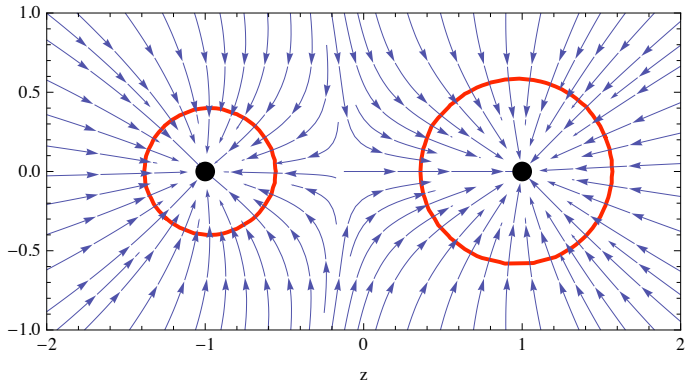

(e) Region V

Fig. 5.3: Classical moduli space in the $\delta_1 - \delta_2$ plane for $\theta_3 \neq 0$. The order of the figures left to right starting at the top are the regions in figure 5.2.

magnetic fields everywhere normal to the surface [132], which is precisely the situation we find ourselves in. Following [103], the lowest Landau degeneracies are given by the total flux through the classical moduli space $\mathcal{M}$. For instance, as we discuss below, the Landau degeneracy of the fixed background is given by κ_{21}. Upon studying the phase diagram and corresponding $\mathcal{M}$ in figures 5.2 and 5.3, we find that the total degeneracy is:

$$\text{I, II and III} \quad : \quad d_{tot} = \kappa_{12} \times |\kappa_{31}| \quad \text{or} \quad \mathrm{d_{tot}} = \kappa_{12} \times |\kappa_{32}| \ , \tag{5.4.27}$$

$$\text{IV and V} \quad : \quad d_{tot} = \kappa_{12} \times |\kappa_{31} + \kappa_{32}| \ . \tag{5.4.28}$$

For regions I, II and III, the degeneracy of states depends on which of the two background centers is encircled by $\mathcal{M}$. Notice there is a jump in the number of ground states as we vary δ_1 and δ_2. Since we are in the probe limit, we expect these results to be correct up to order $\mathcal{O}(\kappa_{31}/\kappa_{12})$ and $\mathcal{O}(\kappa_{32}/\kappa_{12})$.

From the supersymmetric quantum mechanics point of view, recall that $\{Q_\alpha, \bar{Q}^\beta\} = 2\delta_\alpha^\beta H$. In the absence of the probe, the ground state of the background is given by [103]:

$$|\mathbf{b}\rangle = \Psi_\alpha(\vec{x}_1 - \vec{x}_2)\bar{\tilde{\lambda}}^\alpha|0\rangle \ , \quad \tilde{\lambda} \equiv \lambda_1 - \lambda_2 \ . \tag{5.4.29}$$

The center of mass coordinate $\vec{x}_0 \equiv (m_1\vec{x}_1 + m_2\vec{x}_2)/(m_1 + m_2)$ and center of mass spinor $\lambda_0 \equiv (m_1\lambda_1 + m_2\lambda_2)/(m_1 + m_2)$ drop out and thus $|\mathbf{b}\rangle$ is naturally a function of the relative background position vector and spinor. The state $|0\rangle$ is annihilated by $\tilde{\lambda}$ and defines a three-dimensional Hilbert space through action of $\bar{\tilde{\lambda}}$. There are κ_{12} ground states filling a spin-$(\kappa_{12} - 1)/2$ multiplet. From the last term in the Hamiltonian (5.2.7), we observe that there exist spin-spin couplings between the background spinors λ_1 and λ_2 and the probe spinor λ_3. It is convenient to introduce

the relative spinors $\lambda_{13} \equiv \lambda_1 - \lambda_3$ and $\lambda_{23} \equiv \lambda_2 - \lambda_3$ and their associated vacua $|0_{23}\rangle$ and $|0_{13}\rangle$, such that $\lambda_{23}|0_{23}\rangle = 0$ and so on. Both $|0_{23}\rangle$ and $|0_{13}\rangle$ have an associated three-dimensional Hilbert space and the general state must be a tensor product of all linear combinations of all such states, finally tensored with $|\mathbf{b}\rangle$. Given that the probe is sensitive to the background **B**-field, it will go into spin one-half states of $|0_{13}\rangle$ and $|0_{23}\rangle$ aligning with the **B**-fields from the fixed particles at $z = \pm a$. This will split the lowest Landau degeneracies. It would be interesting to compute the explicit ground state wavefunctions.

For the sake of completeness we briefly mention another method to compute the number of ground states. One can associate a quiver diagram Q to the data (κ_{ij}, θ_i) of a particular configuration [119, 103]. It turns out that the dimension of the moduli space $\mathcal{M}(Q, \mathbf{N}, \theta)$ of the quiver Q can be related to the number of BPS ground states. In particular, for the three body problem where each particle is a different species we have a quiver theory Q with $\mathbf{N} = (1, 1, 1)$, κ_{12} arrows between nodes 1 and 2, κ_{13} arrows between nodes 1 and 3 and κ_{23} arrows between nodes 2 and 3. The quiver diagram is presented in figure 5.4. The Fayet-Iliopoulos constants θ_v are additional parameters associated with each node v. Ground state degeneracies for similar setups to the one we are studying have been computed in [105]. Notice that scaling solutions can occur only for quivers with closed loops. In our problem, with $\kappa_{12} > 0$, we find that regions I, II and III correspond to quivers with closed loops and regions IV and V correspond to quivers with no closed loops.

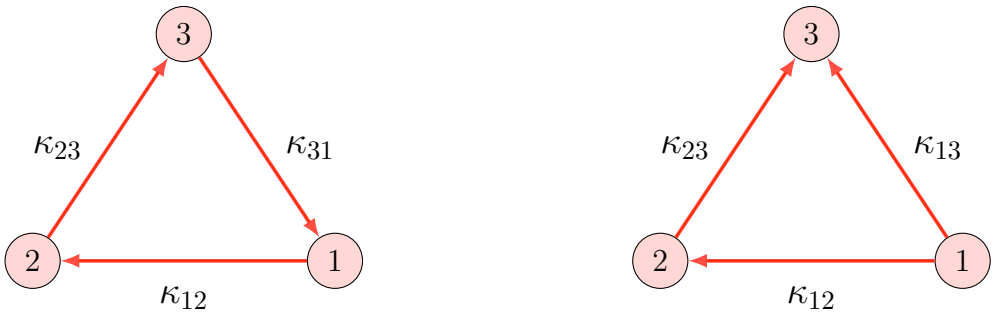

Fig. 5.4: Three node quiver with a closed loop (left) and without a closed loop (right).

5.5 Euler-Jacobi Dynamics: classical integrability

The equations governing the probe are dictated by the Hamiltonian in (5.2.6). There are two obvious constants of motion in this problem, namely the energy and the angular momentum in the direction of the line where the two centers are placed. If the system is to be rendered integrable, there must exist a third constant of motion. Such a constant of motion was found for the problem of a Newtonian probe interacting gravitationally with a background of two fixed massive particles [133, 134], also known as the Euler-Jacobi three-body problem. We will show that the analogous problem in the theory under consideration is also integrable. This was previously shown and discussed in [115, 116, 117, 118].

5.5.1 Setup and coordinate systems

Recall that we are considering two fixed background centers sitting on the z-axis at $z = \pm\kappa_{12}/4a\theta_1 \equiv \pm a$. Let us go to a cylindrical system with metric:

$$ds^2 = d\rho^2 + \rho^2 d\phi^2 + dz^2 \ , \tag{5.5.30}$$

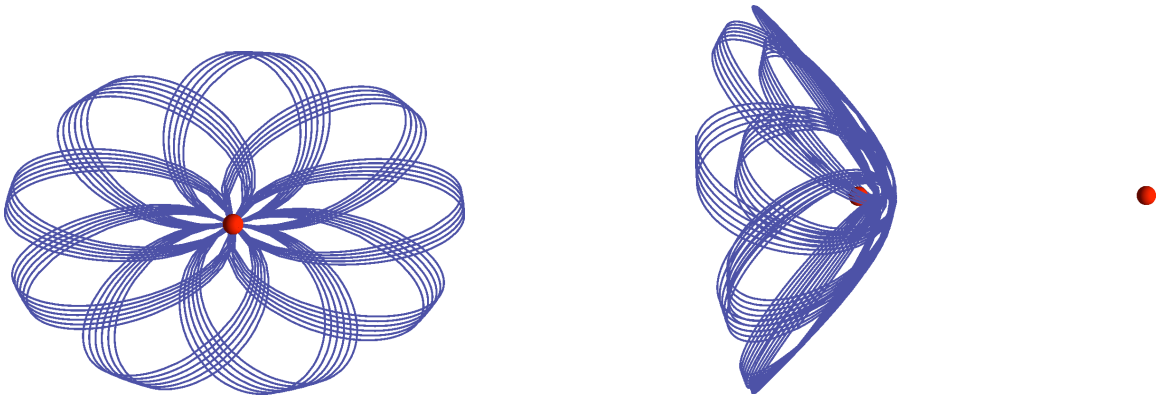

Fig. 5.5: The Euler-Jacobi flower. The red balls represent the fixed background centers and the blue line represents the classical trajectory of the probe. In this case, the trajectory precesses around only one of the fixed centers.

where the Cartesian and cylindrical coordinates are related by $x = \rho\cos\phi$, $y = \rho\sin\phi$ and $z = z$. One observes that the Lagrangian and Hamiltonian are independent of the ϕ coordinate which implies a symmetry. The conserved quantity of this symmetry is given by the angular momentum in the z-direction, such that the canonical momentum $p_\phi = l$ is constant. The probe Hamiltonian (5.4.19) in cylindrical coordinates becomes:

$$H_{probe} = \frac{1}{2m_3}\left(p'_i - A_i(\rho,\phi,z)\right) g^{ij}\left(p'_j - A_j(\rho,\phi,z)\right) + \frac{\left(U_3(\rho,z)\right)^2}{2m_3} \ , \qquad (5.5.31)$$

where the p'_i are the conjugate momenta in the cylindrical coordinates. The relation between conjugate momenta between the primed and unprimed coordinate systems is $p_i = p'_j\ \partial x'^j/\partial x^i$.

The third constant of motion is not manifest in cylindrical coordinates. One must go to the prolate spheroidal coordinates (5.4.24) with metric:

$$ds^2 = a^2(\xi^2-\eta^2)\left[\frac{d\xi^2}{(\xi^2-1)} + \frac{d\eta^2}{(1-\eta^2)}\right] + a^2(\xi^2-1)(1-\eta^2)d\phi^2 \ . \qquad (5.5.32)$$

Once in this coordinate system, we note that our Hamiltonian takes the following form:

$$H_{probe} = \frac{H_\xi + H_\eta}{\xi^2 - \eta^2} \ , \tag{5.5.33}$$

where H_ξ depends *only* on ξ and p_ξ^2 and H_η depends *only* on η and p_η^2. Thus, we can write:

$$H_{probe}\xi^2 - H_\xi = H_\eta + H_{probe}\eta^2 \equiv G \ , \tag{5.5.34}$$

where G must be a constant of motion. More explicitly we have:

$$H_\xi = p_\xi^2\frac{(\xi^2-1)}{2a^2m_3}+\frac{p_\phi^2}{2a^2m_3(\xi^2-1)}+p_\phi\frac{\xi(\kappa_{31}-\kappa_{32})}{2a^2m_3(\xi^2-1)}+\frac{(\kappa_{31}-\kappa_{32})^2}{8a^2m_3(\xi^2-1)}+\frac{\theta_3\xi(\kappa_{31}+\kappa_{32}+a\theta_3\xi)}{2am_3} \ ,$$

and

$$H_\eta = p_\eta^2\frac{(1-\eta^2)}{2a^2m_3}+\frac{p_\phi^2}{2a^2m_3(1-\eta^2)}+p_\phi\frac{\eta(\kappa_{31}+\kappa_{32})}{2a^2m_3(\eta^2-1)}+\frac{(\kappa_{31}+\kappa_{32})^2}{8a^2m_3(1-\eta^2)}+\frac{\theta_3\eta(\kappa_{31}-\kappa_{32}-a\theta_3\eta)}{2am_3} \ .$$

We conclude that the probe-two-center problem of supergoop is integrable, providing another example to the distinguished list of integrable classical systems. In this system, one observes highly symmetric spatial trajectories, as illustrated in figure 5.5.1.

5.6 Beyond Euler-Jacobi: the stringy double pendulum

If we move away from the probe approximation and allow backreaction with the fixed centers, our system is no longer integrable and begins to show chaotic features. For instance, one can study trajectories in phase space and see whether they are

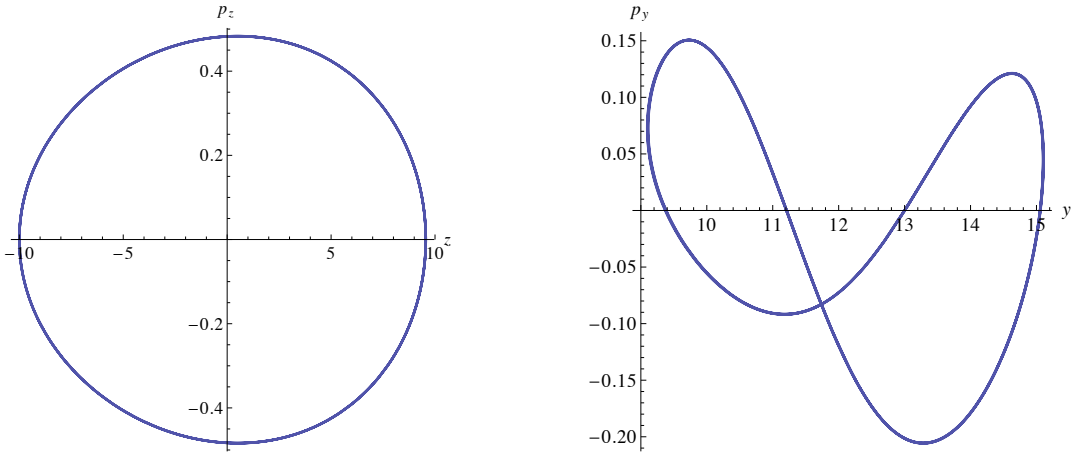

Fig. 5.6: Examples of closed phase space trajectories in the integrable probe regime. The plots show slices of phase space in the Cartesian coordinate system.

closed. One could also compute the Lyapunov coefficient of the system. In figures 5.6 and 5.7 we demonstrate the trajectories in phase space for the probe orbiting around both centers as we exit the probe limit.

As we increase the number of degrees of freedom, the analysis of chaotic systems becomes increasingly challenging. The canonical example of a double pendulum, which already displays a significant set of features generic to chaotic systems at large, can be effectively analyzed with the use of Poincaré sections. For a double pendulum, the phase space is four-dimensional with a single constant of motion – the total energy. Hence the system is not integrable.

5.6.1 Collinear dynamics

Away from the probe limit, as we already noted, our system has an 18-dimensional phase space and becomes a complicated three-body problem. In order to study the

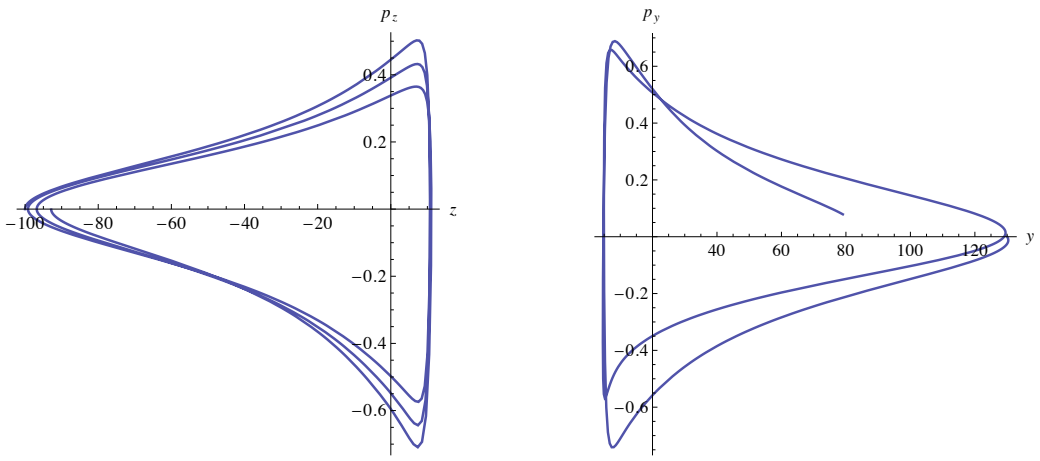

Fig. 5.7: Examples of open phase space trajectories in the chaotic regime. The plots show slices of phase space in the Cartesian coordinate system.

transition to chaos of our system, it is instructive to find a setup that allows us to use the same tools used to analyze the double pendulum. This can be achieved by restricting the particles to be collinear, i.e. placing them on a line and only considering deformations along this direction. Notice that a system consisting of particles on a line will stay on the line so long as the velocities of the particles are parallel to the line itself. This is because the magnetic force $\mathbf{v} \times \mathbf{B}$ will vanish in this situation. Hence, the collinear system is a consistent truncation of our original Lagrangian (5.2.2). This is no longer true for the coplanar case.

As was already discussed, we need at least three particles to find chaotic features. Three backreacting particles on a line have six degrees of freedom with a conserved energy, a situation closer to the triple pendulum. We can however take the mass of one of them to be much larger than the other two such that they behave as two probes in a fixed background. The probes are allowed to interact with each other since we

do not restrict the θ_i and κ_{ij} in any way, except $\sum_i \theta_i = 0$. The equations governing the two probes can be extracted from the two-probe Hamiltonian:

$$H_{col} = \frac{p_2^2}{2m_2} + \frac{p_3^2}{2m_3} + \frac{1}{2m_2}\left(\theta_2 + \frac{\kappa_{21}}{2x_{21}} + \frac{\kappa_{23}}{2x_{23}}\right)^2 + \frac{1}{2m_3}\left(\theta_3 + \frac{\kappa_{31}}{2x_{31}} + \frac{\kappa_{32}}{2x_{32}}\right)^2 . \tag{5.6.35}$$

The above Hamiltonian is a good approximation for the three-particle system in the limit where $m_1 \gg m_2, m_3$. In this limit one particle becomes non-dynamical and the energy is fully contained in the motion of the two light particles. Thus there is a conserved quantity associated to the motion of the light particles and we are left with a three-dimensional phase space, which is also the dimensionality of the double pendulum phase space.

The ground state (x_{21}^*, x_{31}^*) is found by setting $U_2 = U_3 = 0$. In addition to imposing the triangle inequality to fully specify the ground state, we must also declare the ordering of the three particles on the line. A given ground state is mapped to a family of ground states via the scaling relation $(x_{21}^*, x_{31}^*; \kappa_{ij}) \to \lambda(x_{21}^*, x_{31}^*; \kappa_{ij})$. Slightly increasing the energy leads to small oscillations about the equilibrium position (x_{21}^*, x_{31}^*). The linearized normal frequencies are the eigenvalues of the Ω^2 matrix:

$$\Omega_{jl}^2 = M_{jk}^{-1}\partial_k\partial_l H_{col} \ , \quad M_{ij}^{-1} \equiv \frac{1}{m_i}\delta_{ij} \ , \quad i,j,k = \{2,3\} \ . \tag{5.6.36}$$

The derivatives of H_{col} are evaluated at the equilibrium point. Though the general formulae for the normal frequencies are quite involved they are readily computed. As an example, the normal frequencies for $\kappa_{13} = \kappa_{12} = -\kappa_{23} = 1$, $\theta_1 = -\theta_2 = -1$, $\theta_3 = 0$, and $m_2 = m_3 = 1$ are:

$$\omega_\pm^2 = \frac{2}{81}\left(121 \pm 13\sqrt{73}\right) \approx \begin{cases} 5.73 \\ \\ 0.25 \end{cases} . \tag{5.6.37}$$

5.6.2 Poincaré Sections

When the system is integrable or quasi-integrable, i.e. for sufficiently low energies, the trajectories in the four-dimensional phase space will reside on two-dimensional tori, since the system is simply given by two linearly coupled oscillators. Since it is hard to visualize motion on the torus, we study instead particular snapshots of the system, known as Poincaré sections (see [113, 114] for a more complete discussion). For a given energy, we can record (over many different initial conditions) the coordinate and conjugate momentum of one particle every time the other particle has positive momentum and crosses a particular point. The resulting contours in phase space, collectively known as a Poincaré section, display the transition from quasi-integrable to chaotic behavior in our system.

For sufficiently low energies, the Poincaré sections are given by two fixed points surrounded by a set of concentric contours. The fixed points correspond to motion in one of the two normal modes. It is useful to define the winding number w, which is the ratio of the number periods one particle completes for every full period completed by the other. At the linearized level away from the fixed point, the winding number $w = \omega_1/\omega_2$. If w is *not* a rational number, the trajectory will never quite return to its original position and thus fills one of the concentric contours. As the energy is increased, the winding number is detuned and eventually may even become rational. Hence, parts of the phase space acquire new fixed points with their own concentric contours. These correspond to nonlinear resonances. The last tori to break are those with the 'most' irrational w (the golden mean $(\sqrt{5}-1)/2$ is the 'most' irrational number, as defined by the speed of convergence of its continued fraction expansion).

The breaking of the original two islands into an increasing number is qualitatively similar to the case of a double pendulum. Eventually, there is essentially no visible structure left in the Poincaré section and we are in a regime of global chaos.

We give an example of this in figure 5.8. Similar transitions to chaos are found for examples where the κ's form closed and non-closed loops. In several examples where the κ's form a closed loop and obey the triangle inequality, and the θ's have the *same* sign, the formation of islands around fixed points representing nonlinear resonances seems to be far less manifest in the Poincaré sections. In other words, global chaos seems to set in much more quickly. We hope to study these issues systematically in the future.

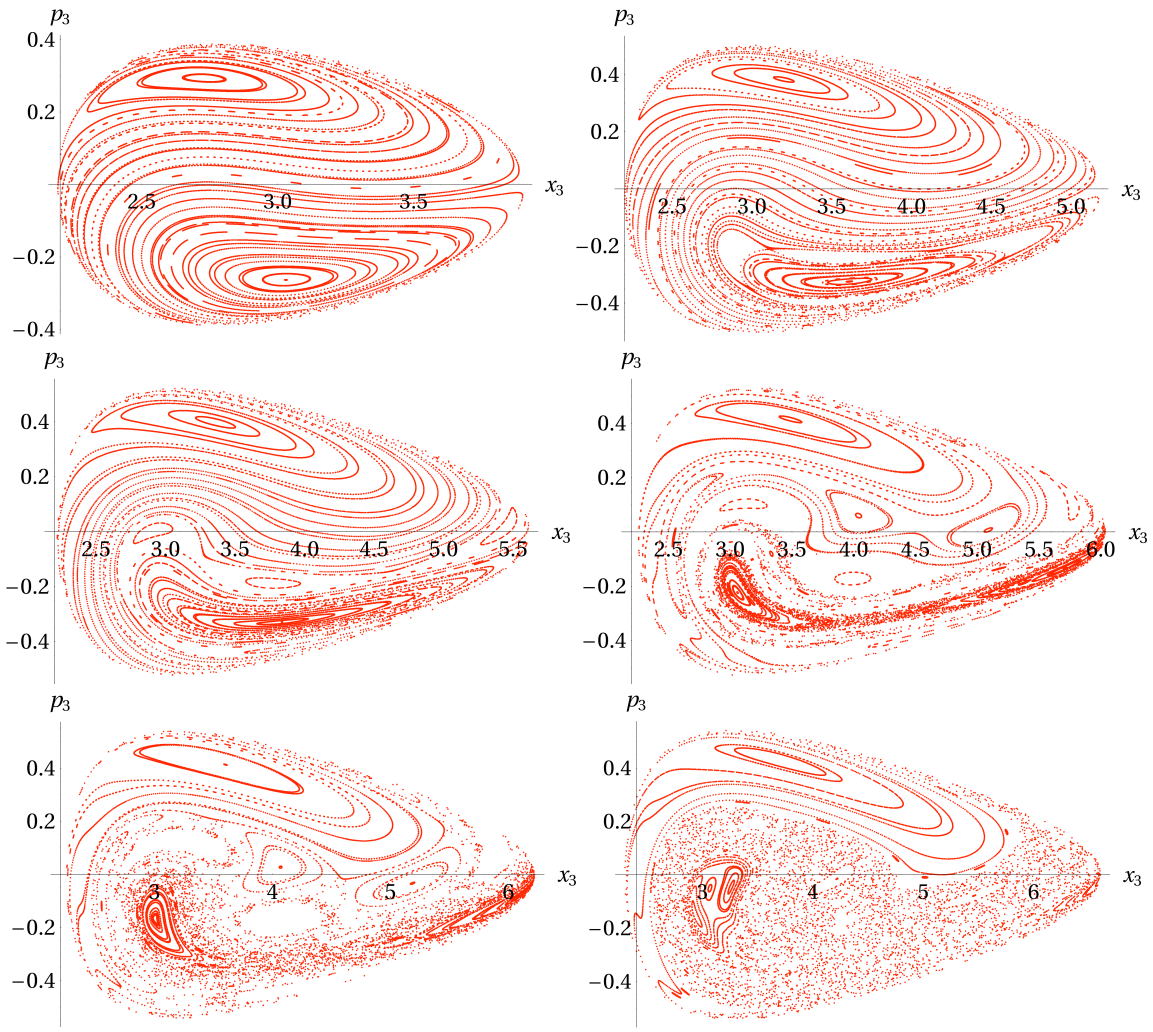

Fig. 5.8

Fig. 5.8 *(Continued)*: Poincaré sections of collinear setup with $\kappa_{31} = 10$, $\kappa_{32} = -10$, $\kappa_{21} = -10$ and $\theta_3 = -1$, $\theta_2 = 1$ and energies $E = \{0.10, 0.20, 0.23, 0.26, 0.27, 0.30\}$. Note that the κ's form a closed loop. The horizontal axis represents the position of particle 3 while the vertical axis represents its conjugate momentum. Any given plot is produced by varying the initial positions and momenta of the two probes subject to a fixed total energy. The pair $(x_3(t), p_3(t))$ is plotted every time the resulting trajectory of particle 2 crosses some fiducial point $(x_2(t) = x_c)$ with positive momentum $(p_2(t) > 0)$, i.e. roughly every time particle 2 completes a full cycle as it oscillates back and forth. In the quasi-integrable regime, different initial conditions correspond to different contours. The first Poincaré section shows a quasi-integrable behavior with two fixed points corresponding to the two low energy normal modes.

5.7 Trapping

In this section, we envision a trapping problem. The setup consists of a localized bound state and another particle, which we take to be a probe, beginning inside the molecule. The probe begins its life at a random position well within the molecule. We explore the dynamical evolution of the probe as we vary the initial energy.

5.7.1 Setup and Energetics

Our setup will consist of a probe with charge $\gamma_p = (1, 0)$ in the presence of a bulk molecule comprised of a number N_c of fixed electric centers of charge $\gamma_c = (0, \kappa)$. The positions of the electric centers will be obtained by drawing random points from a ball of radius R_{mol} using the algorithm in [136, 137]. The classical probe Hamiltonian in this background is given by:

$$H_{probe} = \frac{(\mathbf{p}_p - \mathbf{A}_p)^2}{2m_p} + \frac{1}{2m_p}\left(\sum_{i=1}^{N_c} \frac{\kappa_{pi}}{r_{pi}} + \theta_p\right)^2 . \tag{5.7.38}$$

Since all the background centers have the same charge, the $\kappa_{pi} \equiv \kappa$ are all equal. Also, to ensure that trapping occurs we require that κ and θ_p have opposite signs. The zero energy configurations are given by setting the second term in H_{probe} to zero. As usual, there is a classical moduli space $\mathcal{M}$ due to the fact that we have three probe coordinate degrees of freedom and we are solving only one equation. We could search for non-zero static minima of H_{probe}, but a simple computation of the gradient of the potential shows that there are only zero energy minima. The minimal energy required for the probe to reach infinity is $E_{min} = \theta_p^2/2m_p$.

For probe energies $E_{in} \geq \theta_p^2/2m_p$ the probe can easily escape the molecule. For

energies in the range $E_{in} < \theta_p^2/2m_p$, we observe trapping. Our goal is to begin quantifying the amount of classical trapping. We do this by studying the fractional volume $f_V(E_{in}, t)$ covered by the probe as a function of initial energy E_{in} and total trajectory time t. We estimate f_V by studying how many centers the probe trajectory approaches to within one-half of the average inter-particle distance $r_{i.p.} \sim R_{mol}/N_c^{1/3}$. We again stress that we keep the molecule and initial positions of our probe fixed through all the trials, only varying the initial velocity of the probe. We take $m_p = 1$, $\theta_p = -10$, $R_{mol} = 20$, $N_c = 100$ and $\kappa = 1$ for the presented data.

5.7.2 A trap

At low energies, we witness characteristic trapping: figure 5.9 shows one such example where a probe is confined to less than 20% of the molecule, exploring the same part of the molecule over and over again. We remind the reader that it is possible to be trapped in one region indefinitely and this behavior should not (necessarily) be looked at as a failure of not integrating for a long enough period of time. Indeed, as is seen in the Euler-Jacobi flower of figure 5.5.1, probes can remain in one part of a molecule for arbitrarily long periods of time. As we increase the energy, we see a transition that opens up more of phase space to the probe. Little pockets in the potential landscape form through which the probe particle can escape and begin exploring other regions of the molecule. Often this happens by sudden jumps, as illustrated in the middle row of figure 5.9. We have tracked the energies of the probe and the numerics are stable. The jump is not due to an erroneous kick in the integrator but rather appears to be due to small pockets through which the probe

can escape given enough time. Finally, at high energies (e.g. around one half of the escape energy), the probe uniformly explores the entire molecule, as illustrated in the last row of figure 5.9.

It is also interesting to study the Schrödinger equation for the probe in this background to see if the wavefunction exhibits trapping via some avatar of Anderson localization.[4]

[4]Thanks to Douglas Stanford for discussions on the quantum dynamics.

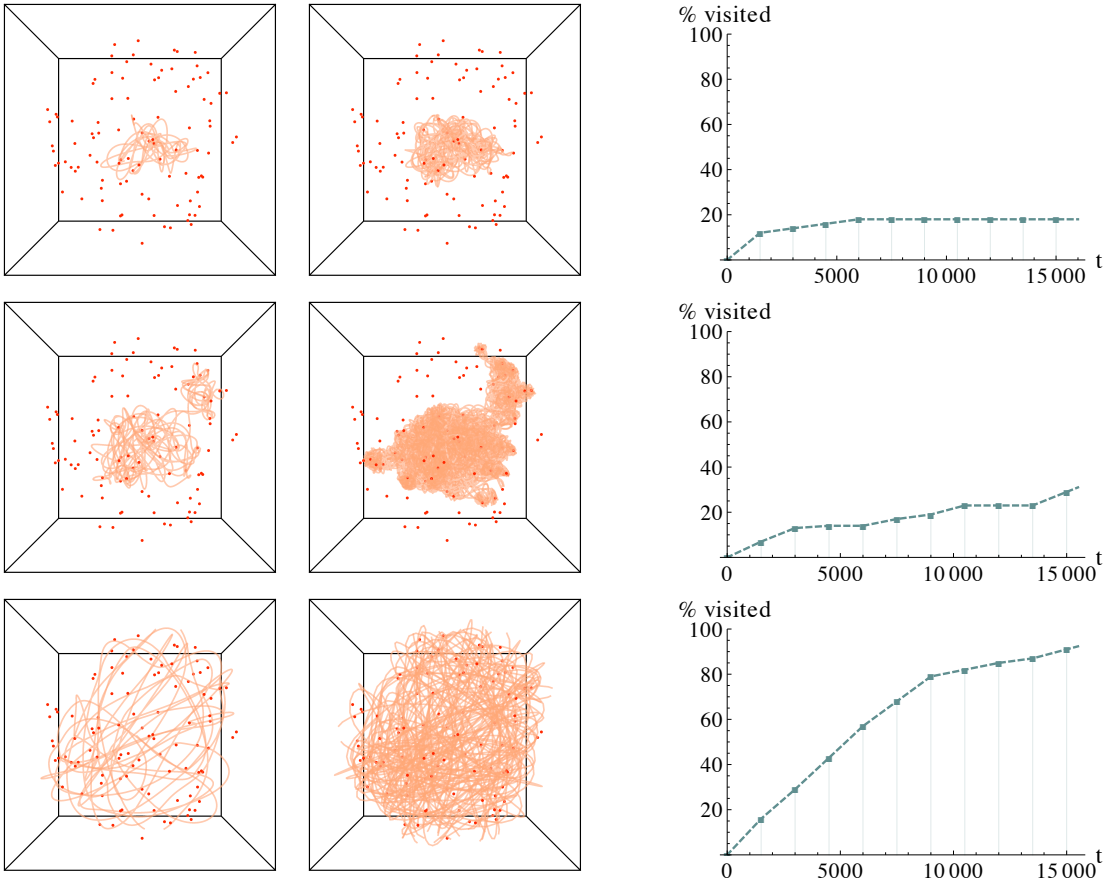

Fig. 5.9: The first row represents a low energy probe, which remains stuck in a subset of the phase space for seemingly arbitrarily long times. The second row represents an intermediate energy probe which illustrates the non-uniform escapes that occur from the low energy trapping behavior. We see that for a while it remains trapped in some subset of phase space, after which it escapes and gets stuck in some other subset of phase space. The final row represents a high energy probe which uniformly explores the molecule. The associated plots represent the percentage of the molecule explored as a function of the integration time, up to 15000 time steps in increments of 1500.

Fig. 5.9 *(Continued)*: The tapering off of the high energy probe is simply due to saturating the entire molecule. Below these points the increase is very uniform. The initial energy increases from 50% of the escape energy in the first row to 60% of the escape energy in the third row. These percentages, however, are very dependent on the parameters (e.g. κ, θ, etc.) in the problem.

5.7.3 Topology of the potential landscape

To illustrate the potential landscape and gain some intuition for the motion of trajectories, we set up a co-planar molecule. Again, all centers in the molecule have equal charge and their positions are chosen by uniformly selecting N_c points on a disk of size R_{mol} [138]. A probe in this background will not remain in the plane due to the magnetic fields which will push it out. However, for a molecule where every center attracts the probe, at low energies the deviations from the plane are small relative to the size of the molecule, which can be made arbitrarily large. Thus, plotting equipotential contours over this two-dimensional molecule gives an accurate picture of the potential landscape which can be used to understand the trajectories. See figure 5.10 for such a comparison. For a fixed molecule size, as the magnitude of κ is increased relative to the magnitude of θ, the topology of the equipotentials changes by expelling the low energy part of the landscape to the outside of the molecule, as can be seen in figure 5.10. This mimics the change in topology of the moduli space in going from Region V to Region IV in figures 5.2 and 5.3. Topology changes in the moduli space of the three center setup also occurs as κ is increased while keeping θ fixed as well as the distance between the background centers.

5.8 Holography of Chaotic Trajectories?

We end our journey by discussing how the picture we are developing may fit into the broader context of holography. The usual interpretation of a large black hole in an asymptotically anti-de Sitter space is that we have prepared the dual CFT in some

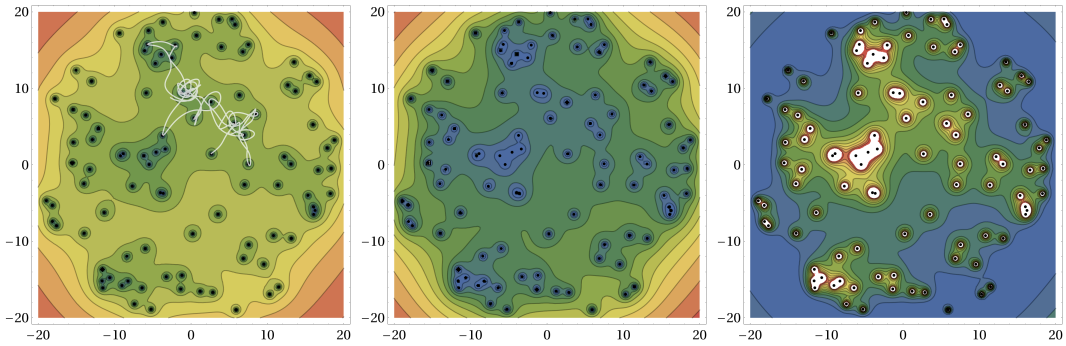

Fig. 5.10: These contour plots show equipotential surfaces in the plane of a 2D molecule consisting of one hundred centers. From left to right, we have chosen $\kappa = 1$, $\kappa = 1.5$, $\kappa = 3.5$, and in all cases $\theta = -10$. We observe that as the magnitude of κ increases, the minima (blue region), which initially lied near each center, are collectively expelled, forming an overall minimum that surrounds the molecule as a whole. For $\kappa = 1$, the trajectory remains close to the plane of the molecule and has been superimposed on the left contour plot (transparent white line). The axes label the x and y positions of the probe particle.

finite temperature state. On the other hand, the presence of a vast number of distinct entropically relevant multicentered black hole configurations inside an anti-de Sitter universe (see chapter 7) implies a vast number of minima in the free energy of the dual CFT (as a function of configuration space). In particular, the usual assumptions of the no-hair theorem fail since a set of macroscopic charges does not uniquely fix the bulk solutions. In fact, the solutions are characterized by a large collection of multipole moments. Furthermore, though most of them do not constitute true ground states, they can be very long lived, decaying mostly through thermal and quantum tunneling.

We can access information about the relaxation and response of the CFT by computing boundary-to-boundary correlators in the bulk. In the large frequency (or large mass) limit two-point functions have been associated to bulk geodesics which begin and end their life near the boundary of AdS [139, 140, 141, 142]. Such geodesics will become highly complex and chaotic in the bulk due to the presence of the non-trivial black molecule, as evidenced by our simpler setup. In fact, a geodesic may become trapped in some very long lived unstable orbit before escaping back to the boundary. Thus, the two-point function expressed as a path integral over bulk trajectories and the applicability of the saddle point approximation may be a somewhat involved issue. This picture suggests that the *linear response* properties of the dual CFT, to the extent that they are captured by the two-point function in the geodesic approximation, in the multicentered/glassy phase are rather different from those in a usual thermal state, where for example the motion of geodesics is integrable. The motion of a very massive probe or high energy graviton falling into the bulk corresponds to a point-like source cascading to lower energies (and covering larger size) in the CFT.

Eventually the excitation returns back to a point-like source at some other point on the two-sphere where the CFT resides. From the bulk point of view this is when the particle dropped into the molecule returns back out. The chaotic nature of the bulk physics suggests chaotic behavior of the boundary theory itself.

One may also consider the dynamical features at zero temperature for which asymptotically AdS_3 multicentered configurations are known [143]. The possible presence of *classical* chaotic behavior of the bulk AdS_3 should correspond to *quantum* dynamics in the dual CFT_2. One effect of particular interest in chaotic systems is known as *quantum scarring*, where it has been observed that the wavefunction of a chaotic system peaks on *closed* classical trajectories [144]. We hope to explore these issues further in future work.

Chapter 6

Hot Halos and Galactic Glasses (Carbonado)

6.1 Layout of the chapter

The main focus of this chapter consists of exploring the nature of finite temperature black hole bound states in $\mathcal{N} = 2$ supergravity in four dimensions. To be more or less self-contained we begin by reviewing in section 7.1 the relevant Lagrangians and notations (more background can be found in [145]). In section 6.3 we present a simple consistent truncation scheme valid for any $\mathcal{N} = 2$ string compactification, within which we derive and describe a family of exact non-extremal black hole solutions (previously found in [146]). These will serve as our galactic black hole cores, dressed by halos of much smaller probe black holes. The probe potentials are introduced in section 6.4 and the existence of nonextremal bound states is established. A systematic exploration of the parameter regime in which metastable and stable bound

states exist is given in section 6.5; the results are shown in fig. 6.3. We discuss the thermodynamic properties of the system and find a phase structure confirming several of the glass-like features outlined above. The diagram is suggestive of quantum critical points attained by dialing the asymptotic moduli to the black hole attractor fixed point. Across this point, the ratio of probe-induced spin to probe induced D6 magnetic dipole moment changes sign. In the appendix we estimate the configurational entropy of multi-probe BPS galaxies and find it grows linearly with the system's size (charge), and that it scales to zero with a nontrivial exponent near the critical points.

In interesting recent work [107, 147], analogous but complementary finite temperature bound states in five dimensions were independently explored, with qualitatively similar results (see appendix D of [107] for a detailed comparison).

6.2 Setup and notation

Four dimensional $\mathcal{N} = 2$ supergravity coupled to massless vector and hypermultiplets has a bosonic action of the general form [148, 149]

$$\begin{aligned} S_{4D} &= \frac{1}{8\pi}\int d^4x\,\sqrt{-g}\left(\tfrac{1}{2}R - G_{A\bar{B}}\,\partial_\mu z^A \partial^\mu \bar{z}^{\bar{B}} - h_{XY}\,\partial_\mu q^X \partial^\mu q^Y\right) \\ &\quad -\frac{1}{32\pi}\int d^4x\,\sqrt{-g}\left(\mathrm{Im}\,\mathcal{N}_{IJ}\,F^I_{\mu\nu}F^{J\mu\nu} - \mathrm{Re}\,\mathcal{N}_{IJ}\,F^I_{\mu\nu}\tilde{F}^{J\mu\nu}\right)\,, \end{aligned}$$

where the z^A $(A = 1, \ldots, n)$ are the vectormultiplet scalars, $F^I_{\mu\nu} = \partial_\mu A^I_\nu - \partial_\nu A^I_\mu$ $(I = 0, 1, \ldots, n)$ are the vector field strengths, $\tilde{F}_{\mu\nu} \equiv \frac{1}{2}\epsilon_{\mu\nu\rho\sigma}\tilde{F}^{\rho\sigma}$, and the q^X are the hypermultiplet scalars. We put $G_N = 1$. As $G_{A\bar{B}}$ and $\mathcal{N}_{IJ}$ only depend on the z^A, and h_{XY} depends only on the q^X, the hypermultiplets decouple from the vector multiplets and we will not need to consider them further. The vectors A^I are

sourced by electric charges Q_I and magnetic charges P^I.[1] The space of charge vectors $\Gamma = (P^I, Q_I)$ carries a canonical, duality invariant, symplectic product, which in the standard symplectic basis can be expressed as

$$\langle \Gamma, \tilde{\Gamma} \rangle = P^I \tilde{Q}_I - Q_I \tilde{P}^I \,. \tag{6.2.1}$$

The metric $G_{A\bar{B}}$ is special Kähler, *i.e.* it is derived from a prepotential $F(X)$:

$$G_{A\bar{B}} = \partial_{z^A} \bar{\partial}_{\bar{z}^{\bar{B}}} \mathcal{K} \,, \qquad \mathcal{K} = -\log i \langle \Omega, \overline{\Omega} \rangle \,, \qquad \Omega = (X^I, \partial_{X^I} F) \,, \qquad X^A = X^0 z^A \,. \tag{6.2.2}$$

The variable X^0 drops out of all observable quantities; we gauge fix $X^0 \equiv 1$. The prepotential $F(X)$ is a locally defined holomorphic function, homogeneous of degree 2 in the X^I. It also determines the electromagnetic couplings $\mathcal{N}_{IJ}$:

$$\mathcal{N}_{IJ} = \bar{F}_{IJ} + 2i \frac{(\mathrm{Im}\, F_{IK}) X^K (\mathrm{Im}\, F_{JL}) X^L}{X^M (\mathrm{Im}\, F_{MN}) X^N}, \qquad F_{IJ} = \partial_{X^I} \partial_{X^J} F \,. \tag{6.2.3}$$

In type IIA Calabi-Yau compactifications the coordinates $z^A = B^A + iJ^A$ are identified complexified Kähler moduli and, ignoring string worldsheet instanton corrections, the prepotential takes the form

$$F(X) = \frac{1}{6X^0} D_{ABC} X^A X^B X^C \tag{6.2.4}$$

where the D_{ABC} are triple 4-cycle intersection numbers. The charges (P_0, P_A, Q_0, Q_A) are identified with wrapped (D6,D4,D0,D2) charges. For a Calabi-Yau with a single Kähler modulus $z = z^1$ (*i.e.* $n = 1$), the cubic prepotential (6.2.4) becomes

$$F(X) = D \frac{(X^1)^3}{6X^0} \,. \tag{6.2.5}$$

[1] Magnetic charges have an upper index, but we will further on often use lower indices for both electric and magnetic charges, to make expressions involving powers of magnetic charges less clumsy.

The examples we consider in this paper will all be effectively reducible to this case. The special Kähler metric (6.2.2) is then just the Poincaré metric on the upper half plane:

$$G_{z\bar{z}} = \frac{3}{4\,(\mathrm{Im}\,z)^2}\,, \tag{6.2.6}$$

and the electromagnetic coupling matrix (6.2.3) becomes, with $z = x + iy$,

$$\mathcal{N} = D \begin{pmatrix} \frac{x^3}{3} + \frac{iyx^2}{2} + \frac{iy^3}{6} & -\frac{x^2}{2} - \frac{iyx}{2} \\ -\frac{x^2}{2} - \frac{iyx}{2} & x + \frac{iy}{2} \end{pmatrix} \tag{6.2.7}$$

$\mathcal{N} = 2$ supersymmetry implies that the mass of any state of charge Γ in a vacuum with asymptotic moduli z_0 is bounded below by the absolute value of the central charge $Z(\Gamma, z_0)$, defined by

$$Z(\Gamma, z) = -e^{\mathcal{K}/2}\,\langle \Gamma, \Omega \rangle\,. \tag{6.2.8}$$

States saturating this bound are supersymmetric and called BPS. In the $n = 1$ case (6.2.5), for a charge $\Gamma = (P_0, P_1, Q_0, Q_1)$, (6.2.8) becomes

$$Z(\Gamma, z) = \frac{\sqrt{3}}{2\sqrt{D(\mathrm{Im}\,z)^3}} \left(\tfrac{D}{6} P_0 z^3 - \tfrac{D}{2} P_1 z^2 + Q_1 z + Q_0\right)\,. \tag{6.2.9}$$

To write down the action of a point particle in a general background, it is convenient to introduce the dual magnetic field strengths

$$G_I = \mathrm{Im}\,\mathcal{N}_{IJ}\,\tilde{F}^J - \mathrm{Re}\,\mathcal{N}_{IJ}\,F^J\,. \tag{6.2.10}$$

The electromagnetic equation of motion $dG_I = 0$ implies the existence of dual magnetic gauge potentials B_I such that $G_{I\mu\nu} = \partial_\mu B_{I\nu} - \partial_\nu B_{I\mu}$. Collecting the electric and magnetic gauge field strengths and potentials into duality covariant vectors

$\mathbb{F} = (F^I, G_I)$ and $\mathbb{A} = (A^I, B_I)$, the action for a point particle of mass m and charge $\gamma = (p^I, q_I)$ is [104, 150]

$$S_\gamma = -\int m\, ds - \frac{1}{2}\int \langle \gamma, \mathbb{A}_\mu \rangle dx^\mu \,. \tag{6.2.11}$$

The mass depends on the scalars z. In particular when the particle is BPS, we have

$$m = |Z(\gamma, z)| \,. \tag{6.2.12}$$

6.3 Non-extremal black hole background

We will now construct a class of exact, spherically symmetric, nonextremal single centered black hole solutions for any prepotential of the form (6.2.4). These are essentially the solutions found in [146, 151]. In the nonsupersymmetric extremal limit they belong to the class studied in [152, 153, 154, 155].

6.3.1 Equations of motion

The black hole metric is of the general form

$$ds^2 = -e^{2U(\tau)}\, dt^2 + e^{-2U(\tau)} \left(\frac{c^4}{\sinh^4 c\tau} d\tau^2 + \frac{c^2}{\sinh^2 c\tau} d\Omega_2^2 \right), \tag{6.3.13}$$

where τ is an (inverse) radial coordinate with $\tau = 0$ corresponding to spatial infinity and $\tau = \infty$ to the horizon. The parameter c is a positive constant parametrizing the deviation from extremality.

The scalars depend on τ only, and the electromagnetic field is given by[2]

$$F^I = P_I\,\omega - (\mathrm{Im}\,\mathcal{N})^{IJ}(Q_J + \mathrm{Re}\,\mathcal{N}_{JK}P_K)\star\omega\,, \qquad \omega = \sin\theta\,d\theta\wedge d\phi\,, \qquad \star\omega = -e^{2U}dt\wedge d\tau \tag{6.3.14}$$

Note that this automatically satisfies the Bianchi identity $dF^I = 0$, because the $\mathcal{N}_{IJ}$ and U depend on τ. Moreover, for this particular form of F^I, we have $G_I = Q_I\omega + (\cdots)\star\omega$, hence the equations of motion $dG_I = 0$ are also automatically satisfied.

The scalar and metric equations of motion can be obtained from an effective particle action [156]

$$S_{\text{eff}} = \int_0^\infty d\tau\left(\dot{U}^2 + G_{A\bar{B}}\dot{z}^A\dot{\bar{z}}^{\bar{B}} - V_{\text{eff}}(U,z,\bar{z})\right)\,, \tag{6.3.15}$$

with effective potential

$$V_{\text{eff}} = -c^2 - e^{2U}\left(|Z|^2 + 4G^{A\bar{B}}\partial_A|Z|\,\bar{\partial}_{\bar{B}}|Z|\right)\,, \tag{6.3.16}$$

supplemented with the constraint that the total particle energy must vanish:

$$\dot{U}^2 + G_{A\bar{B}}\dot{z}^A\dot{\bar{z}}^{\bar{B}} + V_{\text{eff}} = 0\,. \tag{6.3.17}$$

6.3.2 Consistent truncations

Solving this system in general appears intractable, but special classes of solutions can nevertheless be found. First, the general problem with an arbitrary number n of vector multiplets can be consistently reduced to an effective single vector multiplet problem by the truncation [105], for any choice of constant K^A (inside the Kähler

[2]In form notation, $F = \frac{1}{2}F_{\mu\nu}dx^\mu\wedge dx^\nu$, $A = A_\mu dx^\mu$.

cone):

$$z^A = K^A \hat{z}^1 \,, \qquad (F^0, F^A, G_0, G_A) = \left(\hat{F}^0, K^A \hat{F}^1, K^3 \hat{G}_0, (K^2)_A \hat{G}_1\right) \,, \tag{6.3.18}$$

where $(K^2)_A \equiv D_{ABC} K^B K^C$ and $K^3 \equiv D_{ABC} K^A K^B K^C$. It is easily checked that the equations of motion then consistently reduce to the $n = 1$ case (6.2.5), with $D = K^3$. To remain consistent we must also choose the black hole charge to be of the form

$$\Gamma = \left(\hat{P}^0, K^A \hat{P}^1, K^3 \hat{Q}_0, (K^2)_A \hat{Q}_1\right) \,, \tag{6.3.19}$$

which sources the reduced fields as a charge $(\hat{P}^I, \hat{Q}_I)$ in the effective $n = 1$ theory. We will henceforth normalize K^A such that $D = K^3 = 1$, and drop the hats on the reduced quantities.

The effective metric on the scalar space parametrized by $z^1 \equiv z \equiv x + iy$ is given by (6.2.6) and the effective potential is $V_{\text{eff}}(U, x, y) = -c^2 - e^{2U} V(x, y)$ with

$$V = \frac{3}{y^3}\left(Q_0 + Q_1 x - \tfrac{1}{2} P_1 x^2 + \tfrac{1}{6} P_0 x^3\right)^2 + \frac{1}{y}\left(Q_1 - P_1 x + \tfrac{1}{2} P_0 x^2\right)^2 + \frac{y}{4}\left(P_1 - P_0 x\right)^2 + \frac{y^3}{12} P_0^2 \tag{6.3.20}$$

The resulting equations of motion are still hard to solve in the generic case, but when $x = 0$, the coupling matrix (6.2.7) becomes pure imaginary and diagonal, and the system simplifies considerably. This motivates a search for solutions with constant $x(\tau) = 0$. In this case the fields strengths (6.3.14) are of the simple form

$$\begin{aligned} F^0 &= P_0\, \omega - Q_0 \tfrac{6}{y^3} \star \omega \,, & F^1 &= P_1\, \omega - Q_1 \tfrac{2}{y} \star \omega \,, \\ G_0 &= Q_0\, \omega + P_0 \tfrac{y^3}{6} \star \omega \,, & G_1 &= Q_1\, \omega + P_1 \tfrac{y}{2} \star \omega \,. \end{aligned} \tag{6.3.21}$$

Consistency of the ansatz $x(\tau) = 0$ requires $\partial_x V|_{x=0} = 0$, which leads to the conditions $Q_0 Q_1 = Q_1 P_1 = P_0 P_1 = 0$, leaving the possibility to have D4-D0 ($\Gamma = (0, P_1, Q_0, 0)$), D6-D2 ($\Gamma = (P_0, 0, 0, Q_1)$), or D6-D0 ($\Gamma = (P_0, 0, Q_0, 0)$) background charges. In the following we specialize to these cases.

6.3.3 Solving the equations of motion

Putting $y = e^{\phi}$, the remaining equations of motion for U and ϕ derived from (6.3.15) take the form

$$\ddot{U} = e^{2U}\left(v_1 e^{a\phi} + v_2 e^{b\phi}\right), \tag{6.3.22}$$

$$\ddot{\phi} = \tfrac{2}{3} e^{2U}\left(a v_1 e^{a\phi} + b v_2 e^{b\phi}\right), \tag{6.3.23}$$

together with the constraint (6.3.17) (which just fixes the value of c). For the D4-D0 system, we have $(v_1, v_2; a, b) = \left(3Q_0^2, \frac{P_1^2}{4}; -3, 1\right)$, for D6-D2 $(v_1, v_2; a, b) = \left(Q_1^2, \frac{P_0^2}{12}; -1, 3\right)$ and for D6-D0 $(v_1, v_2; a, b) = \left(3Q_0^2, \frac{P_0^2}{12}; -3, 3\right)$. This system is of Toda form [157]. Following the method of [151], we set $\alpha \equiv 2U + a\phi$, $\beta \equiv 2U + b\phi$. The system of equations of motion for U and ϕ then becomes

$$\begin{aligned} \ddot{\alpha} &= \alpha_0\, e^{\alpha} + \gamma_0\, e^{\beta}, \\ \ddot{\beta} &= \delta_0\, e^{\alpha} + \beta_0\, e^{\beta}. \end{aligned}$$

where $\alpha_0 = \frac{2}{3}(3 + a^2)\, v_1$, $\beta_0 = \frac{2}{3}(3 + b^2)\, v_2$, $\gamma_0 = \frac{2}{3}(3 + ab)\, v_2$, and $\delta_0 = \frac{2}{3}(3 + ab)\, v_2$. These two equations decouple if $ab = -3$, which happens to be the case for the D4-D0 and D6-D2 systems. In these cases the equations of motion integrate to

$$\begin{aligned} \alpha(\tau) &= \log\left(\frac{2c_1^2}{\alpha_0 \sinh^2(c_1\tau + c_2)}\right), \\ \beta(\tau) &= \log\left(\frac{2c_3^2}{\beta_0 \sinh^2(c_3\tau + c_4)}\right), \end{aligned} \tag{6.3.24}$$

where c_1, c_2, c_3, c_4 are positive integration constants and $(\alpha_0, \beta_0) = \left(24Q_0^2, \frac{2P_1^2}{3}\right)$ for the D4-D0 while $(\alpha_0, \beta_0) = \left(\frac{8Q_1^2}{3}, \frac{2P_0^2}{3}\right)$ for the D6-D2.

Specializing to the D4-D0 case, this implies for the original fields

$$e^{-4U} = \frac{2|Q_0 P_1^3|}{3c_1 c_3^3} \sinh(c_1\tau + c_2) \sinh^3(c_3\tau + c_4), \tag{6.3.25}$$

$$y^2 = e^{2\phi} = \frac{6|Q_0|}{|P_1|} \frac{c_3}{c_1} \frac{\sinh(c_1\tau + c_2)}{\sinh(c_3\tau + c_4)}. \tag{6.3.26}$$

The constraint (6.3.17) fixes $c^2 = (c_1^2 + 3c_3^2)/4$. Regularity of ϕ at the horizon $\tau = \infty$ requires $c_1 = c_3$. The asymptotic boundary conditions $U(\tau = 0) = 0$, $y(\tau = 0) = y_0$ further imply

$$\sinh c_2 = \frac{c\, y_0^{3/2}}{2\sqrt{3}\,|Q_0|}\,, \qquad \sinh c_4 = \frac{\sqrt{3}\,c}{|P_1|\, y_0^{1/2}}\,. \tag{6.3.27}$$

6.3.4 The D4-D0 solution

Putting everything together, denoting[3]

$$H_0 \equiv \frac{|Q_0|}{c} \sinh(c\tau + c_2)\,, \qquad H_1 \equiv \frac{|P_1|}{c} \sinh(c\tau + c_4)\,, \tag{6.3.28}$$

we get for the metric warp factor and the scalar

$$e^{-2U} = \sqrt{\frac{2}{3} H_0 H_1^3} \tag{6.3.29}$$

$$y = \sqrt{\frac{6H_0}{H_1}}\,, \tag{6.3.30}$$

and for the gauge potentials $\mathbb{A} = (A^I, B_I)$, obtained by integrating the field strengths (6.3.21):

$$\begin{aligned} A^0 &= \tfrac{1}{2Q_0}\left(\sqrt{c^2 + \tfrac{Q_0^2}{H_0^2}} - c\right) dt\,, & A^1 &= P_1(1 - \cos\theta)\, d\phi\,, \\ B_0 &= Q_0(1 - \cos\theta)\, d\phi\,, & B_1 &= -\tfrac{3}{2P_1}\left(\sqrt{c^2 + \tfrac{P_1^2}{H_1^2}} - c\right) dt\,. \end{aligned} \tag{6.3.31}$$

[3]This notation is motivated by the fact that in the $c \to 0$ extremal limit, H_0 and H_1 become the flat space D0 resp. D4 harmonic functions ubiquitous in the description of the well-known extremal solutions.

We have chosen a gauge here in which the electric potentials vanish at the horizon and the Dirac monopole potentials are regular on the northern sphere.

Notice that for $c = 0$ the modulus y at the horizon $\tau = \infty$ is fixed at an attractor point $y_\star$ independent of y_0:

$$y_\star = \sqrt{\frac{6|Q_0|}{|P_1|}}\,. \tag{6.3.32}$$

For $c > 0$, the horizon value of y becomes y_0-dependent, but for $y_0 = y_\star$, it still remains true that the scalars do not flow. In this sense it can still be viewed as some kind of attractor point even in the nonextremal case.

6.3.5 Mass, entropy, temperature and specific heat

The ADM mass of the black hole can be read off from the asymptotic behavior of the metric:

$$M = \frac{c}{4}\left(\coth c_2 + 3\coth c_4\right) \tag{6.3.33}$$

$$= \frac{1}{4}\sqrt{c^2 + \frac{12\,Q_0^2}{y_0^3}} + \frac{3}{4}\sqrt{c^2 + \frac{P_1^2\,y_0}{3}}\,. \tag{6.3.34}$$

In the extremal limit $c = 0$, this becomes $M = \frac{\sqrt{3}}{4}|P_1|y_0^{1/2} + \frac{\sqrt{3}}{2}\frac{|Q_0|}{y_0^{3/2}}$. When P_1 and Q_0 have the same sign, this equals the absolute value of the central charge and the extremal limit is supersymmetric. When P_1 and Q_0 have opposite sign the mass is strictly larger than the absolute value of the central charge and the extremal limit is nonsupersymmetric.

The Bekenstein-Hawking entropy can be read off from the near horizon ($\tau \to \infty$) behavior of the metric. Introducing $r \equiv e^{-c\tau}$, this is:

$$ds^2 \simeq -\frac{4\pi c^2}{S}r^2dt^2 + \frac{4S}{\pi}dr^2 + \frac{S}{\pi}\,d\Omega_2^2\,, \tag{6.3.35}$$

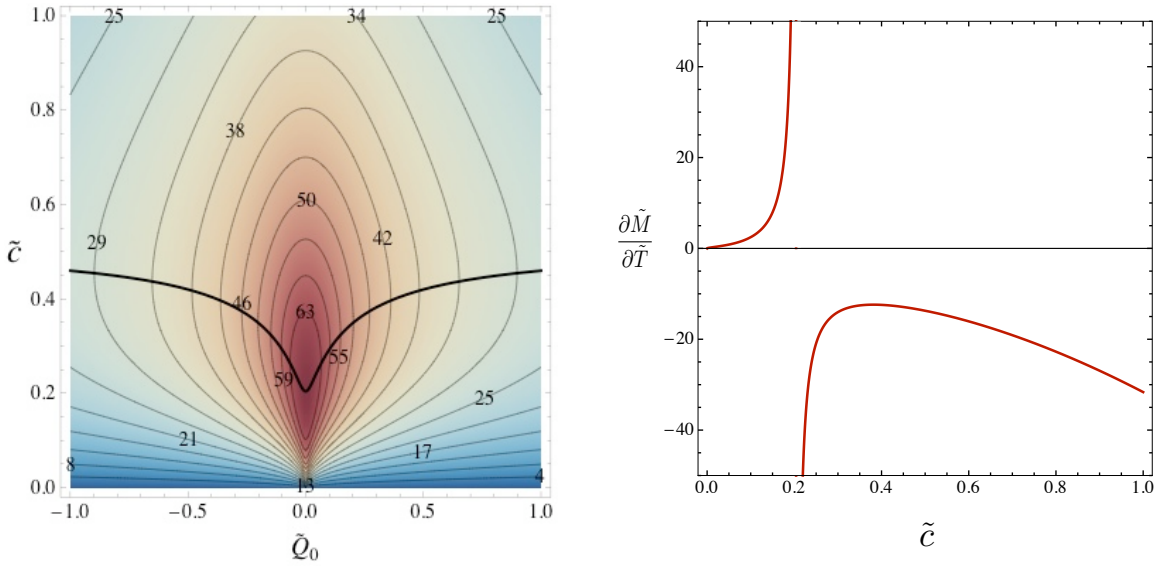

Fig. 6.1: **(a)**: Rescaled temperature $\tilde{T} \equiv \sqrt{y_0} P_1 \, T$ as a function of $\tilde{Q}_0$ and $\tilde{c}$, multiplied by 10^3. Red is warm, blue is cold. The temperature reaches its maximum at fixed $\tilde{Q}_0$ on the thick curve. **(b)**: Specific heat for $\tilde{Q}_0 = 0$, diverging at $c_{\rm crit} = 1/2\sqrt{6} \approx 0.2$, where the temperature reaches a maximum $\tilde{T}_{\rm max} = \sqrt{3}/8\pi \approx 69 \times 10^{-3}$.

where $S = A_{\rm hor}/4$ is the Bekenstein-Hawking entropy:

$$S = \pi \sqrt{\frac{2|Q_0 P_1^3|}{3}} \, e^{(c_2+3c_4)/2} \tag{6.3.36}$$

$$= \pi \left(c + \sqrt{c^2 + \frac{12\, Q_0^2}{y_0^3}} \right)^{1/2} \left(c + \sqrt{c^2 + \frac{P_1^2\, y_0}{3}} \right)^{3/2} . \tag{6.3.37}$$

The temperature can be read off from the near-horizon metric by Wick rotating the time coordinate and fixing its periodicity $\beta = 1/T$ by requiring regularity at the origin $r = 0$. This yields

$$T = \frac{c}{2S} \, . \tag{6.3.38}$$

Whereas the mass and entropy of the single centered D4-D0 black hole are monotonic function of c, this is not so for the temperature, as is clear from figure 6.1 (the

rescaled tilde variables will be defined in (6.3.39) and below): The temperature starts at zero in the extremal limit $c = 0$, acquires a maximal value at some intermediate c, and goes to zero again in the Schwarzchild black hole limit $c \to \infty$. The rescaled specific heat $\frac{\partial M}{\partial T}$ at fixed P_1, Q_0, y_0 diverges at this point [158] and changes sign from positive to negative.

6.3.6 Scaling symmetries

It turns out to be very useful to keep in mind the scaling symmetries $X \to \lambda_1^{n_1}\lambda_2^{n_2}X$, $\lambda_i \in \mathbb{R}^+$, acting on the various quantities defined so far with exponents

	P_1	Q_0	c	y_0	τ	H_0	H_1	M	S	T
n_1	1	1	1	0	-1	0	0	1	2	-1
n_2	1	3	$\frac{3}{2}$	1	$-\frac{3}{2}$	$\frac{3}{2}$	$-\frac{1}{2}$	$\frac{3}{2}$	3	$-\frac{3}{2}$

The first symmetry descends from a general symmetry of Einstein gravity coupled to vectors, the second from a general symmetry valid for cubic prepotentials [105]. The scalings of the derived quantities H_0, H_1, M, S and T follow from the scalings of the charges and of c, y_0 and τ. A consequence of these symmetries is that physical quantities will depend only on invariant combinations of the parameters, up to an overall factor determined by the scaling properties of the quantity under consideration. We choose our independent invariant parameters to be

$$\tilde{Q}_0 \equiv \frac{Q_0}{y_0^2 P_1} \qquad \tilde{c} \equiv \frac{c}{\sqrt{y_0}P_1}\,. \tag{6.3.39}$$

A quantity X with scaling exponents (n_1, n_2) will then have the functional dependence

$$X(P_1, y_0, Q_0, c) = P_1^{n_1} y_0^{n_2-n_1}\tilde{X}(\tilde{Q}_0, \tilde{c})\,, \qquad \tilde{X}(\tilde{Q}_0, \tilde{c}) = X(1, 1, \tilde{Q}_0, \tilde{c})\,. \tag{6.3.40}$$

For example the ADM mass (6.3.34) can be written as $M = P_1\sqrt{y_0}\tilde{M}$ with $\tilde{M} = \left(\frac{1}{4}\sqrt{\tilde{c}^2 + 12\,\tilde{Q}_0^2} + \frac{3}{4}\sqrt{\tilde{c}^2 + \frac{1}{3}}\right)$, the entropy as $S = P_1^2 y_0 \tilde{S}$ and the temperature as $T = \tilde{T}/P_1\sqrt{y_0}$.

6.4 Probe bound states

In this section we explicitly demonstrate the existence of bound states of probe particles in the nonextremal D4-D0 black hole backgrounds described in the previous section.

6.4.1 BPS probes

We will in this paper primarily consider probe particles of charge $\gamma = (p_0, p_1, q_0, q_1)$ that are themselves BPS. These "particles" could themselves be large black holes, but they must be much smaller than the background black hole so backreaction can be neglected. In thermal equilibrium the probe black hole will acquire the temperature of the background black hole, so it will not quite be BPS. However, the background temperature is parametrically suppressed as $T \sim 1/M$ in the limit of large background black hole mass M, as can be seen explicitly from the scaling table in section 7.2.5. Hence for any fixed probe size, the thermal contribution to the probe energy, which is proportional to T, will vanish in the large M limit, and thus the BPS approximation is justified.[4]

[4]More precisely, the probe thermal energy is of order $E_T \sim TS_p$, with S_p the probe entropy. Scaling up the background charges uniformly by a factor of λ_1 while keeping the probe fixed scales $E_T \propto T \propto 1/\lambda_1 \to 0$, whereas the probe potential remains invariant (as we will confirm below). Assuming this potential is not exactly flat, we can therefore neglect the thermal energy. Strictly speaking, this argument only tells us we can assume the probe to be extremal, but not necessarily

The static potential for a BPS particle can be obtained from (7.1.9) and the solutions found in the previous section. It consists of two parts, a gravitational part $V_{\rm g} = e^U |Z(\gamma, y)|$ and an electromagnetic part $V_{\rm em} = \frac{1}{2}\langle \gamma, \mathbb{A}_0 \rangle$. Explicitly $V_p = V_{\rm g} + V_{\rm em}$ with

$$V_{\rm g} = \frac{1}{4}\sqrt{\left(\frac{q_0}{H_0} + \frac{3\,p_1}{H_1}\right)^2 + \frac{6\,H_0}{H_1}\left(\frac{q_1}{H_0} - \frac{p_0}{H_1}\right)^2}\,. \tag{6.4.41}$$

and

$$V_{\rm em} = -\frac{1}{4}\frac{q_0}{Q_0}\left(\sqrt{c^2 + \frac{Q_0^2}{H_0^2}} - c\right) - \frac{3}{4}\frac{p_1}{P_1}\left(\sqrt{c^2 + \frac{P_1^2}{H_1^2}} - c\right)\,, \tag{6.4.42}$$

To avoid complications with marginal stability decays of the probe as it moves around in the nontrivial background, we will only consider probes that are themselves single centered black holes or particles. The BPS probe entropy is given by $S_p \equiv \pi\sqrt{\mathcal{D}}$, where the so-called discriminant $\mathcal{D}$ must be positive for a solution to exist; in the case at hand this is [159]:

$$\mathcal{D} = \frac{2}{3}\,p_1^3 q_0 - \,p_0^2 q_0^2 - 2\,p_0 p_1 q_0 q_1 + \frac{1}{3}\,p_1^2 q_1^2 - \frac{8}{9}\,p_0 q_1^3 \geq 0. \tag{6.4.43}$$

Finding an explicit parametrization of this subset of charges seems hard, but is actually made easy by using the invariance of $\mathcal{D}$ under shifts $(p_0, p_1, q_0, q_1) = \gamma \to \gamma_a = (p_0, p_1 + p_0 a, q_0 - q_1 a - p_1 \frac{a^2}{2} - p_0 \frac{a^3}{6}, q_1 + p_1 a + p_0 \frac{a^2}{2})$ with $a \in \mathbb{R}$. This invariance follows from the axionic shift symmetry $z \to z - a$ of the supergravity theory under consideration, which leaves in particular the black hole entropy invariant.[5]

BPS. However non-BPS extremal black holes are expected to be unstable to decay into lighter particles, as will be confirmed explicitly in section 6.5, and this on a time scale exponentially smaller than possible instabilities of the background black hole. This justifies considering primarily BPS probes.

[5]Explicitly: $\mathcal{D}(\gamma) = \min_z |Z(\gamma, z)|^2 = \min_z |Z(\gamma, z-a)|^2 = \min_z |Z(\gamma_a, z)|^2 = \mathcal{D}(\gamma_a)$.

Thus, in the parametrization

$$p_1/p_0 = k\,, \qquad q_1/p_0 = -b + \frac{k^2}{2}\,, \qquad q_0/p_0 = n + bk - \frac{k^3}{6}\,, \tag{6.4.44}$$

we get simply

$$\mathcal{D} = p_0^4\left(\tfrac{8}{9}b^3 - n^2\right), \tag{6.4.45}$$

and we may explicitly parametrize the solutions to the constraint (6.4.43) as $b = \left(\frac{9}{8}(n^2 + \frac{\mathcal{D}}{p_0^4})\right)^{1/3}$, $\mathcal{D} \geq 0$.

In type IIA compactifications, k may be thought of as the $U(1)$ flux on the wrapped D6, which carries no entropy, while b and n are the "entropic" contributions to the charges [105].

6.4.2 Scalings and validity of probe approximation

Besides the scaling symmetries described in section 7.2.5, we have an additional symmetry uniformly scaling only the probe charge γ, present because we work to linear order in γ. All in all we get the following scalings $X \to \lambda_1^{n_1}\lambda_2^{n_2}\lambda_3^{n_3}X$:

	P_1	Q_0	c	y_0	τ	p_0	p_1	q_1	q_0	k	b	n	m_p	S_p	V_p
n_1	1	1	1	0	-1	0	0	0	0	0	0	0	0	0	0
n_2	1	3	$\frac{3}{2}$	1	$-\frac{3}{2}$	0	1	2	3	1	2	3	$\frac{3}{2}$	3	$\frac{3}{2}$
n_3	0	0	0	0	0	1	1	1	1	0	0	0	1	2	1

The action on the background is the same as before, and we used the third scaling to set to zero the action of the λ_1-scaling symmetry on the probe charge. In addition to these continuous symmetries, there is a $\mathbb{Z}_2$ symmetry inverting the signs of all charges, and another $\mathbb{Z}_2$ inverting only the signs of D2 and D6-charges. We point out here that the probe potential does not scale with the size of the black hole.

Analogous to (6.3.39) and (6.3.40), we can scale out powers p_0 in addition to P_1, y_0 according to the following scaling dimensions:

$$X = P_1^{n_1} y_0^{n_2-n_1} p_0^{n_3} \tilde{X} \,. \tag{6.4.46}$$

So for example $k = y_0\tilde{k}$, $b = y_0^2\tilde{b}$, $n = y_0^3\tilde{n}$, and $S_p = y_0^3 p_0^2 \tilde{S}_p$ with $\tilde{S}_p = \pi\sqrt{\frac{8}{9}\tilde{b}^3 - \tilde{n}^2}$.

Some care has to be taken not to forget the regime of validity of the probe approximation. The ratio probe mass m_p over background black hole mass M has scaling weights $(-1, 0, 1)$, so $\frac{m_p}{M} = \frac{y_0 p_0}{P_1}\frac{\tilde{m}_p}{\tilde{M}}$. From this we see that for typical tilde variables of order 1 (and $p_0 \neq 0$), we must keep $y_0 p_0 \ll P_1$ to guarantee $m_p/M \ll 1$. Indeed, when $y_0 \sim P_1$, a single pure D6 becomes as massive as P_1 D4-branes, i.e. the background black hole, thus spoiling the probe approximation. In particular, since $y_0 \to \infty$ is the M-theory decoupling limit [143], this means that black hole bound states in $\mathrm{AdS}_3 \times S^2$ (of which the exact supersymmetric versions were constructed in [143]) are not reliably captured by the 4d probe analysis of this paper, in particular not for non-BPS configurations. On the other hand, for any fixed value of y_0 and the probe charges, we can always send $P_1 \to \infty$ to make the probe approximation arbitrarily accurate.

6.4.3 Bound states

The probe will form a stationary "molecular" bound state with the black hole whenever the potential has a nontrivial local minimum. In the supersymmetric case, the discovery of such probe bound states led the way to the construction of general nonlinear black hole bound state solutions in $\mathcal{N} = 2$ supergravity [104]. In particular their existence made it clear that such bound states had to exist, and quite

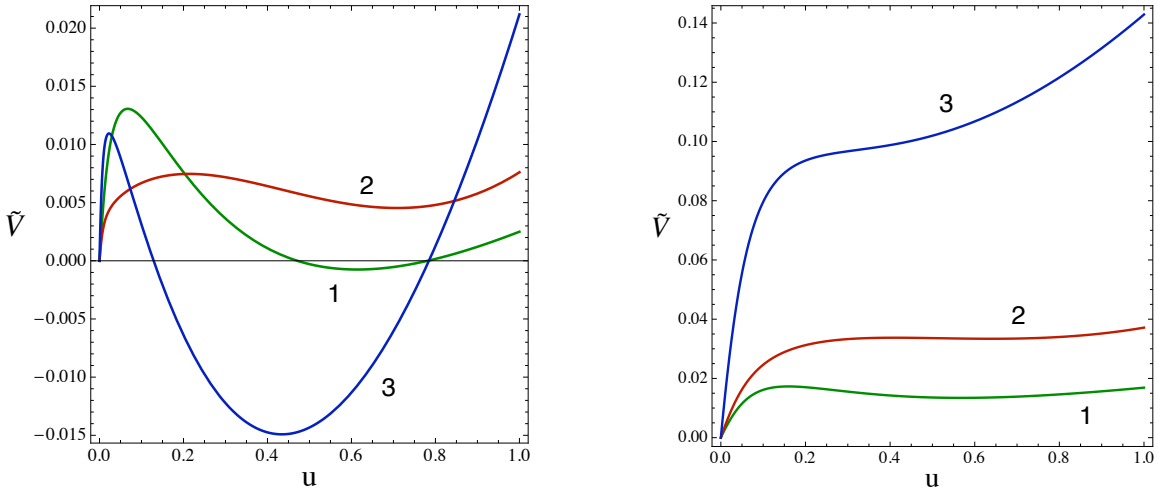

Fig. 6.2: Examples of probe potentials. Local minima give rise to bound states. The radial u coordinate is defined by $\frac{u}{1-u} = \frac{\tilde{c}}{\sinh(\tilde{c}\tilde{r})}$. The horizon is at $u = 0$ and spatial infinity at $u = 1$. In general, the potential always goes up from the horizon (for $c > 0$) and has at most one bump and at most one interior local minimum. On the left we show probe potentials at $(\tilde{Q}_0, \tilde{c}, \tilde{k}, 9\tilde{\mathcal{D}}, \tilde{n})$ equal to $(.01, .01, .5, 0, 0)$ for (1), $(.4, .01, .65, 0, 0)$ for (2) and $(-.4, .01, 2, .01, .15)$ for (3). On the right we show the same but at $\tilde{c} = .08$. At this higher temperature, the minima of (1) and (2) have become positive and more shallow, while (3) has lost its minimum altogether. Increasing $\tilde{c}$ even more wipes out all local minima.

remarkably, the simple explicit formula for the equilibrium radius obtained from the probe analysis is formally exactly the same as the corresponding formula obtained from supergravity. This was later explained as being a consequence of the constraints imposed by supersymmetry [103]. There is no reason to expect a similar exact match in the nonextremal case, but a probe analysis will still provide reliable information about the existence of bound states in suitable regimes.

To reproduce first the supersymmetric result, we consider the case of supersymmetric background, $c \to 0$, $P_1, Q_0 > 0$. The probe potential is then of the form $V_p = \sqrt{V_{\rm em}^2 + \Delta^2} + V_{\rm em}$. This makes the BPS bound $V_p \geq 0$ manifest. If a BPS-saturating supersymmetric minimum $V_p = 0$ exists, it is reached at the radius $r_{\rm eq} = 1/\tau_{\rm eq}$ for which $\Delta(\tau_{\rm eq}) = 0$ and $V_{\rm em}(\tau_{\rm eq}) < 0$. The first condition is $q_1 H_1(\tau_{\rm eq}) - p_0 H_0(\tau_{\rm eq}) = 0$, or explicitly, using $\lim_{c\to 0} H_0 = Q_0\tau + \frac{y_0^{3/2}}{2\sqrt{3}}$ and $\lim_{c\to 0} H_1 = P_1\tau + \frac{\sqrt{3}}{y_0^{1/2}}$:

$$r_{\rm eq,\,BPS} = \frac{p_0 Q_0 - q_1 P_1}{q_1\sqrt{\frac{3}{y_0}} - p_0\sqrt{\frac{y_0^3}{12}}}\,. \tag{6.4.47}$$

This reproduces the standard BPS equilibrium separation formula for two-centered bound states of this kind [104].

In the nonextremal case there is no such simple expression for $r_{\rm eq}$, but by continuity there will obviously still exist bound states for suitable values of the charges and the nonextremality parameter c. Some examples of probe potentials with local minima are shown in fig. 6.2. As suggested by the figure, increasing the nonextremality parameter c typically tends to push up the local minimum, until it eventually disappears altogether and the probe rolls into the black hole. This is to be expected, since going away from extremality means adding more mass. Thus the gravitational pull becomes increasingly more important, eventually overpowering all other forces.

In some cases however, in particular for small positive values of $\tilde{Q}_0$, going away from $c = 0$ initially *decreases* the value of the potential at the local minimum. An example is potential (1) in the figure (as opposed to (2)): At $c = 0$ this is a supersymmetric (*i.e.* $V = 0$) local minimum, whereas for small but nonzero $\tilde{c}$ it is negative. For larger $\tilde{c}$ is goes positive again. Thus, interestingly, slightly heating a supersymmetric black hole with small $\tilde{Q}_0$ will make it unstable to emission of such charges. We view this as an interesting interplay between supersymmetric and thermal physics. For non-BPS extremal black holes ($\tilde{Q}_0 < 0$), negative energy[6] probe bound states exist for sufficiently small $\tilde{c}$ for all values of $\tilde{Q}_0$. An example is potential (3) in the figure.

In the following section we discuss existence and stability in more detail.

6.5 Existence, stability and phases

6.5.1 Supersymmetric bound states

In the supersymmetric case $\tilde{Q}_0 > 0$, $\tilde{c} = 0$, using the parametrization (6.4.44), a straightforward analysis shows that a BPS bound state exists if and only if

$$\tilde{Q}_0 < \tilde{q}_1 < \frac{1}{6} \qquad \text{or} \qquad \frac{1}{6} < \tilde{q}_1 < \tilde{Q}_0 \,, \tag{6.5.48}$$

where $\tilde{q}_1 = \frac{\tilde{k}^2}{2} - b$, and

$$\text{sign } \tilde{k} = \text{sign } p_0 \,, \qquad \tilde{\mathcal{D}} = \frac{8}{9}\tilde{b}^3 - \tilde{n}^2 \geq 0 \,. \tag{6.5.49}$$

[6]Recall we defined the probe potential energy to be zero at the horizon. For a BPS background, this zero coincides with the BPS bound, so the energy must be nonnegative. For a non-BPS background, the total energy still satisfies the BPS bound, of course, but the conventional zero of our potential no longer coincides with it, thus allowing energies to become negative.

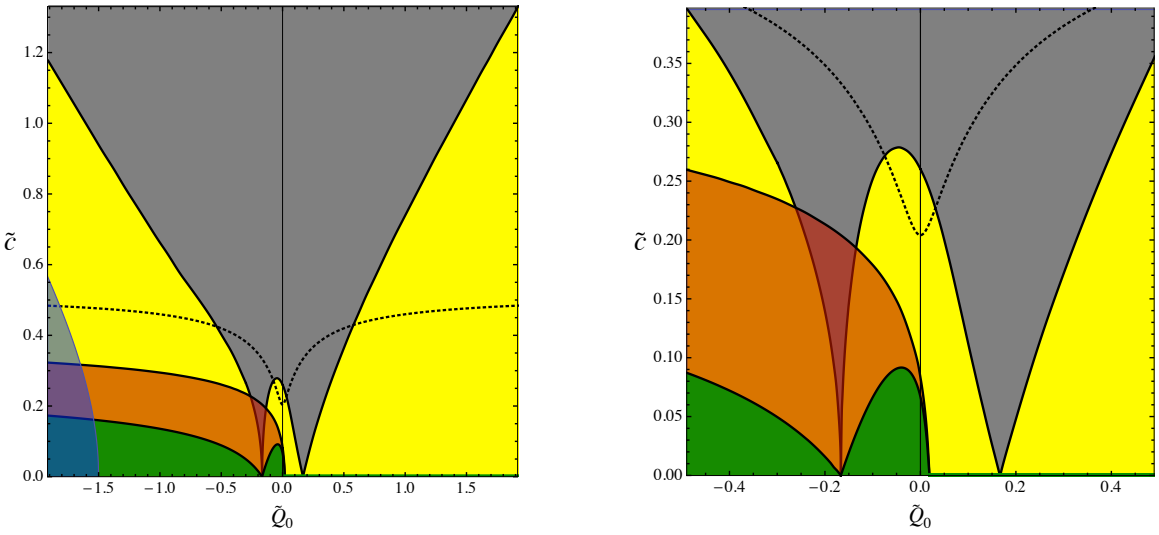

Fig. 6.3: Existence and stability regions of hot black molecules in the $(\tilde{Q}_0, \tilde{c})$-plane. The figure on the right zooms in on a smaller region but is otherwise the same as the figure on the left. No bound states exist in the grey region. In the yellow region bound states exists, but they are all positive energy (curve (2) in fig. 6.2). In the green region, negative energy bound states exist (curve (1) in fig. 6.2a). The orange overlay is the region where the black hole core itself is unstable for emission of particles to infinity. The blue overlay in the lower left corner is the region within the $\tilde{Q}_0 < -\frac{1}{6}$ range where pure fluxed D6 probe bound states exist (when $\tilde{Q}_0 > -\frac{1}{6}$ these always exist and moreover they always produce the lowest energy bound states). The dotted line is the maximal temperature line also shown in fig. 6.1. The grey regions touch the zero temperature axis at $\tilde{Q}_0 = \pm\frac{1}{6}$, or equivalently when y_0 coincides with the black hole fixed point $y_\star$.

The equilibrium distance (6.4.47) expressed in rescaled variables is $\tilde{r}_{\rm eq} = \frac{1}{\sqrt{3}}\frac{\tilde{Q}_0-\tilde{q}_1}{\tilde{q}_1-1/6}$. The boundary $\tilde{\mathcal{D}} = 0$ corresponds to vanishing probe entropy, the boundary $\tilde{q}_1 = \tilde{Q}_0$ to a vanishing bound state radius and hence absorption of the probe by the

background black hole, and finally the boundary $\tilde{q}_1 = \frac{1}{6}$ corresponds to an infinite bound state radius and hence to decay at marginal stability. This is brought in a more conventional form by returning to the non-scaled variables, which turns the existence condition (6.5.48) into $\frac{6Q_0}{P_1} < \frac{6q_1}{p_0} < y_0^2$ or $\frac{6Q_0}{P_1} > \frac{6q_1}{p_0} > y_0^2$. The absorption wall is then clearly seen to correspond to a vanishing probe-background symplectic product $\langle \gamma, \Gamma \rangle = 0$, while the marginal stability wall is at $y_0 = \sqrt{\frac{6q_1}{p_0}}$.

Notice there exist bound states for all values of $\tilde{Q}_0 \geq 0$ except 1/6. The number of possible bound states will not be constant however. In particular when $\tilde{Q}_0 \to 1/6$ (or equivalently $y_0 \to y_\star$, where $y_\star = \frac{6Q_0}{P_1}$ as in (6.3.32)), the allowed region in the probe charge space shrinks to zero. In appendix D.1 we compute the number of probe bound states, allowing multiple probes with different charges and taking into account the lowest Landau level degeneracies due to the magnetic interaction between the background black hole and the probe charges (but ignoring mutual magnetic interactions between the probes themselves). We do *not* count the internal microstates of the black holes. The logarithm of the number of configurations defined in this way is thus the analog of the notion of configurational entropy in the theory of glasses [160, 161, 162]. The final result for the number $\mathcal{N}(\epsilon)$ of such configurations with total probe mass over black hole mass less than ϵ is given by equation (D.1.18):

$$\log \mathcal{N}(\epsilon) \sim \epsilon^{5/6} \left| y_0^2 - y_\star^2 \right|^{1/3} \frac{P_1}{y_0^{1/6}} \,, \tag{6.5.50}$$

with $y_\star = \frac{6Q_0}{P_1}$. Thus we see that the number of allowed configurations indeed goes to zero when the critical point $y_0 = y_\star$ is approached, with a nontrivial scaling exponent 1/3.

It is interesting that even this restricted counting already gives an exponential

growth of the number of configurations $\mathcal{N}$ in the $P_1 \to \infty$ thermodynamic limit. This is typical for glasses [160, 161, 162]. The growth is not as fast as the black hole entropy itself (it is at most $P_1^{3/2}$, if we allow going to the boundary of the probe regime, cf. eq. (D.1.6)), but the exponentially large number of configurations should nevertheless have important consequences for the thermodynamics of this system.

6.5.2 Hot black molecules

For nonsupersymmetric black holes the analysis becomes more complicated, requiring some numerical assistance to scan the space of possible probe bound states for given $(\tilde{Q}_0, \tilde{c})$. The results of this work are summarized in fig. 6.3. We identify four different regions:

1. In the grey region filling the high temperature region, no molecular bound states of any kind exist, as gravity overpowers all other forces.

2. In the yellow regions right below it, bound states exist for some probe charges, but all of them have positive energy at their minimum, so they are metastable (recall we put the zero of the probe potential at the horizon). An example is potential (2) in fig. 6.2. When approaching the grey-yellow boundary, the minima become higher, are pushed to large radii and become very shallow, while the number of probe configurations goes to zero. This should give a scaling law analogous to (6.5.50) but we did not try to extract the scaling exponent. The grey region touches the $T = 0$ axis at the quantum critical points $\tilde{Q}_0 = \pm\frac{1}{6} \approx 0.1667$. For $\tilde{Q}_0 > -\frac{1}{6}$, we numerically observed with high accuracy that the probe particles forming the lowest energy bound states are always zero entropy $b = n = 0$, $k \neq 0$ particles. In IIA language these

are pure D6-branes with $U(1)$ flux, which uplift in M-theory to smooth "bubbling" geometries [163, 164, 165, 166, 167, 168, 169]. In particular the bound state surviving the longest when c is increased is of this type. For $\tilde{Q}_0 < -\frac{1}{6}$ this is no longer the case, and in fact there are no bound states of this type for $-\frac{3}{2} < \tilde{Q}_0 < -\frac{1}{6}$. The blue overlay shows where they reappear in the region $\tilde{Q}_0 < -\frac{3}{2}$.

3. In the green regions enclosed in the yellow, negative energy bound states exist. Such bound states are energetically stable against tunneling of the probe into the black hole or out to infinity. The green line along the positive $\tilde{Q}_0$ axis represents the BPS bound states discussed in section 6.5.1, which have zero energy. The negative $\tilde{Q}_0$ axis represents extremal nonsupersymmetric bound states. There is no BPS bound forbidding negative energy states, and by the rule that everything that is not forbidden is allowed, we find indeed that a large subset has deep negative energy minima. Interestingly, due to the transient dipping effect described at the end of 6.4.3, there is a small but finite region on the $\tilde{Q}_0 > 0$ (i.e. BPS) side at finite temperature where negative energy bound states exist. It extends to $\tilde{Q}_0 = \frac{1}{54} \approx 0.0185$ (see end of next paragraph).

4. The orange overlay is the region where the background black hole itself is unstable to emission of particles to spatial infinity. We take such emissions to be possible whenever there exists some probe charge such that the probe potential becomes negative at spatial infinity. Notice that the red region includes the green region. Hence whenever a bound state exists that is stable against tunneling of the probe out of its minimum, the background black hole will be unstable to emission of particles. We note, however, that whenever the probe potential exhibits a minimum, it is always

found to be lower than the value of the potential at infinity. The destabilizing probe type kicking in first (at the highest c) is again a pure fluxed D6 brane, $b = n = 0$, over the entire range of $\tilde{Q}_0$ we scanned. This allows computing the boundary of the red region analytically as the value of c for which the asymptotic value of V_p has a double zero viewed as a function of k:

$$c_{\text{BH stab}} = \frac{1}{4\sqrt{3}} \frac{3\Delta - 1}{\sqrt{(\Delta+1)(\Delta+5)}}\,, \qquad \Delta \equiv \sqrt{1 - 48\,\tilde{Q}_0}\,. \tag{6.5.51}$$

The critical line reaches zero at $\Delta = \frac{1}{3}$, i.e. $\tilde{Q}_0 = \frac{1}{54}$, which is numerically seen to coincide with the edge of the green region. It asymptotes for $\tilde{Q}_0 \to -\infty$ to $\frac{\sqrt{3}}{4} \approx 0.433$.

6.5.3 Bound states in a box

The black holes under consideration live in asymptotically flat space. Non-BPS black holes are unstable due to Hawking radiation and possibly other emission instabilities, and hot flat space is unstable due to nucleation of black holes [170, 171]. As a result, it is hard to make sense of this infinitely large system as a statistical mechanical model. To make it better defined, we can put the system in a finite box, either by imposing a cutoff by hand at some finite radius or by embedding the system in AdS_4 (as in chapter 7), along the lines of [172, 173, 174, 175], allowing the black hole to achieve thermal equilibrium with its environment in the box. In simple setups that do not give rise to black molecules, one sees that depending on the size of the box and the temperature, the final equilibrium state can either be a big black hole , or an ordinary thermal gas.[7] In the case at hand, we may expect much more complicated,

[7] In the context of AdS_4 this transition is nothing more than the Hawking-Page transition [173].

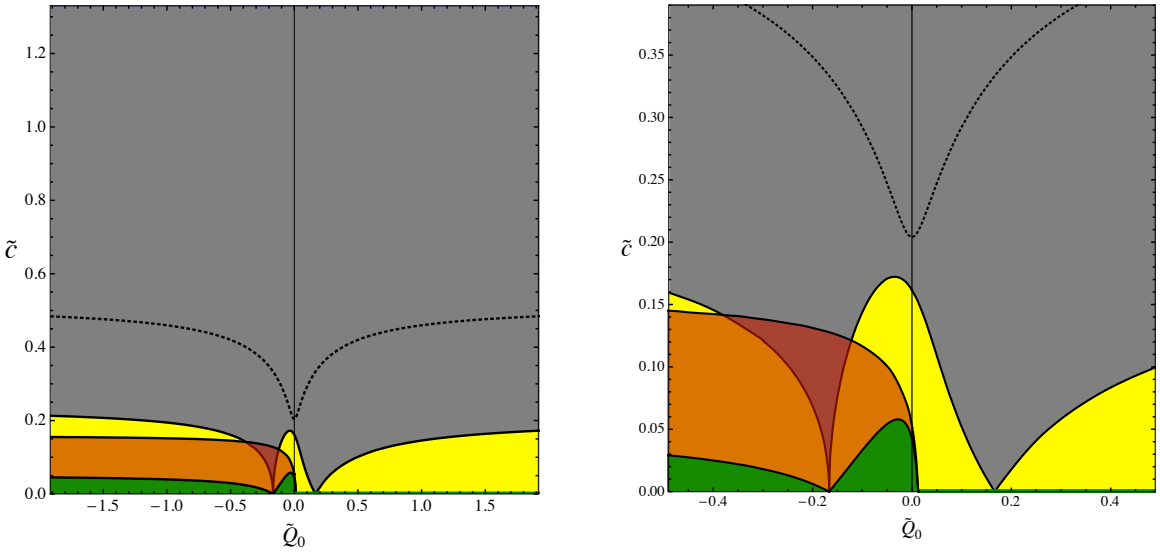

Fig. 6.4: Same as fig. 6.3, but for the system confined in a box, which can be viewed as a rough model for AdS. The box is implemented as a cutoff at radius $\frac{\tilde{c}}{\sinh(\tilde{c}\tilde{\tau})} = 1$, i.e. $u = 1/2$ (with u defined in fig. 6.2). Bound states with equilibrium positions at $u > 1/2$ are discarded, and decay is defined as emission to $u = 1/2$.

glass-like behavior at sufficiently low temperatures, due to the exponentially large number of complex stationary configurations that exist.

Implementing the constraint of putting the system in a box by hand is not too hard. For example we could cut off space at some fixed radial coordinate distance, say $\tilde{r} \equiv \frac{\tilde{c}}{\sinh(\tilde{c}\tilde{r})} = 1$ (that is $r = \sqrt{y_0}P_1$ in unrescaled variables), and hold the system at a fixed temperature, fixed y_0, and fixed total charge. We can then repeat the existence and stability analysis done for the asymptotically flat case. This is shown in fig. 6.4, the boxed analog of fig. 6.3 (not plotting the blue region). All the qualitative features remain intact, except that the phase boundaries are pushed down significantly. In fact, they are pushed down below the dotted line indicating the maximal temperature $\tilde{T}$ as a function of $\tilde{c}$ at fixed $\tilde{Q}_0$. Thus, all bound states occur in the region of positive specific heat, and we can say that at sufficiently high temperature, there is only the black hole solution, and it is stable. For the infinite system we could only make the analogous statement for sufficiently high nonextremality parameter (mass) of the black hole. If we imagine the existence of some holographic dual field theory description of the system under consideration, with the black hole representing the unique disordered high temperature thermodynamic equilibrium state and the multiple bound state configurations as the (meta)stable thermodynamic states characteristic for glassy systems below their critical temperature, then a positive specific heat throughout the parameter regime of interest is certainly an expected feature.

6.5.4 Thermodynamics and phase structure

Figures 6.3 and 6.4 are certainly suggestive of an interesting phase structure, with the attractor points of the extremal black holes at $(\tilde{Q}_0, \tilde{c}) = (\pm\frac{1}{6}, 0)$ corresponding to quantum critical points, the grey regions corresponding to the "normal" disordered high temperature phase and the colored regions to glass-like phases.

However, to say anything definitive about phase structure of this system, a more careful study of the thermodynamic weight of various configurations is needed, as well as an analysis of candidate order parameters and how they scale near phase boundaries and near the critical points. We will leave a full analysis to future work and restrict ourselves here to some simple observations.

At fixed temperature, a thermodynamic system will try to minimize its free energy $F = E - TS$. The free energy satisfies the first law

$$\delta F = -S\delta T + \delta W\,, \tag{6.5.52}$$

where δW denotes the work delivered to the system in some infinitesimal process during which the temperature changes by an infinitesimal amount δT. In particular this means that if we move a probe particle from some position $r = R$ into the black hole, while keeping the temperature fixed, the total change in free energy of the system $\delta F = \delta F_{\rm BH} + \delta F_{\rm p}$ must be equal to $\delta W = V_{\rm p}(\text{horizon}) - V_{\rm p}(\text{R})$, with $V_{\rm p} = V_{\rm g} + V_{\rm em}$ the probe potential defined in (7.4.55).[8] Since $V_{\rm p}(\text{horizon}) = 0$, this

[8]Recall we are treating the probe as a structureless object without internal thermal energy. See footnote 4 for the argument of why this is justified in the probe limit even if the probe itself is a black hole. The argument extends to thermal kinetic energy of the probe moving around in its potential well (provided this lies at finite rescaled radius), which we thus ignore as well.

means

$$F(\text{probe at R}) - F(\text{probe in BH}) = V_{\text{p}}(r = R)\,, \tag{6.5.53}$$

and thus at fixed temperature the configuration with the probe outside of the black hole will be thermodynamically favored over the one with the probe inside simply whenever $V_{\text{p}}(R)$ is negative.

As a check, we note that for $R = \infty$, this is the statement that $\delta F_{\text{BH}} + \delta F_{\text{p}} = -V_{\text{g}}(\infty) - V_{\text{em}}(\infty)$. Since $\delta F_{\text{p}} = -m_{\text{p}} = -V_{\text{g}}(\infty)$ (as the probe is first at infinity and then gone, and we are allowed to ignore as before thermal contributions to the probe free energy), this is equivalent to $\delta F_{\text{BH}} = -V_{\text{em}}$, which can be directly checked from the expressions in 6.3.5, without using the first law, taking care to vary c at the same time as the charges to keep T fixed.

To conclude, figures 6.3 and 6.4 give information about the thermodynamic preferences of the system for perturbations around the single black hole state. For example when in the green region, the black hole will start to populate black hole halos of many different charge types. We should keep in mind however that as soon as the number of such probes becomes macroscopic, or when they coalesce into black holes of size comparable to the background black hole, our neglect of the thermal internal, kinetic and inter-probe interaction energies is no longer justified. Hence we cannot read off the endpoint of this evolution from the diagrams. Nevertheless, the existence of exponentially many bound states with free energy below the black hole free energy strongly suggests glass-like behavior. This is not entirely obvious though, since the plots also show that the black hole core of any negative energy bound state is always unstable to emission of particles to infinity or to the boundary of the confining box,

so for a sufficiently large box, it is conceivable that the final equilibrium state may still be a simple dilute charged gas. We will revisit such questions in future work.

Finally, let us comment on the tentative interpretation of the points $\tilde{Q}_0 = \pm\frac{1}{6}$ at $T = 0$ as quantum critical points. As we mentioned several times already, they correspond to the case in which the scalars at infinity are at the extremal attractor point, $y_0 = y_\star = \sqrt{\frac{6|Q_0|}{|P_1|}}$. In this case, the background scalars do not flow but rather are constant over all of space, and no molecular bound state configurations exist – everything has been sucked into the black hole or pushed away to infinity. (It is known that this remains true away from the probe limit, at least in the BPS case: non-marginal bound states cannot exist at the attractor point of the total charge.) At zero temperature, the geometry is that of an extremal Reissner-Nordström black hole, developing in particular an $\mathrm{AdS}_2 \times S^2$ throat, suggestive of a holographic conformal fixed point.

Taking y_0 away from the attractor point but still keeping $T = 0$, the AdS_2 is preserved but the scalars will now flow from y_0 at infinity to $y_\star$ at the horizon. Putting the system in a box of finite radius R and decreasing R while keeping y_0 fixed will have roughly the same effect as moving y_0 along the attractor flow towards the fixed point $y_\star$; in particular near $\tilde{Q}_0 = \frac{1}{6}$, the configurational entropy will decrease by some power of R dictated by (6.5.50). In a hypothetical field theory dual, regardless of the large r asymptotics of spacetime [43], decreasing R would correspond to flowing to the IR, so this would correspond to a power law decrease of the configurational entropy when coarse graining over increasing length scales.

If $|\tilde{Q}_0| = \frac{1}{6}$ is to be a quantum critical point associated to a quantum phase

transition, then we should see different physical properties on the two sides of it. Near the supersymmetric critical point, one such property can be inferred by inspecting (6.5.48). Recall that pulling a probe out of the background black hole produces a D6 magnetic dipole moment pointing along the radial direction, equal to $\mu = p_0 r_{\rm eq} = p_0\sqrt{y_0}P_1\frac{1}{\sqrt{3}}\frac{\tilde{Q}_0-\tilde{q}_1}{\tilde{q}_1-\frac{1}{6}}$, as well as an angular momentum $J = \frac{1}{2}\langle\gamma,\Gamma\rangle = \frac{1}{2}P_1 y_0^2 p_0(\tilde{Q}_0-\tilde{q}_1)$. Hence

$$\vec{J} = g\vec{\mu}\,, \qquad g \equiv \tfrac{\sqrt{3}}{2}y_0^{3/2}\left(\tilde{q}_1-\tfrac{1}{6}\right)\,. \tag{6.5.54}$$

From (6.5.48) we see that the range of possible values of $|g|$ runs from 0 to a maximal value proportional to $|\tilde{Q}_0-\frac{1}{6}|$, and that it changes sign across the phase boundaries. The coefficient g is a physical observable, and could be used as an order parameter to distinguish the two putative phases.

Chapter 7

Hot Halos in AdS

7.1 The Model

7.1.1 Qualitative features and motivation

The bulk gravity theory we considered in the previous chapter consists of four-dimensional Einstein gravity coupled to two $U(1)$ gauge fields and a non-minimally coupled scalar. In this chapter, we add a scalar potential with an AdS_4 vacuum solution, with tunable parameters controlling the scalar vev and the AdS curvature scale. This allows us to embed our previous solutions in AdS_4. The specific Lagrangian we start from is given below in (7.1.1) and the part we will actually use in this chapter is given in (7.1.5). It can be viewed as a bosonic truncation of the simplest possible $\mathcal{N} = 2$ gauged supergravity theory, sometimes called Fayet-Iliopoulos (FI) gauged supergravity [176, 177, 178] (for a concise review with black holes in mind see [179]).

In the flat space limit (vanishing scalar potential), the model reduces to the one

considered in chapter 6, which was obtained there as a universal consistent truncation of any Calabi-Yau compactification of type IIA string theory. One motivation for our choice of model is that this flat space limit is known to have stationary BPS black hole bound states of arbitrary complexity [104, 105, 180, 181, 182], which persist at finite temperatures (as in the previous chapter and [107]). Hence by continuity we are guaranteed that black hole bound states will also exist in the present model, at least in the limit in which the size of the black holes is much smaller than the AdS radius. Another motivation is that the asymptotically flat background black hole solutions used in chapter 6 have explicit asymptotically AdS counterparts [179, 183]. This allows us to copy the probe strategy followed in chapter 6, making manifest the specific new features induced by the lift to AdS_4. The final motivation is the plausibility that this model has a suitable (stable) embedding in string theory, possibly with a holographic dual description as a three-dimensional conformal field theory.

The string theory embedding will have at least one important imprint on the low energy physics which is not determined by the 4d bulk Lagrangian (7.1.1) itself, namely the spectrum of charged particles. To stay as close as possible to chapter 6, we will assume the charged particles in the model are all much heavier than the AdS curvature scale.[1] This allows treating them as well-localized probes. As detailed in section 7.1.3 below, we will infer their mass by thinking of them as black holes much smaller than any of the length scales of the background.

[1] We should note that if we literally considered $\mathcal{N} = 2$ FI-gauged supergravity and not just its bosonic sector, this assumption would be violated, as the gravitino is charged, and has a mass of order the AdS scale in vacua with unbroken supersymmetry. Moreover the simplest stringy extensions of the model typically have plenty of light charged matter, including bosonic species, leading to superconducting charged condensates [184, 185, 186] which would qualitatively alter the setup. We will return to this in section 7.6.3

7.1.2 Bulk action

Our notation is chosen to parallel that of chapter 6, the asymptotically flat limit of the model.[2] The light field content consists of the metric $g_{\mu\nu}$, a complex scalar $z \equiv x+iy$ and two $U(1)$ gauge fields A^I_μ, $I = 0, 1$, with field strengths $F^I_{\mu\nu} \equiv \partial_\mu A^I_\nu - \partial_\nu A^I_\mu$. The four-dimensional bulk action is taken to be the bosonic sector of Fayet-Iliopoulos $\mathcal{N} = 2$ gauged supergravity with cubic prepotential: $S = \frac{1}{8\pi}\int d^4x\,\sqrt{-g}\,\mathcal{L}$ with

$$\mathcal{L} = \frac{1}{2\ell_p^2}R - \frac{3}{4\ell_p^2}\frac{(\partial x)^2+(\partial y)^2}{y^2} - V_g(x,y) - G_{IJ}F^I_{\mu\nu}F^{J\mu\nu} + \Theta_{IJ}F^I_{\mu\nu}\tilde{F}^{J\mu\nu}\,, \qquad (7.1.1)$$

where $\tilde{F}_{\mu\nu} \equiv \frac{1}{2}\epsilon_{\mu\nu\rho\sigma}F^{\rho\sigma}$, with $\epsilon_{0123} = +\sqrt{-g}$. The scalar is neutral but is non-minimally coupled to the electromangnetic field strengths through the coupling and theta angle matrices

$$G = \begin{pmatrix} \frac{1}{6}y^3 + \frac{1}{2}x^2y & -\frac{1}{2}xy \\ -\frac{1}{2}xy & \frac{1}{2}y \end{pmatrix}, \qquad \Theta = \begin{pmatrix} \frac{1}{3}x^3 & -\frac{1}{2}x^2 \\ -\frac{1}{2}x^2 & x \end{pmatrix}. \qquad (7.1.2)$$

The scalar potential V_g for $\mathcal{N} = 2$ Fayet-Iliopoulos-gauged supergravity is schematically of the form $V_g = |DW|^2 - 3|W|^2$ where $W \sim \frac{1}{y^{3/2}}\big(-g_{p_1}\frac{z^2}{2} + g_{q_0}\big)$, which is also of the form of Gukov-Vafa-Witten-type $\mathcal{N} = 1$ superpotentials arising from flux compactifications [187]. It leads to the following potential:

$$V_g(x,y) = -\frac{3}{2\ell_p^4}g_{p_1}\big(g_{p_1}y + g_{q_0}\frac{1}{y} + g_{p_1}\frac{x^2}{y}\big). \qquad (7.1.3)$$

In the context of flux compactifications, the constants g_{p_1} and g_{q_0} would be fixed by the choice of fluxes supporting the compactification, and by values of moduli we are taking to be frozen here.

[2] To conform to more standard conventions, we will however change the normalization of the gauge fields by a factor $-\frac{1}{2}$: $A^{\rm new}_\mu = -\frac{1}{2}A^{\rm old}_\mu$.

We will take (g_{p_1}, g_{q_0}) to be arbitrarily tunable but fixed real valued parameters of the theory. If they have the same sign, which we assume from now on, the potential is extremized at a negative local maximum $z = z_0$, giving rise to an AdS_4 vacuum with AdS length ℓ, with

$$x_0 = 0\,, \quad v = \sqrt{\frac{g_{q_0}}{g_{p_1}}}\,, \qquad V_g = -\frac{3}{\ell_p^4}\sqrt{g_{p_1}^3 g_{q_0}} = -\frac{3}{\ell_p^2 \ell^2}\,. \tag{7.1.4}$$

In this vacuum the scalar has the conformally coupled value $m^2 = -2/\ell^2$, above the Breitenlohner-Freedman AdS tachyon bound [188], which for AdS_4 is $m_{BF}^2 = -2.25/\ell^2$.

For the background black hole solutions which we consider, it is consistent to put $x \equiv 0$, in which case the coupling matrix G becomes diagonal and the theta angle matrix Θ is zero. Putting furthermore $y \equiv v\, e^{\chi}$, the Lagrangian (7.1.1) then simplifies to

$$\mathcal{L} = \frac{1}{2\ell_p^2}\big(R - \frac{3}{2}(\partial\chi)^2 + \frac{6}{\ell^2}\cosh\chi\big) - \frac{1}{6}v^3\, e^{3\chi}\, F_0^2 - \frac{1}{2}v\, e^{\chi}\, F_1^2\,. \tag{7.1.5}$$

Without making a commitment to any stringy interpretation at this point, we reparametrize the g_i by constants k and N as follows

$$g_{q_0} \equiv \frac{1}{k} \qquad g_{p_1} \equiv \frac{1}{N}\,. \tag{7.1.6}$$

Then we have

$$v = \sqrt{\frac{N}{k}}\,, \qquad \frac{\ell^2}{\ell_p^2} = \frac{N^2}{v} = \sqrt{kN^3}\,. \tag{7.1.7}$$

If the gravity theory has a CFT dual, its central charge is proportional to the second quantity, the AdS radius squared in four dimensional Planck units (see e.g. [189] for a general discussion). This will also be evident from the scaling of various thermodynamic quantities in (7.2.29) further down. In ABJM theory [190], a Chern-Simons-

matter CFT proposed to be dual to type IIA string theory on $AdS_4 \times \mathbb{C}P^3$ with k units of magnetic RR 2-form flux and N units of magnetic 6-form flux turned on in the $\mathbb{C}P^3$, the central charge is of the same form, with N interpreted as the rank of the gauge group, and k as the inverse coupling constant of the Chern-Simons theory. The quantity $v^2 = N/k$ is identified with the 't Hooft coupling λ in this setting, and $\ell_s = \ell/\sqrt{v}$ with the string length. Further down we will see that other quantities such as particle mass spectra have ABJM-like scalings with k and N.

However, the model we are considering is *not* the low energy effective action of the ABJM $AdS_4 \times \mathbb{C}P^3$ compactification, as in this theory one of the $U(1)$s is actually massive, Higgsed by a charged scalar (the universal 4d axion) with D0- and D4-charges proportional to $(g_{q_0}^{-1}, g_{p_1}^{-1}) \propto (k, N)$ [190]. One of the consequences of this is that D2 and D6 charges will come with strings attached and that one of the two electrostatic forces will fall off exponentially rather than by the usual Coulomb law.

7.1.3 Probe action

Since our model has two $U(1)$s, the electromagnetic fields couple to two magnetic charges p^I and two electric charges q_I, $I = 0, 1$. The q_I couple electrically to the A^I, while the p^I couple electrically to the *dual* gauge potentials B_I, defined as

$$dB_I = G_I = G_{IJ}\tilde{F}^J - \Theta_{IJ}F^J \ . \tag{7.1.8}$$

The equations of motion for F^I are the Bianchi identities for G_I and vice versa. With these dual gauge fields one can conveniently write down a general expression for the action of a probe particle in a general background. For a probe charge $\gamma =$

(p^0, p^1, q_0, q_1) this is [150, 104]

$$S_\gamma = -\int m_\gamma(z)\, ds - \int q_I A^I - p^I B_I \,. \tag{7.1.9}$$

We will take probe charges to be quantized in units of order 1, roughly thinking of them as wrapped D6, D4, D2 and D0 brane charges in a type IIA compactification. The mass $m(p, q; z)$ depends on the charges and the local background scalar value $z = x + iy$. We will consider probe black holes which are much smaller than the AdS radius as well as much smaller than the background black hole, albeit at the same temperature. As argued in chapter 6 and as we will check again in section 7.4.1 below, in this limit, the background becomes effectively cold from the point of view of the probe, in the sense that the thermal contribution to its mass becomes negligible. Hence the probe acquires the properties of an extremal black hole in asymptotically flat space. Extremal asymptotically flat black holes in $\mathcal{N} = 2$ supergravity may be BPS or non-BPS. In the first case, their mass is given by the absolute value of the central charge of the asymptotically flat $\mathcal{N} = 2$ supersymmetry algebra, which for our model is

$$m_\gamma(z) = \frac{1}{\ell_p}\sqrt{\frac{3}{4y^3}}\left|\frac{1}{6}p^0 z^3 - \frac{1}{2}p^1 z^2 + q_1 z + q_0\right| . \tag{7.1.10}$$

In the second case, the mass is strictly greater than this. As in chapter 6, we restrict ourselves to probe charges that are in fact BPS. Besides being the simplest to analyze systematically, BPS probes are also the most stable. Although non strictly supersymmetric in AdS, the phase space for decay of these nearly-BPS probes will generically be much smaller than for probe charges which have a non-BPS flat space limit.

When $x = 0$, (7.1.10) reduces to $m_\gamma = \frac{\sqrt{3}}{2\ell_p}\big[(\frac{1}{6}p^0 y^{3/2} - q_1 y^{-1/2})^2 + (\frac{1}{2}p^1 y^{1/2} +$

$q_0 y^{-3/2})^2\big]^{1/2}$. Since we work with normalization conventions in which charges are integrally quantized, we can read off the orders of magnitude of the masses of various types of charge. Expressed in terms of the AdS scale ℓ and the the parameters v, N and k introduced in (7.1.4) and (7.1.7), these are:

$$\ell\, m_{\rm D0} \sim \frac{N}{v^2} = k\,, \quad \ell\, m_{\rm D2} \sim \frac{N}{v} = \sqrt{Nk}\,, \quad \ell\, m_{\rm D4} \sim N\,, \quad \ell\, m_{\rm D6} \sim Nv = \sqrt{\frac{N^3}{k}}\,. \tag{7.1.11}$$

Notice that this agrees with the masses of wrapped D0- and D4-branes in ABJM theory [190] (D2- and D6-branes carry magnetic charge for the massive $U(1)$ in ABJM, and as a result would come with additional magnetic flux strings attached to them). The condition that all charged particles be much heavier than the AdS scale is thus $\frac{1}{N} \ll v \ll \sqrt{N}$, or equivalently $N^3 \gg k \gg 1$.

As in chapter 6, we may parametrize the charges as $\gamma = (p^0, p^1, q_1, q_0) = g(1, \kappa, -b + \frac{\kappa^2}{2}, n + b\kappa - \frac{\kappa^3}{6})$. The parameter κ can be thought of as proportional to $U(1)$ world-volume flux on the wrapped D-brane; switching it on effectively shifts $z \to z - \kappa$ in (7.1.10). The (flat) BPS black hole entropy is independent of κ and given by $s_\gamma = \pi g^2 \sqrt{\frac{8}{9} b^3 - n^2}$ [159]. For charges $\gamma = g(0, 1, \kappa, n - \frac{\kappa^2}{2})$, this becomes $s_\gamma = \pi g^2 \sqrt{\frac{2}{3} n}$. Evidently the quantities under the square root must be positive for the black hole to exist. We should note however that not all BPS particles have a realization as a single centered black hole in supergravity, even when we allow singular limits in which the horizon goes to zero size. Some BPS states are realized as multi-centered bound states [104]. A notable example is a pure wrapped D4-brane, which has a *negative* worldvolume curvature-induced D0-charge $q_0 = -p_1^3/24$, and is realized as a two particle bound state of charges $(1, \frac{p_1}{2}, \frac{p_1^2}{8}, -\frac{p_1^3}{48})$ and $(-1, \frac{p_1}{2}, -\frac{p_1^2}{8}, -\frac{p_1^3}{48})$ [105].

7.2 Background solution

We consider a spherically symmetric nonextremal charged black hole metric of the form

$$ds^2 = -V(r)\,dt^2 + \frac{1}{V(r)}dr^2 + W(r)\,d\Omega_2^2\,. \tag{7.2.12}$$

The scalar z is assumed to only depend on the radial coordinate r. Note that r is in principle not the Schwarzschild radial coordinate; namely because it can go negative. In general the black hole may have arbitrary electric and magnetic charges Q_I and P^I, but as in chapter 6 we limit ourselves to a setup with $P^0 = 0$ and $Q_1 = 0$, in which case we can consistently set $x = 0$ throughout, and the field strengths

$$F^0 = Q_0\,\frac{3}{y(r)^3}\frac{dt\wedge dr}{W(r)}\,, \qquad F^1 = -\frac{1}{2}\,P_1\,\sin\theta\,d\theta\wedge d\phi \tag{7.2.13}$$

automatically solve the Bianchi identities and equations of motion chapter 6.

Exact solutions satisfying this ansatz, for arbitrary charges P_1, Q_0 and mass M, were constructed in [183] (related solutions were considered in [191, 192, 193, 194, 195, 196, 198, 199, 200, 201, 202, 203, 204, 205, 206, 207]). These solutions will be the starting point for our analysis.[3]

[3]This is not the most general set of solutions compatible with the ansatz. Indeed in the neutral limit, it reduces to the standard hairless AdS-Schwarzschild solution, while it is known that there also exist hairy solutions with the same boundary conditions [208] (for a recent discussion see [209]). The (numerically constructed) hairy neutral black hole is thermodynamically disfavored compared to the hairless one [208], and thus by continuity the same will be true for at least a finite range of charged black holes, for which this restriction will not invalidate the thermodynamic analysis. It is not known however if this continues to hold for arbitrary charges. In principle it should be possible to address this question by (numerically) analyzing the reduced equations of motion obtained e.g. in [202].

7.2.1 Metric, scalar and gauge potentials

For any given mass M and charges P_1, Q_0, the solution of [183] can be written in the form (7.2.12) with $x = 0$ and

$$V(r) = \frac{1}{W}\left(r^2 - c^2 + \frac{1}{\ell^2}W^2\right), \qquad W(r) = \sqrt{f_0 f_1^3}\,, \qquad y(r) = v\sqrt{\frac{f_0}{f_1}}\,, \tag{7.2.14}$$

where the f_i are functions linear in r:

$$f_0(r) = r + a_0\,, \quad f_1(r) = r + a_1\,, \tag{7.2.15}$$

the AdS length ℓ and asymptotic scalar $v = y|_{r=\infty}$ are fixed by g_{q_0} and g_{p_1} as in (7.1.4), and c, a_0 and a_1 are positive constants determined by the mass M and charges Q_0 and P_1 of the black hole:

$$a_0 = \sqrt{c^2 + \tfrac{12}{v^3}\ell_p^2 Q_0^2}, \qquad a_1 = \sqrt{c^2 + \tfrac{v}{3}\ell_p^2 P_1^2}\,, \tag{7.2.16}$$

with $c = c(M, Q_0, P_1)$ the unique positive solution to

$$M\ell_p^2 = \tfrac{1}{4}a_0 + \tfrac{3}{4}a_1 = \tfrac{1}{4}\sqrt{c^2 + \tfrac{12}{v^3}\ell_p^2 Q_0^2} + \tfrac{3}{4}\sqrt{c^2 + \tfrac{v}{3}\ell_p^2 P_1^2}\,. \tag{7.2.17}$$

The definition and computation of the mass M is subtle due to the presence of the $m^2 < 0$ scalar. We computed it as in [208, 210]. The parameter c is a measure for the deviation from extremality, as in the asymptotically flat case studied in chapter 6. However in the case at hand the point $c = 0$ is not physically reachable: extremality occurs at some nonzero value of c, as will be clear from the discussion further down. Notice that when $a_0 = a_1$, i.e. when $|Q_0| = v^2|P_1|/6$, the profile of the scalar field becomes constant everywhere and the metric becomes that of the ordinary Reissner-Nordstrom-AdS black hole.

We denote the radial location of the outer horizon by r_+. It satisfies $V(r_+) = 0$, that is:

$$r_+^2 - c^2 + \frac{1}{\ell^2}(r_+ + a_0)(r_+ + a_1)^3 = 0\,, \tag{7.2.18}$$

and in addition $W(r) > 0$ and $V(r) > 0$ for all $r > r_+$.

The gauge potentials A^I and their magnetic duals B_I are obtained by integrating the field strengths F^I and G_I specified by (7.2.13) and (7.1.8):

$$A^0 = \left(\frac{3}{v^3}\frac{Q_0}{r + a_0} - \phi_0\right) dt\,, \qquad A^1 = \frac{1}{2}P_1\big(\cos\theta \pm 1\big)\, d\phi\,, \tag{7.2.19}$$

$$B_0 = \frac{1}{2}Q_0\big(\cos\theta \pm 1\big)\, d\phi\,, \qquad B_1 = -\left(\frac{v}{4}\frac{P_1}{r + a_1} - \phi_1\right) dt\,. \tag{7.2.20}$$

We choose the integration constants ϕ_0 and ϕ_1 such that the electric potentials vanish at the black hole horizon $r = r_+$. This guarantees regularity of the gauge connection after Euclidean continuation of the solution, and fixes

$$\phi_0 = \frac{3}{v^3}\frac{Q_0}{r_+ + a_0}\,, \qquad \phi_1 = \frac{v}{4}\frac{P_1}{r_+ + a_1}\,, \tag{7.2.21}$$

The asymptotic scalar profile in the standard Schwarzschild radial coordinate $r_s = \sqrt{W(r)}$ is given by $\log y(r_s) = \frac{\alpha}{r_s} + \frac{\beta}{r_s^2} + \cdots$, where $\alpha = (a_0 - a_1)/2$ and $\beta = -\alpha^2/2$. Thus all solutions found in [183] obey the generalized conformally invariant boundary condition $\beta = f\alpha^2$ of [208], for a specific value of f (which depends on the normalization of the scalar).[4]

[4]These generalize the "standard" Dirichlet ($\alpha = 0$) and "alternate" Neumann ($\beta = 0$) zero source boundary conditions. In language of the dual CFT, the $\alpha = 0$ boundary conditions corresponds to a CFT where the operator $\mathcal{O}$ dual to the scalar has dimension $\Delta = 2$, while $\beta = 0$ boundary conditions correspond to a CFT where this operator has dimension $\Delta = 1$. The $\alpha = 0$ CFT is the IR fixed point of a relevant double trace deformation $\Delta\mathcal{L}_{\rm CFT} \propto \mathcal{O}^2$ of the $\beta = 0$ CFT, while the $\beta + \frac{\alpha^2}{2} = 0$ CFT is obtained from the $\beta = 0$ one by an approximately marginal triple trace deformation $\Delta\mathcal{L}_{\rm CFT} \propto \mathcal{O}^3$.

7.2.2 Parametrization

We found it most convenient to parametrize the vacua by ℓ and v and the black hole solutions by r_+, u_0 and u_1, where we define

$$u_I \equiv r_+ + a_I. \tag{7.2.22}$$

The parameters c, a_0, a_1 appearing in the solution as given above can be written in terms of (r_+, u_I) as:

$$c = \sqrt{r_+^2 + \frac{1}{\ell^2} u_0 u_1^3}\,, \qquad a_I = u_I - r_+\,, \tag{7.2.23}$$

and thus the conserved quantitities Q_0, P_1 and M are obtained using the relations (7.2.16)-(7.2.17). Explicitly:

$$\ell_p |Q_0| = \sqrt{\frac{v^3}{12}} \sqrt{u_0(u_0 - 2r_+) - \frac{u_0 u_1^3}{\ell^2}}\,, \quad \ell_p |P_1| = \sqrt{\frac{3}{v}} \sqrt{u_1(u_1 - 2r_+) - \frac{u_0 u_1^3}{\ell^2}}\,,$$
$$\ell_p^2 M = \frac{1}{4}(u_0 + 3u_1) - r_+\,. \tag{7.2.24}$$

The AdS-Reissner-Nordstrom limit corresponds to $u_0 = u_1 \equiv u$, while the neutral AdS-Schwarzschild limit has $r_+ = \frac{1}{2}(u - \frac{1}{\ell^2}u^3)$, with $M = \frac{1}{2}(u + \frac{1}{\ell^2}u^3)/\ell_p^2$.

7.2.3 Entropy and temperature

The black hole entropy is one quarter of the horizon area, which in our parametrization takes the simple form

$$S = \frac{\pi \sqrt{u_0 u_1^3}}{\ell_p^2}\,. \tag{7.2.25}$$

Its temperature T is obtained in the standard way by requiring regularity of the Euclidean continuation at $r = r_+$ by imposing Euclidean time periodicity $1/T$, giving

$$T = \frac{V'(r_+)}{4\pi} = \frac{2r_+ + u_1^2(3u_0 + u_1)/\ell^2}{4\pi\sqrt{u_0 u_1^3}}\,. \tag{7.2.26}$$

Notice that in the flat space limit, the BPS black holes would have $r_+ = 0$ and are thus connected to finite temperature black holes in AdS where we do not take the strict $\ell \to \infty$ limit.

7.2.4 Physical region of parameter space

The physical parameter range is given by the values of (r_+, u_0, u_1) for which the constants a_I and c appearing in the metric are all positive, and for which $T > 0$ and $\phi_I \in \mathbb{R}$. This implies in particular that $u_I > 0$, as can be seen by making use of (7.2.16) and (7.2.23). The horizon radial position can be either positive or negative: for example a large neutral AdS-Schwarzschild black hole has $r_+ < 0$ while a small neutral black hole has $r_+ > 0$.

To obtain all possible black hole solutions for a given (T, ϕ_0, ϕ_1), we solve numerically for (r_+, u_0, u_1) and retain the solutions with $u_0, u_1 > 0$. This guarantees the solution is physical and that r_+ is indeed the outer horizon, i.e. $V(r) > 0$, $W(r) > 0$ for all $r > r_+$.[5]

7.2.5 Scaling symmetries and invariant parametrization

We have parametrized the solutions by a total of 5 parameters (v, ℓ, r_+, u_0, u_1), with the first two fixing the AdS vacuum and the last three parametrizing the black hole solutions within a given vacuum. However, as in the asymptotically flat case chapter 6, there are two scaling symmetries trivially relating different solutions. They

[5]To see this, express V and W in terms of (r_+, u_0, u_1) and $x \equiv r - r_+$. Then $W = \sqrt{(u_0 + x)(u_1 + x)^3}$, which is manifestly positive for $x > 0$, since $u_I > 0$. Furthermore $WV = \left(2r_+ + \frac{1}{\ell^2} u_1^2 (3u_0 + u_1)\right) x + \left(1 + \frac{3}{\ell^2} u_1 (u_0 + u_1)\right) x^2 + \frac{1}{\ell^2}(u_0 + 3u_1) x^3 + \frac{1}{\ell^2} x^4$, which is also manifestly positive, since the coefficient of x equals $4ST > 0$, and $u_I > 0$.

act as $X \to \lambda_1^{n_1}\lambda_2^{n_2}X$, $\lambda_i \in \mathbb{R}^+$, on the various quantities X defined so far, with the exponents (n_1, n_2) indicated in the first two lines of this table:

	ℓ	v	k	N	r_+	u_0	u_1	M	Q_0	P_1	S	T	ϕ_0	ϕ_1	r
n_1	1	0	1	1	1	1	1	1	1	1	2	-1	0	0	1
n_2	0	1	$-\frac{3}{2}$	$\frac{1}{2}$	0	0	0	0	$\frac{3}{2}$	$-\frac{1}{2}$	0	0	$-\frac{3}{2}$	$\frac{1}{2}$	0
δ	-1	0	0	0	-1	-1	-1	1	0	0	0	1	1	1	-1
$N^{\#}$	0	0	1	1	0	0	0	2	1	1	2	0	1	1	0
$v^{\#}$	0	1	-2	0	0	0	0	-1	1	-1	-1	0	-2	0	0

The third line shows the mass dimension δ. Physical observables will depend only on invariant combinations of the parameters, up to an overall factor determined by the scaling properties of the observable. Specifically, we will express any quantity X of mass dimension δ and scaling exponent (n_1, n_2) in terms of a dimensionless, scaling invariant $\tilde{X}$, as follows:

$$X = \ell^{-\delta} N^{n_1+\delta}\, v^{n_2-(n_1+\delta)/2}\tilde{X} \ . \tag{7.2.27}$$

The quantities N and k were introduced in (7.1.7). The last two lines of the table indicate the powers of N and v appearing in various quantities. We will display our phase diagrams as functions of the rescaled intensive variables $\left(\tilde{T}, \tilde{\phi}_0, \tilde{\phi}_1\right)$ related to the original ones by

$$T = \frac{1}{\ell}\,\tilde{T}\,, \qquad \phi_0 = \frac{N}{v^2\ell}\,\tilde{\phi}_0\,, \qquad \phi_1 = \frac{N}{\ell}\,\tilde{\phi}_1\,. \tag{7.2.28}$$

The extensive variables (7.2.24) and (7.2.25) are related to their invariant counterparts by

$$Q_0 = Nv\,\tilde{Q}_0\,, \qquad P_1 = \frac{N}{v}\,\tilde{P}^1, \qquad M = \frac{N^2}{v\ell}\,\tilde{M}\,, \qquad S = \frac{N^2}{v}\,\tilde{S}\,. \tag{7.2.29}$$

Working consistently with the rescaled variables instead of the original ones effectively sets

$$\ell_p \equiv 1, \qquad \ell \equiv 1 \qquad v \equiv 1 \tag{7.2.30}$$

in the expressions of the previous sections. In what follows we will always use rescaled variables, and to avoid cluttering we will therefore drop the tildes, keeping in mind that in order to get the actual physical quantities, we need to rescale as indicated above.

Finally note that besides the obvious charge conjugation symmetry $(P_1, Q_0) \to (-P_1, -Q_0)$, the background metric and scalar profile are also invariant under $(P_1, Q_0) \to (P_1, -Q_0)$. This descends from an enhanced $\mathbb{Z}_2$ symmetry of the action that exists only when the pseudoscalar x is zero.

7.3 Background thermodynamics

Before moving on to examine probe black holes in the black hole background, we analyze the phase structure of the background itself, which is already quite interesting. For AdS-Reissner-Nordstrom black holes without running scalars this was done in [174, 211]. This case corresponds to the locus $u_0 = u_1$ in our setup, since then $y(r) = v$ is constant. The general case exhibits a considerably richer structure.

7.3.1 Thermodynamic equilibrium and stability

We will mostly work in a thermodynamic ensemble with fixed temperature T and chemical potentials ϕ_0, ϕ_1 dual to the charges Q_0 and P_1, and fixed charges $P^0 = 0$, $Q_1 = 0$. That is to say, if we imagine coupling the system to a reservoir at fixed temperature T and potentials ϕ_I, the total (system plus reservoir) entropy will change as $\Delta S_{\text{tot}} = \Delta S - \frac{1}{T}\Delta E + \frac{\phi_0}{T}\Delta Q_0 + \frac{\phi_1}{T}\Delta P_1 = -\Delta F/T$, where ΔE, ΔQ_0, ΔP_1

and ΔS refer to the system, and we have defined

$$F \equiv E - T\,S - \phi_0 Q_0 - \phi_1 P_1. \tag{7.3.31}$$

Stable equilibrium with the reservoir requires $S_{\rm tot}$ to be maximized, or equivalently F to be minimized under variations of energy and charges; locally this requires

$$F' = 0\,, \qquad F'' > 0\,. \tag{7.3.32}$$

The derivatives are understood to be with respect to the system's extensive variables, at fixed, externally tuned values of T, ϕ_0 and ϕ_1. The parametrization of the extensive variables can be arbitrary. We will work with the black hole metric parameters (u_0, u_1, r_+) defined in 7.2.2. Thus, using (7.2.24) and (7.2.25) keeping in mind (7.2.30),

$$F = \frac{1}{4}u_0 + \frac{3}{4}u_1 - r_+ - \pi T\sqrt{u_0 u_1^3} - \frac{\phi_0}{2\sqrt{3}}\sqrt{u_0^2 - 2u_0 r_+ - u_0 u_1^3} \\ - \sqrt{3}\,\phi_1\sqrt{u_1^2 - 2u_1 r_+ - u_0 u_1^3}. \tag{7.3.33}$$

Solving $F' = 0$ in (7.3.32) at fixed (T, ϕ_0, ϕ_1) then provides the local equilibrium relation between (T, ϕ_0, ϕ_1) and (r_+, u_0, u_1):

$$T = \frac{2r_+ + 3u_0 u_1^2 + u_1^3}{4\pi\sqrt{u_0 u_1^3}}\,, \\ \phi_0 = \frac{\sqrt{3}}{2}\frac{\sqrt{u_0^2 - 2u_0 r_+ - u_0 u_1^3}}{u_0}\,, \quad \phi_1 = \frac{\sqrt{3}}{4}\frac{\sqrt{u_1^2 - 2u_1 r_+ - u_0 u_1^3}}{u_1}\,, \tag{7.3.34}$$

in agreement with the values obtained earlier in (7.2.21) and (7.2.26) by requiring regularity of the Euclidean continuation. The corresponding equilibrium free energy is remarkably simple:

$$F_{\rm eq} = \frac{r_+}{2}\,. \tag{7.3.35}$$

This can also be obtained as the on shell Euclidean action $I_E = F/T$, provided the action is defined with the appropriate boundary counterterms, as in [208]. Note that this simple expression suggests a nice interpretation of the radial coordinate r. Roughly, it is to free energy what the Schwarzschild radial coordinate is to entropy. We can also give a more physical interpretation to the parameters u_0, u_1 by noticing that at equilibrium

$$u_0 = 3\,\frac{Q_0}{\phi_0}\,, \qquad u_1 = \frac{1}{4}\,\frac{P_1}{\phi_1}\,. \tag{7.3.36}$$

This shows that u_0 and u_1 can be thought of as the black hole's D0- and D4-charge susceptibilities.

For the system-reservoir equilibrium to be stable under small fluctuations, we need a positive definite Hessian, that is $F'' > 0$ at fixed T, and ϕ_I. Stability under arbitrarily large fluctuations requires the minimum to be global.

Note that although we are analyzing stability in this (partial) grand canonical ensemble, this does not necessarily mean we are actually considering a physical situation in which the system is truly coupled to a reservoir. Indeed, in the case of global AdS black holes (dual to thermal states of a CFT_3 living on a 2-sphere), it is physically most natural to consider the physical system to be isolated, since there is no natural "outside" environment for the 2-sphere. However even for isolated systems, a grand canonical stability analysis provides information. More specifically, an instability in the grand canonical ensemble will, for sufficiently large isolated systems, indicate a thermodynamic tendency towards the formation of inhomogeneities in the distribution of the energy and charge. Essentially, for a subsystem small compared to the complete system, this is because the remainder of the system acts as a reservoir. In

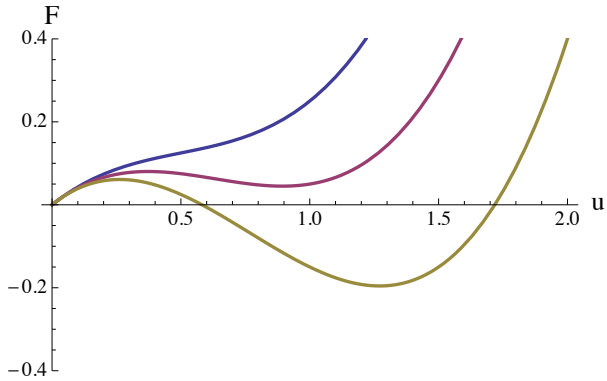

Fig. 7.1: AdS-Schwarzschild free energy F for a black hole of size u coupled to a heat bath at temperatures (from left to right) $\pi T = 0.75, 0.95, 1.15$. A local minimum corresponds to a perturbatively stable black hole, which is globally stable if it is negative. A local maximum corresponds to a perturbatively unstable black hole.

view of the fact that instabilities towards the formation of inhomogeneities is exactly what we want to investigate in this chapter, this is therefore an appropriate ensemble to consider.[6]

7.3.2 Schwarzschild illustration

As a simple check and illustration of the above discussion, consider first the AdS-Schwarzschild black hole (fig. 7.1). This amounts to setting $u_0 = u_1 \equiv u$ and $r_+ = \frac{1}{2}(u - u^3)$, so $S = \pi u^2$, $M = \frac{1}{2}(u + u^3)$, and:

$$F = M - TS = \frac{1}{2}(u + u^3) - \pi T u^2 \,. \tag{7.3.37}$$

[6]By the same token, it would actually have been even more appropriate for us to consider the ensemble where all charges are allowed to fluctuate, including P^0 and Q_1. Unfortunately this is obstructed by the lack of explicit black holes solutions for the general charge case.

The local equilibrium condition (7.3.32) is $\partial_u F = \frac{1}{2} + \frac{3}{2}u^2 - 2\pi T u = 0$ and $\partial_u^2 F = 3u - 2\pi T > 0$. The first equation expresses the equilibrium temperature in terms of u: $T_{\rm eq}(u) = \frac{1}{4\pi}(u^{-1} + 3u)$. Plugging this value for T into (7.3.37) gives $F_{\rm eq} = \frac{1}{4}(u - u^3) = \frac{1}{2}r_+$, confirming (7.3.35). The minimum value of $T_{\rm eq}(u)$, reached at $u = 1/\sqrt{3}$, is $T_{\rm min} = \sqrt{3}/2\pi$; there are no black holes at temperatures below this. For any given $T > T_{\rm min}$, there are two solutions u to the equilibrium equation, hence two black hole solutions. The larger one will be at a local minimum of $F(u)$ ($F''(u) > 0$), the smaller one at a local maximum. The local minimum of $F(u)$ is not necessarily a global minimum. To verify global minimality, we also have to compare to the free energy at the boundary points of state space, in this case at $u = 0$. From the third expression in (7.3.37), it follows that for any value of T, we have $F = 0$ when $u = 0$.[7] Therefore global stability requires $F_{\rm eq} < 0$. This is the case if and only if $u > 1$. Hence a first order phase transition occurs at $u = 1$, where $T_{\rm eq} = 1/\pi$. This was first pointed out by Hawking and Page [173]. The transition is accompanied by a macroscopic jump in mass and entropy in the large N limit and can thus be considered to be a first order phase transition. In the context of the AdS-CFT correspondence, it can be interpreted as a confinement-deconfinement phase transition occurring on the sphere at a temperature of the order of the inverse curvature radius [212].

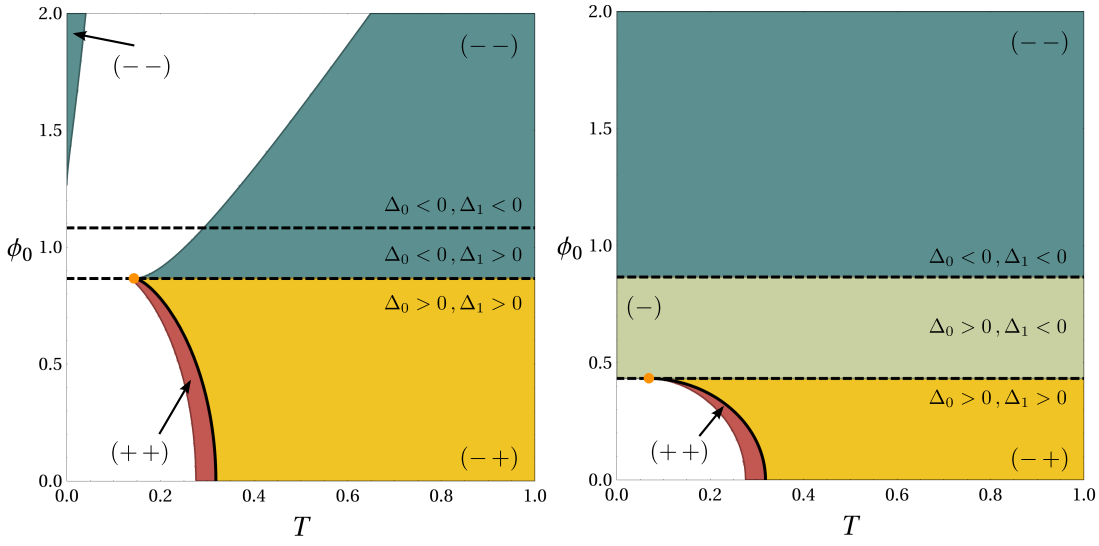

Fig. 7.2: Phase diagrams for the black hole background. On the left we have $\phi_1 = 0.4\,\phi_0$ and on the right $\phi_1 = \phi_0$. The different regions are labeled by a the signs of the free energies of the black hole solutions in the region. For example $(-+)$ is a region with two black holes, one with negative and one with positive free energy, while $(-)$ indicates a region with just one black hole, with negative free energy. Across the dotted lines either Δ_0 or Δ_1 changes sign. The white regions represent configurations where no black holes exist. The Hawking-Page transition occurs at the thick black line, terminating in the orange dot.

7.3.3 Background phase diagram

Figure 7.2 shows the phase diagrams in the (ϕ_0, T) plane, for two different fixed ϕ_1/ϕ_0 ratios. The diagrams are obtained by solving (7.3.34) for r_+, u_0 and u_1. For

[7]This is true in the classical gravity approximation $N \to \infty$ where N was defined in (7.2.27). At one loop, there will be a contribution from thermal fluctuations, capturing the free energy of an ideal thermal gas in global AdS, but this will be of order 1 in a large N expansion, and hence negligible to leading order.

the ϕ_0 and ϕ_1 equations this can be done in a relatively simple closed form:

$$r_+ = \frac{u_1}{2}\frac{\Delta_0\Delta_1 - u_1^4}{\Delta_0 + u_1^2}\,, \quad u_0 = u_1\,\frac{\Delta_1 + u_1^2}{\Delta_0 + u_1^2}\,, \quad \text{where} \quad \Delta_0 \equiv 1 - \frac{4}{3}\phi_0^2, \quad \Delta_1 \equiv 1 - \frac{16}{3}\phi_1^2\,, \tag{7.3.38}$$

The remaining relation to be inverted is

$$T = \frac{\Delta_0 + 3u_1^2}{4\pi u_1}\sqrt{\frac{\Delta_1 + u_1^2}{\Delta_0 + u_1^2}}\,. \tag{7.3.39}$$

This can be reduced to finding the roots of a cubic polynomial but as usual the explicit expression for the solutions is not illuminating. The charges and entropy in terms of u_1 and ϕ_0, ϕ_1 are

$$Q_0 = \frac{u_1\phi_0}{3}\frac{\Delta_1 + u_1^2}{\Delta_0 + u_1^2}\,, \quad P_1 = 4\,u_1\phi_1\,, \quad S = \pi u_1^2\sqrt{\frac{\Delta_1 + u_1^2}{\Delta_0 + u_1^2}} = \pi\frac{\sqrt{Q_0 P_1^3}}{\sqrt{\phi_0\phi_1^3}}\,, \tag{7.3.40}$$

the free energy is $F = r_+/2$ with r_+ as in (7.3.38), and the energy is

$$M = \frac{u_1}{4}\,\frac{4u_1^2 + 2u_1^4 + 3\Delta_0 + \Delta_1 - 2\Delta_0\Delta_1}{\Delta_0 + u_1^2}\,. \tag{7.3.41}$$

Recall that the Reissner-Nordstrom limit corresponds to $u_0 = u_1$, which implies $\Delta_0 = \Delta_1$, or $\phi_1 = \phi_0/2$.

We list some notable features:

1. The temperature (7.3.39) diverges for $u_1 \to \infty$, so at high temperatures there will always be at least one solution, with negative free energy. It is continuously connected to the large AdS-Schwarzschild black hole by tuning ϕ_0 and ϕ_1 to zero. As long as Δ_0 and Δ_1 are positive (corresponding to the region below the lower dotted line in the figure), the temperature goes infinite again when $u_1 \to 0$, providing a second high temperature solution branch. This solution is

continuously connected to the small Schwarzschild black hole. It ceases to exist when crossing over to $\Delta_0 < 0$ or $\Delta_1 < 0$ (from below to above the (lower) dotted line in the figure), as the quantity under the square root then becomes negative for $u_1 \to 0$. When $\Delta_0 > 0$ and $\Delta_1 < 0$ (region between the dotted lines), there is only one high temperature solution. However when $\Delta_0 < 0$ (region above the (upper) dotted line), a new high temperature branch emerges for values of u_1 approaching the zero of the denominator, i.e. for $u_1^2 \to -\Delta_0$. In contrast to the small u_1 branch, it has negative free energy.

2. In regions with two black holes, the one with the lowest free energy is locally stable ($F'' > 0$), the other one unstable. When there is a unique black hole solution, it is locally stable. When crossing the dotted lines (corresponding to sign changes of the Δ_I), the stable black hole always continues smoothly, whereas the unstable black hole becomes singular. Consider for example the case $\Delta_1 > 0$ with Δ_0 small and negative. Putting $u_1 = w\sqrt{-\Delta_0}$ and dropping subleading terms turns (7.3.39) into $T \approx \frac{\sqrt{\Delta_1}(3w^2-1)}{4\pi w\sqrt{w^2-1}}$, which relates a finite fixed w to a finite fixed T. Sending Δ_0 up to zero at fixed w thus corresponds to a black hole with $u_1 \to 0$, $u_0 \approx \frac{w\Delta_1}{\sqrt{-\Delta_0}(v^2-1)} \to \infty$, $r_+ \sim -\sqrt{-\Delta_0} \to 0-$, $Q_0 \sim 1/\sqrt{-\Delta_0} \to \infty$, and $M \sim 1/\sqrt{-\Delta_0} \to \infty$. The scalar profile and geometry becomes singular in this limit; for instance at the horizon we have $y = \sqrt{u_0/u_1} \sim -1/\Delta_0 \to \infty$.

3. The white gaps in the plot occur when the black hole free energy at fixed reservoir temperature and potentials fails to have a local extremum as a function of the extensive variables (r_+, u_0, u_1), the analog of the upper curve in fig.

7.1. In this case none of the family of black holes we consider can exist in equilibrium with the reservoir. When crossing over into a white gap a stable and an unstable saddle point of the free energy coalesce and disappear. At the boundary the Hessian F'' develops a zeromode and $\det F'' = 0$. It can be checked that $\det F'' \propto (3\,u_0 + u_1 - 4\,r_+)(2\,u_0 u_1^5 + r_+(u_0 - u_1)u_1^2 - 2\,r_+^2)$, up to factors that remain positive throughout; this provides the boundaries of the white gaps.

4. For the white gaps below the dotted line ($\Delta_0, \Delta_1 > 0$), a Hawking-Page transition occurs before reaching the gap. This is indicated by the thick line forming the boundary between the yellow and red regions. In the red region the free energy still has a local minimum, but it is positive, so the black holes we consider are thermodynamically disfavored compared to a thermal gas in empty AdS. This is the analog of the middle curve in fig. 7.1. The transition temperature $T_{\rm HP}$ is obtained by solving $F = \frac{1}{2}r_+ = 0$, which gives $u_1 = (\Delta_0\Delta_1)^{1/4}$ and

$$T_{\rm HP} = \frac{\sqrt{\Delta_0} + 3\sqrt{\Delta_1}}{4\pi}\,. \tag{7.3.42}$$

which is real if $\Delta_0, \Delta_1 > 0$. On the Reissner-Nordstrom locus, we have $\Delta_0 = \Delta_1$ and this becomes $T_{\rm HP} = \sqrt{\Delta_0}/\pi$, reproducing [174]. For neutral black holes we have $\Delta_0 = \Delta_1 = 1$ and $T_{\rm HP} = 1/\pi$, reproducing [173].

5. When $\Delta_0 < \Delta_1$, as is the case in the figure on the left, there is also a white gap above the dotted line, i.e. for $\Delta_0 < 0$. The instability associated to it is of a very different nature than the Hawking-Page instability. It is still true that the disappearance of black hole solutions is due to the coalescence and then

disappearance of a pair of saddle points of the free energy (7.3.33) (one locally stable, the other one unstable), but now this happens for saddle points at a *negative* value of F, so the thermodynamically preferred state cannot possibly be that of a thermal gas in empty AdS (which has $F = 0$). Indeed there is a much more violent instability in this regime: whenever $\phi_0 > \frac{\sqrt{3}}{2}$, the free energy (7.3.33) is unbounded below, with a runway in the large u_0 direction. To see this, it is convenient to first eliminate r_+ in favor of the charge $P_1 = \partial_{\phi_1} F = \sqrt{3}\sqrt{u_1(u_1 - 2r_+) - u_0 u_1^3}$, in terms of which

$$F = \frac{u_0}{4}\big(1+2u_1^2-\frac{2\phi_0}{\sqrt{3}}\big[\big(1-\frac{u_1}{u_0}\big)\big(1+u_1^2\big)+\frac{P_1^2}{3u_0u_1}\big]^{1/2}\big)-\pi T\sqrt{u_0u_1^3}-\phi_1 P_1+\frac{P_1^2}{6u_1}+\frac{u_1}{4}\,. \tag{7.3.43}$$

In the large u_0 limit at fixed u_1 and P_1, the leading term is linear in u_0, with coefficient proportional to $1 + 2u_1^2 - \frac{2\phi_0}{\sqrt{3}}\sqrt{1+u_1^2}$. When $\phi_0 > \frac{\sqrt{3}}{2}$, this becomes negative for a range of u_1 values, implying the free energy is unbounded below in this regime. When brought in contact with an infinite reservoir, the system will soak up Q_0-charge without bound. For large systems in isolation, one expects a corresponding instability to formation of clumps with large Q_0 densities. In the limit of an infinitely large system (the planar limit, which will be detailed in section 7.3.5), the system acts as an infinite reservoir for finite subsystems, and there again appears to be no limit on how large the charge accumulation can get. This would appear rather unphysical. However, in this limit the solution becomes singular, with the scalar y and curvature growing without bound towards the black hole, outside the regime of validity of the 4d (truncated) supergravity approximation. Presumably, assuming the model has

a UV completion, the runaway will therefore be cured by degrees of freedom beyond those considered in our setup. .

6. The limit $\Delta_1 \to \Delta_0$ is subtle when $\Delta_0 < 0$. Naively, (7.3.38) would seem to imply that the limiting solution is just the $u_0 = u_1$ AdS-Reissner-Nordstrom black hole with constant scalar profile. This is indeed one of the limiting solutions, but it misses the solution branch with u_1^2 approaching $-\Delta_0$: From (7.3.38) and (7.3.39) it follows that with $\Delta_1 - \Delta_0 \equiv \delta$ and $u_1^2 + \Delta_0 \equiv \epsilon$ both small, we have $2\pi T \approx \sqrt{-\Delta_0(1+\delta/\epsilon)}$ and $u_0/u_1 \approx 1 + \delta/\epsilon \approx -(2\pi T)^2/\Delta_0$. This is different from 1 in general so the limiting black hole will not be the RN solution and in particular it will have a nontrivial scalar profile. For $T < \frac{\sqrt{-\Delta_0}}{2\pi}$, this black hole has lower free energy than the AdS-RN solution, for $T > \frac{\sqrt{-\Delta_0}}{2\pi}$ it has higher free energy. When $T = \frac{\sqrt{-\Delta_0}}{2\pi}$ the two solutions coincide with $u_0 = u_1 = \sqrt{-\Delta_0}$, and the Hessian degenerates. This is also the location where the white gap begins to open up when $\Delta_0 < \Delta_1$.

7. The orange dot in the figure corresponds to the singular point $u_1 \to 0$ with either $\Delta_0 = 0$ and $T = \frac{3\sqrt{\Delta_1}}{4\pi}$ (as in the left panel of the figure) or $\Delta_1 = 0$ and $T = \frac{\sqrt{\Delta_0}}{4\pi}$ (as in the right panel). When $\Delta_1 = 0$, Q_0/P_1 diverges, and when $\Delta_0 = 0$, P_1/Q_0 diverges. This results in singular limiting solutions, similar to the other degenerations we discussed.

7.3.4 The flat space / small black hole limit

The asymptotically flat space limit (analyzed in chapter 6) corresponds to taking $N \propto \ell/\ell_p \to \infty$ keeping the original, unrescaled Q_0, P_1 and $M\ell_p$ fixed. From (7.2.29)

it can be seen that in terms of the rescaled variables we are working with here (which were indicated by tildes in (7.2.29)), this means we take $(Q_0, P_1, M) \sim \frac{1}{N} \to 0$, or equivalently $(r_+, u_0, u_1) \sim \frac{1}{N} \to 0$. From (7.3.34) it follows that for generic nonextremal black holes in this scaling limit we have $T \to \infty$ while the ϕ_I remain finite. This is evident as well from (7.2.28)), as we are taking the limit with fixed physical temperature and potentials in Planck units. At any rate, since we can now drop terms of higher order in u_1 in expressions such as (7.3.39), it becomes easy to invert the relations between intensive and extensive variables; in particular $Q_0 = \frac{\phi_0}{12\,\pi\,T}\sqrt{\frac{\Delta_1^3}{\Delta_0}}$, $P_1 = \frac{\phi_1}{\pi T}\sqrt{\Delta_0\Delta_1}$, $M = \frac{\sqrt{\Delta_0\Delta_1^3}}{16\pi T}(\frac{1}{\Delta_0} + \frac{3}{\Delta_1} - 2)$, $S = \frac{\sqrt{\Delta_0\Delta_1^3}}{16\pi T^2}$, and $F = \frac{\sqrt{\Delta_0\Delta_1^3}}{16\pi T} > 0$.

From these expressions we see there is another limit which sends the extensive quantities to zero in the appropriate way, namely taking $(\Delta_0, \Delta_1) \sim \frac{1}{N} \to 0$ (hence $|\phi_0| \to \frac{\sqrt{3}}{2}$, $|\phi_1| \to \frac{\sqrt{3}}{4}$), keeping T, the physical temperature in AdS units, fixed. Curiously, from the flat space point of view, this is in fact an extremal limit, since the temperature goes to zero in Planck units: $T\ell_p \sim 1/N$. Indeed in this limit the entropy becomes $S = \pi\sqrt{\frac{2}{3}|Q_0 P_1^3|}$, reproducing the well-known flat space extremal D4-D0 entropy formula.

7.3.5 The planar / large black hole limit

It is often simpler to work in a limit in which we can effectively replace the spherical S^2 black hole geometry by an $\mathbb{R}^2$ planar one. This is achieved by zooming in on a small solid angle of the geometry, say around the north pole, while simultaneously scaling up all extensive quantities. In the dual CFT this limit can be thought of as a thermodynamic limit in which the system of interest is living on a flat two-dimensional

plane and in contact with a heat reservoir with which it can exchange energy and charge, through a far away boundary.

The required scalings parallel those used in [174] in the RN case. Introducing a new radial coordinate $\rho > 0$ related to the old one r by $r = r_+ + \rho$, we put:

$$u_0 = \lambda\, \bar{u}_0\,, \quad u_1 = \lambda\, \bar{u}_1\,, \quad r_+ = \lambda^3\, \bar{r}_+\,, \quad \rho = \lambda\, \bar{\rho}\,, \quad t = \bar{t}/\lambda\,, \quad \theta = \bar{\theta}/\lambda\,, \quad \phi = \bar{\phi}\,, \tag{7.3.44}$$

sending $\lambda \to \infty$ while keeping the barred quantities fixed. For the conformal boundary metric we thus get $d\Omega_2^2 = d\theta^2 + \sin^2\theta d\phi^2 \to (d\bar{\theta}^2 + \bar{\theta}^2 d\bar{\phi}^2)/\lambda^2$. The quantity in brackets is the flat planar metric in polar coordinates; let $\bar{x}, \bar{y}$ be the corresponding Cartesian coordinates. Then in the limit $\lambda \to \infty$ the metric and scalar (7.2.12) become[8]

$$ds^2 = -\bar{V}\, d\bar{t}^2 + \frac{1}{\bar{V}} d\bar{\rho}^2 + \bar{W}(d\bar{x}^2 + d\bar{y}^2)\,, \qquad y = \sqrt{\frac{\bar{u}_0 + \bar{\rho}}{\bar{u}_1 + \bar{\rho}}}\,, \tag{7.3.45}$$

where

$$\bar{V} = \frac{2\,\bar{r}_+\bar{\rho} + (\bar{u}_0 + \bar{\rho})(\bar{u}_1 + \bar{\rho})^3 - \bar{u}_0\bar{u}_1^3}{\sqrt{(\bar{u}_0 + \bar{\rho})(\bar{u}_1 + \bar{\rho})^3}}\,, \quad \bar{W} = \sqrt{(\bar{u}_0 + \bar{\rho})(\bar{u}_1 + \bar{\rho})^3}\,. \tag{7.3.46}$$

In fact the original spherical solution differs from this one only in that we have dropped a term $\bar{\rho}^2/\lambda^2$ in the numerator of $\bar{V}$. Under this scaling we have $M \sim \lambda^3$, $Q_0 \sim \lambda^2$, $P_1 \sim \lambda^2$, $\phi_I \sim \lambda$, $T \sim \lambda$. In the global phase diagram discussed in section 7.3.3, the planar limit thus corresponds to going along diagonal rays out to infinity. Analogous to (7.3.44) we can introduce barred quantities for these physical variables. These actually satisfy largely the same relations as the unbarred quantities in section 7.3.3, except that the constant $+1$ drops out in the relation between ϕ_I and Δ_I in

[8] Explicit factors of ℓ or v do not appear here because we are still working in the rescaled invariant coordinates of section 7.2.5, including for the metric and coordinates.

(7.3.38), and that the lower order terms drop out in the expression for the mass in (7.3.41), so that in fact $\bar{M} = -\bar{r}_+ = -2\bar{F}$. Since the mass must be positive, the free energy of planar black holes must be negative. Similarly, in (7.3.34), the quadratic terms u_0^2 and u_1^2 under the square roots in the expressions for the potentials drop out in the planar limit.

The gauge potentials (7.2.19) remain unchanged, apart from the small θ expansion:

$$\bar{A}^0 = \bar{\phi}_0\big(\frac{\bar{u}_0}{\bar{u}_0+\bar{\rho}} - 1\big)d\bar{t} \qquad \bar{A}^1 = -\frac{1}{4}\bar{P}_1\bar{\theta}^2 d\bar{\phi}\,, \tag{7.3.47}$$

$$\bar{B}_0 = -\frac{1}{4}\bar{Q}_0\bar{\theta}^2 d\bar{\phi}\,, \qquad \bar{B}_1 = -\bar{\phi}_1\big(\frac{\bar{u}_1}{\bar{u}_1+\bar{\rho}} - 1\big)d\bar{t}\,. \tag{7.3.48}$$

Here we used the relations (7.2.21), $Q_0 = u_0\phi_0/3$ and $P_1 = 4u_1\phi_1$. Note that in the planar limit we get (by construction) an additional scaling symmetry $\bar{X} \to \lambda^{n_3}\bar{X}$ besides those listed in section 7.2.5, with scaling exponents k given by

	v	ℓ	$\bar{r}_+$	$\bar{u}_0$	$\bar{u}_1$	$\bar{M}$	$\bar{Q}_0$	$\bar{P}^1$	$\bar{S}$	$\bar{T}$	$\bar{\phi}_0$	$\bar{\phi}_1$	$\bar{\rho}$
n_3	0	0	3	1	1	3	2	2	2	1	1	1	1

This scaling is that of a CFT in a 2d box of fixed size L, in the limit that T and the ϕ_I are all much larger than the IR cutoff $1/L$ imposed by the box. Thermodynamic quantities will only depend nontrivially on scale invariant ratios. This allows us to plot the full planar phase diagram in terms of the two scale-invariant variables, for example T/ϕ_0 and ϕ_1/ϕ_0 as shown in the panel on the right of figure 7.3.

7.3.6 Hyperscaling violating limits

Upon setting P_1/Q_0 or Q_0/P_1 to zero, as was the case for most degenerations discussed in section 7.3.3, our planar backgrounds reduce to the hyperscaling violating geometries studied in [213, 214, 215, 216, 217] and other recent works. These are

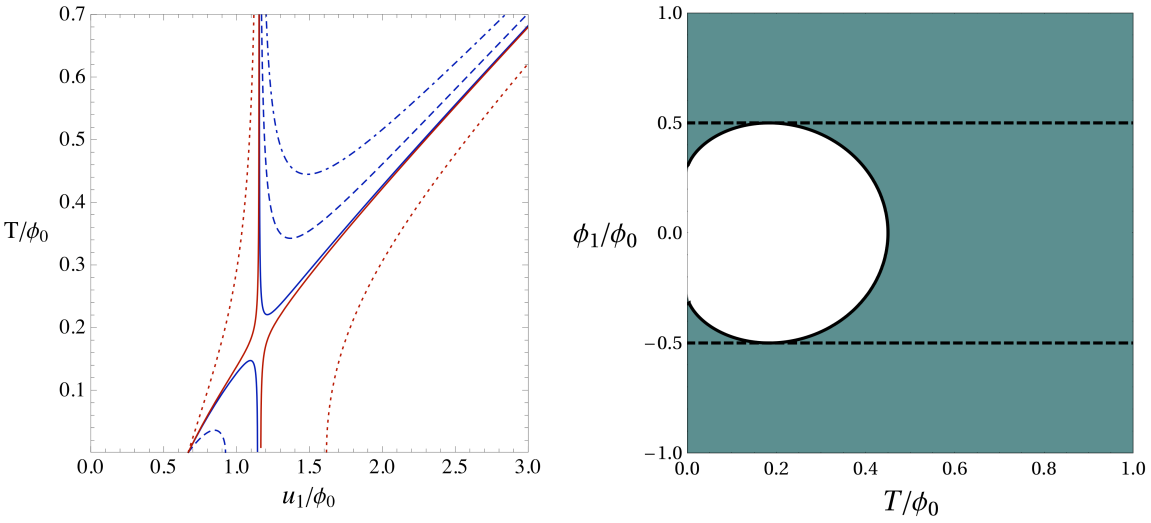

Fig. 7.3: **Left**: Planar black hole temperature T/ϕ_0 as a function of u_1/ϕ_0, using (7.3.39), for $\phi_1/\phi_0 = 0.1, 0.4, 0.495, 0.505, 0.7$, corresponding respectively to the dash-dotted, dashed and solid blue curves, and to the solid and dotted red curves. Lines of constant T/ϕ_0 intersect the curves in two points or not at all, illustrating that for given intensive variables, there are always either two black hole solutions or none at all. **Right**: Planar black hole phase diagram. The colored region has two black holes, the white has none. It corresponds to the gaps in accessible temperatures for the curves on the left. The dotted lines denote the Reissner-Nordstrom locus, where one of the planar solutions has no scalar hair. In the white gap, the background becomes unstable to soaking up Q_0 charge as discussed in remark 5 in the previous section.

characterized in general by a dynamic critical exponent z and a hyperscaling violation exponent θ, parametrizing the radial scaling behavior of the metric (cf. eq. (1.1) of [214]).

To see this, we fix the temperature T and use (7.3.34) to write $r_+ = -\frac{3}{2}u_0 u_1^2 -$

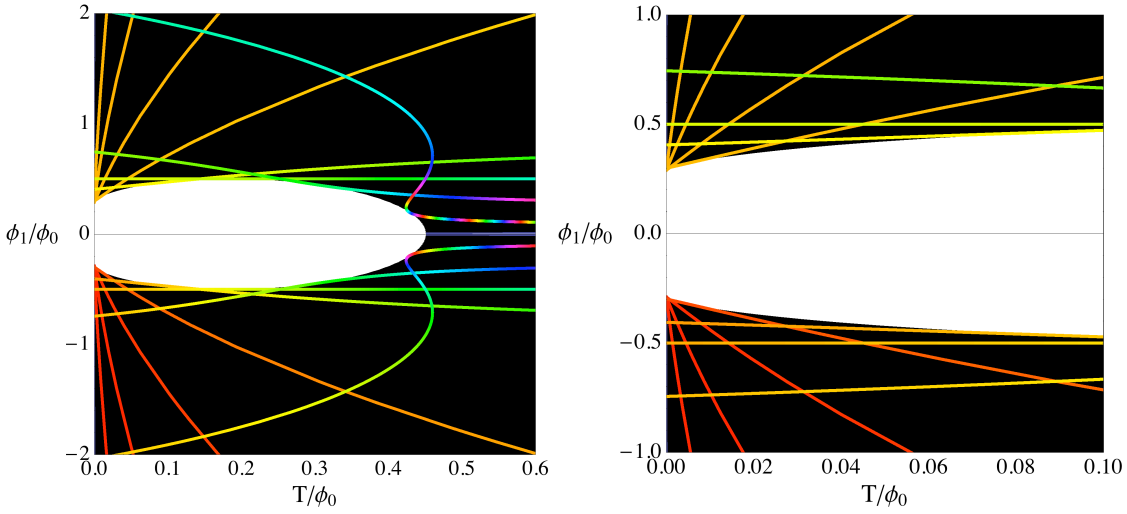

Fig. 7.4: Lines of constant charge for $\bar{P}^1 = 1$, $\pm\bar{Q}_0 = 10^{-5}, 10^{-4}, 10^{-3}, 10^{-2}, 10^{-1}, 1/6, 0.316, 1$, with the larger values of $|\bar{Q}_0|$ being closest to the $\phi_1 = 0$ axis at high temperatures. The value $\bar{Q}_0 = 1/6$ corresponds to the Reissner-Nordstrom solution. In the lower half of the plane, the hue of the lines goes up according to entropy (going up in red to yellow direction), while in the upper half of the plane, the mass (=free energy) is indicated in this way. At low temperatures the lowest values of $|\bar{Q}_0|$ have the lowest free energy and the lowest entropy. The stable and unstable branches connect at the boundary of the white gap.

$\frac{1}{2}u_1^3 + 2\pi T\sqrt{u_0 u_1^3}$, and obtain from (7.3.46)[9]

$$V = \frac{4\pi T\sqrt{u_0 u_1^3}\,\rho + 3(u_0 u_1 + u_1^2)\,\rho^2 + (u_0 + 3u_1)\,\rho^3 + \rho^4}{W}\,,$$

$$W = (\rho + u_0)^{1/2}(\rho + u_1)^{3/2}\,. \quad (7.3.49)$$

For finite nonzero u_0 and u_1, the solution is regular; in particular when $T = 0$ it has

[9]We drop the bars in the notation of planar quantities in this section.

an $AdS_2 \times \mathbb{R}^2$ near horizon geometry. However if we send $u_1 \to 0$ then for $\rho \ll u_0$:

$$ds^2 = -u_0^{1/2}\rho^{3/2}dt^2 + \frac{d\rho^2}{u_0^{1/2}\rho^{3/2}} + u_0^{1/2}\rho^{3/2}\left(dx^2+dy^2\right) \ , \qquad y = \sqrt{u_0/\rho} \ . \quad (7.3.50)$$

This is a hyperscaling violating geometry with $\theta = -1$ and $z = 1$. Similarly, if we send $u_0 \to 0$ then for $\rho \ll u_1$:

$$ds^2 = -3u_1^{1/2}\rho^{3/2}dt^2 + \frac{d\rho^2}{3u_1^{1/2}\rho^{3/2}} + u_1^{3/2}\rho^{1/2}\left(dx^2+dy^2\right) \ , \qquad y = \sqrt{\rho/u_1} \ . \quad (7.3.51)$$

This is a hyperscaling violating geometry with θ and z tending to infinity with the ratio $\eta \equiv -z/\theta = 1$ fixed. Notice that the above metric (7.3.51) is conformal to $AdS_2 \times \mathbb{R}^2$. These geometries were studied in the context of the $U(1)^4$ truncation of $\mathcal{N} = 8$ gauged supergravity in [218].

To see what this limit corresponds to in our phase diagram, we use (the planar limit of) (7.3.34), obtaining

$$\phi_0 = \frac{\sqrt{3}}{2}\sqrt{3u_1^2 - 4\pi T\sqrt{u_1^3/u_0}} \, , \qquad \phi_1 = \frac{\sqrt{3}}{4}\sqrt{u_1^2 + 2u_0u_1 - 4\pi T\sqrt{u_0u_1}} \, . \quad (7.3.52)$$

Combining this with (7.3.36) provides the charges $Q_0 = u_0\phi_0/3$ and $P_1 = 4u_1\phi_1$. Notice that for these expressions to be real, and therefore the solution to be physical, T must be bounded above for a given u_0, u_1. Specifically when $u_1 \to 0$, we need $4\pi T < \sqrt{u_0u_1} \to 0$ and when $u_0 \to 0$, we need $4\pi T < 3\sqrt{u_0u_1} \to 0$.

Thus, when $u_0 \to 0$ (metric (7.3.51)), we get $\phi_0 \propto u_1$, $\phi_1 \propto u_1$ and $T \propto \sqrt{u_0u_1}$, implying $T/\phi_0 \to 0$ while ϕ_1/ϕ_0 remains finite and tunable to any desired value satisfying $|\phi_1/\phi_0| > 1/\sqrt{12}$. Hence this limit corresponds to the zero temperature boundary in the phase diagram fig. 7.3. The charge ratio in this limit is $P_1/Q_0 \propto u_1/u_0 \to \infty$, that is the black hole becomes purely D4-charged in this limit.

Similarly, when $u_1 \to 0$, we get $\phi_1/\phi_0 \to \infty$, while T/ϕ_1 remains finite; this is the boundary at infinity in fig. 7.3. The charge ratio is $P_1/Q_0 \propto \sqrt{u_1/u_0} \to 0$; the black hole becomes purely D0-charged in this limit.

Besides the $u_0 \to 0$ solutions we just described, there are also regular $T = 0$ solutions with u_0 and u_1 finite that have $\mathrm{AdS}_2 \times \mathbb{R}^2$ near-horizon geometries. Their free energy is $F = -\frac{4}{3}\phi_0\phi_1^2 + \frac{1}{27}\phi_0^3$, whereas the free energy of the $u_0 = 0$ solution is $F = -\frac{16}{3\sqrt{3}}\phi_1^3$. Away from the boundary point $\phi_1/\phi_0 = 1/\sqrt{12}$, the latter is always lower than the former, so the hyperscaling-violating geometry is always thermodynamically preferred. At the boundary point, the two solutions coincide.

The entropy $S = \pi\sqrt{u_0 u_1^3}$ vanishes when $u_0 = 0$ or $u_1 = 0$. Hence we conclude that at $T = 0$, the system under study has vanishing entropy in its thermodynamically preferred state; it does not suffer from the entropy anomaly typical for Einstein-Maxwell setups with scalar-independent couplings.

7.4 Probe bound states

We now proceed to establish the existence of bound states of these black holes with suitably charged probes. The probes are assumed much heavier than the AdS scale, and in particular they can be black holes themselves, as long as they are much smaller than the length scales set by the background solution. We compute the probe potentials from (7.1.9); a local minimum indicates a bound state. We take the probe potential to be zero at the horizon, so negative/positive values of the potential energy indicate stable/metastable bound states. On the other hand, since the probes are massive, an escape to infinity would require an infinite amount of energy; the

global AdS metric acts as a confining box. This is a significant difference with the asymptotically flat case studied in chapter 6.

Most of our analysis is numerical. We provide some analytic results in the planar zero temperature limit in section 7.4.5.

7.4.1 Probe potential and validity of the approximation

Consider a probe with (D6,D4,D2,D0)-brane charge (p^0, p^1, q_1, q_0). In the spirit of section 7.2.5 it will be convenient to introduce rescaled charges

$$\hat{p}^0 = v^2 \frac{p^0}{g}\,, \quad \hat{p}^1 = v \frac{p^1}{g}\,, \quad \hat{q}_1 = \frac{q_1}{g}\,, \quad \hat{q}_0 = \frac{1}{v}\frac{q_0}{g}\,, \tag{7.4.53}$$

with g an at this point arbitrary constant. This differs from the rescaling used for the background black hole charges (7.2.29) in that there is no factor of N involved here; in its place we now have g, which we can think of as parametrizing the order of magnitude of the probe charges. We do this because we want to keep the quantized probe charges fixed and finite while taking the $N \to \infty$ limit. Notice that since charge is quantized in order 1 units in our conventions, the hatted probe charges are quantized in units given by the above scaling factors. At fixed finite v, these can be made arbitrarily small by taking g large, making the rescaled charges effectively continuous. Furthermore, ratios of probe to background charges, masses and length scales will involve the rescaled variables (tilde-variables for the background, hatted variables for the probes) and a universal overall factor $\frac{g}{N}$. For example $\frac{q_0}{Q_0} = \frac{g}{N}\frac{\hat{q}_0}{\tilde{Q}_0}$ and, using (7.1.11), $\frac{m_{p_0 D6}}{M} \sim \frac{g}{N}\frac{\hat{p}^0}{\tilde{M}}$. The discussion in section 7.1.3 implies that for order 1 rescaled probe charges, the probe black hole entropy will be of order $g^2 v^{-1}$, hence the ratio of its linear size over the AdS length scale will be of order $g v^{-1/2} \ell_p / \ell = \frac{g}{N}$.

Thus, for finite rescaled variables, the probe approximation will be justified provided $g \ll N$.

The static potential V_p obtained from (7.1.9) and the solutions described in section 7.2.1 consists of two parts, a gravitational part $V_{\rm grav}(r) = \sqrt{V(r)}\, m_\gamma(y(r))$ and an electromagnetic part $V_{\rm em} = q_I A^I - p^I B_I$. Explicitly

$$V_p = \frac{gN}{\ell v}\hat{V}_p\,, \qquad \hat{V}_p = \hat{V}_{\rm grav} + \hat{V}_{\rm em}\,, \tag{7.4.54}$$

with:

$$\hat{V}_{\rm grav} = \frac{\sqrt{3}}{2}\sqrt{(\rho(\rho+2r_+) + f_0 f_1^3 - u_0 u_1^3)\left[\left(\frac{\hat{p}_1}{2f_1} + \frac{\hat{q}_0}{f_0}\right)^2 + \frac{f_0}{f_1}\left(\frac{\hat{p}_0}{6\,f_1} - \frac{\hat{q}_1}{f_0}\right)^2\right]}\,, \tag{7.4.55}$$

and

$$\hat{V}_{\rm em} = -\frac{\phi_0 \hat{q}_0 \rho}{f_0} - \frac{\phi_1 \hat{p}^1 \rho}{f_1}\,, \tag{7.4.56}$$

where as before

$$f_0 = \rho + u_0\,, \quad f_1 = \rho + u_1\,, \quad \rho \equiv r - r_+\,. \tag{7.4.57}$$

The radial coordinate ρ vanishes at the horizon. In the above expressions, the background variables are understood to be rescaled as in section 7.2.5, but we have suppressed the tildes here.

In contrast to the background metric and scalar, the probe potential is qualitatively altered when flipping the sign of Q_0 or P^1. Because of this we have to consider both possible signs of ϕ_1/ϕ_0 separately. Notice however that we still have the following symmetry:

$$(\hat{p}^0, \hat{p}^1, \hat{q}_1, \hat{q}_0) \to (-\hat{p}^0, +\hat{p}^1, -\hat{q}_1, +\hat{q}_0)\,. \tag{7.4.58}$$

This allows us to assume $\hat{p}^0 \geq 0$ without loss of generality.

Finally let us check the claim made in section 7.1.3 that from the probe point of view the background temperature is effectively zero. The fraction of the probe's energy that is thermal when it has the same temperature as the background is, for order 1 values of the rescaled variables, $Ts_\gamma/m_\gamma \sim (g^2 v^{-1})/(gNv^{-1}) = g/N$, so again if $g \ll N$, the probe will effectively be extremal.

In what follows we will mostly drop the hats (and tildes) in our notation, which is equivalent to setting $\ell \equiv 1$, $N \equiv 1$, $v \equiv 1$, $g \equiv 1$. To restore the factors ℓ, N, v and g in equations, one should keep in mind the following scaling weights:

$$[\ell] = (1,0,0)\,, \qquad [v] = (0,1,0)\,, \qquad [N] = (1,\frac{1}{2},0)\,, \qquad [g] = (0,\frac{1}{2},1)\,. \quad (7.4.59)$$

The first two entries correspond to the weights (n_1, n_2) for background quantities given in section 7.2.5, the third one is nonzero only for quantities involving the probe; it is its overall multiplicative scale (because we are working to linear order for the probes, there is an additional scaling symmetry associated to scaling up the probe charge and mass). From this we see that for example the weights of the probe potential are $[V_p] = (0,0,1)$. We will restore the original factors in the concluding sections.

7.4.2 Thermodynamic interpretation

When a small probe charge is expelled from a black hole, the black hole entropy changes by an amount

$$\delta S_{\rm BH} = \frac{1}{T}\delta E_{\rm BH} - \frac{\phi_0}{T}\delta Q_{0,\rm BH} - \frac{\phi_1}{T}\delta P^1_{\rm BH}\,. \quad (7.4.60)$$

Here we used the microcanonical definitions of temperature and chemical potentials, taking into account that the potentials for D2 and D6 charge are zero. Conservation

of charge implies $\delta Q_{0,\mathrm{BH}} = -q_0$ and $\delta P^1_{\mathrm{BH}} = -p^1$. Conservation of energy implies $\delta E_{\mathrm{BH}} = -E_p^{\mathrm{tot}}$, where E_p^{tot} is the sum of the probe's rest mass energy plus the binding energy due to the probe-black hole interaction. Up to an additive constant E_0 this equals the natural total energy E_p obtained from the probe action given in section 7.1.3:

$$E_p^{\mathrm{tot}} = E_p + E_0\,, \qquad E_p \equiv V_p + E_p^{\mathrm{kin}}\,, \tag{7.4.61}$$

where V_p is the probe potential derived there, and E_p^{kin} is the probe kinetic energy. The additive constant E_0 is easily obtained by considering a probe at rest asymptotically far away from the black hole. In this case there is no binding energy so E_p^{tot} is just the probe's gravitational rest mass energy V_{grav}, defined in (7.4.55). On the other hand in this situation we have $E_p = V_p = V_{\mathrm{grav}} - q_0\phi_0 - p^1\phi_1$, as can be seen from (7.4.56). Hence $E_0 = q_0\phi_0 + p^1\phi_1$. Putting everything together, the constant term cancels with the other potential dependent terms in δS_{BH}, leaving us with the simple result

$$\delta S_{\mathrm{BH}} = -\frac{E_p}{T}\,, \tag{7.4.62}$$

where $E_p = V_p(\rho) + E_p^{\mathrm{kin}}$. The change in the total microcanonical entropy of the system for a given final state $|\alpha\rangle$ of the probe viewed as a particle (here α is a one particle state label which includes charge and energy E_p) is thus

$$\delta S|_\alpha = S_p - \frac{E_p}{T} \equiv -\frac{F_p}{T}\,, \tag{7.4.63}$$

where S_p is the probe's internal entropy. Recall that $V_p/T \propto \frac{gN}{v}$ while $S_p \propto \frac{g^2}{v}$, so in the probe limit $g \ll N$, the probe's internal entropy contribution to F_p is generically subleading.

In the planar limit it is also natural to take the system $\mathcal{S}$ of interest to correspond to a finite (but parametrically large) part of the xy-plane, with the remainder of the plane viewed as the reservoir. In this case, by definition, $\delta S_{\rm tot} = -\delta F_{\mathcal{S}}/T$, and (7.4.63) reduces to

$$\delta F_{\mathcal{S}} = F_p \,. \tag{7.4.64}$$

We can now take the system size to infinity, and view this as a formula for the change of total free energy in the grand canonical ensemble.

Thus, in equilibrium, the probability of finding a single probe in a given state α relative to the probability of having no probes is $e^{-F_\alpha/T}$. In particular we see that if the minimum of the probe potential is negative, ejecting such probes is thermodynamically preferred at large N, while if it is positive, swallowing them is preferred. If F_α is positive for all possible probe charges, we get a cold, exponentially dilute gas in the large N limit (so interactions can be neglected), with average occupation number of the 1-particle state $|\alpha\rangle$ given by

$$\langle N_\alpha \rangle = e^{-F_\alpha/T} \,. \tag{7.4.65}$$

Alternatively these occupation numbers can be obtained by considering the thermal atmosphere of the black hole as a statistical mechanical system in the grand canonical ensemble, with the black hole acting as a reservoir. We do not distinguish between Bose or Fermi statistics here because the gas is dilute (the average occupation number is e^{-N} suppressed).

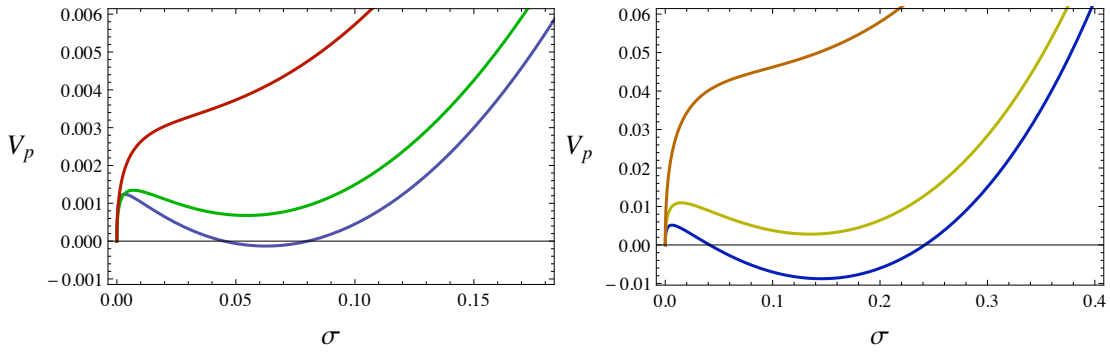

Fig. 7.5: Probe potentials at different temperatures for $\phi_1/\phi_0 = -0.49$ and $\phi_0 = 1.15$. The coordinate σ used here is defined as $\sigma \equiv \rho/(1+\rho)$. The plots are made for pure fluxed D6 probes. **Left**: $\kappa = 0.2908$ and the probe potential is plotted for $T = 0.01, 0.02$, and 0.04 for probes around the stable background. **Right**: $\kappa = 1.0566$ and the probe potential is plotted for $T = 0.01, 0.02$ and 0.06 for probes around the unstable background.

7.4.3 Probe bound states for spherical black holes

We will focus in particular on bound states with "pure fluxed D6" probes — these are probes with charges $\hat{\gamma} = (\hat{p}^0, \hat{p}^1, \hat{q}_1, \hat{q}_0)$ defined by expanding $e^{\kappa x} = 1 + \hat{p}^1 x + \hat{q}_1 x^2 - \hat{q}_0 x^3 + \mathcal{O}(x^4)$, i.e.:

$$\hat{\gamma} = \left(1, \kappa, \frac{\kappa^2}{2}, -\frac{\kappa^3}{6}\right) \qquad \rightsquigarrow \qquad \gamma = \frac{g}{v^2}\left(1, \kappa v, \frac{(\kappa v)^2}{2}, -\frac{(\kappa v)^3}{6}\right), \tag{7.4.66}$$

in other words $b = n = 0$ in the parametrization introduced at the end of section 7.1.3. Note that our charge quantizations then require (up to possible $O(1)$ factors or shifts):

$$g \in v^2\mathbb{Z}\,, \qquad \kappa \in \frac{1}{v}\mathbb{Z}\,. \tag{7.4.67}$$

(Recall $v^2 = N/k$.) Such probes can be thought of as wrapped D6-branes with world-volume flux $F_2 \propto \kappa v$ turned on, which lift to smooth, locally Taub-NUT "bubbling" geometries in M-theory [165, 169]. The motivation for this restriction is in part simplifying the search for bound states, and in part the observation made in chapter 6 that in the asymptotically flat case, at least in a large part of parameter space, these charges form bound states more easily than any other charge which has a single centered realization. Numerical explorations in the present setup confirm this, although we do not investigate this exhaustively.

The search for bound states proceeds by looking for local minima of $V_p = V_{\text{grav}} + V_{\text{em}}$ defined in equations (7.4.55) and (7.4.56), for all possible values of κ. This is done numerically. Note that $V_p = 0$ at the event horizon and therefore probe bound states with $V_p < 0$ are thermodynamically favorable configurations as explained in section 7.4.2. Thus, such bound states are stable, and conversely, local minima of the probe potential such that $V_p > 0$ are metastable to tunneling into the black hole. Some examples are shown in figure 7.5.

A universal feature we observe is that for any given (ϕ_0, ϕ_1) all bound states with fixed charges disappear at sufficiently high temperatures (depending on the probe charge). Intuitively the reason is clear: when the temperature is increased, black holes gain mass rather than charge, the gravitational pull becomes stronger, and eventually gravitational collapse is inevitable — the probe is pulled into the black hole.

We display the existence regions of probe bound states in figures 7.6-7.9 which correspond to slices of phase space where the background potentials satisfy $\phi_1/\phi_0 =$

$\pm 0.49\,, \pm 0.6$ and ± 1. The bound state existence regions have many common features which we describe below.

1. Bound states around the stable black hole background —the black hole with lowest free energy— are represented by the green and yellow regions with labels $(s\pm)$ in figures 7.6-7.9. The green $(s-)$ regions demarcate where stable bound states exist, in the sense that these bound states have negative potential energy. Metastable bound states live in the yellow $(s+)$ regions. Bound states around the unstable black hole background are shown in the orange $(u+)$ and blue $(u-)$ regions of our diagrams, with the $(u-)$ regions representing stable bound states and $(u+)$ regions labelling metastable bound states.

2. Recall that the probes are sensitive to the signs of ϕ_0 and ϕ_1. Figures 7.6, 7.7 and 7.9 are slices of phase space where the potentials satisfy, respectively, $\phi_1/\phi_0 = \pm 0.49\,, \pm 0.6$ and ± 1, with the minus sign holding in the left hand columns. When the potentials have opposite sign, there exist stable bound states between the probe and the black holes. As in chapter 6, in a small region, there also exist stable (negative energy) bound states when the potentials have the same sign. In this case the $(u-)$ bound states lie in a thin sliver below the lower dotted line (where Δ_1 changes sign). This happens for $\phi_1/\phi_0 > 1/2$ for arbitrarily high T.

3. The $(u\pm)$ regions disappear as we cross the lower dotted line from below. This is expected since the background to which the probes are bound have diverging charge as we cross the dotted line from below and stop existing altogether above

it. One caveat is shown in figure 7.6 where the $(u\pm)$ regions seep across the dotted line near the orange dot. These are probes bound to a black hole with negative free energy and are closer in nature to the bound state regions across the white gap than those across the dotted line. Naturally there are no bound states of type $(u\pm)$ above the dotted line when $\phi_1/\phi_0 > 1/2$ as we cross into a region where only one black hole exists.

4. While the $(u\pm)$ bound states generically disappear when crossing the lower dotted line from below, nothing analogous can be said for the $(s\pm)$ bound states above the dotted line as we cross it from above. Since nothing singular happens for the stable backgrounds as the lower dotted line is crossed, this matches with our expectations. A clear example of bound states dipping below the dotted line can be seen in the left hand column of figure 7.8.

5. When $|\phi_1/\phi_0| = 1$ there are no $(u\pm)$ regions above the dotted lines, even when the potentials have opposite signs. This should not be taken to mean that there are no bound states around the unstable black hole above the dotted line beyond a certain ratio of ϕ_1/ϕ_0. As in chapter 6, the disappearance of bound states may indicate that the favored probes for forming bound states are not pure fluxed D6 branes in this region of parameter space.

6. In all cases considered, the $(s+)$ regions open up at large ϕ_0. By this we mean that bound states at large chemical potential exist for larger values of T. This is consistent with the existence of a large region of $(s+)$ bound states in the planar limit as shown in section 7.4.4 below.

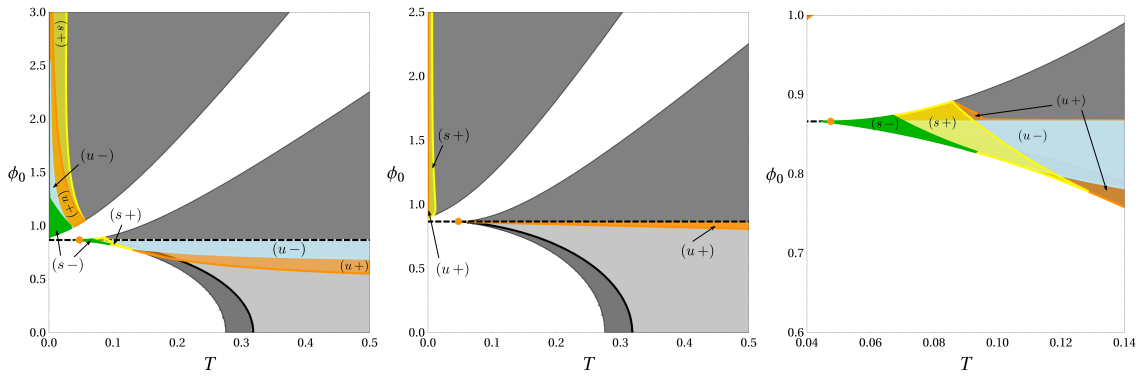

Fig. 7.6: Existence regions for probe bound states with background potentials set at $\phi_1/\,\phi_0 = \pm 0.49$, with the negative ratio in the left column. We label bound state regions with $(s/u\pm)$. A bound state region labeled s means it forms around the stable black hole and similarly, u regions represents probes bound to the unstable black hole. The $\pm$ denote whether the bound state has positive resp. negative potential energy. States with positive potential energy are unstable to tunneling into the black hole. The grayscale background echoes the background phase diagrams of section 7.3.3. The rightmost panel shows a close-up near the orange dot cusp for $\phi_1/\,\phi_0 = -0.49$. Notice that the top corner of the $(s+)$ region smoothly connects to the top corner of the $(u+)$ region. The top of the $(s-)$ region connects to the $(u-)$ region in the same way. This can be understood simply from continuity in the extensive variable u_1.

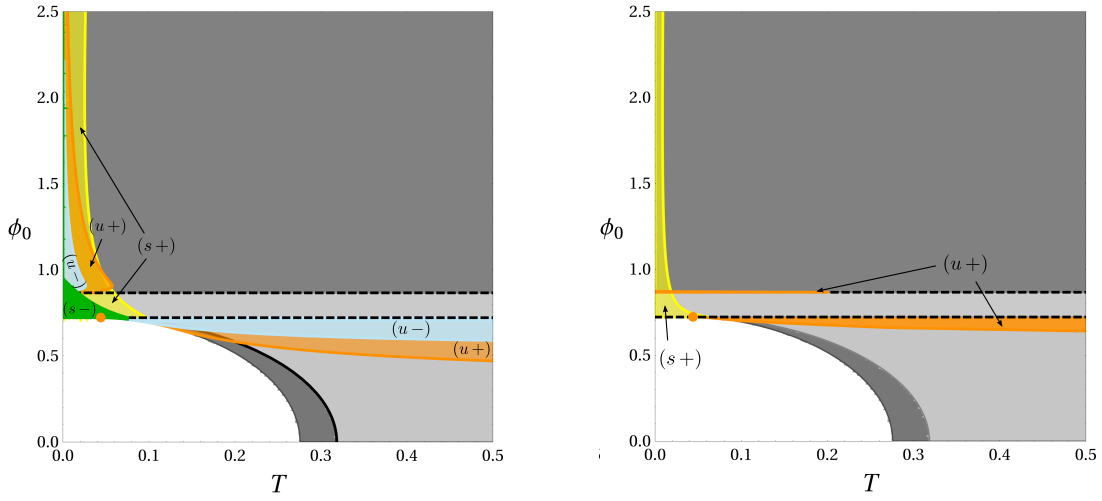

Fig. 7.7: Existence regions for probe bound states with $\phi_1/\phi_0 = \pm 0.6$, with the negative ratio being in the left column.

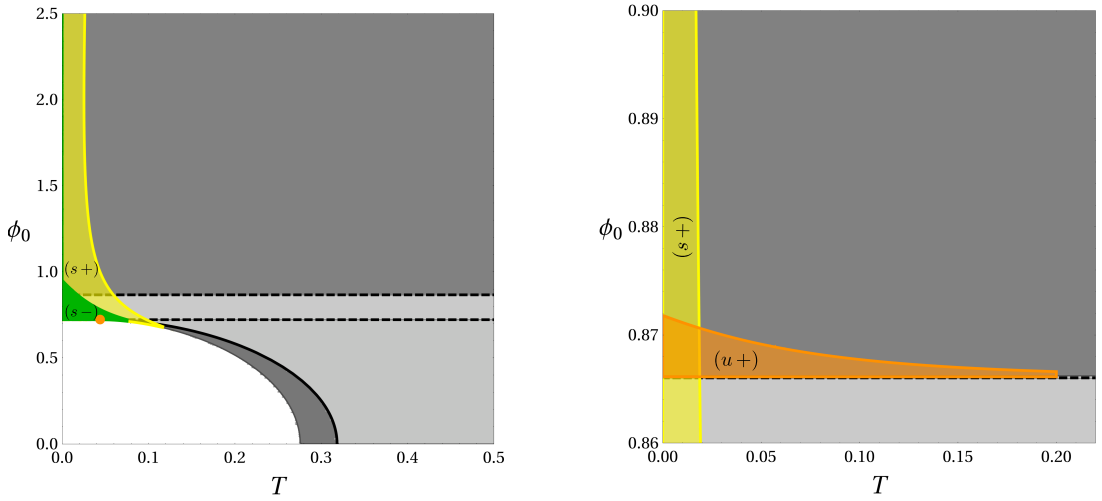

Fig. 7.8: **Left**: Probe bound states with $\phi_1/\phi_0 = -0.6$, around the stable background. Note that the $(s\pm)$ regions dip below the dotted line. **Right**: Zoom of the $(u+)$ bound states above the dotted line with $\phi_1/\phi_0 = 0.6$.

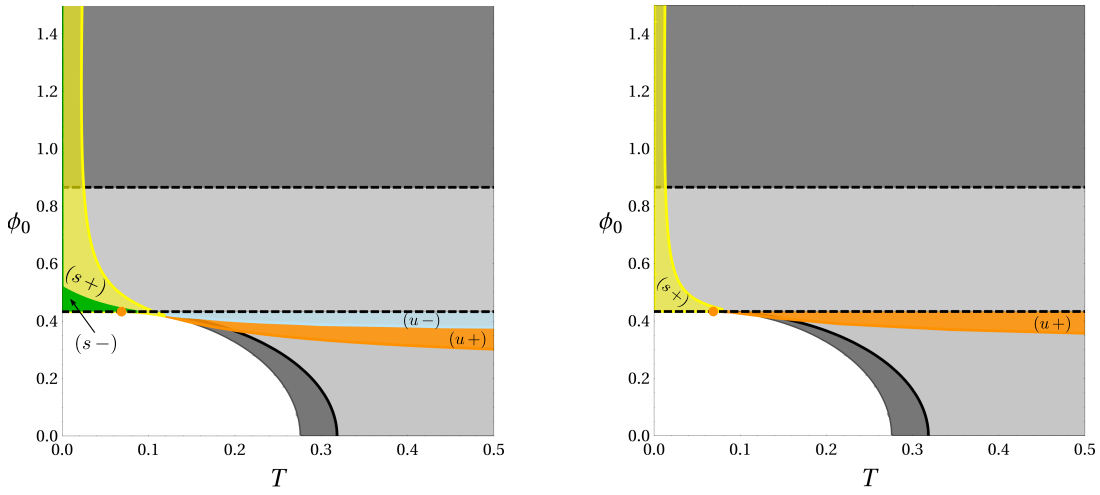

Fig. 7.9: Existence regions for probe bound states with $\phi_1/\,\phi_0 = \pm 1$, with the negative sign holding in the left hand column.

7.4.4 Probe bound states in the planar limit

One can obtain the probe potential in the planar limit (7.3.44) either directly from the probe particle action (7.1.9) or by scaling the parameters in (7.4.55-7.4.56). In the latter case one must be careful to divide by an overall factor of λ coming from the fact that we have scaled $dt = d\bar{t}/\lambda$ in the probe action. The planar black hole probe potential equals the spherical black hole potential except that the ρ^2 term under the square root disappears:

$$V_{\rm grav} = \frac{\sqrt{3}}{2}\sqrt{(2\rho r_+ + f_0 f_1^3 - u_0 u_1^3)\left[\left(\frac{p_1}{2f_1} + \frac{q_0}{f_0}\right)^2 + \frac{f_0}{f_1}\left(\frac{p_0}{6\,f_1} - \frac{q_1}{f_0}\right)^2\right]}\,, \quad (7.4.68)$$

and

$$V_{\rm em} = -\frac{\phi_0 q_0 \rho}{f_0} - \frac{\phi_1 p^1 \rho}{f_1}\,. \quad (7.4.69)$$

Here all background quantities should be understood as rescaled variables as in (7.3.44), but again to avoid cluttering we drop the bars here, referring to section 7.6.1 for a

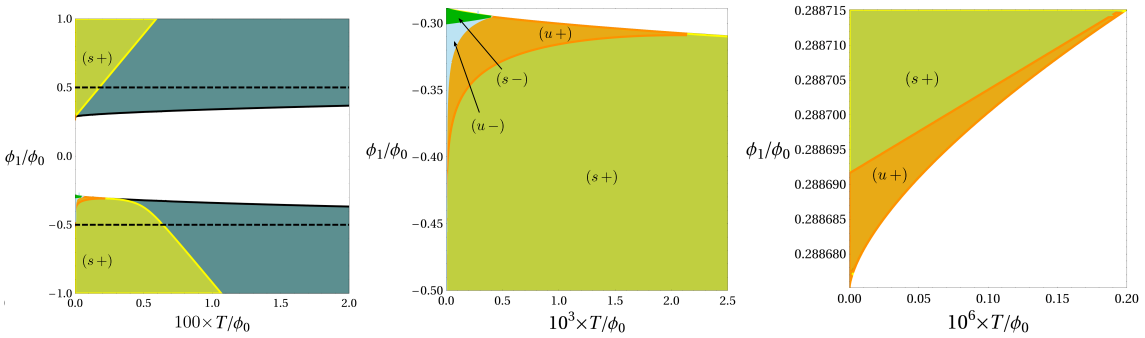

Fig. 7.10: Existence regions for planar bound states. The regions labeled $(s+)$ show bound states around the stable black brane with positive potential energy. If we zoom in closer to small T/ϕ_0 near the boundary of the white gaps, we see more interesting features as shown in the two rightmost panels. We find no evidence for $(u\pm)$ bound states below $\phi_1/\phi_0 < -1/2$, even when considering more general charges corresponding to b, $n \neq 0$ in the parametrization given at the end of section 7.1.3.

recap of how to restore the original scales. Because of the extra scaling symmetry discussed in section 7.3.5, we can scale out the appropriate powers of ϕ_0 from the various quantities occurring in the expression for the potential, reducing its dependence on ϕ_0 to an overall factor. Accordingly all nontrivial dependence of the probe potential on the electric potentials and temperature will be in terms of scale invariant quantities e.g. the ratios ϕ_1/ϕ_0 and T/ϕ_0. The bound state existence regions are shown in figures 7.10.

As expected from our spherical analysis, bound states with negative energy only exist when $\phi_1/\phi_0 < 0$. Bound states about the unstable black hole only live in a very thin sliver of parameter space for $\phi_1/\phi_0 > 0$.

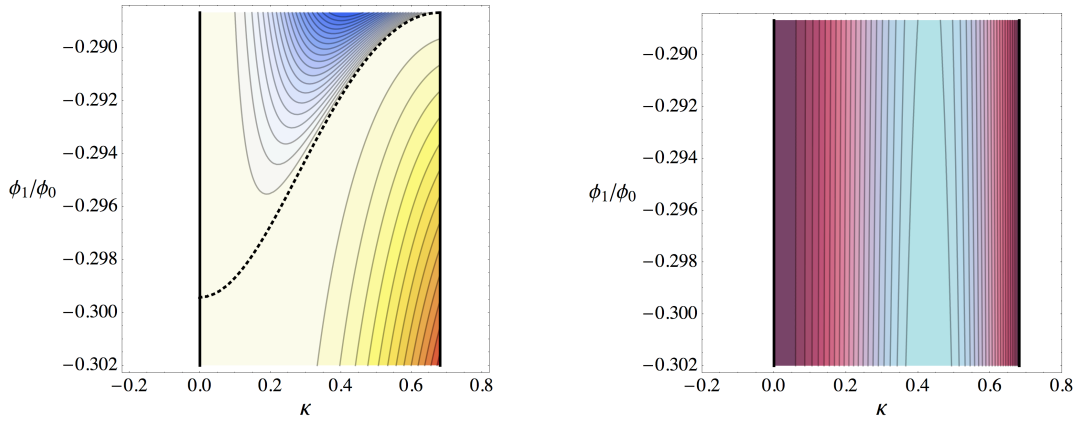

Fig. 7.11: **Left**: Minimal values of the potential as a function of probe charge parameter κ and background parameter ϕ_1/ϕ_0, computed using the expansion of V_p to second order in τ. The minima are negative above the dotted line, positive below. The lowest minimum attained for a given value of ϕ_1 is $V_{\rm min} \approx -4 \times 10^{-4}\phi_1$. **Right**: Separation $\rho_{\rm eq} = u_1\tau_{\rm eq}$ of the minimum from the horizon, where $u_1 = 4|\phi_1|/\sqrt{3}$. Lighter is further away. The rescaled separation $\tau_{\rm eq}$ only depends on κ, not on the potentials. The maximal separation is given by $\tau_{\rm max} \approx 0.025$; at the edge values of κ the separation drops to zero.

7.4.5 Analytic results for $T = 0$

In simple limits, it is straightforward to confirm our numerical results analytically. At zero temperature, the thermodynamically preferred planar solution is the $u_0 = 0$ solution discussed in section 7.3.6. In this limit the explicit probe potential for the charges (7.4.66) becomes quite simple:

$$V_p = \frac{\phi_0\kappa^3}{6} - \frac{\phi_1\,\kappa\,\tau}{1+\tau} + \frac{|\phi_1|}{3}\sqrt{(3+3\tau+\tau^2)\big(\kappa^2+\frac{\tau}{1+\tau}\big)^3}\,, \qquad \tau \equiv \rho/u_1\,, \quad (7.4.70)$$

with $u_1 = 4|\phi_1|/\sqrt{3}$. Expanded to first order at small τ, this becomes, say for $\phi_1 > 0$:

$$\frac{V_p}{\phi_1} = \frac{|\kappa|^3}{6}\left(\operatorname{sgn}\kappa \cdot \frac{\phi_0}{\phi_1} + \sqrt{12}\right) + \frac{|\kappa|}{\sqrt{12}}\left(|\kappa|^2 + 3 - \sqrt{12}\operatorname{sgn}\kappa\right)\tau + \mathcal{O}(\tau^2)\,. \quad (7.4.71)$$

Since we need $|\phi_1/\phi_0| \geq 1/\sqrt{12}$ to have a black hole solution, the zeroth order term is always nonnegative.[10] The first order term is negative if $0 < \kappa < \sqrt{\sqrt{12} - 3} \approx 0.68125$. In this case a bound state exists, which may have negative energy if ϕ_1/ϕ_0 is sufficiently close to $-1/\sqrt{12}$, This is illustrated in figure 7.11. These observations are consistent with the numerical results of figure 7.10.

We can repeat this analysis for the thermodynamically disfavored planar solution, again at $T = 0$. In this branch, $u_1 = 2|\phi_0|/3$ and $u_0 = \frac{|\phi_0|}{3}(12\phi_1^2/\phi_0^2 - 1)$. In this limit, V_p is slightly more complicated than (7.4.70), however expanded to first order in $\tau = \rho/u_0$ we find:

$$\frac{V_p}{|\phi_0|} = \left(-\frac{\kappa^3}{6} - \frac{\kappa}{2}\frac{\phi_1}{\phi_0}\left(12\tfrac{\phi_1^2}{\phi_0^2} - 1\right) + \frac{1}{24}\sqrt{\left(1 + 12\,\tfrac{\phi_1^2}{\phi_0^2}\right)\left(-1 + 2\,\kappa^2 + 12\,\tfrac{\phi_1^2}{\phi_0^2}\right)^3}\right)\tau + \mathcal{O}(\tau^2)\,. \quad (7.4.72)$$

If the coefficient of τ is negative in this expansion, then the potential admits a minimum with negative energy. It is straightforward to check that this only happens for a special range of values with $0 < \kappa < 1$ and $-1/2 < \phi_1/\phi_0 < -1/\sqrt{12}$ shown in figure 7.12. These results are consistent with those presented in figure 7.10.

The thick lines in figures 7.11 and 7.12 coincide with $\rho_{\text{eq}} = 0$ and represent the boundary of the allowed region of κs admitting bound states for a given ϕ_1/ϕ_0 at $T = 0$. Naturally, one might wonder if $\rho_{\text{eq}} = 0$ identically at the edges of the various

[10] The fact that this is nonzero is an artifact of the degenerate limit $u_0 \to 0$. At any finite u_0, the potential will drop to zero for $\rho \ll u_0$.

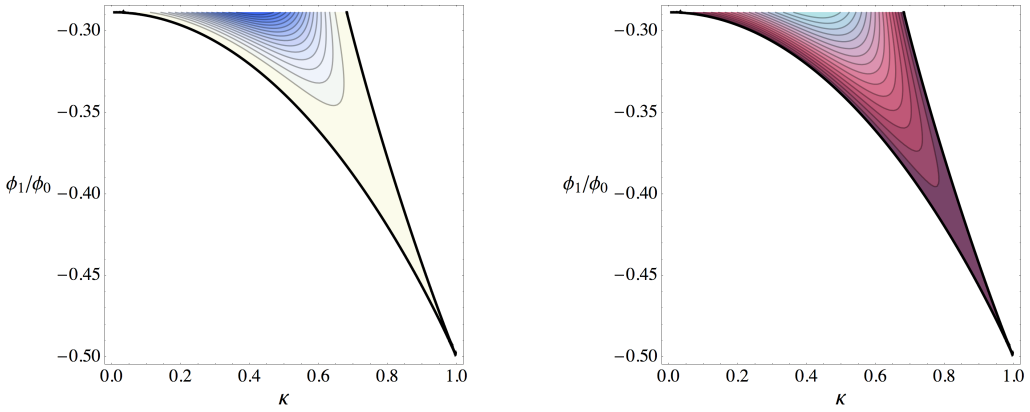

Fig. 7.12: **Left**: Minimal values of the potential as a function of probe charge parameter κ and background parameter ϕ_1/ϕ_0, using the expansion of V_p to second order in τ. Minima exist (and are negative) within the black curve. **Right**: Separation $\rho_{\rm eq} = u_0\tau_{\rm eq}$ of the minimum from the horizon. Lighter is further away, along the black curve the distance drops to zero.

$(s/u\pm)$ regions in figure 7.10. The answer is no. To show this, in figure 7.13 we plot $\rho_{\rm eq}$ as a function of T/ϕ_0 for fixed $\phi_1/\phi_0 = -0.297$ and -0.32 for the numerically found probe charge such that V_p is lowest at its minimum. Within the exitence region, $\rho_{\rm eq}$ never vanishes, remaining finite until the bound state disappears completely.

7.5 Small black holes, caged wall crossing and AdS-goop

7.5.1 Small black hole limit

Consider again the small black hole / asymptotically flat space limit discussed in section 7.3.4, more specifically the flat space BPS limit, i.e. $\Delta_0 = \epsilon\delta_0$, $\Delta_1 = \epsilon\delta_1$,

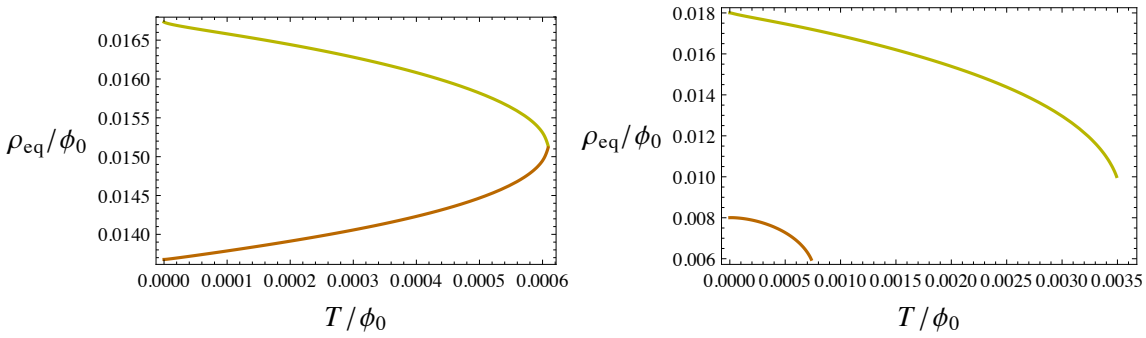

Fig. 7.13: **Left**: Equilibrium distances ρ_{eq}/ϕ_0 for $\phi_1/\phi_0 = -0.297$ with $\phi_0 > 0$. The upper curve shows bound state distances for probes bound to the stable black brane, the lower curve for probes bound to the unstable brane. The probe charge is chosen such that V_p is lowest at its minimum. The two curves meet at the boundary of the white region where the solutions degenerate. **Right**: Equilibrium distances ρ_{eq}/ϕ_0 for $\phi_1/\phi_0 = -0.32$ and $\phi_0 > 0$. Again the upper curve shows bound state distances for probes bound to the stable black brane. Note that ρ_{eq} never vanishes within the existence regions for bound states.

$\epsilon \to 0$, $\phi_0 \to \frac{\sqrt{3}}{2}$, $\phi_1 \to \frac{\sqrt{3}}{4}$. In this limit (7.3.39) is solved on the small black hole branch by

$$u_1 = \frac{\epsilon}{4\pi T}\sqrt{\delta_0 \delta_1}\,, \tag{7.5.73}$$

where T is the temperature in AdS units, which can take any finite value. Furthermore $r_+ = \frac{\epsilon^2}{4\pi T}\sqrt{\delta_0 \delta_1^3}$ and $u_0 = \frac{\epsilon}{4\pi T}\sqrt{\frac{\delta_1^3}{\delta_0}}$, and if we restrict to values of ρ of order ϵ, the probe potential is given by

$$V_p = \frac{\sqrt{3}}{2}\rho\left[\sqrt{\left(\frac{p_1}{2f_1}+\frac{q_0}{f_0}\right)^2 + \frac{f_0}{f_1}\left(\frac{p_0}{6\,f_1}-\frac{q_1}{f_0}\right)^2} - \left(\frac{p_1}{2f_1}+\frac{q_0}{f_0}\right)\right], \tag{7.5.74}$$

up to subleading terms at small $\epsilon \to 0$. This is minimized at $V_p = 0$ when $\frac{p_0}{6\,f_1} - \frac{q_1}{f_0} = 0$, or equivalently at $r \approx \rho = \rho_{\rm eq}$ where

$$\rho_{\rm eq} = \frac{\epsilon}{4\pi T}\sqrt{\frac{\delta_1}{\delta_0}}\frac{p_0\delta_1 - 6\,q_1\delta_0}{6\,q_1 - p_0} = \sqrt{12}\,\frac{p^0 Q_0 - q_1 P^1}{6\,q_1 - p_0}\,. \tag{7.5.75}$$

Returning to the original, non-rescaled variables, this becomes

$$\rho_{\rm eq} = \ell_p \frac{p^0 Q_0 - q_1 P_1}{q_1\sqrt{\frac{3}{v}} - p^0\sqrt{\frac{v^3}{12}}}\,, \tag{7.5.76}$$

reproducing the well known BPS equilibrium separation formula [104]. Bound states of this kind exist if $1 < \xi < \alpha$ or $\alpha < \xi < 1$, where $\alpha \equiv \frac{\Delta_1}{\Delta_0} = \frac{6\,Q_0}{P_1 v^2}$ and $\xi \equiv \frac{6\,q_1}{p_0 v^2}$ (restoring the original v dependence here to make the dependence on the scalar manifest). When $\xi \to 1$, the expression for $\rho_{\rm eq}$ given in (7.5.76) diverges. In the asymptotically flat case, this corresponds to decay at marginal stability, also know as wall crossing: the bound state disappears from the spectrum once ξ has crossed the wall. In the present case however, the divergence merely signals we exit the regime of validity of the small ρ approximation. Indeed, since AdS acts as an infinitely deep gravitational potential well, the true radius cannot diverge; instead when $\rho_{\rm eq}$ becomes

of order ℓ the bound state will start feeling the confining effect of AdS. We return to this below. When $\xi \to \alpha$, the bound state radius vanishes and the two centers merge. When $\alpha = 1$, the bound states around the small black hole disappear altogether. This is easy to understand: At this locus, the background solution reduces to the constant scalar Reissner-Nordstrom solution, and without running scalars, there cannot be a stable potential. We refer to chapter 6 for further discussion.

7.5.2 Confined wall crossing

When ρ is no longer restricted to order ϵ values and is allowed to get larger, the potential given in (7.5.74) — i.e. the probe potential in asymptotically flat space — is no longer accurate. Instead of the factor ρ, the gravitational part of the potential gets a factor $\sqrt{\rho^2+\rho^4}$. Thus the proper potential is $V_p = V_p(_{\text{above}}) + \delta V_p$, where the correction term is (still to leading order at small ϵ):

$$\delta V_p = \left(\sqrt{1+\rho^2}-1\right)\cdot\frac{\sqrt{3}}{2}\,\rho\sqrt{\left(\frac{p_1}{2f_1}+\frac{q_0}{f_0}\right)^2+\frac{f_0}{f_1}\left(\frac{p_0}{6\,f_1}-\frac{q_1}{f_0}\right)^2}\,. \tag{7.5.77}$$

When ρ is of order ϵ, this is a negligible correction. When $\rho \gg \epsilon$ on the other hand, we have $f_0 \approx f_1 \approx \rho$, and

$$\delta V_p \approx \left(\sqrt{1+\rho^2}-1\right)\frac{\sqrt{3}}{2}\sqrt{\left(\frac{p_1}{2}+q_0\right)^2+\left(\frac{p_0}{6}-q_1\right)^2}\,. \tag{7.5.78}$$

The quantity multiplying the ρ-dependent factor is nothing but the (rescaled) mass of the probe in the vacuum; that is, $\delta V_p \approx m_\gamma(\sqrt{1+\rho^2}-1)$. As alluded to earlier, the presence of this confining potential term is that no actual decay will happen when crossing the analog of a wall of marginal stability, i.e. when varying parameters such that we pass through $\xi \equiv \frac{6\,q_1}{p_0 v^2} = 1$ (from above or below depending on the ratio $\frac{\Delta_1}{\Delta_0}$).

However, something nontrivial does happen when ξ approaches 1. As long as ξ is bounded away from 1, the minimum of the potential $\rho_{\rm eq}$ will be of order ϵ. When ξ approaches 1, this will rapidly increase to a much large radius, and roughly stabilise there. At the same time, the local minimum will get lifted well above its near-BPS value, thus becoming metastable for decay back into the global minimum at $\rho = 0$. Eventually the local minimum may disappear altogether.

To get some intuition, let us use the following toy model for the potential:

$$V(\rho) = \left(\frac{\epsilon}{\rho} + \theta\right)^2 + \rho^2 \,. \tag{7.5.79}$$

The first term represents the flat space potential, the second term the AdS correction. This captures the typical behavior of the probe potential of interest quite well as long as ρ is well below 1 but not much smaller than ϵ. Now, as long as $\theta \ll -\epsilon$, there will be a local minimum near $\rho = -\epsilon/\theta$ (obtained by minimizing the first term at zero), with energy $V \sim \epsilon^2/\theta^2$ (from the correction). This corresponds to bound state of size ϵ, very close to its flat space BPS analog. When θ becomes positive, the flat space state disappears. In contrast, the full potential in AdS still has a local minimum, at $\rho \approx \theta^{1/3}\epsilon^{1/3}$, with an energy $V \sim \theta^2$ (for $\theta \gg \sqrt{\epsilon}$). These scalings with ϵ are consistent with numerical observations. Note however that this is entirely due to the gravitational trapping effect of AdS, the additional inter-particle interaction being now repulsive over the entire range of distances.

7.5.3 AdS supergoop

A natural question is how to generalize the two-particle black hole - probe picture developed so far to a system of $n > 2$ interacting dyonic particles in AdS. In asymp-

totically flat space with unbroken $\mathcal{N} = 2$ supersymmetry, at low energies and for well-separated dyons (which can be black holes, solitons or D-particles), a universal description is provided by a particular $\mathcal{N} = 4$ supersymmetric "quiver" quantum mechanics [103] as described in chapter 5 (see also [111, 112, 120, 121, 122, 123, 124, 125, 126, 127, 128, 129, 219, 220, 221, 222, 223]). The supersymmetry completely fixes the static potential and magnetic interactions up to a set of integers κ_{ij} equal to the symplectic product of the electromagnetic charges of particle pairs (i, j), $i, j = 1, \ldots, n$, and a set of real numbers θ_i determined by the charges and by vacuum moduli. In turn this completely determines the degeneracies of BPS bound states (which tends to be large due to the large Landau level degeneracies induced by the simultaneous presence of magnetic and electric monopole charges). Explicitly in flat space the n-particle static potential is of the form

$$V^{(n)}_{\rm flat} = \sum_{i=1}^{n} \frac{1}{2m_i} \left(\sum_{j=1}^{n} \frac{\kappa_{ij}}{2|\mathbf{x}_i - \mathbf{x}_j|} + \theta_i \right)^2 . \tag{7.5.80}$$

The magnetic interaction is of Dirac monopole form and completely determined by the κ_{ij}; we refer to [103]) for details.

In AdS we do not have the same bulk supersymmetry structure, and hence it is not obvious what the appropriate generalization should be. However the considerations made in section 7.5.2, as well as more elementary considerations regarding the effective Newtonian description of nonrelativistic particles confined to global AdS, suggest the following simple modification of the static potential:

$$V^{(n)}_{\rm AdS} = V^{(n)}_{\rm flat} + \sum_{i=1}^{n} \frac{1}{2} \frac{m_i \mathbf{x}_i^2}{\ell^2} , \tag{7.5.81}$$

where ℓ is the AdS length and $\mathbf{x}_i$ is the position of the i-th particle in isotropic

coordinates. Indeed this is the effective Newtonian potential one gets for a nonrelativistic probe particle moving in global AdS_4, when expanding the metric in isotropic coordinates,

$$ds^2 = \frac{-\left(1+\frac{\mathbf{x}^2}{4\ell^2}\right)^2 dt^2 + d\mathbf{x}^2}{\left(1-\frac{\mathbf{x}^2}{4\ell^2}\right)^2} \ , \tag{7.5.82}$$

at small velocities and small potential energies. Isotropic coordinates are appropriate here, as they allow us to keep the translationally invariant flat space expressions for the static and magnetic interaction potentials.

It would be interesting to study dynamical aspects of this system, along the lines of the analogous flat space study of [220]. Due to the magnetic interactions, the dynamics has rather peculiar properties, with magnetic trapping, dynamical rigidity and precession drift being some of the more striking features. A key differences with the flat space system is that supersymmetry is broken. At the classical level one expects the high-dimensional moduli space to get lifted; at the quantum level one expects similarly the lowest Landau level to split up.

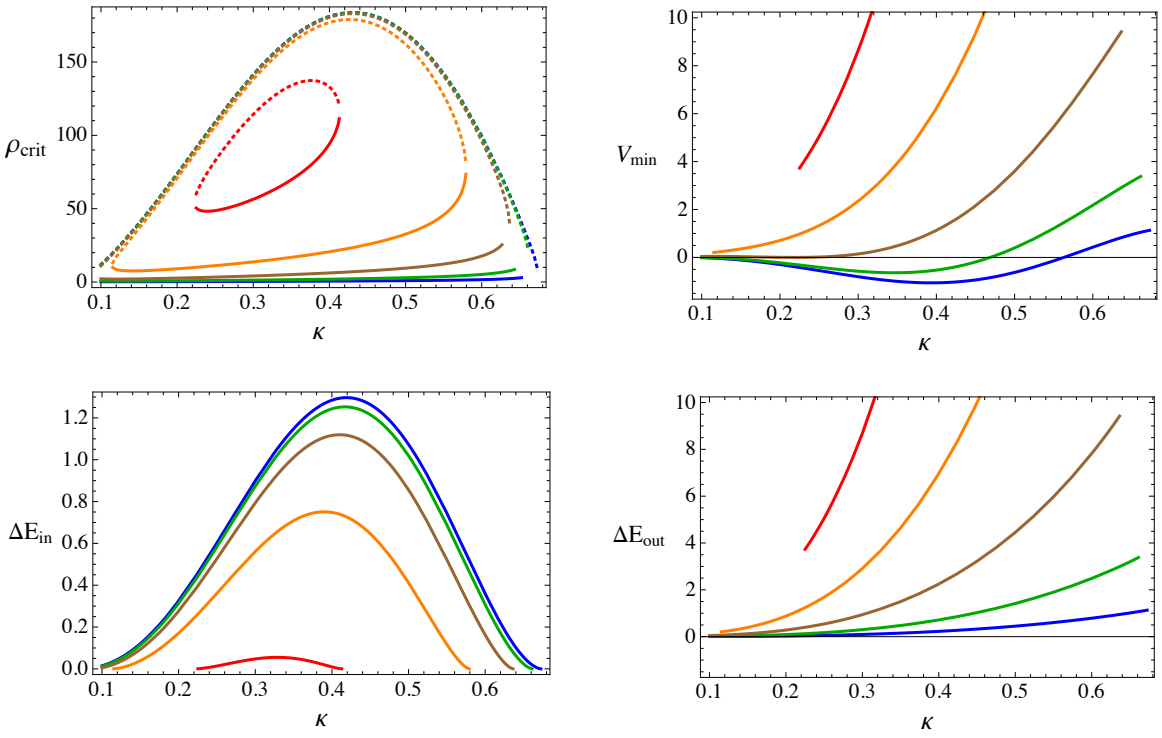
ρ_{crit}
150
100
50
0
0.1
0.2
0.3
0.4
0.5
0.6
κ
V_{min}
10
8
6
4
2
0
ΔE_{in}
1.2
1.0
0.8
0.6
0.4
0.2
0.0
ΔE_{out}

Fig. 7.14

Fig. 7.14 *(Continued)*: Here we show various features of the potential as a function of the probe charge parameter κ, for fixed $P^1 = 1$, $Q_0 = -10^{-3}$, and incremental values of M (or T). Parametrizing $M = (1+\delta)M_{\text{extr}}$ with $M_{\text{extr}} \approx 0.2205$ the minimal ($T = 0$) mass for the given charges, the blue, green, brown, orange and red curves correspond to $\delta = (10^{-8}, 10^{-7}, 10^{-6}, 10^{-5}, 10^{-4})$. The vertical axis is rescaled by a factor 10^4 in all four plots. **Top left**: positions of the local minimum (dotted) and of the top of the barrier separating it from the horizon (solid). **Top right**: values of the potential in the local minimum. **Bottom left**: Barrier height for absorption into the black hole. **Bottom right**: Barrier height for emission from the black hole.
We see the local minima lie at increasingly higher energies and become increasingly more shallow when the temperature is raised, until they eventually disappear. Note also that at low temperatures, charges with small κ do not minimize the energy of the local minimum (hence are not thermodynamically favored in equilibrium), but they do have the lowest and thinnest barriers to climb (hence their transition rates can be expected to be the fastest).

7.6 Holographic interpretation

In the previous sections we have demonstrated the existence of black hole bound states in the probe approximation. As long as the conditions for the probe approximation to be valid are met, i.e. $g \ll N$, there is no limit on the size, charge or number of bound black holes. In the large N limit, each of these configurations corresponds to a (generically metastable) macroscopic thermodynamic state, with individual black holes representing pockets of mutually thermalized degrees of freedom at different positions and scales. These need not be in equilibrium with each other, since they may have different temperatures and chemical potentials. Furthermore, generically, these individual configurations will not minimize the free energy. However as there are exponentially many of them, and equilibration over the space of configurations will typically be slow (as it requires tunneling or thermal activation of large objects), the existence of these configurations can be expected to have a large impact on the thermodynamic behavior of the system at finite time scales. This picture leads us to conjecture that in such phases, the system behaves as a glass.

As a first step to make this idea more precise, we now turn to a number of preliminary observations regarding the holographic interpretation of our results, assuming a dual CFT exists. For simplicity, and because it has the most straightforward thermodynamical interpretation, we will mainly comment on the planar limit. In this section we will make the distinction between rescaled variables introduced in section 7.2.5 and the original variables explicit again.

7.6.1 Holographic dictionary for background

The dual CFT has central charge proportional to

$$c \equiv \frac{\ell^2}{\ell_p^2} = \frac{N^2}{v}\,. \tag{7.6.83}$$

Spherical black holes are dual to thermal states of the CFT on a 2-sphere of some arbitrary radius R. Bulk energies in units of $1/\ell$ are identified with CFT energies in units of $1/R$; for example $\ell\, T = R\, T_{\rm CFT}$, $\ell\, \phi = R\, \phi_{\rm CFT}$, $\ell\, M = R\, E_{\rm CFT}$. Planar black holes are dual to thermal states on the infinite plane. They are obtained by zooming in on a small solid angle of the 2-sphere and taking the radius R of the 2-sphere to infinity while keeping the intensive variables fixed in the CFT. Indeed, defining $\lambda \equiv R/\ell \to \infty$, thermodynamic quantities will then scale with λ exactly as in the planar limit discussed in section 7.3.5. With this identification, the barred intensive thermodynamic variables introduced there are directly identified with their CFT counterparts: $T_{\rm CFT} = \frac{\ell}{R} T = \bar{T}$, $\phi_{\rm CFT} = \bar{\phi}$. The barred extensive quantities on the other hand get identified with planar densities of the CFT, upon multiplication by a factor $1/4\pi\ell^2$; for example the entropy density of the CFT, defined as the entropy per unit coordinate volume, is $s \equiv s_{\rm CFT} \equiv \frac{S}{4\pi R^2} = \frac{\bar{S}}{4\pi\ell^2}$, and the energy density is $e \equiv e_{\rm CFT} = \frac{\bar{M}}{4\pi\ell^2}$.

The CFT interpretation of the charges Q_0 and P^1 depends on the duality frame chosen in the bulk [224]. In our explicit bulk Lagrangian, we used a duality frame in which Q_0 is electric and P^1 is magnetic, but to streamline the discussion, and since we have been working throughout in a grand canonical ensemble with fixed dual potentials ϕ_0 and ϕ_1, we will for the purpose of holographic interpretations consider a duality frame in which both Q_0 and P^1 are considered electric. In this case the bulk

$U(1)$ gauge charges are identified with global $U(1)$ charges in the CFT. Denoting the associated charge densities by J_0^t and J_1^t, we have (for homogeneous planar solutions) the identifications $J_0^t = \frac{\bar{Q}_0}{4\pi\ell^2}$, $J_1^t = \frac{\bar{P}_1}{4\pi\ell^2}$.

In summary, CFT quantities are related as follows to the dimensionless, scaling invariant tilde-variables of section 7.2.5 (which we used for example in all the phase diagrams of the preceding sections):

$$T_{\rm CFT} = \frac{1}{\ell}\,\tilde{\tilde{T}}\,, \qquad \phi_{0,\rm CFT} = \frac{N}{v^2\ell}\,\tilde{\tilde{\phi}}_0\,, \qquad \phi_{1,\rm CFT} = \frac{N}{\ell}\,\tilde{\tilde{\phi}}_1\,, \tag{7.6.84}$$

and

$$s = \frac{N^2}{v}\frac{\tilde{\tilde{S}}}{4\pi\ell^2}\,, \qquad e = \frac{N^2}{v\ell}\frac{\tilde{\tilde{M}}}{4\pi\ell^2}\,, \qquad J_0^t = Nv\frac{\tilde{\tilde{Q}}_0}{4\pi\ell^2}\,, \qquad J_1^t = \frac{N}{v}\frac{\tilde{\tilde{P}}^1}{4\pi\ell^2}\,, \tag{7.6.85}$$

where for example $\tilde{\tilde{S}} = \pi\sqrt{\tilde{\tilde{u}}_0\tilde{\tilde{u}}_1^3}$. Transport coefficients are easily obtained by making use of the general formulae of e.g. [55]. The D0-charge DC conductivity σ_0, susceptibility Ξ_0 and diffusion coefficient D_0 are:

$$\sigma_0 = \frac{y_{\rm hor}^3}{12\pi} = \frac{v^3}{12\pi}\frac{\tilde{\tilde{u}}_0^{3/2}}{\tilde{\tilde{u}}_1^{3/2}}\,, \qquad \Xi_0 = \frac{J_0^t}{\phi_{0,\rm CFT}} = \frac{v^3}{12\pi\ell}\,\tilde{\tilde{u}}_0\,, \qquad D_0 = \ell\,\frac{\tilde{\tilde{u}}_0^{1/2}}{\tilde{\tilde{u}}_1^{3/2}}\,. \tag{7.6.86}$$

Here we made use of (7.3.36) and the explicit expressions for metric and scalar given in (7.3.45). Similarly the D4-charge transport coefficients are

$$\sigma_1 = \frac{1}{\pi y_{\rm hor}} = \frac{1}{\pi v}\frac{\tilde{\tilde{u}}_1^{1/2}}{\tilde{\tilde{u}}_0^{1/2}}\,, \qquad \Xi_1 = \frac{J_1^t}{\phi_{1,\rm CFT}} = \frac{1}{\pi v\ell}\,\tilde{\tilde{u}}_1\,, \qquad D_1 = \ell\,\frac{1}{\tilde{\tilde{u}}_0^{1/2}\tilde{\tilde{u}}_1^{1/2}}\,. \tag{7.6.87}$$

The charge transport coefficients satisfy the Einstein relation $\sigma = \Xi D$, as they should [55]. As always (in single black hole setups at finite temperature), the viscosity is given by $\eta = s/4\pi$. The expressions given above imply various relations, for instance $s = \frac{c}{4\sqrt{D_0 D_1^3}}$.

To give a simple fully explicit (albeit degenerate) example, consider the hyperscaling violating limit (7.3.51), at $T = 0$, $\tilde{\bar{\phi}}_0/\tilde{\bar{\phi}}_1 = \sqrt{12}$, i.e. at the boundary of the existence region in figure 7.3. Denoting $u \equiv \tilde{\bar{u}}_1$, we have $\tilde{\bar{\phi}}_1 = \frac{\sqrt{3}}{4}u$, $\tilde{\bar{\phi}}_0 = \frac{3}{2}u$, so

$$T_{CFT} = 0\,, \qquad \phi_{0,CFT} = \frac{N}{v^2\ell}\cdot\frac{3}{2}\,u\,, \qquad \phi_{1,CFT} = \frac{N}{\ell}\cdot\frac{\sqrt{3}}{4}\,u\,, \tag{7.6.88}$$

and

$$s = 0\,, \qquad e = \frac{N^2}{v\ell}\cdot\frac{1}{4\pi\ell^2}\cdot\frac{u^3}{2}\,, \qquad J^t_0 = 0\,, \qquad J^t_1 = \frac{N}{v}\cdot\frac{1}{4\pi\ell^2}\cdot\sqrt{3}\,u^2\,, \tag{7.6.89}$$

while the metric and scalar are given by

$$ds^2 = -3\sqrt{\frac{u\bar{\rho}^3}{\ell^3}}\,d\bar{t}^2 + \frac{d\bar{\rho}^2}{3\sqrt{\frac{u\bar{\rho}^3}{\ell^3}}} + \sqrt{\frac{u^3\bar{\rho}}{\ell}}\left(d\bar{x}^2 + d\bar{y}^2\right)\,, \qquad y = v\sqrt{\frac{\bar{\rho}}{u\ell}}\,. \tag{7.6.90}$$

In this limit the D0-charge transport coefficients vanish while the D4 conductivity and diffusion coefficient diverge.

7.6.2 Holographic dictionary for bound states

We now turn to the holographic interpretation of the black hole bound states. Consider first the case of pure Maxwell electrodynamics with Lagrangian $\mathcal{L} = -\frac{1}{8\pi\gamma}F_{\mu\nu}F^{\mu\nu}$, and a particle with q units of electric charge at rest in a fixed planar empty AdS background, i.e. in a metric $ds^2 = \ell^2\frac{-dt^2+dz^2+dx^2+dy^2}{z^2}$ (where $z \equiv \ell^2/\rho$). Without loss of generality we can assume the particle to be at $(x, y, z) = (0, 0, z_p)$. Since the metric is conformally flat and Maxwell's equations are conformally invariant, the electromagnetic field is identical to the field produced by a particle at rest in flat space. The electrostatic potential satisfies Dirichlet boundary conditions at the plane $z = 0$, that is $A_t = 0$ and hence $F_{tx} = F_{ty} = 0$ (or $E_\parallel = 0$) at $z = 0$. This is nothing but the

classic textbook problem of a charge in the presence of an infinite perfect conductor, solved most elegantly by the method of image charges. The potential is thus, with our charge conventions (compare to (7.1.5), (7.1.9) and (7.2.19)):

$$A_t = \frac{\gamma q}{2}\left(\frac{1}{\sqrt{(z-z_p)^2+x^2+y^2}} - \frac{1}{\sqrt{(z+z_p)^2+x^2+y^2}}\right). \tag{7.6.91}$$

The expectation value of the charge density in the dual CFT is given by the electric field strength at the boundary [225] (as is the induced charge density on the conducting plate in the classic electrostatics problem):

$$j^t = \frac{1}{2\pi\gamma}\, F_{zt}|_{z=0} = \frac{q z_p}{2\pi s^3}\,, \qquad s \equiv \sqrt{z_p^2+x^2+y^2}\,. \tag{7.6.92}$$

We fixed the normalization by requiring the density to integrate to the total charge q. The radius of the charge density peak is $R \sim z_p = \ell^2/\rho_p$.

Let us now consider instead a magnetically charged particle. Dirichlet boundary conditions on the vector potential imply $B_\perp \equiv F_{xy} = \partial_x A_y - \partial_y A_x = 0$; they forbid magnetic flux through the $z = 0$ boundary surface. The boundary conditions thus break electromagnetic duality: The magnetic field sourced by a magnetic charge, subject to the boundary conditions at hand, is not obtained by dualizing the electrostatic field 7.6.91, as this would give a magnetic field with $B_\parallel = 0$ instead of $B_\perp = 0$. Rather it is obtained by dualizing the electrostatic field of a point charge with boundary conditions $E_\perp = 0$. This can again be constructed by the method of image charges, but this time with an image charge $+q$ instead of $-q$. The nonvanishing components of the electromagnetic field strength at $z = 0$ are then $(F_{xt}, F_{yt}) = \frac{\gamma q}{s^3}(x, y)$. This dualizes to the magnetostatic fields $(F_{zx}, F_{zy}) = \frac{p}{s^3}(-y, x)$ where p is now the magnetic charge. In the CFT dual, this corresponds to a medium with zero net charge density

but with a nontrivial stationary vortex current,

$$(j^x, j^y) = \frac{p}{2\pi\gamma s^3}(-y, x)\,. \tag{7.6.93}$$

This can also be viewed as a "magnetization" current $j = \nabla \times m = (\partial_y m, -\partial_x m)$ where the magnetization density is

$$m = \frac{p}{2\pi\gamma s}\ . \tag{7.6.94}$$

In the context of two dimensional incompressible fluid dynamics (see e.g. [245]), m is called the stream function, and $\omega \equiv \nabla \times j = -\nabla^2 m$ is called the vorticity. The total current through a line from the origin to infinity is given by $m(\infty) - m(0) = \frac{p}{2\pi z_p}$.

Putting things together, we see that a general dyonic particle with charge (q, p) at $(x, y, z) = (0, 0, z_p)$ will correspond to a charge density $j^t = \frac{q z_p}{2\pi s^3}$ and a magnetization density $m = \frac{p}{2\pi\gamma s}$.

Applying this to our model with the D0 and D4 charges considered to be electric charges (and the scalar kept fixed), we see from (7.1.5) that we have $\gamma_0 = \gamma_{D0} = \frac{6}{v^3}$ and $\gamma_1 = \gamma_{D4} = \frac{v}{2}$. Hence for an arbitrary probe charge (p^0, p^1, q_1, q_0), we get, in the notation (7.4.53): the following D0 and D4 charge and magnetization densities:

$$j_0^t = \frac{g v z_p}{2\pi s^3}\,\hat{q}_0\,, \qquad j_1^t = \frac{g z_p}{2\pi v s^3}\,\hat{p}^1\,, \tag{7.6.95}$$

$$m_0 = \frac{g v}{12\pi s}\,\hat{p}^0 \qquad m_1 = \frac{g}{\pi v s}\,\hat{q}_1\,, \tag{7.6.96}$$

where we recall $s = \sqrt{z_p^2 + x^2 + y^2}$. Note that under the symmetry (7.4.58), the magnetizations flip sign, while the charge densities remain invariant.

For typical values of $\tilde{\rho}_p = \rho_p/\ell$, i.e. order 1 or smaller, z_p is of order ℓ or larger, causing the current density to be concentrated in a region of order ℓ or larger. The

charge density due to the probe will generically be much smaller than the background charge density (7.6.85) provided $g \ll N$, which, not surprisingly, was the condition for the probe approximation to be valid. However since the background magnetization was zero, the magnetizations and corresponding spatial currents are entirely due to the probe.

Probes located at different positions will produce these currents appropriately translated in the (x, y)-plane, and multiple probes will produce currents which are superpositions of single probe currents. An example is shown in figure 7.15.

More generally, the probes will also source the scalar and the metric, which in the CFT corresponds to fluctuations in the expectation value of some scalar operator and in the energy-momentum tensor. This can be studied in a similar way but we will not do this here.

For global AdS, a similar analysis can be done, although we can no longer make use of the simple map to flat space electromagnetism, so the gauge field propagator will be somewhat more involved. We give the relevant expressions in appendix E.1. To get a solution involving magnetic charge which is also consistent with Dirichlet boundary conditions on the vector potential, the total magnetic charge must be zero (otherwise the magnetic flux through the boundary cannot be everywhere zero). In a dynamic setup, where we start off with a purely electrically charged black hole, this will be guaranteed by charge conservation.

A linearized analysis using the vacuum propagators for the supergravity fields would give fairly detailed information about the holographic dual of multi-dyon configurations in the AdS supergoop limit, when all particles involved are small. However

to treat the case of a large black hole with probe bound states, more work is needed, since even at the linearized level the propagators for the gauge and other fields are significantly affected by the background geometry. However one can expect the basic features outlined above to carry over. For example in the example illustrated in figure 7.11, we see that the probe separation ρ_p takes values in a range $[0, 0.025\, u\, \ell]$, with u as in (7.6.88). Defining as before $z_p \equiv \ell^2/\rho_p$, we thus get that z_p takes values in a range going from $z_p = \infty$ down to values of order $z_p^{\min} \sim \ell/u \sim N/\phi_{1,\text{CFT}}$. So in this regime the typical size of the current vortices and other features may reasonably be expected to be $r_{\text{feature}} \sim N/\phi_{1,\text{CFT}}$. Though reasonable, it is certainly not obvious, since the probes in this example are located inside a near-horizon throat, quite different from the asymptotic AdS geometries they connect to. Nevertheless on general grounds one expects a relation between the equilibrium separation of the probe in the bulk and the energy scale of the corresponding structure in the CFT. Indeed this can be seen more directly by considering the energy scale of the probe potential V_p and its relation to the probe equilibrium position ρ_p and some CFT energy scale, say $\phi_{1,\text{CFT}}$. Since these all scale with the same power of λ in the planar limit, their overall scales must be proportional. More explicitly, recalling that $\bar{V}_p = \frac{gN}{v\ell}\hat{\bar{V}}_p$, $\bar{\rho}_p = \ell\tilde{\bar{\rho}}$ and $\phi_{1,\text{CFT}} = \frac{N}{\ell}\tilde{\bar{\phi}}_1$, we see that up to factors depending only on the rescaled variables, we get the scale relations $\bar{V}_p \propto \frac{gN}{v\ell^2}\,\bar{\rho}_p \propto \frac{g}{v}\,\phi_{1,\text{CFT}}$.

We defer a more in depth analysis of the structure of the holographic dual to black hole bound states to future work. For now we conclude that probe bound states correspond to thermodynamic states with disordered, frozen regions characterized by changes in the charge density and most notably by (possibly metastable) persistent

currents. The total charge and current generated by each bound charge is proportional to g. Relative sizes of the two different charge densities and currents are set by the individual charges (which for a particular background will be constrained to a specific range). The spatial size and energy scales are set by the separation of the probe from the horizon; the closer to the horizon the lower the energy scale. There is in general an upper bound on the horizon separation and therefore an upper bound on the energy scale. Thus although localized in the bulk, the probes correspond to delocalized IR effects in the CFT, and the contributions of many different probes get superimposed onto each other. Local densities will therefore not significantly differ from the single black hole case. However dynamically one would expect things to differ substantially, due to the fact that the bound state structure packages degrees of freedom into pockets that only weakly interact with each other in the bulk. This we will be further discussed in section 7.7. When temperature is increased, the vortex/magnetization structures become increasingly less stable and one by one, over a range of temperatures, they decay; the currents drop to zero and the charge excesses melt away into the background.

7.6.3 String realizations?

It would of course be desirable to have an explicit dual CFT realization of all this. A first step towards this goal is to find an explicit bulk string realization. The model we have studied can be characterized as the bosonic sector of an $\mathcal{N} = 2$ Fayet-Iliopoulos gauged supergravity with cubic prepotential. The two massless $U(1)$s we have are sourced by charges which are parametrically heavier than the AdS scale —

they can be thought of as wrapped D0, D2, D4 and D6 branes in type IIA.

In the flat space limit, this model is a universal subsector of any type IIA Calabi-Yau compactification, providing a consistent truncation of the corresponding four dimensional effective theories. It would therefore seem logical that it should be equally easy to embed the AdS version of the model in string theory. In particular, flux compactifications such as type IIA on $\mathbb{CP}^3$ with N units of RR 6-form flux and k units of RR 2-form flux through the $\mathbb{CP}^3$ (this one specifically being dual to the ABJM quiver Chern-Simons CFT [190]), or related compactifications [226, 227, 228, 229, 230, 232, 233, 234, 235, 236, 237], would appear to be natural candidates.

However there is a general obstruction to this idea. Any $\mathrm{AdS}_4 \times M_6$ Freund-Rubin compactification of type IIA string theory which is supported by magnetic RR 6-form flux (plus any other fluxes) — i.e. any IIA theory which is holographically dual to a theory involving D2-branes (plus any other branes) — will have the property that some linear combination of the $U(1)s$ obtained by naively reducing the RR potentials coupling to wrapped D-branes is in fact Higgsed and thus massive. The mechanism for this was exhibited explicitly for $\mathbb{CP}^3$ e.g. in [190], and it can be argued in general as follows. When a $U(1)$ is Higgsed, magnetic monopole charges necessarily come with confining strings attached. They are magnetic flux lines squeezed together by the Meissner effect. In the present context, the Higgs field is the universal 4d dilaton-axion, and the corresponding flux strings are actually fundamental strings. And indeed in the presence of N units of RR 6-form flux on M_6, a D6 wrapped on M_6 must come with N fundamental strings attached, and similarly a D2-brane wrapped on a 2-cycle threaded by k units of 2-form flux must come with k fundamental

strings attached. This follows directly from integrating the Maxwell equations for the worldvolume $U(1)$ gauge field on the D-branes: Without the additional strings there would be an uncanceled tadpole. This shows that a $U(1)$ coupling to these charges has become massive. For particular combinations of D6- and D2-charges, the tadpoles will cancel, but generically they will not and in any case it will not be possible to increase for example just the D6-charge at will, in contrast to the situation in the model we considered.

Thus, in such setups, one of the $U(1)s$ we have presumed massless will actually be massive. This will cause generic probes to come with strings attached (stretched from the horizon to the probe), and it will cause the massive photon to decay exponentially rather than polynomially. It can be checked that generically these "stringy" effects scale in exactly the same way as the other forces we considered. For example the probe potential (7.4.54) for a D6 is $V_p \propto \hat{p}^0 gN/v\ell$ (times something of order 1). A single D6 means $p^0 = 1$, which by (7.4.53) implies $\hat{p}^0 = v^2/g$, so we conclude $V_p \propto Nv/\ell$. On the other hand, a string stretched over a coordinate distance $\Delta\rho$ would have an energy (w.r.t. our t-coordinate) of order $E_s \sim \Delta\rho/\ell_s^2 \propto v/\ell$ (times something of order 1, assuming $\Delta\rho/\ell$ is of other 1). But by the above arguments, a single D6 comes not with one, but with N strings attached. Hence $E_s \propto Nv/\ell$, the same scaling as the potential. This turns out to be the case for various other similar comparisons of scales. We conclude that in these models, the features we have exhibited are not obviously obliterated, nor are they obviously preserved.

There are of course compactifications which can consistently be truncated to the model we consider. The simplest case in perhaps M-theory on $\mathrm{AdS}_4 \times S^7$, which

corresponds to the case $k = 1$ of the IIA $\mathbb{CP}^3$ compactification considered above. The problem with these is that they have very light charged matter, with masses of the order of the AdS scale, which will tend to condense and form superconducting condensates [184, 185]. This would again qualitatively affect our discussion. To physically trust our model, we need all charged matter to be parametrically heavy, which in at least the simpler examples means charges should be wrapped D-branes in a type II picture; in the usual Freund-Rubin compactifications, towers of charged KK modes tend to have masses going all the way down to the AdS scale [241].

Borrowing language originating from the study of AdS_5 - CFT_4 pairs [238, 239, 240], we might call such heavy charges "baryonic". Indeed since it takes as many quarks as there are colors to make a baryon, states with nonzero baryon number in the CFT are guaranteed to be heavy. From the bulk dual point of view, baryons are heavy because they correspond to internally wrapped D- or M-branes. Similar considerations hold for the $AdS_4 \times Y_7$ - CFT_3 analogs [242, 243]. Examples are M-theory compactifications on Sasaki-Einstein manifolds with nonzero betti number, such as $Q^{111} = SU(2)^3/U(1)^2$, or quotients thereof [226, 228, 229, 230, 233, 234, 235, 236, 242, 243]. Although this comes closer, our model is again not quite a consistent truncation of the low energy effective action of such models [226, 228, 231]; there are additional light scalars involved, which again may be expected to qualitatively change the analysis.

It would be very interesting to follow a more direct top-down approach and see if bound states of the type we have found in our model (or variants thereof) persist in models with a UV completion in string theory.

7.7 Conclusions and outlook

Let us summarize our findings and the picture it suggests of the holographic dual of a structural glass.

7.7.1 Black hole bound states

Most of the this work was concerned with a complete analysis of the thermodynamic phases of a well-known class of charged AdS black holes with running scalars [183], and with establishing the existence of stationary bound states of such black holes with other charged black holes. These are the simplest generalization to AdS of the rich and extensively studied class of stationary BPS black hole bound states in ungauged $\mathcal{N} = 2$ supergravity, and of their (less studied) finite temperature counterparts. Our analysis was done in a probe approximation. The probe itself was allowed to be an arbitrarily large black hole, as long as the background black hole was much larger. Although these are not exact solutions, they do establish the existence of such solutions in the same way as the solution to the Kepler problem establishes the existence of a solution to Einstein's equations describing the Earth orbiting the Sun.

We found that bound states are ubiquitous at low temperatures, including in the planar limit. Some of these bound states are energetically stable (in which case they are also thermodynamically favored), while others are metastable to absorption by the black hole. This depends on the charges of the probe and the background and on the temperature. When a given bound state is heated up, it will always become metastable and eventually disappear altogether, as the probe is pulled into the background black hole. This is intuitive: increasing the temperature means increasing

the energy and hence the gravitational pull.

The intuition for the actual existence of bound states is somewhat more subtle. The presence of a nonminimally coupled scalar is crucial. Electrostatic forces by themselves are not sufficient. The electrostatic repulsion is maximized with respect to the gravitational attraction by choosing the charge of the probe black hole to be proportional to that of the background black hole and the temperature to be zero. In the asymptotically flat case, this situation leads to an exact cancelation between electrostatic repulsion and gravitational attraction; in all other cases the gravitational attraction wins. In AdS, there is an additional gravitational force pushing the black holes together, so even in the case of proportional charges, the gravitational attraction wins, and indeed no black hole bound states exist for pure Einstein-Maxwell in AdS. However, in the presence of nonminimally coupled scalars (i.e. scalar-dependent electromagnetic coupling constants), the situation changes, and stationary bound states can be formed with (say) an electrically charged black hole, provided the probe black hole has repulsive electric charge and, crucially, some magnetic charge. The required additional scalar-driven repulsive force can be understood as being due to a conflict of interest between electric and magnetic charges. Part of the energy of any charged black hole is electromagnetic. The electrostatic energy increases when the coupling constant increases, while the magnetostatic energy increases when the coupling is decreased. In an electrically charged background with a scalar dependent coupling constant, the scalar will thus be driven towards lower values of the coupling when approaching the black hole. A magnetically charged probe in such a background will therefore become heavier when moved towards the black hole. Under favorable

circumstances, this effect (combined with electrostatic repulsion) is strong enough to more than compensate for the increase in gravitational attraction by the black hole, and a net repulsive force can arise close to the black hole. Given the confining nature of AdS, there will therefore be a minimum of the potential somewhere, and we get a stationary black hole bound state.

This intuition is corroborated by the fact that for solutions without running scalars (i.e. on the Reissner-Nordstrom locus in parameter space), no bound states ever exist, and by the fact that we found no bound states with probes that do not have magnetic charge. It also fits the observation that bound states are formed most easily around backgrounds for which the scalar runs over the longest range, which is the case in particular for solutions approaching the hyperscaling-violating limit detailed in sections 7.3.6 and 7.4.5.

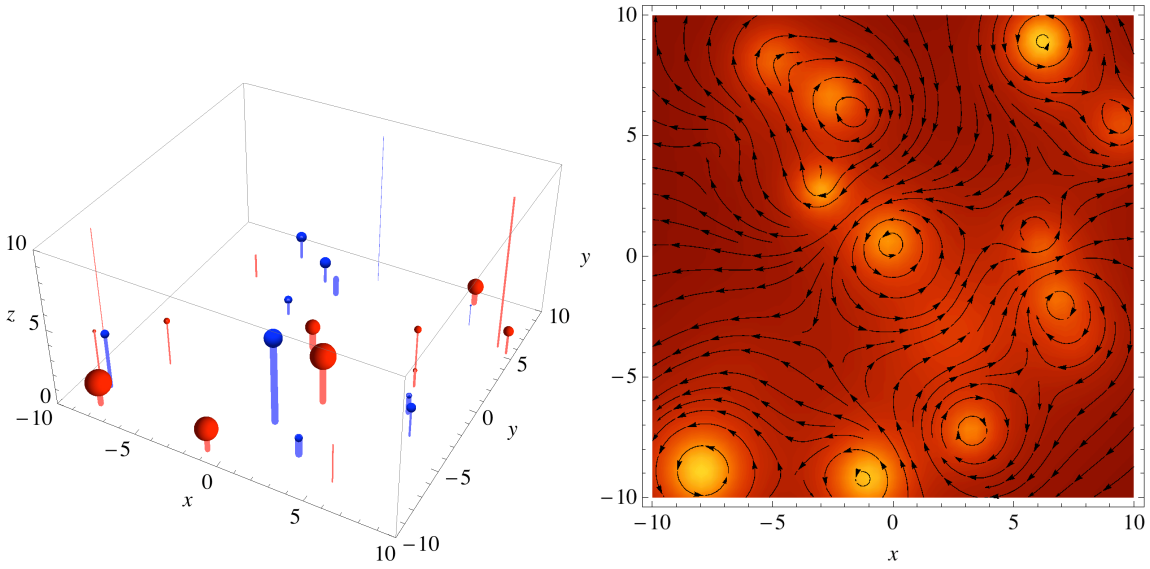

Fig. 7.15: **Left**: A random collection of probe black holes, represented by spheres. The size of each sphere is proportional to the D0-charge, while the thickness of the line projecting the probe onto the boundary $z = 0$ is proportional to the D6-charge. Red/blue = positive/negative D6-charge. Notice that because of the symmetry (7.4.58), one expects positive and negative D6-charge probes to be present in equal abundance. **Right**: Corresponding 3-currents in the CFT. Brighter means higher charge density j_0^t, flow lines indicate the direction of the current $\vec{j}_0$. D0-charge determines charge density, D6-charge determines current density. Smaller values of z_p lead to smaller structures. Positive and negative D6-charges produce oppositely circulating currents.

Appendix A

de Sitter Fluids

A.1 Scalar Perturbations

Gravitational perturbations in static dS_4 consist of a scalar and vector mode of the $SO(3)$ of the two-sphere. There are no tensor modes in four dimensions. Scalar harmonic perturbations can be reduced to a single Ishibashi-Kodama master field [50, 51], which obeys the same effective equation as that of the vector perturbations except that the angular number l begins at $l = 0$ (instead of $l = 1$ in the vector case).

An incompressible fluid requires a divergenceless velocity field v_i. The scalar harmonic allows only the possibility $v_i \propto \mathcal{S}_i \equiv -\nabla_i \mathcal{S}$. $\mathcal{S}$ is the scalar harmonic on the sphere which satisfies:

$$\left(\nabla^2_{S^2} + k_S^2\right)\mathcal{S} = 0 \ , \quad k_S^2 = l(l+1) \ , \quad l = 0, 1, 2, \ldots \tag{A.1.1}$$

Imposing incompressibility leads to

$$\nabla^i_{S^2} v_i \propto \nabla^2_{S^2}\mathcal{S} = -k_S^2 \mathcal{S} \tag{A.1.2}$$

which vanishes for $k_S = 0$, i.e. the spherically symmetric mode $l = 0$. In this case $v_i = 0$ and we are left with a trivial fluid.

Thus, in the case of an incompressible fluid, the scalar mode only consists of trivial fluids. It would be interesting to investigate the case of a compressible fluid which allows for sound modes.[1]

A.2 The $l = 1$ Vector Perturbation

Gravitational vector perturbations with $l = 1$ differ from $l > 2$. We follow the discussion in [50, 51]. In addition to equation 2.3.9, spherical vector harmonics satisfy the following equation:

$$\left(\nabla^2_{S^2} + k_V^2 - 3\right)\mathcal{V}_{ij} = 0 \quad , \quad \mathcal{V}_{ij} \equiv -\frac{1}{2k_V}\left[D_i\mathcal{V}_j + D_j\mathcal{V}_i\right] \ , \tag{A.2.3}$$

where $D_i \equiv (\nabla_{S^2})_i$. For $k_V^2 - 3 \leq 0$ it can be shown that $\mathcal{V}_{ij}$ vanishes and therefore, $\mathcal{V}^i$ must be a Killing vector on the sphere. In this case, we parametrize the perturbations as:

$$\delta g_{ai} = r f_a \mathcal{V}_i, \tag{A.2.4}$$

where $x^a = \{t, r\}$ and $x^i = \{\theta, \phi\}$. Given that $\mathcal{V}_{ij} = 0$ implies $\delta g_{ij} = 0$, we can no longer fix the gauge freedom by imposing $\delta g_{ij} = 0$. Instead, we will fix the gauge $f_r = 0$. From [51], using the only gauge invariant object F_{ab}:

$$r^{-1}F_{ab} = D_a\left(\frac{f_b}{r}\right) - D_b\left(\frac{f_a}{r}\right) \ , \quad D_a \equiv \left(\nabla_{g^{(2)}}\right)_a \tag{A.2.5}$$

[1] In [43], it was shown for planar horizons that the speed of sound for the scalar sound mode goes to infinity and effectively decouples from the non-relativistic fluid sector.

the Einstein equation imply that F_{ab} is:

$$F_{ab} = \frac{3J}{r^3}\epsilon_{ab} \tag{A.2.6}$$

with J constant. In the case of a perturbation about a spherically symmetric black hole, this corresponds to giving it a small amount of angular momentum [51].

We can study the r dependence of the metric components. Given that the connection term will drop out due to anti-symmetrization, we can replace the covariant derivatives with ordinary derivatives and find:

$$-\frac{3J}{r^4} = \partial_r\left(\frac{f_t}{r}\right) \ . \tag{A.2.7}$$

The above integrates to

$$f_t(r) = J\left(\frac{1}{r^2} - \frac{r}{r_c^3}\right) \ , \tag{A.2.8}$$

where we have set Dirichlet boundary conditions on δg_{it} at $r = r_c$. Hence, the perturbed metric reads

$$ds^2 = ds_0^2 + J\left[\frac{1}{r} - \frac{r^2}{r_c^3}\right]\mathcal{V}_i(\theta,\phi)dtdx^i \tag{A.2.9}$$

with $\mathcal{V}_i$ a Killing vector on S^2.

A.3 Mind the Gap

Looking at the last two plots in figure 2.5, we see that as we move the cutoff surface away from the cosmological horizon, the zeroes for $l = 9$ and $l = 10$ modes jump discontinuously. We would like to describe how this behavior arises. Recall that our goal was to find the lowest lying zero of $\delta g_{i\tau}^{out}(\rho = 1)$ as a function of ω on the

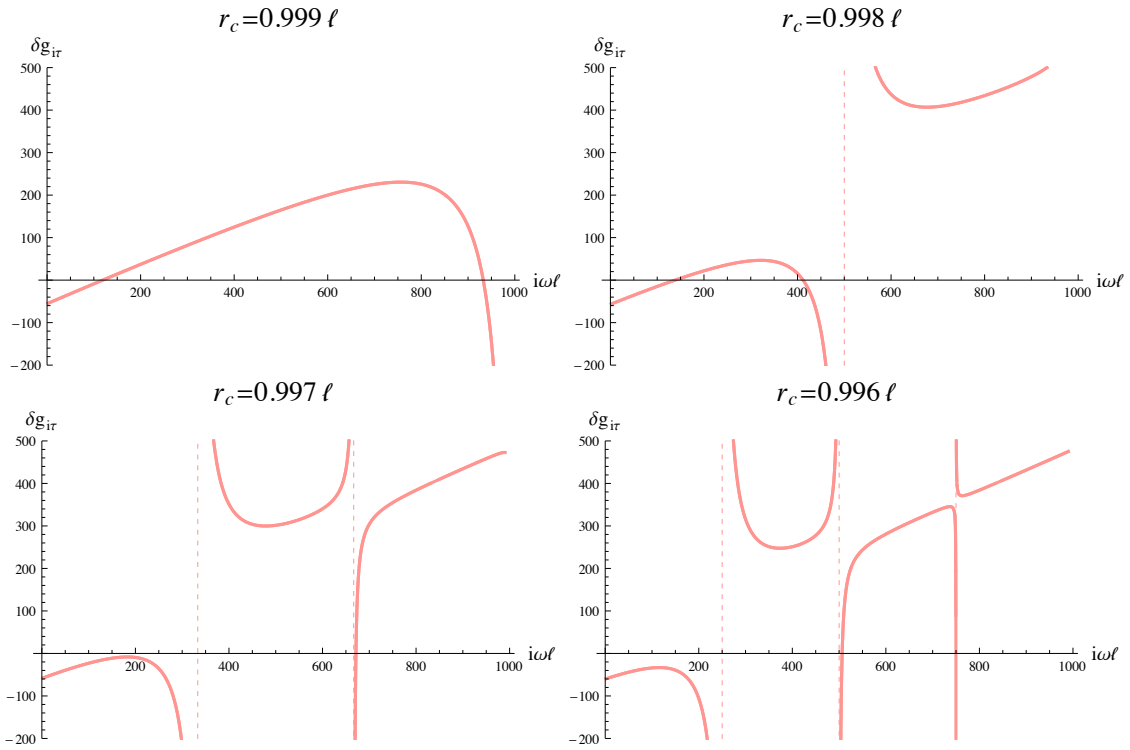

Fig. A.1: Flow of $\delta g_{i\tau}^{out}(\rho = 1)$ for $l = 10$ as we move r_c away from the cosmological horizon. We wish to find frequencies that make this function vanish. As we vary r_c the lowest lying zero jumps.

negative imaginary axis as we move r_c. Notice in figure A.1 that as we move r_c to smaller values, the lowest lying zero disappears and the new lowest lying zero is at a finite distance away in frequency space.

A.4 Hypergeometric Gymnastics

For $(c-a-b)$ positive integer the following relation holds [64]:

$$
\begin{aligned}
{}_2F_1\left(a;b;c;z\right) &= \frac{\Gamma(c-a-b)\Gamma(c)}{\Gamma(c-b)\Gamma(c-a)} \sum_{n=0}^{c-a-b-1} \frac{(a)_n(b)_n}{(1+a+b-c)_n n!}(1-z)^n \\
&+ (z-1)^{c-a-b}\frac{\Gamma(c)}{\Gamma(a)\Gamma(b)} \sum_{n=0}^{\infty} \frac{(c-b)_n(c-a)_n}{n!(n+c-a-b)!}\left[k_n - \log(1-z)\right](1-z)^n \ , \quad \text{(A.4.10)}
\end{aligned}
$$

where $(a)_n \equiv \Gamma(a+n)/\Gamma(a)$ are the Pochhammer symbols and

$$
k_n = \psi(n+1) + \psi(n+1+c-a-b) - \psi(n+c-a) - \psi(n+c-b) \qquad \text{(A.4.11)}
$$

with $\psi(z) = d\log\Gamma(z)/dz$.

We treat the case covered by equation (A.4.10) as it is relevant to the text. To eliminate the log terms, we require $1/\Gamma(a)\Gamma(b) = 0$. In the case of $a = -n_1,\ n_1 = 0, 1, 2, \ldots$, if $c - b > 0$ (which in the spacelike case becomes $n_1 \geq l$), then the whole second sum vanishes and we get [65]:

$$
{}_2F_1\left(a;b;c;z\right) = \frac{\Gamma(c-a-b)\Gamma(c)}{\Gamma(c-b)\Gamma(c-a)}{}_2F_1\left(a;b;1-c;1-z\right) \qquad \text{(A.4.12)}
$$

which goes to a constant as $r \to 1$ (here $z = \ell^2/r^2$) and translates into the modes with no incoming flux from the Northern patch. So, these are the modes we want.[2]

In the other regime $c-b \leq 0$, the first sum vanishes completely due to the gamma function's poles. Naively, we would think that the whole expression is zero, however, the second term contains a divergent term $\psi(n+c-b)$ in the sum that will cancel out the divergence in $1/\Gamma(a)$ for $n \leq -(c-b)$. then we actually have

$$
\frac{\psi(n+c-b)}{\Gamma(a)} \sim \Gamma(-a+1) \qquad \text{(A.4.13)}
$$

[2]In the case of $b = -n_2,\ n_2 = 0, 1, 2, \ldots$, the analogous inequality in the first regime is $c-a > 0$. However, our parameters imply that $c-a > 0$ is always true. Thus we are always in this first regime which gives the modes that we want and there is no further restriction on n_2.

leading to[65]:

$$ {}_2F_1\left(a;b;c;z\right) \sim \frac{\Gamma(c)\Gamma(-a+1)}{(c-a-b)!\Gamma(b)}\left(1-z\right)^{c-a-b}{}_2F_1\left(c-b;c-a;1+c;1-z\right). \tag{A.4.14} $$

This implies that the φ_v^+ tends to $(r^2-1)^{i\omega/2}$ (as $r \to 1$) which is an incoming wave from the Northern patch and should be excluded.

Appendix B

Rotating Black Holes

B.1 Explicit Thermodynamic Expressions

Below we present explicit expressions for the specific heat at fixed angular momentum, C_J, the second partial derivative of the entropy with respect to the angular momentum and the determinant of the Hessian given in 3.3.26. Our results are given in the (r_+, a)-basis.

The specific heat is given by:

$$C_J(r_+, a) = \frac{1}{(a^2+\ell^2)} \times \frac{2\ell^4\pi \left(a^2+r_+^2\right)^2 \left(3r_+^4 - \ell^2 r_+^2 + a^2\left(\ell^2+r_+^2\right)\right)}{\left(\ell^2-r_+^2\right)a^6 + \left(-3\ell^4+13r_+^2\ell^2-6r_+^4\right)a^4 + r_+^2\left(-6\ell^4+23r_+^2\ell^2-9r_+^4\right)a^2 + \ell^2 r_+^4\left(\ell^2+3r_+^2\right)}. \tag{B.1.1}$$

The second derivative of the entropy with respect to J is given by:

$$\frac{\partial^2 S_{BH}}{\partial J^2} = 8\left(a^2+\ell^2\right)\pi r^2 \times \\ \frac{\left(-3\ell^4+6r^2\ell^2+r^4\right)a^4+\left(\ell^6-13r^2\ell^4+23r^4\ell^2-3r^6\right)a^2+\ell^2r^2\left(\ell^2-3r^2\right)^2}{\ell^2\left(3r^4-\ell^2r^2+a^2\left(\ell^2+r^2\right)\right)^3}. \quad \text{(B.1.2)}$$

The determinant of the Hessian is given by:

$$\det H_{ij} = -\frac{64\left(a^2+\ell^2\right)^4\pi^2 r_+^4\left(\left(\ell^2-r_+^2\right)a^2+r_+^2\left(\ell^2+3r_+^2\right)\right)}{\ell^2\left(3r_+^4-\ell^2r_+^2+a^2\left(\ell^2+r_+^2\right)\right)^4}. \quad \text{(B.1.3)}$$

We note that it is negative definite in the physical configuration space.

B.2 Thermal Evolution

We obtain three qualitative possibilities for thermal evolution assuming that the emission rates are dominated by angular momentum, energy and a combination thereof. Below, we show plots of the vector field $(c_J\ \partial_J S_{tot}, c_M\ \partial_M S_{tot})$ where c_J and c_M are constants determining the relative emission rate.

The first case corresponds to a situation where there is an 'energy pump' between the two horizons keeping the energy fixed for each horizon, i.e. $c_M \ll 1$. In this case, depicted in Fig. 5 (a), the thermal flow will be along lines of constant energy depicted in Fig. 3 (b), and will lead to the complete spin-down of the black hole.

The second case corresponds to a situation where there is an 'angular momentum' pump between the two horizons keeping the angular momentum fixed for each horizon and depicted in Fig. 5 (b), i.e. $c_J \ll 1$. One notices that large extremal black holes

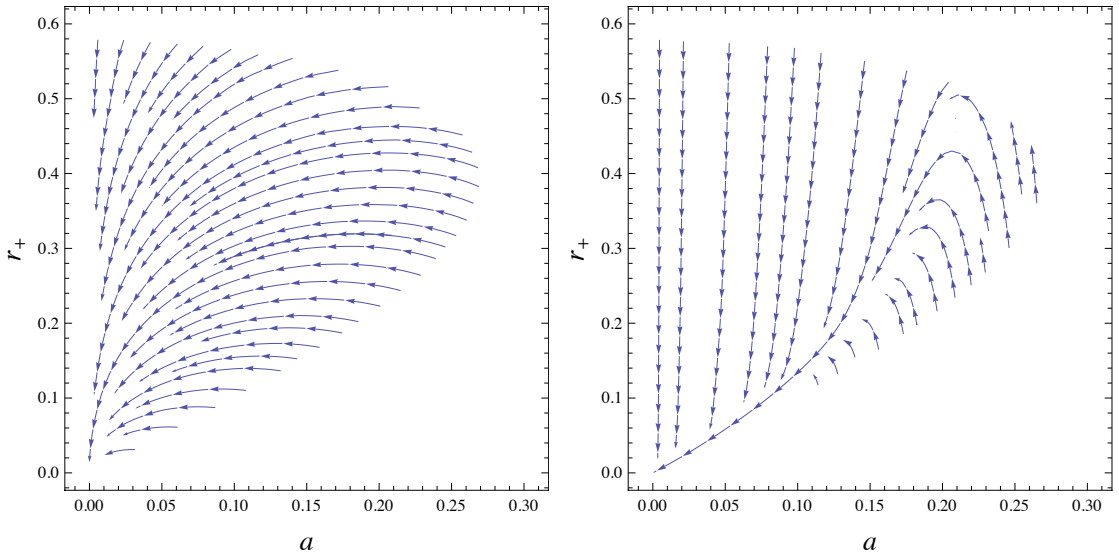

Fig. B.1: **Left**: Thermal evolution when emission of energy is suppressed. **Right**: Thermal evolution when emission of angular momentum is suppressed.

evolve toward the rotating Nariai limit before spinning down and evolving toward the origin. Notice that once the lukewarm line is reached the system evolves along it.

Finally, we can consider a situation where both angular momentum and energy are emitted at similar rates, i.e. $c_J \sim c_M$, as depicted in Fig. B.2.

B.3 Explicit Expressions for α and β

The explicit expressions for α and β are as follows:

$$\alpha = \frac{\lambda^{h_- - i(n_R + \tilde{\omega}/\lambda)} \csc\left[\pi\left(h_- - i(n_R + \tilde{\omega}/\lambda)\right]\right] \Gamma[h_- - ikm]\Gamma\left[h_- + i\left(n_R + \tilde{\omega}/\lambda\right)\right]}{\pi\Gamma[2h_-]Q}, \tag{B.3.4}$$

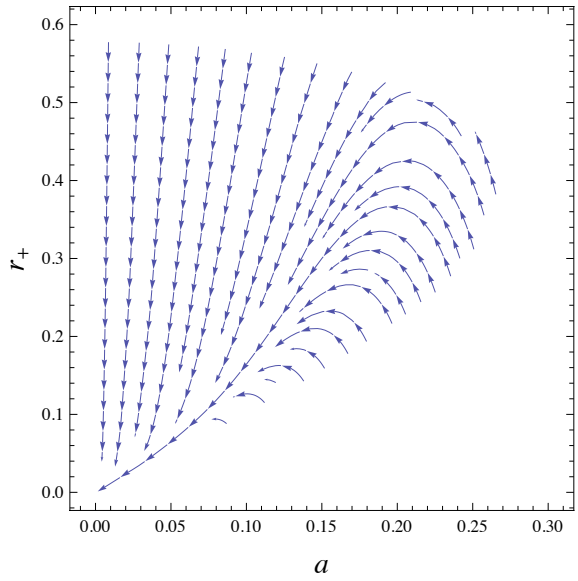

Fig. B.2: Thermal evolution when emission of energy and angular momentum is comparable.

$$\beta \;=\; -\frac{\lambda^{h_+ - i(n_R+\tilde{\omega}/\lambda)}\csc\left[\pi\left(h_- + i(n_R+\tilde{\omega}/\lambda)\right]\Gamma[h_+ - ikm]\Gamma\left[h_+ + i\left(n_R+\tilde{\omega}/\lambda\right)\right]}{\pi\Gamma[2h_+]Q} \tag{B.3.5}$$

where we have defined:

$$\begin{aligned}\frac{Q}{\Gamma\left[1-\frac{2i\tilde{\omega}}{\lambda}\right]] } \equiv \csc[\pi(h_- - ikm)]\csc\left[\pi\left(h_- - i(n_R+\tilde{\omega}/\lambda)\right)\right] \\ - \csc[\pi(h_- + ikm)]\csc\left[\pi\left(h_- + i\left(n_R+\tilde{\omega}/\lambda\right)\right)\right].\end{aligned} \tag{B.3.6}$$

B.4 Thermal Boundary-to-Boundary Correlator

We will discuss in some more detail the computation of the retarded thermal boundary-to-boundary correlator.[1] Begin with a wave-packet expressed as a sum over modes

$$\Phi(x,\hat{t},\Omega)=\sum_{m,l}\int\frac{d\tilde{\omega}}{2\pi}\left(\gamma_{lm\tilde{\omega}}e^{-i\tilde{\omega}\hat{t}}e^{im\hat{\phi}}Y_{lm}(\theta)R(x)\right). \tag{B.4.7}$$

The on-shell action for a massless scalar field is given by

$$I_{matter}=\frac{1}{2}\int_{\mathcal{M}}d^4x\sqrt{-g}\partial_\mu\Phi\partial^\mu\Phi=\frac{1}{2}\int_{\partial\mathcal{M}}d^3x\sqrt{-g}n^\mu\Phi\partial_\mu\Phi \tag{B.4.8}$$

where we have integrated by parts and set the bulk integral to zero since it vanishes on-shell. The only boundary term relevant to us will be the one at $\mathcal{I}^+$. The n^μ is a unit normal vector which is orthogonal to the boundary. Using the late time behavior of the $R(x)$ function in the rotating Nariai limit 3.4.54 and evaluating the action we find

$$I_{matter}=\frac{1}{2}\sum_{m,l}\int\frac{d\tilde{\omega}}{2\pi}\alpha(\tilde{\omega},m,l)\beta(-\tilde{\omega},-m,l)+\dots \tag{B.4.9}$$

where the dots correspond to terms that oscillate infinitely fast at the boundary. We may drop such terms by adding a small imaginary part to x, as is done for the vacuum state of the harmonic oscillator.

In order to obtain this expression, we have used the following completeness and orthonormality properties of the spheroidal harmonics,

$$\sum_{l,m}Y_{lm}(\theta)e^{im\hat{\phi}}Y_{lm}(\theta')e^{-im\hat{\phi}'} = \delta^2(\Omega,\Omega'), \tag{B.4.10}$$

$$\int d\theta d\hat{\phi}\sqrt{\tilde{h}}Y_{lm}(\theta)e^{im\hat{\phi}}Y_{l'm'}(\theta)e^{-im'\hat{\phi}} = \delta_{m-m'}\delta_{l-l'} \tag{B.4.11}$$

[1] A similar situation for AdS is discussed in [89, 90].

where $\tilde{h}_{ij}$ is the induced metric at fixed x and t and we are working in a basis where $Y_{lm}(\theta)$ are real.

To compute the thermal boundary-to-boundary correlator, we must define which excitation, i.e. α or β, corresponds to the boundary value of the field. Once we have defined the boundary value, we can take variational derivatives with respect to it. For instance, choosing α as the boundary value at $\mathcal{I}^+$ we can write the action as

$$I_{matter} = \frac{1}{2}\sum_{m,l}\int \frac{d\tilde{\omega}}{2\pi}\alpha(\tilde{\omega}, m, l)\alpha(-\tilde{\omega}, -m, l)G_R^{th}(l, m, \tilde{\omega}) \tag{B.4.12}$$

where the thermal boundary-to-boundary correlator in momentum space is thus found to be:

$$G_R^{th} \sim \frac{\beta}{\alpha}. \tag{B.4.13}$$

Appendix C

Substringy Bound States

C.1 Two-Body Problem

In this appendix we discuss the motion of a single probe particle in the background of a fixed charge sitting at the origin. This was studied at length in [112]. The Hamiltonian of this system is given by

$$H = \frac{1}{2m}(\mathbf{p} - \mathbf{A})^2 + \frac{1}{2m}\left(\frac{\kappa}{2r} + \theta\right)^2 \quad , \quad \mathbf{p} \equiv m\dot{\mathbf{x}} + \mathbf{A} \tag{C.1.1}$$

and is conserved. For simplicity we choose $\kappa > 0$ and allow θ to be either positive or negative. Other than the Hamiltonian, this system admits two vector-valued conserved quantities known as the angular momentum $\mathbf{L}$ and the Runge-Lenz vector $\mathbf{n}$. Explicitly

$$\mathbf{L} = \mathbf{x} \times (\mathbf{p} - \mathbf{A}) + \frac{\kappa}{2r}\mathbf{x} \ , \quad \text{and} \quad \mathbf{n} = \left(\mathbf{x} + \frac{1}{\theta}\mathbf{L}\right) \times (\mathbf{p} - \mathbf{A}) \ . \tag{C.1.2}$$

Since this system is superintegrable, the probe particle's trajectories can be found algebraically.

First, notice that $\mathbf{n}\cdot\dot{\mathbf{x}} = 0$ implying that $\mathbf{n}$ is perpendicular to the plane of motion of the probe particle. We use this fact to orient our axes such that $\mathbf{n} = |\mathbf{n}|\hat{z}$. It is straightforward to show that

$$|\mathbf{n}| = \sqrt{\frac{2mH}{\theta^2}\left(\mathbf{L}^2 - \frac{\kappa^2}{4}\right)}\,, \tag{C.1.3}$$

which implies that $|\mathbf{L}| \geq \kappa/2$. With this choice of coordinates, the particle's trajectory is constrained to lie in a plane of constant z. The magnitude of z can be obtained by computing $\mathbf{n}\cdot\mathbf{x} = |\mathbf{n}|z = -\left(\mathbf{L}^2 - \frac{\kappa^2}{4}\right)/\theta$, giving

$$z = -\frac{|\theta|}{\theta}\sqrt{\frac{\mathbf{L}^2 - \frac{\kappa^2}{4}}{2mH}}\,. \tag{C.1.4}$$

We have yet to choose an orientation for the $x-y$ plane; we do so by aligning our coordinates such that $L_y = 0$ and L_x points in the positive x direction. The components of the angular momentum are given by

$$L_x = \sqrt{\mathbf{L}^2 - \frac{\theta^2}{2mH}\left(\mathbf{L}^2 - \frac{\kappa^2}{4}\right)}\,, \quad L_z = \sqrt{\frac{\theta^2}{2mH}\left(\mathbf{L}^2 - \frac{\kappa^2}{4}\right)}\,. \tag{C.1.5}$$

We can determine the particle's trajectory explicitly by noticing that (C.1.2) implies that $\mathbf{L}\cdot\mathbf{x} = \kappa\, r/2$ or

$$\left(1-e^2\right)(x-x_0)^2 + 2\ell e(x-x_0) + y^2 = \ell^2\,, \tag{C.1.6}$$

which is the equation for a conic section in cartesian coordinates. The quantities e and ℓ are the eccentricity and the semi-latus rectum of the conic section respectively and are given by

$$e = \frac{2L_x}{\kappa} = \frac{2}{\kappa}\sqrt{\mathbf{L}^2 - \frac{\theta^2}{2mH}\left(\mathbf{L}^2 - \frac{\kappa^2}{4}\right)}\,, \quad \ell = \frac{4\mathbf{L}^2 - \kappa^2}{\kappa\sqrt{8mH}}\,. \tag{C.1.7}$$

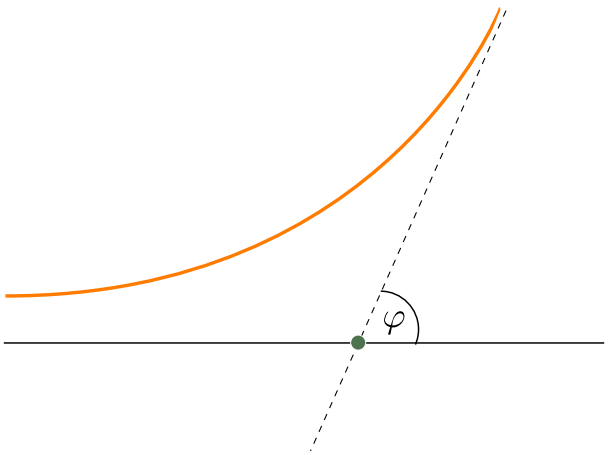

Fig. C.1: Scatering angle.

The quantity $x_0 \equiv \sqrt{\mathbf{L}^2 - \frac{\theta^2}{2mH}\left(\mathbf{L}^2 - \frac{\kappa^2}{4}\right)}/(|\theta| - \sqrt{2mH})$ is the location of one of the foci of the conic section.

The overall shape of a conic section is determined by its eccentricity, with elliptic orbits corresponding to $e < 1$, while parabolic and hyperbolic orbits correspond to $e = 1$ and $e > 1$ respectively. Intuition predicates that bound orbits should only happen for $\theta < 0$, while $\theta > 0$ gives rise to parabolic or hyperbolic orbits. For positive θ the Hamiltonian is bound such that $2mH \geq \theta^2$ which implies that $e \geq 1$, thus verifying our intuition.

For $e < 1$ the length of the semi-major axis a of the elliptic orbit is given by

$$a = \frac{2\ell}{1 - e^2} \sim \frac{\kappa\sqrt{H/2m}}{H_{\text{escape}} - H} + \mathcal{O}(1) \tag{C.1.8}$$

so as the energy approaches the escape energy $H_{\text{escape}} = \theta^2/2m$ (or as e approaches 1), the size of the bound orbit diverges. We end this appendix with a discussion of scattering for $e \geq 1$. Since the trajectory of the particle is given by a conic section in

the $x - y$ plane, the scattering angle as defined in figure C.1 is given by

$$\varphi = 2\,\mathrm{arccot}\left(\sqrt{\mathrm{e}^2 - 1}\right) \ . \tag{C.1.9}$$

For parabolic orbits ($e = 1$), $\varphi = \pi$ and we see that the particle completely back scatters. As we increase e the scattering angle decreases monotonically.

Appendix D

Flat Space Hot Bound States

D.1 Counting configurations

There exist supersymmetric probe bound state solutions for all values of $\tilde{Q}_0 \geq 0$ except 1/6. The number of possible bound state solutions will not be constant however. In particular when $\tilde{Q}_0 \to 1/6$, the allowed region in the probe charge space shrinks to zero. In this appendix we obtain an estimate for the number of supersymmetric probe bound state solutions near this point. First we consider the case in which we simply count the number of allowed probe charges, later on we will include the lowest Landau level degeneracies for each choice of probe.

D.1.1 Single probe

For a single probe, this number is $\mathcal{N}_1 = \sum_{\gamma \in A} 1$, where A is the allowed region in probe charge space, bounded by the requirement that the bound state exists and the probe approximation is satisfied. As we take the limit $P_1 \to \infty$, A will contain an

increasingly large number of charges, hence the number of lattice points contained in A can be estimated by computing the volume of A in charge space:

$$\mathcal{N}_1 \approx \int_A dp_0\, dp_1\, dq_1\, dq_0\, 1 = \int dp_0\, p_0^3 y_0^6 \int_{\tilde{A}} d\tilde{b}\, d\tilde{n}\, d\tilde{k}\,. \tag{D.1.1}$$

Here $\tilde{A}$ is the region of allowed values of $(\tilde{k}, \tilde{n}, \tilde{b})$. Since $|\tilde{k}|$ is bounded by $\sqrt{2(\tilde{Q}_0 + \tilde{b})}$ and $\sqrt{2(\frac{1}{6} + \tilde{b})}$ according to (6.5.48), the integral over $\tilde{k}$ gives a factor $f_1(\tilde{b}) \sim \left|\sqrt{\frac{1}{6} + \tilde{b}} - \sqrt{\tilde{Q}_0 + \tilde{b}}\right|$. (We drop irrelevant numerical factors here and in what follows.) Because of the constraint $\tilde{n}^2 \leq \frac{8}{9}\tilde{b}^3$, the integral over $\tilde{n}$ gives a factor $f_2(\tilde{b}) \sim \tilde{b}^{3/2}$. Performing the integral over $\tilde{b}$ gives

$$\int d\tilde{b}\, f_1(\tilde{b})\, f_2(\tilde{b}) \sim |\tilde{Q}_0 - \tfrac{1}{6}|\, \tilde{b}_{\rm max}^2\,. \tag{D.1.2}$$

Here $\tilde{b}_{\rm max}^2$ is the maximal value of $\tilde{b}$, which we have assumed to be very large so we are allowed to drop terms of order $\tilde{b}_{\rm max}$ and lower. The reason $b_{\rm max}$ is not infinite is the requirement that the probe approximation should be valid. To estimate it, recall that $m_p/M = \frac{y_0 p_0}{P_1}\frac{\tilde{m}_p}{\tilde{M}}$. Since we are exploring the region $\tilde{Q}_0 \approx 1/6$, $\tilde{M}$ is of order 1. For large $\tilde{b}$, $\tilde{m}_p \sim \tilde{q}_0 \sim \tilde{b}^{3/2}$, so the probe approximation requires $\tilde{b}_{\rm max} = \left(\epsilon \frac{P_1}{y_0 p_0}\right)^\alpha$, where $\alpha = 2/3$ and $\epsilon \sim m_p/M$ is some small number, the maximal m_p/M we allow. We are then left with the integral over p_0:

$$\begin{aligned}
\mathcal{N}_1(\tfrac{m_p}{M} < \epsilon) &\sim \epsilon^{2\alpha} \left|\tilde{Q}_0 - \tfrac{1}{6}\right| \int_0^{\epsilon P_1/y_0} dp_0\, p_0^{3-2\alpha} y_0^{6-2\alpha} P_1^{2\alpha} && \text{(D.1.3)}\\
&\sim \epsilon^4 \left|\tilde{Q}_0 - \tfrac{1}{6}\right| y_0^2 P_1^4 && \text{(D.1.4)}\\
&= \epsilon^4 \left|\tfrac{6Q_0}{P_1} - y_0^2\right| P_1^4\,. && \text{(D.1.5)}
\end{aligned}$$

The upper integral bound $p_0 < \epsilon P_1/y_0$ comes again from requiring that we remain within the probe approximation, this time in the limit of large p_0. Notice that the final

result does not depend on the actual value of α. In fact, we could have inferred the prefactor simply from the scaling symmetries of the system: From (D.1.1) it is clear that $\mathcal{N}_1$ has scaling weights $(0, 6, 4)$ under the symmetries of 6.4.2, while ϵ, P_1 and y_0 have scaling weights $(-1, 0, 1)$, $(1, 1, 0)$ and $(0, 1, 0)$, respectively. This uniquely determines their powers.

The above expressions are valid when $\left|\tilde{Q}_0 - \frac{1}{6}\right| \ll 1$, i.e. $\left|\frac{6Q_0}{P_1} - y_0^2\right| \ll \frac{Q_0}{P_1}$, or in other words close to the attractor point: $y_0 \to y_\star = \sqrt{\frac{6Q_0}{P_1}}$. Notice that since the probe approximation requires $y_0 \ll P_1$ (as discussed in section 6.4.2), self-consistency in this regime requires $Q_0 \ll P_1^3$, i.e. we are necessarily in the non-Cardy regime.

Pushing y_0 and ϵ as high up as possible while conceivably still yielding more or less sensible results, i.e.

$$y_0 \sim P_1\,, \qquad Q_0 \sim P_1^3\,, \qquad \epsilon \sim 1\,, \tag{D.1.6}$$

we get

$$\mathcal{N}_{1,\max} \sim P_1^6\,. \tag{D.1.7}$$

D.1.2 Multiple probes

In the probe approximation we can also easily build multi-probe bound states: By assumption, the probes do not backreact so we can simply superimpose the single probe configurations, as long as we keep the total probe mass $\sum_i m_{pi}$ small compared to M.[1] Imagine a general situation in which the number of single probe states with

[1] In general the probes will interact with each other, with interaction strength given by their mutual symplectic products. For probes which happen to have small symplectic products with the background black hole, i.e. probes which are close to be swallowed by the black hole, these interactions become important even in the probe limit. We will ignore such boundary cases here.

$m_p/M < \epsilon$ is given by

$$\mathcal{N}_1(\epsilon) = A\epsilon^n \,, \tag{D.1.8}$$

where A is some large number. In the case at hand $n = 4$, but we will keep things slightly more general here for future reference. The density of single particle states at $\frac{m_p}{M} = \epsilon$ is then $d\mathcal{N}_1(\epsilon) = n\epsilon^{n-1}A$. For K labeled probes, the density of states at $\frac{m_i}{M} = \epsilon_i$, $i = 1, \ldots, K$ is

$$d\mathcal{N}_K(\epsilon_1, \ldots, \epsilon_K) = (nA)^K \epsilon_1^{n-1} \cdots \epsilon_K^{n-1}\, d\epsilon_1 \cdots d\epsilon_K \,. \tag{D.1.9}$$

The total number of states with an arbitrary number K of unlabeled probes satisfying $\sum_i \frac{m_i}{M} < \epsilon$ is therefore

$$\mathcal{N}(\epsilon) = \sum_{K=0}^{\infty} \frac{(nA)^K}{K!} \int_{\sum_i \epsilon_i < \epsilon} d\epsilon_1 \cdots d\epsilon_K\, \epsilon_1^{n-1} \cdots \epsilon_K^{n-1} \,. \tag{D.1.10}$$

The $1/K!$ corrects in a classical way for overcounting.[2] The integral can be factorized by representing the constraint $\sum_i \epsilon_i < \epsilon$ as the contour integral $\frac{1}{2\pi i}\int \frac{d\lambda}{\lambda} e^{\lambda(\epsilon - \sum_i \epsilon_i)}$, where the contour is taken to be on the right of the pole at $\lambda = 0$. This yields

$$\begin{aligned} \mathcal{N}(\epsilon) &= \frac{1}{2\pi i}\int \frac{d\lambda}{\lambda}\, e^{\lambda\epsilon} \sum_{K=0}^{\infty} \frac{(nA)^K}{K!} \left(\int d\epsilon_1\, \epsilon_1^{n-1}\, e^{-\lambda\epsilon_1} \right)^K \\ &= \frac{1}{2\pi i}\int \frac{d\lambda}{\lambda}\, \exp\left(\lambda\epsilon + \frac{n!A}{\lambda^n} \right) . \end{aligned} \tag{D.1.11}$$

At large A this can be computed by saddle point evaluation. To leading order, dropping order one numerical factors:

$$\log \mathcal{N}(\epsilon) \sim (A\epsilon^n)^{\frac{1}{n+1}} \,. \tag{D.1.12}$$

[2] We do not use quantum statistics because the probability that two probes occupy the same quantum microstate is completely negligible in this setup. This is already true if the probes are considered to be point particles without internal degrees of freedom, but becomes obvious without work when one takes into account the huge number of internal microstates the individual probe black holes can choose from.

Applying this to (D.1.5) gives for the total number of distinct probe configurations

$$\mathcal{N}(\epsilon) \approx \exp\left(\kappa\, \epsilon^{4/5} \left|y_\star^2 - y_0^2\right|^{1/5} P_1^{4/5}\right) , \tag{D.1.13}$$

where κ is some order 1 constant and $y_\star = \frac{6Q_0}{P_1}$ is the attractor fixed point.

In the regime (D.1.6), we thus get a configurational entropy

$$\log \mathcal{N}_{\rm max} \sim P_1^{6/5} . \tag{D.1.14}$$

D.1.3 Including Landau level degeneracies

A single probe bound to the background black hole has classically an S^2 moduli space, but because a magnetic field threads the sphere, the space of quantum BPS ground states (i.e. the lowest Landau level) will be degenerate. The degeneracy is given by the effective magnetic flux as seen by the probe [103]:

$$d_\gamma = |p_0 Q_0 - q_1 P_1| = p_0 P_1 y_0^2 |\tilde{Q}_0 - \tilde{q}_1| . \tag{D.1.15}$$

To count the total number of such one particle ground states (ignoring the internal degrees of freedom of the probe and of the black hole), it suffices to replace the 1 in (D.1.1) by the LLL degeneracy factor d_γ. Because this has scaling dimensions $(1, 3, 1)$, doing so will add an additional factor $\epsilon y_0 P_1^2$ to the final result (D.1.5). Furthermore, because the insertion $|\tilde{Q}_0 - \tilde{q}_1|$ is of generically of order $|\tilde{Q}_0 - \frac{1}{6}|$ over the integration domain, its effect will be to modify the power of $|\tilde{Q}_0 - \frac{1}{6}|$ from linear to quadratic. All in all we get

$$\mathcal{N}_{\rm LLL,1}(\epsilon) \sim \epsilon^5 \left|\tilde{Q}_0 - \tfrac{1}{6}\right|^2 y_0^3 P_1^6 \tag{D.1.16}$$

$$= \epsilon^5 \left|\tfrac{6Q_0}{P_1} - y_0^2\right|^2 \frac{P_1^6}{y_0} . \tag{D.1.17}$$

For the multi-probe system we get from this, using (D.1.12),

$$\log \mathcal{N}_{\text{LLL}}(\epsilon) \sim \epsilon^{5/6} \left| \tfrac{6Q_0}{P_1} - y_0^2 \right|^{1/3} \frac{P_1}{y_0^{1/6}} \tag{D.1.18}$$

Finally, in regime (D.1.6), we get a configurational entropy

$$\log \mathcal{N}_{\text{LLL, max}} \sim P_1^{3/2} \,. \tag{D.1.19}$$

Recall that the entropy of the black hole scales as P_1^3.

Appendix E

Electric Charges in AdS

E.1 Gauge Field Propagator in Global AdS_4

The electric potential due to a stationary charge q sitting at a point $\vec{x}_p$ in Minkowski space is given by

$$A_t = \frac{q}{4\pi|\vec{x} - \vec{x}_p|} \ . \tag{E.1.1}$$

This seemingly simple expression gives us a lot of information about the electric field of a particle in flat space. Notably, we can discern that multipole moments of the electric field get washed out as we get farther away from the particle. This is an obvious sanity check, as a point charge sitting at $\vec{x}_p$ is no different than a point charge sitting at the origin when regarded by a far away observer.

We wish to determine the exact form of A_μ in analogy with (E.1.1). That is, for a static particle sitting at an arbitrary point $\vec{x}_p$ in the bulk of AdS_4 with metric given by

$$ds^2 = -\left(1 + \frac{r^2}{\ell^2}\right) dt^2 + \frac{dr^2}{\left(1 + \frac{r^2}{\ell^2}\right)} + r^2 d\Omega^2 \ . \tag{E.1.2}$$

We follow the derivation of [244], which is formulated in Euclidean space. This amounts to taking $t \to i\tau$ in (E.1.2).

The action of a gauge field in Euclidean AdS_4 is given by

$$S_A = \int d^4x\sqrt{g}\left(\tfrac{1}{4}F^{\mu\nu}F_{\mu\nu} - A_\mu J^\mu\right) \ , \tag{E.1.3}$$

and its response to an external current J^ν is

$$A_\mu(x) = \int d^4x'\sqrt{g}\, G_{\mu\nu'}\left(x,x'\right) J^{\nu'}\left(x'\right) \ , \tag{E.1.4}$$

where $G_{\mu\nu'}\left(x,x'\right)$ is the propagator. Maxwell's equations $\nabla_\mu F^{\mu\nu} = -J^\nu$ impose

$$\nabla^\mu\left(\partial_\mu G_{\nu\nu'} - \partial_\nu G_{\mu\nu'}\right) = -g_{\nu\nu'}\frac{\delta(x,x')}{\sqrt{g}} \ . \tag{E.1.5}$$

The expression for the gauge invariant part of $G_{\mu\nu'}\left(x,x'\right)$ can be given in a manifestly coordinate independent way. To do this we note that Euclidean AdS can be constructed by embedding the hyperboloid

$$-X_0^2 + X_E^2 + X_1^2 + X_2^2 + X_3^2 = -\ell^2 \tag{E.1.6}$$

in 5-dimensional minkowski space with metric

$$ds^2_{5\mathrm{d}} = g^{5\mathrm{d}}_{\mu\nu}dX^\mu dX^\nu = -dX_0^2 + dX_E^2 + dX_1^2 + dX_2^2 + dX_3^2 \ . \tag{E.1.7}$$

We obtain the metric (E.1.2) by parametrizing the hyperboloid as

$$\begin{gathered} X_1 = x = r\sin\theta\cos\phi \ , \quad X_2 = y = r\sin\theta\sin\phi \ , \quad X_3 = z = r\cos\theta \\ X_0 = \sqrt{\ell^2+r^2}\cosh\left(\tau/\ell\right) \ , \quad X_E = \sqrt{\ell^2+r^2}\sinh\left(\tau/\ell\right) \ . \end{gathered} \tag{E.1.8}$$

For two points corresponding to $\vec{X}$ and $\vec{X}'$ on the hyperboloid in (E.1.6), we define a bilinear

$$u\left(X,X'\right) = -1 - \frac{P\left(X,X'\right)}{\ell^2} \tag{E.1.9}$$

where $P(X, X') = g_{\mu\nu} X^\mu X'^\nu$ is the dot product in the ambient minkowski space. The quantity P is related to the geodesic distance D between points $\vec{X}$ and $\vec{X}'$ by $P = \cosh D/\ell$. In terms of u, the gauge invariant part of the propagator is given by

$$G_{\mu\nu'}(x, x') = -(\partial_\mu \partial_{\nu'} u) F(u) , \tag{E.1.10}$$

where

$$F(u) = \frac{1}{4\pi^2} \frac{1}{u(2+u)} . \tag{E.1.11}$$

In terms of the coordinates (E.1.8), $u(X, X')$ is given by

$$u = -1 - \frac{\vec{x} \cdot \vec{x}'}{\ell^2} + \sqrt{1 + \frac{r^2}{\ell^2}} \sqrt{1 + \frac{r'^2}{\ell^2}} \cosh\left(\frac{\tau - \tau'}{\ell}\right) , \tag{E.1.12}$$

where $\vec{x} \cdot \vec{x}'$ the standard flat Euclidean dot product between the two vectors and $r^2 = \vec{x} \cdot \vec{x}$.

We wish to evaluate (E.1.4) for a point charge sitting motionless at $\vec{x}_p$, that is

$$J^{\nu'}(\vec{x}') = \left(q \frac{\delta(\vec{x}' - \vec{x}_p)}{\sqrt{g}}, 0, 0, 0\right) . \tag{E.1.13}$$

This boils down to computing

$$A_\mu = -\frac{q}{4\pi^2} \int d\tau' (\partial_\mu \partial_{\tau'} u) \frac{1}{u(2+u)} \bigg|_{\vec{x}' = \vec{x}_p} . \tag{E.1.14}$$

Because $F(u)$ is even in τ' and $\partial_{\tau'} u$ is odd, the integral vanishes for all components of A_μ except A_τ. Computing the integral is straightforward and the final result is

$$A_\tau = \frac{q}{4\pi^2 \ell} \left(\frac{2 + w - v}{\sqrt{v(2+w)}} \arctan\left[\frac{\sqrt{v(2+w)}}{v}\right] + \frac{2 + v - w}{\sqrt{w(2+v)}} \arctan\left[\frac{w}{\sqrt{w(2+v)}}\right] \right) , \tag{E.1.15}$$

where we have defined the quantities

$$v \equiv -1 - \frac{\vec{x} \cdot \vec{x}_p}{\ell^2} + \sqrt{1 + \frac{r^2}{\ell^2}} \sqrt{1 + \frac{r_p^2}{\ell^2}} \quad \text{and} \quad w \equiv -1 + \frac{\vec{x} \cdot \vec{x}_p}{\ell^2} + \sqrt{1 + \frac{r^2}{\ell^2}} \sqrt{1 + \frac{r_p^2}{\ell^2}} . \tag{E.1.16}$$

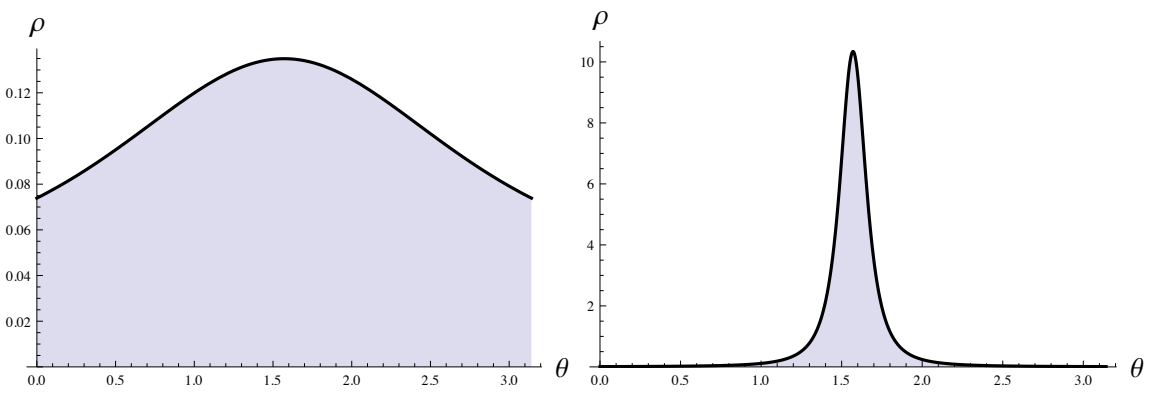

Fig. E.1: Charge density σ_0 for a point charge with $q = 1$ induced on the conformal sphere in units where $\ell = 1$. We take $\phi = 0$. **Left**: the charge is located at $\vec{x_p} = (0.4, 0, 0)$. **Right**: the charge is located at $\vec{x_p} = (8, 0, 0)$.

For large ℓ we find

$$v = \frac{(\vec{x} - \vec{x}_p)^2}{2\ell^2} + \mathcal{O}\left(\ell^{-4}\right) \ , \quad w = \frac{(\vec{x} + \vec{x}_p)^2}{2\ell^2} + \mathcal{O}\left(\ell^{-4}\right) \ , \tag{E.1.17}$$

and

$$A_\tau = \frac{q}{4\pi|\vec{x} - \vec{x}_p|} + \mathcal{O}\left(\ell^{-2}\right) \ . \tag{E.1.18}$$

We have chosen our normalization such that we get the correct result in the $\ell \to \infty$ limit, this is why our conventions differ by a factor of 4 in $F(u)$ from those used in [244].

The charge density induced on the conformal sphere is given simply by $\sigma_0 = \lim_{r\to\infty} r^2 F^{tr}$. We provide some plots of this charge density in figure E.1. We have checked that our expression correctly gives q when integrated over the S^2.

In order to obtain the $U(1)$ currents induced by a magnetic charge, as explained in the main text, it is not possible to dualize the field strength formed by A_τ as the corresponding magnetic field would not obey the correct Dirichlet conditions on the

boundary sphere. The currents are obtained by dualizing the field strength obtained from

$$A_\tau^{\text{mag}} = \frac{p}{4\pi^2\ell}\left(\frac{2+w-v}{\sqrt{v\,(2+w)}}\arctan\left[\frac{\sqrt{v\,(2+w)}}{v}\right]-\frac{2+v-w}{\sqrt{w\,(2+v)}}\arctan\left[\frac{w}{\sqrt{w\,(2+v)}}\right]\right)\,, \tag{E.1.19}$$

in which case $(j^\theta, j^\phi) = \lim_{r\to\infty} r^2(\tilde{F}^{r\theta}_{\text{mag}}, \tilde{F}^{r\phi}_{\text{mag}})$.

Bibliography

[1] S. Perlmutter *et al.* [Supernova Cosmology Project Collaboration], "Measurements of Omega and Lambda from 42 high redshift supernovae," Astrophys. J. **517**, 565-586 (1999). [astro-ph/9812133].

[2] A. G. Riess *et al.* [Supernova Search Team Collaboration], "Observational evidence from supernovae for an accelerating universe and a cosmological constant," Astron. J. **116**, 1009-1038 (1998). [astro-ph/9805201].

[3] G. W. Gibbons and S. W. Hawking, "Cosmological Event Horizons, Thermodynamics, And Particle Creation," Phys. Rev. D **15**, 2738 (1977).

[4] A. Strominger and C. Vafa, "Microscopic origin of the Bekenstein-Hawking entropy," Phys. Lett. B **379**, 99 (1996) [hep-th/9601029].

[5] J. M. Maldacena, A. Strominger and E. Witten, JHEP **9712**, 002 (1997) [hep-th/9711053].

[6] A. Strominger, "Black hole entropy from near horizon microstates," JHEP **9802**, 009 (1998) [hep-th/9712251].

[7] J. L. Cardy, "Operator Content of Two-Dimensional Conformally Invariant Theories," Nucl. Phys. B **270**, 186 (1986).

[8] H. W. J. Bloete, J. L. Cardy and M. P. Nightingale, "Conformal Invariance, the Central Charge, and Universal Finite Size Amplitudes at Criticality," Phys. Rev. Lett. **56**, 742 (1986).

[9] S. Hawking, J. M. Maldacena and A. Strominger, "DeSitter entropy, quantum entanglement and AdS/CFT," JHEP **0105**, 001 (2001) [arXiv:hep-th/0002145].

[10] M. Banados, T. Brotz and M. E. Ortiz, "Quantum three-dimensional de Sitter space," Phys. Rev. D **59**, 046002 (1999) [arXiv:hep-th/9807216].

[11] T. Banks, "Some Thoughts on the Quantum Theory of de Sitter Space," arXiv:astro-ph/0305037.

[12] T. Banks, "More thoughts on the quantum theory of stable de Sitter space," arXiv:hep-th/0503066.

[13] T. Banks, B. Fiol and A. Morisse, "Towards a quantum theory of de Sitter space," JHEP **0612**, 004 (2006) [arXiv:hep-th/0609062].

[14] E. Witten, "Quantum gravity in de Sitter space," arXiv:hep-th/0106109.

[15] A. Strominger, "The dS/CFT correspondence," JHEP **0110**, 034 (2001) [arXiv:hep-th/0106113].

[16] J. M. Maldacena, "Non-Gaussian features of primordial fluctuations in single field inflationary models," JHEP **0305**, 013 (2003) [arXiv:astro-ph/0210603].

[17] J. M. Maldacena, "The Large N limit of superconformal field theories and supergravity," Adv. Theor. Math. Phys. **2**, 231 (1998) [hep-th/9711200].

[18] R. Bousso, "Proliferation of de Sitter space," Phys. Rev. D **58**, 083511 (1998) [arXiv:hep-th/9805081].

[19] A. M. Polyakov, "De Sitter Space and Eternity," Nucl. Phys. B **797**, 199 (2008) [arXiv:0709.2899 [hep-th]].

[20] N. C. Tsamis and R. P. Woodard, "The quantum gravitational back-reaction on inflation," Annals Phys. **253**, 1 (1997) [arXiv:hep-ph/9602316].

[21] J. B. Hartle, S. W. Hawking, "Wave Function of the Universe," Phys. Rev. **D28**, 2960-2975 (1983).

[22] C. M. Hull, "Timelike T duality, de Sitter space, large N gauge theories and topological field theory," JHEP **9807**, 021 (1998). [hep-th/9806146].

[23] D. Harlow, D. Stanford, "Operator Dictionaries and Wave Functions in AdS/CFT and dS/CFT," [arXiv:1104.2621 [hep-th]].

[24] D. Anninos, G. S. Ng, A. Strominger, "Asymptotic Symmetries and Charges in De Sitter Space," Class. Quant. Grav. **28**, 175019 (2011). [arXiv:1009.4730 [gr-qc]].

[25] D. Anninos, T. Hartman, A. Strominger, "Higher Spin Realization of the dS/CFT Correspondence," [arXiv:1108.5735 [hep-th]].

[26] N. Goheer, M. Kleban, L. Susskind, "The Trouble with de Sitter space," JHEP **0307**, 056 (2003). [hep-th/0212209].

[27] M. K. Parikh, E. P. Verlinde, "De Sitter holography with a finite number of states," JHEP **0501**, 054 (2005). [hep-th/0410227].

[28] D. Anninos, "De Sitter Musings," Int. J. Mod. Phys. A **27**, 1230013 (2012) [arXiv:1205.3855 [hep-th]].

[29] T. Banks, W. Fischler, S. Paban, "Recurrent nightmares? Measurement theory in de Sitter space," JHEP **0212**, 062 (2002). [hep-th/0210160].

[30] L. Susskind, "Addendum to Fast Scramblers," [arXiv:1101.6048 [hep-th]].

[31] M. K. Parikh, J. P. van der Schaar, "Not One Bit of de Sitter Information," JHEP **0809**, 041 (2008). [arXiv:0804.0231 [hep-th]].

[32] A. Castro, N. Lashkari, A. Maloney, "A de Sitter Farey Tail," Phys. Rev. **D83**, 124027 (2011). [arXiv:1103.4620 [hep-th]].

[33] M. Alishahiha, A. Karch, E. Silverstein, D. Tong, "The dS/dS correspondence," AIP Conf. Proc. **743**, 393-409 (2005). [hep-th/0407125].

[34] E. Silverstein, "AdS and dS entropy from string junctions: or, The Function of junction conjunctions," In *Shifman, M. (ed.) et al.: From fields to strings, vol. 3* 1848-1863. [hep-th/0308175].

[35] D. Anninos, G. S. Ng, A. Strominger, "Future Boundary Conditions in De Sitter Space," [arXiv:1106.1175 [hep-th]].

[36] D. Anninos, S. A. Hartnoll, D. M. Hofman, "Static Patch Solipsism: Conformal Symmetry of the de Sitter Worldline," [arXiv:1109.4942 [hep-th]].

[37] P. H. Ginsparg and M. J. Perry, "Semiclassical Perdurance Of De Sitter Space," Nucl. Phys. B **222**, 245 (1983).

[38] H. Nariai, Sci. Re. Tohoku Univ. Ser. 1 **34**, 160 (1950). H. Nariai, "On a new cosmological solution of Einstein's field equations of gravitation," General Relativity and Gravitation **31**, 963 (1999).

[39] T. Damour, in: "Quelques propriétés mécaniques, électromagnétiques, thermodynamiques et quantiques des trous noirs"; Thèse de Doctorat d'Etat, Université Pierre et Marie Curie, Paris VI, 1979.

[40] T. Damour, "Surface effects in Black Hole Physics," in *Proceedings of the second Marcel Grossmann Meeting on general Relativity*, Ed. R.Ruffini, North-Holland, 1982.

[41] R. H. Price and K. S. Thorne, "Membrane Viewpoint on Black Holes: Properties and eEvolution of the Stretched Horizon," Phys. Rev. D **33**, 915 (1986).

[42] J. Khoury, M. Parikh, "Mach's Holographic Principle," Phys. Rev. **D80**, 084004 (2009). [hep-th/0612117].

[43] I. Bredberg, C. Keeler, V. Lysov, A. Strominger, "Wilsonian Approach to Fluid/Gravity Duality," JHEP **1103**, 141 (2011). [arXiv:1006.1902 [hep-th]].

[44] I. Bredberg, C. Keeler, V. Lysov and A. Strominger, "From Navier-Stokes To Einstein," [arXiv:1101.2451].

[45] I. Bredberg, A. Strominger, "Black Holes as Incompressible Fluids on the Sphere," [arXiv:1106.3084 [hep-th]].

[46] G. Policastro, D. T. Son and A. O. Starinets, "The shear viscosity of strongly coupled N = 4 supersymmetric Yang-Mills plasma," Phys. Rev. Lett. **87**, 081601 (2001) [arXiv:hep-th/0104066].

[47] S. Bhattacharyya, S. Minwalla and S. R. Wadia, "The Incompressible Non-Relativistic Navier-Stokes Equation from Gravity," JHEP **0908**, 059 (2009) [arXiv:0810.1545 [hep-th]].

[48] S. Bhattacharyya, V. E. Hubeny, S. Minwalla and M. Rangamani, "Nonlinear Fluid Dynamics from Gravity," JHEP **0802**, 045 (2008). [arXiv:0712.2456 [hep-th]].

[49] G. Compére, P. McFadden, K. Skenderis and M. Taylor "The holographic fluid dual to vacuum Einstein gravity," [arXiv:1103.3022 [hep-th]].

[50] H. Kodama, A. Ishibashi, O. Seto, "Brane world cosmology: Gauge invariant formalism for perturbation," Phys. Rev. **D62**, 064022 (2000). [hep-th/0004160].

[51] H. Kodama, A. Ishibashi, "A Master equation for gravitational perturbations of maximally symmetric black holes in higher dimensions," Prog. Theor. Phys. **110**, 701-722 (2003). [hep-th/0305147].

[52] M. Abramowitz, I. Stegun, eds., "Handbook of Mathematical Functions with Formulas, Graphs, and Mathematical Tables," (1972), New York: Dover Publications, ISBN 978-0-486-61272-0

[53] P. Kovtun, D. T. Son, A. O. Starinets, "Viscosity in strongly interacting quantum

field theories from black hole physics," Phys. Rev. Lett. **94**, 111601 (2005). [hep-th/0405231].

[54] A. Lopez-Ortega, "Quasinormal modes of D-dimensional de Sitter spacetime," Gen. Rel. Grav. **38**, 1565-1591 (2006). [gr-qc/0605027].

[55] N. Iqbal, H. Liu, "Universality of the hydrodynamic limit in AdS/CFT and the membrane paradigm," Phys. Rev. **D79**, 025023 (2009). [arXiv:0809.3808 [hep-th]].

[56] D. Forster, D. R. Nelson and M. J. Stephen, "Large-distance and long-time properties of a randomly stirred fluid," Phys. Rev. A **16**, 732 (1977).

[57] I. S. Booth, R. B. Mann, "Cosmological pair production of charged and rotating black holes," Nucl. Phys. **B539**, 267-306 (1999). [gr-qc/9806056].

[58] D. Anninos, T. Hartman, "Holography at an Extremal De Sitter Horizon," JHEP **1003**, 096 (2010). [arXiv:0910.4587 [hep-th]].

[59] D. Anninos, T. Anous, "A de Sitter Hoedown," JHEP **1008**, 131 (2010). [arXiv:1002.1717 [hep-th]].

[60] D. Birmingham, "Topological black holes in Anti-de Sitter space," Class. Quant. Grav. **16**, 1197-1205 (1999). [hep-th/9808032].

[61] D. Birmingham, S. Mokhtari, "Exact Gravitational Quasinormal Frequencies of Topological Black Holes," Phys. Rev. **D74**, 084026 (2006). [hep-th/0609028].

[62] R. Emparan, "AdS / CFT duals of topological black holes and the entropy of zero energy states," JHEP **9906**, 036 (1999). [hep-th/9906040].

[63] G. Horowitz, A. Lawrence, E. Silverstein, "Insightful D-branes," JHEP **0907**, 057 (2009). [arXiv:0904.3922 [hep-th]].

[64] A. Erdelyi, "Higher transcendental functions, Vol. 1," (1955), New York, McGraw-Hill, ISBN 0-486-44614-X

[65] Z. X. Wang and D. R. Guo, "Special Functions," (1989), Singapore, World Scientific.

[66] C. Eling, I. Fouxon and Y. Oz, "The Incompressible Navier-Stokes Equations from Black Hole Membrane Dynamics," [arXiv:0905.3638[hep-th]].

[67] P. C. W. Davies, "Thermodynamic phase transitions of Kerr-Newman black holes in de Sitter space," Class. Quant. Grav. **6**, 1909 (1989).

[68] M. H. Dehghani, "Quasilocal thermodynamics of Kerr de Sitter spacetimes and the dS/CFT correspondence," Phys. Rev. D **65**, 104030 (2002) [arXiv:hep-th/0201128].

[69] T. Tachizawa and K. i. Maeda, "Superradiance in the Kerr-de Sitter space-time,"

[70] P. R. Brady, C. M. Chambers, W. G. Laarakkers and E. Poisson, "Radiative falloff in Schwarzschild-de Sitter spacetime," Phys. Rev. D **60**, 064003 (1999) [arXiv:gr-qc/9902010].

[71] N. A. Chernikov and E. A. Tagirov, "Quantum theory of scalar fields in de Sitter space-time," Annales Poincare Phys. Theor. A **9**, 109 (1968).

[72] E. Mottola, "Particle Creation In De Sitter Space," Phys. Rev. D **31**, 754 (1985).

[73] B. Allen, "Vacuum States In De Sitter Space," Phys. Rev. D **32**, 3136 (1985).

[74] D. Anninos and T. Hartman, "Holography at an Extremal De Sitter Horizon," arXiv:0910.4587 [hep-th].

[75] J. D. Brown and M. Henneaux, "Central Charges in the Canonical Realization of Asymptotic Symmetries: An Example from Three-Dimensional Gravity," Commun. Math. Phys. **104**, 207 (1986).

[76] M. Guica, T. Hartman, W. Song and A. Strominger, "The Kerr/CFT Correspondence," Phys. Rev. D **80**, 124008 (2009) [arXiv:0809.4266 [hep-th]].

[77] A. M. Ghezelbash and R. B. Mann, "Entropy and mass bounds of Kerr-de Sitter spacetimes," Phys. Rev. D **72**, 064024 (2005) [arXiv:hep-th/0412300].

[78] V. Balasubramanian, J. de Boer and D. Minic, "Mass, entropy and holography in asymptotically de Sitter spaces," Phys. Rev. D **65**, 123508 (2002) [arXiv:hep-th/0110108].

[79] J. D. Brown and J. W. . York, "Quasilocal energy and conserved charges derived from the gravitational action," Phys. Rev. D **47**, 1407 (1993) [arXiv:gr-qc/9209012].

[80] R. Bousso and S. W. Hawking, "The Probability for primordial black holes," Phys. Rev. D **52**, 5659 (1995) [arXiv:gr-qc/9506047].

[81] I. Bredberg, T. Hartman, W. Song and A. Strominger, "Black Hole Superradiance From Kerr/CFT," arXiv:0907.3477 [hep-th].

[82] A. Castro and F. Larsen, "Near Extremal Kerr Entropy from AdS_2 Quantum Gravity," JHEP **0912**, 037 (2009) [arXiv:0908.1121 [hep-th]].

[83] D. Anninos, "Sailing from Warped AdS_3 to Warped dS_3 in Topologically Massive Gravity," arXiv:0906.1819 [hep-th].

[84] J. Doukas, H. T. Cho, A. S. Cornell and W. Naylor, "Graviton emission from simply rotating Kerr-de Sitter black holes: Transverse traceless tensor graviton modes," Phys. Rev. D **80**, 045021 (2009) [arXiv:0906.1515 [hep-th]].

[85] N. D. Birrell and P. C. W. Davies, "Quantum Fields In Curved Space," *Cambridge, UK: Univ. Pr. (1982) 340p*

[86] S. P. Kim and D. N. Page, "Schwinger Pair Production in dS_2 and AdS_2," Phys. Rev. D **78**, 103517 (2008) [arXiv:0803.2555 [hep-th]].

[87] Abramowitz, M. and Stegun, I. A. 1965 "Handbook of Mathematical Functions". *New York, NY: Dover (1965)* pp 559.

[88] V. Cardoso and J. P. S. Lemos, "Quasinormal modes of the near extremal Schwarzschild-de Sitter black hole," Phys. Rev. D **67**, 084020 (2003) [arXiv:gr-qc/0301078].

[89] I. R. Klebanov and E. Witten, "AdS/CFT correspondence and symmetry breaking," Nucl. Phys. B **556**, 89 (1999) [arXiv:hep-th/9905104].

[90] D. T. Son and A. O. Starinets, "Minkowski-space correlators in AdS/CFT correspondence: Recipe and applications," JHEP **0209**, 042 (2002) [arXiv:hep-th/0205051].

[91] U. Khanal, "Rotating Black Hole In Asymptotic De Sitter Space: Perturbation Of The Space-Time With Spin Fields," Phys. Rev. D **28**, 1291 (1983).

[92] R. Bousso, A. Maloney and A. Strominger, "Conformal vacua and entropy in de Sitter space," Phys. Rev. D **65**, 104039 (2002) [arXiv:hep-th/0112218].

[93] J. L. Cardy, "Conformal Invariance and Universality in finite size scaling," In *Itzykson, C. (ed.) ed al.: Conformal Invariance and applications to statistical mechanics* (J. Phys. A17 (1984) L385-L387)

[94] B. Chen and C. S. Chu, "Real-time correlators in Kerr/CFT correspondence," arXiv:1001.3208 [hep-th].

[95] H. Liu, J. McGreevy and D. Vegh, "Non-Fermi liquids from holography," arXiv:0903.2477 [hep-th].

[96] T. Faulkner, H. Liu, J. McGreevy and D. Vegh, "Emergent quantum criticality, Fermi surfaces, and AdS2," arXiv:0907.2694 [hep-th].

[97] P. G. Debenedetty "Supercooled and glassy water" 2003 J. Phys.: Condens. Matter 15 R1669 doi:10.1088/0953-8984/15/45/R01

[98] J. Jurchan, "Glasses" , *Seminaire Poincare XIII* (2009)

[99] D. Anninos and F. Denef, "Cosmic Clustering," arXiv:1111.6061 [hep-th].

[100] F. Denef, "TASI lectures on complex structures," arXiv:1104.0254 [hep-th].

[101] D. A. Roberts and D. Stanford, "On memory in exponentially expanding spaces," arXiv:1210.5238 [hep-th].

[102] M. Mezard, G. Parisi and M. A. Virasoro, "Spin Glass Theory and Beyond," vol. 9, Lecture Notes in Physics, (World Scientific, 1987). ISBN 9971501155. URL http://books.google.com/books?id=ZIF9QgAACAAJ.

[103] F. Denef, "Quantum quivers and Hall / hole halos," JHEP **0210**, 023 (2002). [hep-th/0206072].

[104] F. Denef, "Supergravity flows and D-brane stability," JHEP **0008**, 050 (2000). [hep-th/0005049].

[105] F. Denef and G. W. Moore, "Split states, entropy enigmas, holes and halos," JHEP **1111**, 129 (2011) [hep-th/0702146 [HEP-TH]].

[106] D. Anninos, T. Anous, J. Barandes, F. Denef and B. Gaasbeek, "Hot Halos and Galactic Glasses," JHEP **1201**, 003 (2012) [arXiv:1108.5821 [hep-th]].

[107] B. Chowdhury and B. Vercnocke, "New instability of non-extremal black holes: spitting out supertubes," JHEP **1202**, 116 (2012) [arXiv:1110.5641 [hep-th]].

[108] H. Kim, J. Park, Z. Wang and P. Yi, "Ab Initio Wall-Crossing," JHEP **1109**, 079 (2011) [arXiv:1107.0723 [hep-th]].

[109] T. Dimofte and S. Gukov, "Refined, Motivic, and Quantum," Lett. Math. Phys. **91**, 1 (2010) [arXiv:0904.1420 [hep-th]].

[110] E. Andriyash, F. Denef, D. L. Jafferis and G. W. Moore, "Wall-crossing from supersymmetric galaxies," JHEP **1201**, 115 (2012) [arXiv:1008.0030 [hep-th]].

[111] J. Manschot, B. Pioline and A. Sen, "Wall Crossing from Boltzmann Black Hole Halos," JHEP **1107**, 059 (2011) [arXiv:1011.1258 [hep-th]].

[112] S. G. Avery and J. Michelson, "Mechanics and Quantum Supermechanics of a Monopole Probe Including a Coulomb Potential," Phys. Rev. D **77**, 085001 (2008) [arXiv:0712.0341 [hep-th]].

[113] L. N. Hand and J. Finch, "Analytical Mechanics," Cambridge University Press (1998) ISBN 0521573270

[114] V. Arnold, "Mathematical Methods of Classical Mechanics," Springer-Verlag (1989) ISBN 0387968903

[115] A. Nersessian and V. Ohanyan, Theor. Math. Phys. **155**, 618 (2008) [arXiv:0705.0727 [math-ph]].

[116] S. Krivonos, A. Nersessian and V. Ohanyan, Phys. Rev. D **75**, 085002 (2007) [hep-th/0611268].

[117] S. Bellucci and V. Ohanyan, Phys. Lett. A **372**, 5765 (2008) [arXiv:0802.1671 [hep-th]].

[118] S. Bellucci, S. Krivonos and V. Ohanyan, Phys. Rev. D **76**, 105023 (2007) [arXiv:0706.1469 [hep-th]].

[119] M. R. Douglas and G. W. Moore, "D-branes, quivers, and ALE instantons," hep-th/9603167.

[120] D. -E. Diaconescu and R. Entin, "A Nonrenormalization theorem for the d = 1, N=8 vector multiplet," Phys. Rev. D **56**, 8045 (1997) [hep-th/9706059].

[121] E. D'Hoker and L. Vinet, "Spectrum (super)symmetries Of Particles In A Coulomb Potential," Nucl. Phys. B **260**, 79 (1985).

[122] E. D'Hoker and L. Vinet, "Hidden Symmetries And Accidental Degeneracy For A Spin 1/2 Particle In The Field Of A Dyon," Lett. Math. Phys. **12**, 71 (1986).

[123] E. D'Hoker and L. Vinet, "Constants Of Motion For A Spin 1/2 Particle In The Field Of A Dyon," Phys. Rev. Lett. **55**, 1043 (1985).

[124] L. Feher, P. A. Horvathy and L. O'Raifeartaigh, "Separating The Dyon System," Phys. Rev. D **40**, 666 (1989).

[125] L. G. Feher and P. A. Horvathy, "Non-relativistic scattering of a spin-1/2 particle off a self-dual monopole," Mod. Phys. Lett. A **3**, 1451 (1988) [arXiv:0903.0249 [hep-th]].

[126] F. Bloore and P. A. Horvathy, "Helicity supersymmetry of dyons," J. Math. Phys. **33**, 1869 (1992) [hep-th/0512144].

[127] R. A. Coles and G. Papadopoulos, "The Geometry of the one-dimensional supersymmetric nonlinear sigma models," Class. Quant. Grav. **7**, 427 (1990).

[128] P. A. Horvathy, "The Biedenharn approach to relativistic Coulomb-type problems," Rev. Math. Phys. **18**, 311 (2006) [hep-th/0601123].

[129] E. Ivanov, S. Krivonos and O. Lechtenfeld, "New variant of N=4 superconformal mechanics," JHEP **0303**, 014 (2003) [hep-th/0212303].

[130] M. R. Douglas, D. N. Kabat, P. Pouliot and S. H. Shenker, "D-branes and short distances in string theory," Nucl. Phys. B **485**, 85 (1997) [hep-th/9608024].

[131] http://en.wikipedia.org/wiki/Superintegrable_Hamiltonian_system; http://en.wikipedia.org/wiki/Integrable_system

[132] R. Alicki, J. R. Klauder and J. Lewandowski, "Landau-level ground state degeneracy and its relevance for a general quantization procedure," Phys. Rev. A, vol. 48, Num. 4 (1993)

[133] H. Waalkens, H. R. Dullin and P. Richter, "The Problem of Two Fixed Centers: Bifurcations, Actions, Monodromy," Physica D: Non-linear Phenomena, Vol. 196, Issue 3-4 (2004)

[134] L. Euler, Nov. Comm. Acad. Imp. Petropolitanae, 10, pp. 207-242, 11, pp. 152-184; Mémoires de l'Acad. de Berlin, 11, 228-249.

[135] E. W. Weisstein, "Sphere Point Picking," From MathWorld–A Wolfram Web Resource. http://mathworld.wolfram.com/SpherePointPicking.html

[136] F. Barthe, O. Guedon, S. Mendelson and A. Naor, "A Probabilistic Approach to the Geometry of the ℓ_p^n-Ball," Ann. Probab. 33, 480-513 (2005)

[137] E. W. Weisstein, "Ball Point Picking," From MathWorld–A Wolfram Web Resource. http://mathworld.wolfram.com/BallPointPicking.html

[138] E. W. Weisstein, "Disk Point Picking," From MathWorld–A Wolfram Web Resource. http://mathworld.wolfram.com/DiskPointPicking.html

[139] J. Louko, D. Marolf and S. F. Ross, "On geodesic propagators and black hole holography," Phys. Rev. D **62**, 044041 (2000) [hep-th/0002111].

[140] L. Fidkowski, V. Hubeny, M. Kleban and S. Shenker, "The Black hole singularity in AdS / CFT," JHEP **0402**, 014 (2004) [hep-th/0306170].

[141] G. Festuccia and H. Liu, "Excursions beyond the horizon: Black hole singularities in Yang-Mills theories. I.," JHEP **0604**, 044 (2006) [hep-th/0506202].

[142] P. Kraus, H. Ooguri and S. Shenker, "Inside the horizon with AdS / CFT," Phys. Rev. D **67**, 124022 (2003) [hep-th/0212277].

[143] J. de Boer, F. Denef, S. El-Showk, I. Messamah and D. Van den Bleeken, "Black hole bound states in AdS(3) x S**2," JHEP **0811**, 050 (2008) [arXiv:0802.2257 [hep-th]].

[144] E. J. Heller, Phys. Rev. Lett. **16**, 1515 (1984)

[145] B. Vercnocke, "Hidden Structures of Black Holes," [arXiv:1011.6384 [hep-th]].

[146] P. Galli, T. Ortin, J. Perz, C. S. Shahbazi, "Non-extremal black holes of N=2, d=4 supergravity," JHEP **1107**, 041 (2011). [arXiv:1105.3311 [hep-th]].

[147] I. Bena, A. Puhm, B. Vercnocke, "Metastable Supertubes and non-extremal Black Hole Microstates," [arXiv:1109.5180 [hep-th]].

[148] B. de Wit, P. G. Lauwers, A. Van Proeyen, "Lagrangians of N=2 Supergravity - Matter Systems," Nucl. Phys. **B255**, 569 (1985).

[149] L. Andrianopoli, M. Bertolini, A. Ceresole, R. D'Auria, S. Ferrara, P. Fre, T. Magri, "N=2 supergravity and N=2 superYang-Mills theory on general scalar manifolds: Symplectic covariance, gaugings and the momentum map," J. Geom. Phys. **23**, 111-189 (1997). [arXiv:hep-th/9605032 [hep-th]].

[150] M. Billo, S. Cacciatori, F. Denef, P. Fre, A. Van Proeyen, D. Zanon, "The 0-brane action in a general D = 4 supergravity background," Class. Quant. Grav. **16**, 2335-2358 (1999). [hep-th/9902100].

[151] G. W. Gibbons, "Antigravitating Black Hole Solitons with Scalar Hair in N=4 Supergravity," Nucl. Phys. **B207**, 337-349 (1982).

[152] A. Ceresole and G. Dall'Agata, "Flow Equations for Non-BPS Extremal Black Holes," JHEP **0703**, 110 (2007) [arXiv:hep-th/0702088].

[153] J. Perz, P. Smyth, T. Van Riet, B. Vercnocke, "First-order flow equations for extremal and non-extremal black holes," JHEP **0903**, 150 (2009). [arXiv:0810.1528 [hep-th]].

[154] S. Ferrara, A. Gnecchi and A. Marrani, "d=4 Attractors, Effective Horizon Radius and Fake Supergravity," Phys. Rev. D **78**, 065003 (2008) [arXiv:0806.3196 [hep-th]].

[155] E. G. Gimon, F. Larsen, J. Simon, "Constituent Model of Extremal non-BPS Black Holes," JHEP **0907**, 052 (2009). [arXiv:0903.0719 [hep-th]].

[156] S. Ferrara, G. W. Gibbons, R. Kallosh, "Black holes and critical points in moduli space," Nucl. Phys. **B500**, 75-93 (1997). [hep-th/9702103].

[157] D. I. Olive, "Classical Solutions In Gauge Theories - Spherically Symmetric Monopoles - Lax Pairs And Toda Lattices," In *Bad Honnef 1980, Proceedings, Current Topics In Elementary Particle Physics*, 199-217 and London Imp. Coll. - ICTP-80-81-01 (80,REC.NOV.) 19p.

[158] P. C. W. Davies, "Thermodynamics Of Black Holes," Proc. Roy. Soc. Lond. **A353**, 499-521 (1977).

[159] M. Shmakova, "Calabi-Yau black holes," Phys. Rev. **D56**, 540-544 (1997). [hep-th/9612076].

[160] D. J. Thouless, P. W. Anderson, R. G. Palmer, *Phil. Mag.* **35** 593 (1977)

[161] A. J. Bray, M. A. Moore, "Metastable States in Spin Glasses," J. Phys. **C**: Solid St. Phys., 13 (1980) L469-76

[162] R. Monasson, "Structural Glass Transition and the Entropy of the Metastable States," *Phys. Rev. Let.*, Vol. **75**, Issue 15 (1995) [arXiv:cond-mat/9503166]

[163] I. Bena, C. -W. Wang, N. P. Warner, "Mergers and typical black hole microstates," JHEP **0611**, 042 (2006). [hep-th/0608217].

[164] P. Berglund, E. G. Gimon and T. S. Levi, "Supergravity microstates for BPS black holes and black rings," JHEP 0606 (2006) 007 [arXiv:hep-th/0505167].

[165] I. Bena and N. P. Warner, "Bubbling supertubes and foaming black holes," Phys. Rev. D 74 (2006) 066001 [arXiv:hep-th/0505166].

[166] I. Bena, C. W. Wang and N. P. Warner, "The foaming three-charge black hole," [arXiv:hep-th/0604110].

[167] V. Balasubramanian, E. G. Gimon and T. S. Levi, "Four dimensional black hole microstates: From D-branes to spacetime foam," [arXiv:hep-th/0606118].

[168] A. Saxena, G. Potvin, S. Giusto and A. W. Peet, "Smooth geometries with four charges in four dimensions," JHEP 0604 (2006) 010 [arXiv:hep-th/0509214].

[169] M. C. N. Cheng, "More Bubbling Solutions," JHEP **0703**, 070 (2007). [hep-th/0611156].

[170] S. W. Hawking, "Black Holes and Thermodynamics," Phys. Rev. **D13**, 191-197 (1976).

[171] D. J. Gross, M. J. Perry, L. G. Yaffe, "Instability of Flat Space at Finite Temperature," Phys. Rev. **D25**, 330-355 (1982).

[172] D. N. Page, "Black Hole Formation In A Box," Gen. Rel. Grav. **13**, 1117-1126 (1981).

[173] S. W. Hawking, D. N. Page, "Thermodynamics of Black Holes in anti-De Sitter Space," Commun. Math. Phys. **87**, 577 (1983).

[174] A. Chamblin, R. Emparan, C. V. Johnson, R. C. Myers, "Charged AdS black holes and catastrophic holography," Phys. Rev. **D60**, 064018 (1999). [hep-th/9902170].

[175] S. Carlip, S. Vaidya, "Phase transitions and critical behavior for charged black holes," Class. Quant. Grav. **20**, 3827-3838 (2003). [gr-qc/0306054].

[176] B. de Wit, P. G. Lauwers, R. Philippe, S. Q. Su and A. Van Proeyen, "Gauge and Matter Fields Coupled to N=2 Supergravity," Phys. Lett. B **134**, 37 (1984).

[177] A. Van Proeyen, "Supergravity with Fayet-Iliopoulos terms and R-symmetry," Fortsch. Phys. **53**, 997 (2005) [hep-th/0410053].

[178] P. Binetruy, G. Dvali, R. Kallosh and A. Van Proeyen, "Fayet-Iliopoulos terms in supergravity and cosmology," Class. Quant. Grav. **21**, 3137 (2004) [hep-th/0402046].

[179] K. Hristov, "Lessons from the Vacuum Structure of 4d N=2 Supergravity," arXiv:1207.3830 [hep-th].

[180] K. Behrndt, D. Lust, W. A. Sabra, "Stationary solutions of N=2 supergravity," Nucl. Phys. **B510**, 264-288 (1998). [hep-th/9705169].

[181] G. Lopes Cardoso, B. de Wit, J. Kappeli, T. Mohaupt, "Stationary BPS solutions in N=2 supergravity with R**2 interactions," JHEP **0012**, 019 (2000). [hep-th/0009234].

[182] B. Bates, F. Denef, "Exact solutions for supersymmetric stationary black hole composites," [hep-th/0304094].

[183] M. J. Duff and J. T. Liu, "Anti-de Sitter black holes in gauged N = 8 supergravity," Nucl. Phys. B **554**, 237 (1999) [hep-th/9901149].

[184] S. S. Gubser, "Breaking an Abelian gauge symmetry near a black hole horizon," Phys. Rev. D **78**, 065034 (2008) [arXiv:0801.2977 [hep-th]].

[185] S. A. Hartnoll, C. P. Herzog and G. T. Horowitz, "Building a Holographic Superconductor," Phys. Rev. Lett. **101**, 031601 (2008) [arXiv:0803.3295 [hep-th]].

[186] F. Denef and S. A. Hartnoll, "Landscape of superconducting membranes," Phys. Rev. D **79**, 126008 (2009) [arXiv:0901.1160 [hep-th]].

[187] S. Gukov, C. Vafa and E. Witten, "CFT's from Calabi-Yau four folds," Nucl. Phys. B **584**, 69 (2000) [Erratum-ibid. B **608**, 477 (2001)] [hep-th/9906070].

[188] P. Breitenlohner and D. Z. Freedman, "Stability in Gauged Extended Supergravity," Annals Phys. **144**, 249 (1982).

[189] P. Kovtun and A. Ritz, "Universal conductivity and central charges," Phys. Rev. D **78**, 066009 (2008) [arXiv:0806.0110 [hep-th]].

[190] O. Aharony, O. Bergman, D. L. Jafferis and J. Maldacena, "N=6 superconformal Chern-Simons-matter theories, M2-branes and their gravity duals," JHEP **0810**, 091 (2008) [arXiv:0806.1218 [hep-th]].

[191] M. M. Caldarelli and D. Klemm, "Supersymmetry of Anti-de Sitter black holes," Nucl. Phys. B **545**, 434 (1999) [hep-th/9808097].

[192] K. Behrndt, M. Cvetic and W. A. Sabra, "Nonextreme black holes of five-dimensional N=2 AdS supergravity," Nucl. Phys. B **553**, 317 (1999) [hep-th/9810227].

[193] W. A. Sabra, "Anti-de Sitter BPS black holes in N=2 gauged supergravity," Phys. Lett. B **458**, 36 (1999) [hep-th/9903143].

[194] A. H. Chamseddine and W. A. Sabra, "Magnetic and dyonic black holes in D = 4 gauged supergravity," Phys. Lett. B **485**, 301 (2000) [hep-th/0003213].

[195] S. Cucu, H. Lu and J. F. Vazquez-Poritz, "Interpolating from AdS(D-2) x S**2 to AdS(D)," Nucl. Phys. B **677**, 181 (2004) [hep-th/0304022].

[196] Z. -W. Chong, M. Cvetic, H. Lu and C. N. Pope, "Charged rotating black holes in four-dimensional gauged and ungauged supergravities," Nucl. Phys. B **717**, 246 (2005) [hep-th/0411045].

[197] M. Cvetic, G. W. Gibbons, H. Lu, C. N. Pope and , "Rotating black holes in gauged supergravities: Thermodynamics, supersymmetric limits, topological solitons and time machines," hep-th/0504080.

[198] S. L. Cacciatori and D. Klemm, "Supersymmetric AdS(4) black holes and attractors," JHEP **1001**, 085 (2010) [arXiv:0911.4926 [hep-th]].

[199] T. Kimura, "Non-supersymmetric Extremal RN-AdS Black Holes in N=2 Gauged Supergravity," JHEP **1009**, 061 (2010) [arXiv:1005.4607 [hep-th]].

[200] K. Goldstein, N. Iizuka, S. Kachru, S. Prakash, S. P. Trivedi and A. Westphal, "Holography of Dyonic Dilaton Black Branes," JHEP **1010**, 027 (2010) [arXiv:1007.2490 [hep-th]].

[201] D. D. K. Chow, "Two-charge rotating black holes in four-dimensional gauged supergravity," Class. Quant. Grav. **28**, 175004 (2011) [arXiv:1012.1851 [hep-th]].

[202] G. Dall'Agata and A. Gnecchi, "Flow equations and attractors for black holes in N = 2 U(1) gauged supergravity," JHEP **1103**, 037 (2011) [arXiv:1012.3756 [hep-th]].

[203] K. Hristov and S. Vandoren, "Static supersymmetric black holes in AdS_4 with spherical symmetry," JHEP **1104**, 047 (2011) [arXiv:1012.4314 [hep-th]].

[204] C. Toldo and S. Vandoren, "Static nonextremal AdS4 black hole solutions," JHEP **1209**, 048 (2012) [arXiv:1207.3014 [hep-th]].

[205] D. Klemm and O. Vaughan, "Nonextremal black holes in gauged supergravity and the real formulation of special geometry," arXiv:1207.2679 [hep-th].

[206] D. Klemm and O. Vaughan, "Nonextremal black holes in gauged supergravity and the real formulation of special geometry II," Class. Quant. Grav. **30**, 065003 (2013) [arXiv:1211.1618 [hep-th]].

[207] A. Gnecchi and C. Toldo, "On the non-BPS first order flow in N=2 U(1)-gauged Supergravity," JHEP **1303**, 088 (2013) [arXiv:1211.1966 [hep-th]].

[208] T. Hertog and K. Maeda, "Black holes with scalar hair and asymptotics in N = 8 supergravity," JHEP **0407**, 051 (2004) [hep-th/0404261].

[209] A. J. Amsel and M. M. Roberts, "Stability in Holographic Theories with Irrelevant Deformations," arXiv:1211.2840 [hep-th].

[210] V. Balasubramanian and P. Kraus, "A Stress tensor for Anti-de Sitter gravity," Commun. Math. Phys. **208**, 413 (1999) [hep-th/9902121].

[211] J. Louko and S. N. Winters-Hilt, "Hamiltonian thermodynamics of the Reissner-Nordstrom anti-de Sitter black hole," Phys. Rev. D **54**, 2647 (1996) [gr-qc/9602003].

[212] E. Witten, "Anti-de Sitter space, thermal phase transition, and confinement in gauge theories," Adv. Theor. Math. Phys. **2**, 505 (1998) [hep-th/9803131].

[213] N. Ogawa, T. Takayanagi and T. Ugajin, "Holographic Fermi Surfaces and Entanglement Entropy," JHEP **1201**, 125 (2012) [arXiv:1111.1023 [hep-th]].

[214] L. Huijse, S. Sachdev and B. Swingle, "Hidden Fermi surfaces in compressible states of gauge-gravity duality," Phys. Rev. B **85**, 035121 (2012) [arXiv:1112.0573 [cond-mat.str-el]].

[215] N. Iizuka, S. Kachru, N. Kundu, P. Narayan, N. Sircar, S. P. Trivedi and H. Wang, "Extremal Horizons with Reduced Symmetry: Hyperscaling Violation, Stripes, and a Classification for the Homogeneous Case," arXiv:1212.1948 [hep-th].

[216] E. Shaghoulian, "Holographic Entanglement Entropy and Fermi Surfaces," JHEP **1205**, 065 (2012) [arXiv:1112.2702 [hep-th]].

[217] X. Dong, S. Harrison, S. Kachru, G. Torroba and H. Wang, "Aspects of holography for theories with hyperscaling violation," JHEP **1206**, 041 (2012) [arXiv:1201.1905 [hep-th]].

[218] A. Donos, J. P. Gauntlett and C. Pantelidou, "Semi-local quantum criticality in string/M-theory," JHEP **1303**, 103 (2013) [arXiv:1212.1462 [hep-th]].

[219] A. Nersessian and V. Ohanyan, Theor. Math. Phys. 155, 618 (2008) [arXiv:0705.0727 [math-ph]].

[220] D. Anninos, T. Anous, F. Denef, G. Konstantinidis and E. Shaghoulian, "Supergoop Dynamics," arXiv:1205.1060 [hep-th].

[221] J. Manschot, B. Pioline, A. Sen and , "On the Coulomb and Higgs branch formulae for multi-centered black holes and quiver invariants," arXiv:1302.5498 [hep-th].

[222] J. Manschot, B. Pioline, A. Sen and , "From Black Holes to Quivers," JHEP **1211**, 023 (2012) [arXiv:1207.2230 [hep-th]].

[223] J. Manschot, B. Pioline, A. Sen and , "A Fixed point formula for the index of multi-centered N=2 black holes," JHEP **1105**, 057 (2011) [arXiv:1103.1887 [hep-th]].

[224] E. Witten, "SL(2,Z) action on three-dimensional conformal field theories with Abelian symmetry," In *Shifman, M. (ed.) et al.: From fields to strings, vol. 2* 1173-1200 [hep-th/0307041].

[225] E. Witten, "Anti-de Sitter space and holography," Adv. Theor. Math. Phys. **2**, 253 (1998) [hep-th/9802150].

[226] D. Cassani, P. Koerber and O. Varela, "All homogeneous N=2 M-theory truncations with supersymmetric AdS4 vacua," JHEP **1211**, 173 (2012) [arXiv:1208.1262 [hep-th]].

[227] A. Tomasiello, "New string vacua from twistor spaces," Phys. Rev. D **78**, 046007 (2008) [arXiv:0712.1396 [hep-th]].

[228] D. Cassani and A. -K. Kashani-Poor, "Exploiting N=2 in consistent coset reductions of type IIA," Nucl. Phys. B **817**, 25 (2009) [arXiv:0901.4251 [hep-th]].

[229] S. Franco, A. Hanany, J. Park and D. Rodriguez-Gomez, "Towards M2-brane Theories for Generic Toric Singularities," JHEP **0812**, 110 (2008) [arXiv:0809.3237 [hep-th]].

[230] S. Franco, I. R. Klebanov and D. Rodriguez-Gomez, "M2-branes on Orbifolds of the Cone over Q111," JHEP **0908**, 033 (2009) [arXiv:0903.3231 [hep-th]].

[231]

[231] J. P. Gauntlett, S. Kim, O. Varela and D. Waldram, "Consistent supersymmetric Kaluza-Klein truncations with massive modes," JHEP **0904**, 102 (2009) [arXiv:0901.0676 [hep-th]].

[232] A. Tomasiello and A. Zaffaroni, "Parameter spaces of massive IIA solutions," JHEP **1104**, 067 (2011) [arXiv:1010.4648 [hep-th]].

[233] D. Martelli and J. Sparks, "Notes on toric Sasaki-Einstein seven-manifolds and AdS(4) / CFT(3)," JHEP **0811**, 016 (2008) [arXiv:0808.0904 [hep-th]].

[234] M. Gabella, D. Martelli, A. Passias and J. Sparks, "N=2 supersymmetric AdS_4 solutions of M-theory," arXiv:1207.3082 [hep-th].

[235] D. Martelli and J. Sparks, "Toric geometry, Sasaki-Einstein manifolds and a new infinite class of AdS/CFT duals," Commun. Math. Phys. **262**, 51 (2006) [hep-th/0411238].

[236] J. P. Gauntlett, D. Martelli, J. F. Sparks and D. Waldram, "A New infinite class of Sasaki-Einstein manifolds," Adv. Theor. Math. Phys. **8**, 987 (2006) [hep-th/0403038].

[237] O. Aharony, O. Bergman and D. L. Jafferis, "Fractional M2-branes," JHEP **0811**, 043 (2008) [arXiv:0807.4924 [hep-th]].

[238] E. Witten, "Baryons and branes in anti-de Sitter space," JHEP **9807**, 006 (1998) [hep-th/9805112].

[239] S. S. Gubser and I. R. Klebanov, "Baryons and domain walls in an N=1 superconformal gauge theory," Phys. Rev. D **58**, 125025 (1998) [hep-th/9808075].

[240] D. Berenstein, C. P. Herzog and I. R. Klebanov, "Baryon spectra and AdS /CFT correspondence," JHEP **0206**, 047 (2002) [hep-th/0202150].

[241] M. J. Duff, B. E. W. Nilsson and C. N. Pope, "Kaluza-Klein Supergravity," Phys. Rept. **130**, 1 (1986).

[242] I. R. Klebanov, S. S. Pufu and T. Tesileanu, "Membranes with Topological Charge and AdS_4/CFT_3 Correspondence," Phys. Rev. D **81**, 125011 (2010) [arXiv:1004.0413 [hep-th]].

[243] A. Donos and J. P. Gauntlett, "Supersymmetric quantum criticality supported by baryonic charges," JHEP **1210**, 120 (2012) [arXiv:1208.1494 [hep-th]].

[244] E. D'Hoker, D. Z. Freedman, S. D. Mathur, A. Matusis and L. Rastelli, "Graviton and gauge boson propagators in AdS(d+1)," Nucl. Phys. B **562**, 330 (1999) [hep-th/9902042].

[245] C. E. Wayne "Vortices and Two-Dimensional Fluid Motion" Notices of the AMS. Vol 58, no. 1 (2011)